2013

Numerical simulations of plasma dynamics using the flowfield dependent variation (FDV) method

Bassem Girgis

NUMERICAL SIMULATIONS OF PLASMA DYNAMICS USING THE FLOWFIELD DEPENDENT VARIATION (FDV) METHOD

by

BASSEM GIRGIS

A DISSERTATION

Submitted in partial fulfillment of the requirements
for the degree of Doctor of Philosophy
in
The Department of Mechanical and Aerospace Engineering
to
The School of Graduate Studies
of
The University of Alabama in Huntsville

HUNTSVILLE, ALABAMA

2013

In presenting this dissertation in partial fulfillment of the requirements for a doctoral degree from The University of Alabama in Huntsville, I agree that the Library of this University shall make it freely available for inspection. I further agree that permission for extensive copying for scholarly purposes may be granted by my advisor or, in his/her absence, by the Chair of the Department or the Dean of the School of Graduate Studies. It is also understood that due recognition shall be given to me and to The University of Alabama in Huntsville in any scholarly use which may be made of any material in this dissertation.

Bassem Girgis 06/28/13

Bassem Girgis (date)

DISSERTATION APPROVAL FORM

Submitted by Bassem Girgis in partial fulfillment of the requirements for the degree of Doctor of Philosophy in Mechanical Engineering and accepted on behalf of the Faculty of the School of Graduate Studies by the dissertation committee.

We, the undersigned members of the Graduate Faculty of The University of Alabama in Huntsville, certify that we have advised and/or supervised the candidate of the work described in this dissertation. We further certify that we have reviewed the dissertation manuscript and approve it in partial fulfillment of the requirements for the degree of Doctor of Philosophy in Mechanical Engineering.

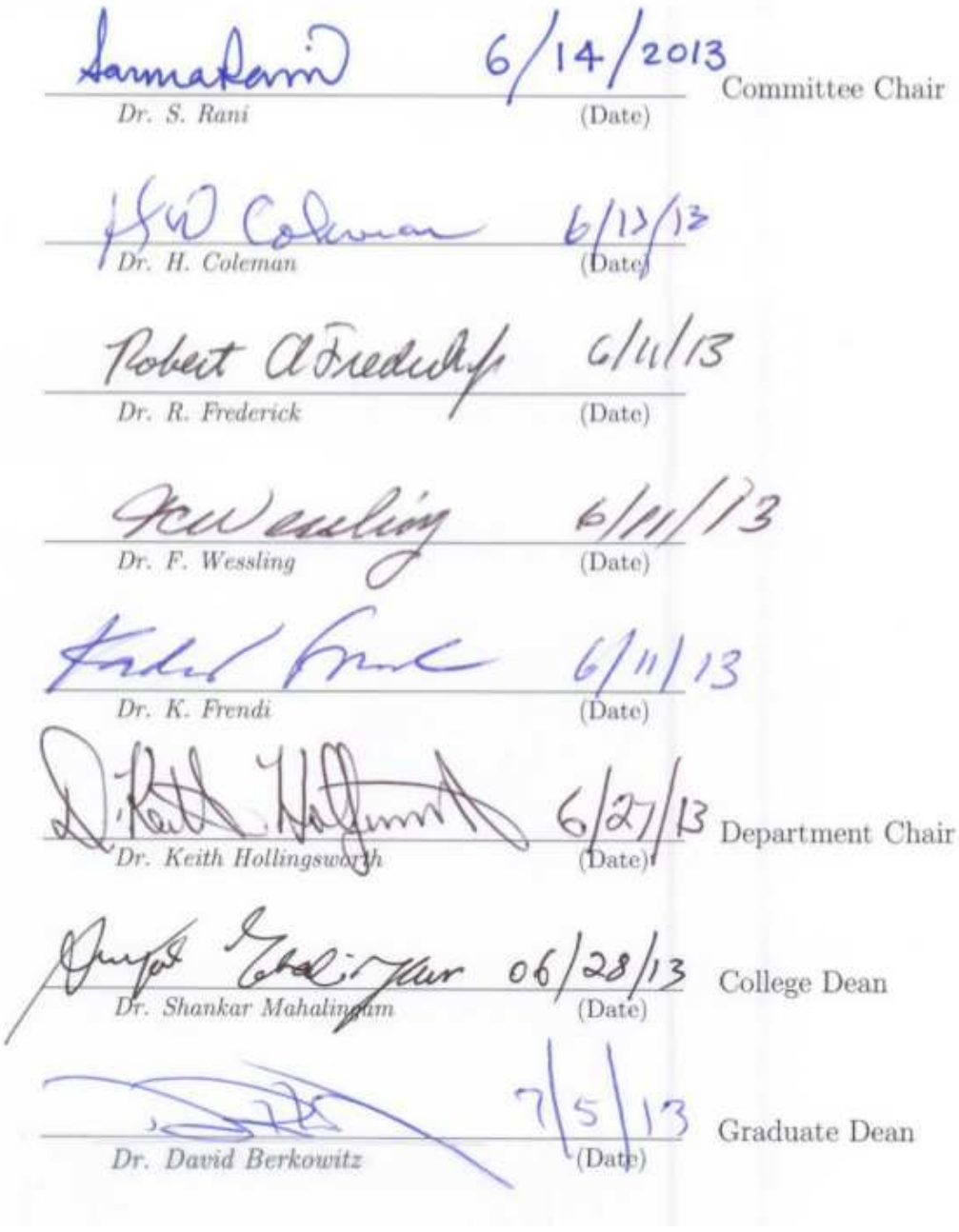

ABSTRACT

School of Graduate Studies
The University of Alabama in Huntsville

Degree Doctor of Philosophy College/Dept. Engineering/Mechanical and Aerospace Engineering

Name of Candidate Bassem Girgis

Title Numerical Simulations of Plasma Dynamics Using the Flowfield Dependent Variation (FDV) Method

The Flowfield Dependent Variation (FDV) method is a generalized numerical method for solving the partial differential equations that govern fluid dynamics, heat transfer, as well as multi-physics scenarios involving external electric and magnetic fields, and shock-turbulent boundary layer interactions. A unique feature of the FDV method is that most of the currently available Finite Difference Method (FDM) and Finite Element Method (FEM) computational schemes can be obtained from it as special cases. For this reason, the FDV method has the potential for application to a broad range of problems in science and engineering.

The principal objective of this dissertation is to extend the FDV method to magnetohydrodynamic applications, specifically those applications that involve plasma dynamics. To achieve this objective, a parallel, arbitrarily high order, unstructured, implicit, 1D/2D/3D finite element method-based numerical framework has been developed and implemented. An Element-by-Element (EBE) data structure is used to store the linear system of equations, and the Generalized Minimal RESidual (GMRES) iterative solver is employed to solve the linear system. To ensure load balancing and achieve efficient parallel processing, domain decomposition is performed

using the METIS software package. In addition, an EBE data structure-based distributed memory model is introduced that uses the Message Passing Interface (MPI) library.

The efficiency of the parallel framework and the accuracy of the numerical method implementation were ensured through comprehensive verifications. Code verification involved a large number of benchmark problems in fluid dynamics and plasma dynamics that covered a broad spectrum of flow conditions. Results from the test cases considered showed good to excellent agreement with the data from the published literature. After completing the verification of the code, an in-depth study of the problems involving freely decaying isotropic and anisotropic turbulence was undertaken. The anisotropic turbulence problems involved exploring the effects of combining isotropic turbulence with an external, applied uniform magnetic field.

Abstract Approval: Committee Chair _____
Dr. S. Rani

Department Chair _____
Dr. Keith Hollingsworth

Graduate Dean _____
Dr. David Berkowitz

ACKNOWLEDGMENTS

All gratitude and thanks are due to the creator of all, the Lord God almighty. "So then neither he who plants is anything, nor he who waters, but God who gives the increase" (1 Corinthians 3:7).

Special thanks are due to Dr. Kader Frendi for the many discussions we had together, the sincere advice, and the fatherly figure he has been to me since I joined UAHuntsville. I would like also to thank Dr. Sarma Rani for his great help especially during the final stages of my PhD study.

I would like to thank Dr. T.J. Chung for his support during my first semester at UAHuntsville and for suggesting this research topic. I would like also to thank all my PhD committee members for their great support and attention to my work at its various stages. Special gratitude is due to Ms. Claudia Meyering for her administrative help. I would like also to acknowledge Alabama Supercomputer Authority for providing me with free CPU hours.

Finally, I owe all my love and appreciation to my wife Catherine, my parents Raafat and Atiat Girgis, my sisters Bassma and Nancy Girgis, and the rest of my family.

TABLE OF CONTENTS

LIST OF FIGURES

LIST OF TABLES

LIST OF ALGORITHMS

LIST OF LISTINGS

LIST OF SYMBOLS

SYMBOL	DEFINITION
A	arbitrary surface area
a	speed of sound
$\mathbf{a}_i$	convection Jacobian tensor
$\mathbf{B}$	magnetic field
$\mathbf{b}_i$	diffusion Jacobian tensor
$\mathbf{C}$	total electric current
$\mathbf{c}_{ij}$	diffusion gradient Jacobian tensor
c_p	specific heat at constant pressure
c_v	specific heat at constant volume
$\mathbf{D}$	electric displacement
δ_{ij}	Kronecker delta $= \begin{cases} 1 & \text{if } i = j \\ 0 & \text{if } i \neq j \end{cases}$
E	velocity field power spectrum
E^m	magnetic field power spectrum
$\mathbf{E}$	electric field
$\mathbf{E}'$	Lorentz transformed electric field

e	internal energy
e_t	total internal gas energy
e_t^m	total internal plasma energy with magnetic component
ϵ_{ijk}	permutation symbol $= \begin{cases} 1 & \text{if } (i,j,k) = (1,2,3),(2,3,1),(3,1,2) \\ -1 & \text{if } (i,j,k) = (1,3,2),(2,1,3),(3,2,1) \\ 0 & \text{if } i = j, j = k, i = k \end{cases}$
ϵ_0^m	permitivity of free space
ϵ_r^m	relative medium permitivity
$\epsilon^m = \epsilon_r^m \epsilon_0^m$	medium permitivity
f	Boltzmann distribution function
$\mathbf{F}_i$	convection flux
$\mathbf{F}^m$	Lorentz force
$\mathbf{G}_i$	diffusion flux
γ	specific heat ratio $= \frac{c_p}{c_v}$
$\mathbf{H}$	magnetic field intensity
H_v	velocity field helicity
H_m	modified magnetic field helicity
H_{vm}	cross magnetic helicity
$\mathbf{h}$	heat conduction flux vector

$\mathbf{h}^m$	magnetic heating flux vector
Ha	Hartmann number
η	resistivity
$\mathbf{J}$	electric current density
k	thermal conductivity
k_b	Boltzmann constant
κ	spectral wave number
λ	second coefficient of viscosity $= \frac{-2}{3}\mu$
λ^m	magnetic diffusivity
M	Mach number
M^m	magnetic Mach number
m	particles mass
μ	viscosity coefficient
μ_0^m	permeability of free space
μ_r^m	relative medium permeability
$\mu^m = \mu_r^m \mu_0^m$	medium permeability
N	magnetic interaction number
n	particles number density
$\hat{n}_i$	normal unit vector pointing outward

NN	number of grid nodes
NEQ	number of equations at each grid node
$\mathbf{P}$	pressure stress tensor
p	pressure
p^m	magnetic pressure
Pe	Peclet number
Pm	magnetic Prandtl number
Pr	Prandtl number
Π	Maxwell stress tensor
Q	Q-criterion
q	particles charge
R	universal gas constant
R_{ij}	velocity rotation tensor
$\mathbf{R}$	acceleration vector field
Re	Reynolds number
Rm	magnetic Reynolds number
ρ	fluid or plasma density
ρ_e	electric charge density
S	contour of an arbitrary surface

$\mathbf{S}$	strain rate tensor
S_L	Lundquist number
s_a	first order FDV parameter
s_b	second order FDV parameter
s_1	first order FDV parameter associated with convection
s_2	second order FDV parameter associated with convection
s_3	first order FDV parameter associated with diffusion
s_4	second order FDV parameter associated with diffusion
σ_{ij}	conductivity tensor
σ	scalar conductivity for isotropic media
T	temperature
t	time
$\boldsymbol{\tau}$	shear stress tensor
$\boldsymbol{\tau}^m$	magnetic product stress tensor
$\mathbf{U}$	conservation variables
V	arbitrary volume
$\mathbf{v}$	velocity vector field
v_a	Alfvén wave speed
ω	vorticity

Ω_v	velocity field enstrophy
Ω_m	magnetic field enstrophy
$\mathbf{x}$	position vector
$\mathbf{Z}$	source term

Acronyms

r.m.s. root-mean-square.

CFD Computational Fluid Dynamics.

EBE Element-by-Element.

EU European Union.

FDM Finite Difference Method.

FDV Flowfield Dependent Variation.

FEM Finite Element Method.

FVM Finite Volume Method.

GMRES Generalized Minimal Residual.

ITER International Thermonuclear Experimental Reactor.

LSWRM Least-Squares Weighted Residual Method.

MHD Magnetohydrodynamics.

MMS Method of Manufactured Solutions.

MPI Message Passing Interface.

NSTX National Spherical Torus Experiment.

SUPG Streamline Upwind Petrov-Galerkin.

USA United States of America.

To my family

CHAPTER 1

INTRODUCTION

Meeting the human energy requirements has been the defining challenge that the mankind has faced since the dawn of time. The burgeoning human population, and the associated increase in energy consumption have made solving this challenge ever more critical to continuing the human way of life. Traditional fossil fuels continue to be the principal source of energy powering mankind's needs. Multiple renewable energy alternatives are struggling to emerge and most alternatives are still in their infancy. Nuclear fission and fusion are two forms of energy generation that are considered among the most viable options to replace fossil fuels in the near-to-distant future.

An analysis of the world's current fossil fuel reserves reveals the impermanence of these energy sources. At the current rates of energy consumption, the estimated number of years for which the current reserves will last are as follows [1]:

- Coal: ~ 148 years
- Oil: ~ 43 years
- Natural gas: ~ 61 years

Renewable energy sources (such as wind, solar, algae, and fuel cells) have not yet emerged as economically viable alternatives to fossil fuels. The one viable alternative, *i.e.*, the nuclear energy is fraught with inherent safety hazards. The environmental and human toll of the nuclear disasters at Chernobyl (1986) and Fukushima (2011) power plants are a stark reminder of the potentially disastrous safety issues of nuclear energy. The current economic unavailability of alternative energy sources, and the persistent safety concerns of nuclear energy make plasma fusion a promising alternative.

A single fusion reaction can generate 27.6 MeV (Mega electron volts) [2]. Therefore, 1 kg of plasma fusion fuel can potentially generate 1 GW (GigaWatt) of electrical energy, which can sustain a small-to-medium sized power station for a day [2]. Sea water is considered one of the main sources of Deuterium (plasma fusion fuel), which is indicative of the abundance of resources for plasma fusion. Moreover, the energy content of plasma fusion fuel is unmatched by the traditional fossil fuels. For example, one liter of sea water can generate 1010 Joules of Deuterium fusion energy, which is about 300 times the combustion energy of 1 liter of gasoline [3].

This unprecedented potential for generating clean and safe energy has attracted significant international attention, so much so that several experimental reactors have already been built. Currently, the main research reactors in the United States of America (USA) include the National Spherical Torus Experiment (NSTX) in Princeton, NJ, and DIII-D in San Diego, CA [2]. The largest plasma fusion research reactor is an international collaboration project called International Thermonuclear Experimental Reactor (ITER), which started in 2007 A.D. This project is funded and

operated by seven international members; USA, European Union (EU), China, Japan, Russia, India, and South Korea. ITER is located in the southern part of France, and its budget is about €15 billions. This construction of this reactor is expected to last through the year 2038 A.D. [2].

So far, experimental research has been the principal driving force behind the plasma fusion efforts. Computational research has not received the attention it deserves. This is due to the lack of accurate and robust numerical methods capable of simulating the complex physics and the complex geometries of the plasma fusion reactors. Simulation of plasmas without the complexities of the fusion process is itself in its infancy given the exorbitant computational requirements.

This chapter is organized as follows. Section 1.1 provides a brief summary of the currently available numerical methods for simulating the transport processes one encounters in the various engineering applications. A brief introduction to the Flowfield Dependent Variation (FDV) method is provided in Section 1.2. Finally, a layout of this dissertation is discussed in Section 1.3.

1.1 Numerical Methods

During the past 50 years, research in computational physics and Computational Fluid Dynamics (CFD) has been an important scientific activity. Numerical solutions have been obtained to the Einstein's field equations, the Boltzmann equation (microscopic), Magnetohydrodynamics (MHD) equations (macroscopic), and the Navier-Stokes system of equations (fluid dynamics). However, many computational issues remain unresolved to this day. The current computational issues include:

- Physical instabilities associated with the shock wave-turbulent boundary layer interactions, particularly in plasma environments.
- Simultaneous occurrence in a flow domain of compressible/incompressible flow regions, and viscous/inviscid flow. Examples of such scenarios include the combustion chamber boundary layer flows of hypersonic aircraft, and the nuclear plasma fusion.
- Difficulty in properly applying the design boundary conditions in three-dimensional configurations (especially for fusion reactors).

In the past, various computational methods were developed to deal with the different aspects of transport phenomena. Such methods include the following:

- Finite Difference Method (FDM)
- Finite Element Method (FEM)
- Finite Volume Method (FVM)
- Particle-In-Cell (PIC) method
- Monte-Carlo (MC) Method
- Boundary Element Method (BEM)
- Lattice-Boltzmann Method (LBM)

Important components of numerical simulation methods are:

- Specification of precise boundary and initial conditions.
- Development of a single code capable of simulating as many physical phenomena as possible.

- Capability to deal with complex multi-dimensional geometries.
- Capability to deal with the smallest time and length scales such as in shock waves, turbulence, as well as the scales arising from the interactions between these two aspects of physics.

Conventional research in CFD uses either the Finite Volume Methods (FVMs) or the Finite Element Methods (FEMs). While FVMs can handle unstructured grids, the ability to achieve higher order accuracy with these methods on irregular grids is not well established [4,5]. Most, if not all, FVM-based research codes that are higher order accurate utilize concepts such as multi-block structured grids [6, 7], or similar curvilinear grid-based ideas. Although some success has been obtained in understanding the physics, the problem of complex geometries remains hard to tackle using FVM. Not to mention the load balancing issues with FVM-based data structures, and the challenges in extending/maintaining the physical models included. FEMs, on the other hand, can handle higher order data structure requirements naturally. The theoretical basis of FEMs are well-established [8–10]. Also, FEM data structures are very flexible and naturally facilitate the addition and extension of different physical models.

Among various forms of FEMs, the most commonly used one is the Taylor-Galerkin Method [11–13], which is derived using the so-called weak form. The weak form results through the integration by parts of a Taylor series expansion of the governing transport equation. The higher order derivatives are expressed in terms of derivatives of the flux vector in the conservation laws. However, in many cases,

Gibbs-type oscillations of the solutions can still be observed owing to the presence of discontinuities, which are the principal difficulty in the numerical solution of first-order hyperbolic conservation laws. An artificial viscosity, or a limiter function, is needed to control such oscillatory behavior in the Taylor-Galerkin method.

Another form of FEMs is the Least-Squares Weighted Residual Method (LSWRM), in which the weighting function is replaced by the derivative of the residual itself. This method has good stability properties due to its minimization nature, and has been applied for the solution of a variety of problems [14–16]. Despite the fact that the implementation of least squares is straight forward, this method in general suffers from excessive, inherent, and uncontrollable dissipation, which, in some cases, results in inaccurate results.

Using the idea of upwind schemes in the Finite Difference Method (FDM), the Streamline Upwind Petrov-Galerkin (SUPG) method was introduced [17, 18]. In this method, the weighting function is modified by adding a perturbation to the standard Galerkin test function. The added perturbation creates an upwind effect by weighting more heavily the upstream nodes within the elements than the downstream nodes. Although this method was a huge success for FEM in the CFD literature, the shock capturing ability of the method needed improvements. This was achieved by adding non-linear operators to the perturbation to account for the compressible Navier-Stokes and Euler equations [19].

1.2 The Flow Dependent Variation (FDV) Method

The FDV method is a generalized computational approach that leads to most of the current FDM and FEM-based schemes as special cases. The original idea of the FDV method began from the need to address the physics involved in shock wave turbulent boundary layer interactions [20, 21]. In shock wave turbulent boundary layer interactions, transition between the various aspects of flow physics dominate the flowfield.

In such flows, strong coupling exists between the sub-flowfields that are inviscid/viscous, compressible/incompressible, or laminar/turbulent in nature. Numerical solution of such flows presents complexities not only in terms of physics, but also in terms of the computations. For example, the velocity in the vicinity of the wall is very low, with a Mach number $M \approx 0$, and Reynolds number $Re \approx 0$. This is accompanied by very high velocities far away from the wall. For example, regions with $M \approx 3$, $Re \approx 10^6$, coexist with the low velocity regions within the domain of study. Transitions from one type of flow to another, and the interactions between different flow regimes have been studied for many years, both experimentally and numerically. The FDV method has been principally devised toward solving such complex, multi-physics problems [22–24]. Several applications of the FDV method have been introduced in the literature including heat transfer and fluid dynamics [25], launch vehicles acoustics [26, 27], and computational relativistic astrophysics [28, 29].

This dissertation investigates the application of the FDV method to the physics of plasma dynamics. With the complex plasma fusion physics in mind, this research

effort is the first step toward constructing a numerical analysis tool that encompasses the FDV method's wide range of validity and the advantages of its implicit FEM formulation. An efficient computational implementation using an unstructured grid domain decomposition capability and the Element-by-Element (EBE) solution technique with the Message Passing Interface (MPI) library, will give this tool a unique advantage in dealing with the multi-physics nature of plasma dynamics. The extension to plasma physics and the addition of higher order elements will add to the inherent strength of the developed tool.

1.3 Dissertation Layout

The organization of this dissertation is as follows. The governing equations of the visco-resistive, one-fluid plasma dynamics are introduced in Chapter 2. The classical laws of electromagnetics are derived from first principles in the partial differential equation form. The one-fluid continuum approximation of plasma is derived in detail from the multi-species representation of the Boltzmann equation with the Lorentz force term. Non-dimensionalization of the resulting equations is discussed along with the necessary simplifications to arrive at the ideal MHD equations, the Navier-Stokes equations, and the Euler equations.

The FDV method is introduced in Chapter 3. Starting from the vector form of the governing equations and the special form of Taylor series expansion in time, derivation of the FDV method is discussed in detail. Introduction of the FDV parameters necessary for the method's numerical stability (in the case of plasma dynamics), and the physical interpretation of these parameters are discussed briefly. The finite

element equations are obtained by applying the standard Galerkin method to the final residual form of the FDV scheme. The flux vector gradients and their Jacobians necessary for the FDV method are introduced in Appendix A.

Based on the finite element implementation of the FDV method introduced in Chapter 3 and the governing equations discussed in Chapter 2, a parallel processing framework has been developed. This framework supports arbitrarily higher order unstructured isoparametric elements for 1D, 2D, and 3D problems. The architecture of the framework is designed to be independent of the scheme as well as the set of equations solved. An EBE data structure is used for the linear system storage and the Generalized Minimal Residual (GMRES) iterative solver is employed for its solution. Domain decomposition using the METIS software package [30] is used to ensure optimized load balancing. A distributed memory model based on the EBE data structure is developed with the MPI library for parallel processing. The general structure of the framework is presented in Chapter 4 along with the different possible communication strategies and the proposed parallel EBE-GMRES solver. The effects of different communication strategies, of grid refinement, and of systematical higher order accuracy increase are also investigated. Results show a good scalability of the proposed framework when compared with published literature.

In order to verify the developed framework, a comprehensive set of test cases is analyzed in detail in Chapter 5. These test cases were carefully selected to include different types of physics. The order of accuracy of the FEM framework is systematically established through the Method of Manufactured Solutions (MMS). Fluid dynamics test cases involving solution of the Euler and Navier-Stokes equations are

employed to compare the developed framework with published literature. The fluid dynamics test cases range from nearly incompressible flows to supersonic flows. Some of the test cases have multiple flow regimes interacting within the same flowfield. The ability of the FDV method to accurately represent acoustics waves, shock waves, and turbulent flows is also established. A set of plasma dynamics test cases is selected to establish the ability of the FDV method to handle the different physical phenomena occurring in the visco-resistive plasma dynamics problems.

Appendix B summarizes the Lagrange polynomial-based family of shape functions used in the finite element implementation. The necessary mathematical analysis to compute the shape functions and their derivatives is introduced for arbitrary polynomial orders. The derivative transformation Jacobian between the natural element coordinates and the physical coordinates systems is also summarized.

A novel approach was developed to implement the subsonic inlet/outlet characteristic boundary conditions for implicit finite element methods on unstructured arbitrarily higher order grids. The details of the implementation and mathematical basis of this new technique are given in Appendix C.

Chapter 6 introduces the FDV method solution for the problems of isotropic and anisotropic turbulence. Different cases are selected to study the effect of a background uniform magnetic field on an initially isotropic hydrodynamic velocity field. The analysis provided verifies the findings through basic energy budget estimates and flow statistics analysis. Finally, Chapter 7 presents the conclusions of the current work and discusses recommendations for future research.

CHAPTER 2

GOVERNING EQUATIONS

In this chapter, the governing equations of the visco-resistive, one-fluid plasma dynamics are derived from first principles. The system of equations governing electromagnetics, often called Maxwell's equations, is introduced in Section 2.1. Section 2.2 introduces the six-dimensional Boltzmann equation for plasma species kinetics, as well as the macroscopic equations resulting from integrating the Boltzmann equation over the velocity space. Section 2.3 presents the one-fluid plasma dynamics equations in vector form; the resulting system of equations is non-dimensionalized for numerical simulations. The reduction of the governing equations to relevant special cases concerning plasma dynamics and fluid dynamics is discussed in Section 2.4.

2.1 Electromagnetics

A plasma medium contains charged particles of different species due to its ionized nature. The charged particles within this medium are in a constant state of motion because of the thermal energy content and the frequent collisions between the particles. To comprehensively study the electromagnetic behavior of plasma media, the Maxwell system of equations has to be solved along with the charge conservation

law and Ohm's law. In the following subsections, the governing equations of classical electromagnetics in the case of plasma are introduced in differential form from first principles.

2.1.1 Charge Conservation

Consider the different charged species in a plasma medium. The charge density, ρ_e, is defined by

$$\rho_e = \sum_{s=1}^{SP} n_s q_s, \tag{2.1}$$

where n_s and q_s are the number density and the charge of the s^{th} species, respectively, and SP is the total number of species. The electric current density, $\mathbf{J}$, is defined by

$$J_i = \sum_{s=1}^{SP} n_s q_s \left\langle v_i \right\rangle_s, \tag{2.2}$$

where $\left\langle v_i \right\rangle_s$ is the mean velocity of the s^{th} species.

The electric current flux leaving an arbitrary volume, V, bounded by a closed surface, S, has to be equal to the net rate of change of charge contained in the volume V. This is the charge conservation law given by

$$\int_A J_i \hat{n}_i dA = -\frac{\partial}{\partial t} \int_V \rho_e dV, \tag{2.3}$$

where $\hat{n}_i$ is the outward-pointing unit normal vector.

Using the Green-Gauss theorem, Equation (2.3) can be written as

$$\int_V \left(J_{i,i} + \frac{\partial \rho_e}{\partial t} \right) dV = 0. \tag{2.4}$$

Since the integration volume is arbitrary, Equation (2.4) has to be satisfied at the differential level. This leads to the charge conservation law given by

$$\frac{\partial \rho_e}{\partial t} + J_{i,i} = 0. \tag{2.5}$$

2.1.2 Lorentz Force

The Lorentz force, $\mathbf{F}^m$, applied on a charged particle with an electric charge, q, in a static electrical field, $\mathbf{E}$, is given by

$$F_i^m = qE_i. \tag{2.6}$$

In the case of a moving particle with a velocity, $\mathbf{v}$, and the existence of a magnetic field, $\mathbf{B}$, the Lorentz force becomes

$$F_i^m = q\left(E_i + \epsilon_{ijk} v_j B_k\right). \tag{2.7}$$

The particle velocity *w.r.t.* the moving frame of reference is zero, and the Lorentz force term reduces to the static form given in Equation (2.6). This representation is called the Lorentz transformation, in which the electric field is replaced by the

transformed electric field, $\mathbf{E}'$, given by

$$E_i' = E_i + \epsilon_{ijk} v_j B_k. \tag{2.8}$$

2.1.3 Ohm's Law

The electric current density, $\mathbf{J}$, is related to the electrical field, $\mathbf{E}$, by Ohm's law, which is given in its simplest form by

$$J_i = \sigma_{ij} E_j, \tag{2.9}$$

where σ_{ij} is the anisotropic conductivity tensor. For isotropic media

$$\sigma_{ij} = \delta_{ij} \sigma, \tag{2.10}$$

and Ohm's law becomes

$$J_i = \sigma E_i. \tag{2.11}$$

In the case of moving particles in magnetic fields, the static electric field, $\mathbf{E}$, is replaced by the transformed electric field, $\mathbf{E}'$, yielding the following form of the Ohm's law

$$\eta J_i = E_i' = E_i + \epsilon_{ijk} v_j B_k, \tag{2.12}$$

where η is the resistivity given by

$$\eta = \frac{1}{\sigma}. \tag{2.13}$$

The Hall effect and the electron pressure terms are neglected in Equation (2.12).

2.1.4 Faraday's Law

Faraday's law of induction, also known as the Maxwell-Faraday law, states that every change in magnetic flux that traverses a given surface produces in its boundary an electromagnetic force. This electromagnetic force is numerically equal to the change in electric flux but opposite in sign.

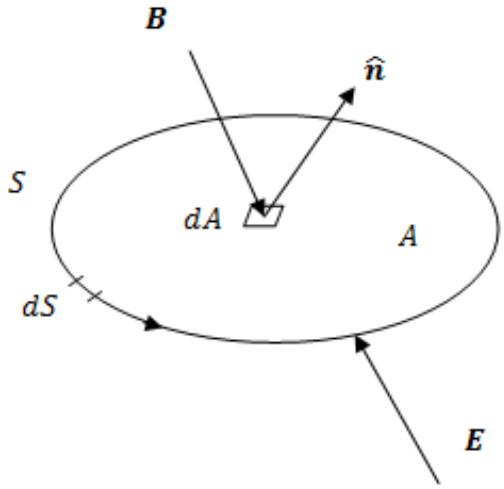

Figure 2.1 Faraday's law.

Consider the arbitrary surface, A, enclosed by the contour, S, that is exposed to both electric and magnetic fields as shown in Figure 2.1. Applying Faraday's law to this system yields

$$\frac{d}{dt}\int_A B_i \hat{n}_i dA = -\oint_S E_i \hat{n}_i dS. \tag{2.14}$$

From Stokes theorem

$$\frac{d}{dt}\int_A B_i \hat{n}_i dA = -\int_A \epsilon_{ijk} E_{k,j} \hat{n}_i dA. \tag{2.15}$$

Rearranging

$$\int_A \left(\dot{B}_i + \epsilon_{ijk} E_{k,j}\right) \hat{n}_i dA = 0, \tag{2.16}$$

which leads to the Faraday's law in differential form given by

$$\dot{B}_i + \epsilon_{ijk} E_{k,j} = 0. \tag{2.17}$$

2.1.5 Ampere's Law

Ampere's law states that the total electric current flux that traverses a surface is accompanied by a magnetic force equal to the electric current flux.

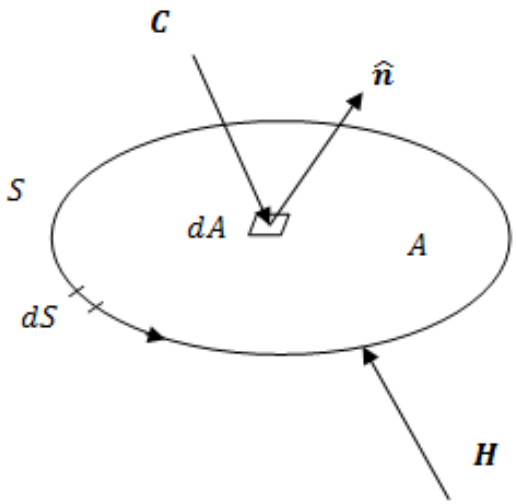

Figure 2.2 Ampere's law.

Consider the magnetic field intensity, $\mathbf{H}$, applied on the arbitrary surface, A, with the closed contour, S, shown in Figure 2.2. Also shown is the total electric current, $\mathbf{C}$, given by

$$C_i = J_i + \dot{D}_i, \tag{2.18}$$

where D_i is the electric displacement given by

$$D_i = \epsilon^m E_i. \tag{2.19}$$

The electric field intensity, $\mathbf{H}$, is related to the magnetic field, $\mathbf{B}$, through the constitutive relation given by

$$H_i = \frac{1}{\mu^m} B_i. \tag{2.20}$$

Applying the Ampere's law to the system shown in Figure 2.2 yields

$$\int_A C_i \hat{n}_i dA = \oint_S H_i \hat{n}_i dS. \tag{2.21}$$

From Stokes theorem

$$\int_A C_i \hat{n}_i dA = \int_A \epsilon_{ijk} H_{k,j} \hat{n}_i dA. \tag{2.22}$$

Rearranging

$$\int_A \left(C_i - \epsilon_{ijk} H_{k,j}\right) \hat{n}_i dA = 0, \tag{2.23}$$

which leads to the Faraday's law in differential form given by

$$J_i + \dot{D}_i = \epsilon_{ijk} H_{k,j}. \tag{2.24}$$

Neglecting the electric current density change, Ampere's law takes the form

$$J_i = \epsilon_{ijk} H_{k,j}. \tag{2.25}$$

2.1.6 Gauss's Law

Applying the divergence operator to Ampere's law given in Equation (2.24) yields

$$J_{i,i} + \dot{D}_{i,i} = \epsilon_{ijk} H_{k,ji}. \tag{2.26}$$

The *r.h.s.* term vanishes identically because

$$\epsilon_{ijk} H_{k,ji} = -\epsilon_{jik} H_{k,ij} = -\epsilon_{ijk} H_{k,ji}. \tag{2.27}$$

Using Equations (2.27) and (2.5) in Equation (2.26)

$$\frac{d}{dt}\left(-\rho_e + D_{i,i}\right) = 0. \tag{2.28}$$

Integrating Equation (2.28) *w.r.t.* time

$$-\rho_e + D_{i,i} = c, \tag{2.29}$$

where c is an integration constant chosen to be zero without loss of generality leading to

$$D_{i,i} = \rho_e. \tag{2.30}$$

2.1.7 Solenoidal Condition of the Magnetic Field

Applying the divergence operator to Faraday's law given in Equation (2.17) yields

$$\dot{B}_{i,i} + \epsilon_{ijk} E_{k,ji} = 0. \tag{2.31}$$

The second term vanishes identically similar to Equation (2.27), which leads to

$$\dot{B}_{i,i} = 0. \tag{2.32}$$

Integrating Equation (2.32) *w.r.t.* time yields

$$B_{i,i} = c, \tag{2.33}$$

where c is an integration constant. If the divergence of the magnetic field at any point in space and/or time is zero, this will yield $c = 0$ everywhere. This can be represented by the solenoidal condition of the magnetic field given by

$$B_{i,i} = 0. \tag{2.34}$$

2.1.8 Magnetic Induction Equation

Substituting Ampere's law, Equation (2.25), and Equation (2.20) into Ohm's law, Equation (2.12), we get

$$E_i = \frac{\eta}{\mu^m} \epsilon_{ijk} B_{k,j} + \epsilon_{ijk} v_j B_k. \tag{2.35}$$

From Faraday's law, Equation (2.17), we get

$$\dot{B}_i + \epsilon_{ijk}\epsilon_{kmn}\left(\lambda^m B_{n,m} + v_m B_n\right)_{,j} = 0, \tag{2.36}$$

where λ^m is the magnetic diffusivity given by

$$\lambda^m = \frac{\eta}{\mu^m}. \tag{2.37}$$

Note that

$$\epsilon_{ijk}\epsilon_{kmn} = \delta_{im}\delta_{jn} - \delta_{in}\delta_{jm}. \tag{2.38}$$

Using Equations (2.38) and (2.34) into Equation (2.36) and expanding we get

$$\dot{B}_i - \lambda^m B_{i,jj} - v_{i,j}B_j + v_{j,j}B_i + v_j B_{i,j} = 0. \tag{2.39}$$

Collecting the terms and using Equation (2.34) we get the modified Maxwell equation

$$\dot{B}_i + \left(v_j B_i - v_i B_j\right)_{,j} - \lambda^m B_{i,jj} = 0. \tag{2.40}$$

2.2 Plasma Kinetics

The kinetic representation of a plasma medium can be modeled by studying the development of the time-dependent distribution functions, $f_s(\mathbf{x}, \mathbf{v}, t)$, of the various

species, s, present. This is done using the Boltzmann equation given by

$$\frac{df_s}{dt} = \left(\frac{\partial f_s}{\partial t}\right)_{col.}. \tag{2.41}$$

By expanding the total derivative term, Equation (2.41) becomes

$$\frac{\partial f_s}{\partial t} + \frac{\partial f_s}{\partial x_i}\frac{\partial x_i}{\partial t} + \frac{\partial f_s}{\partial v_i}\frac{\partial v_i}{\partial t} = \left(\frac{\partial f_s}{\partial t}\right)_{col.}. \tag{2.42}$$

From the definition of the velocity vector

$$v_i = \frac{\partial x_i}{\partial t}, \tag{2.43}$$

and the acceleration vector

$$R_i = \frac{\partial v_i}{\partial t}, \tag{2.44}$$

and the Lorentz force given in Equation (2.7), the Boltzmann equation is given by

$$\frac{\partial f_s}{\partial t} + v_i\frac{\partial f_s}{\partial x_i} + \frac{q_s}{m_s}\left(E_i + \epsilon_{ijk}v_jB_k\right)\frac{\partial f_s}{\partial v_i} = \left(\frac{\partial f_s}{\partial t}\right)_{col.}. \tag{2.45}$$

Note that the acceleration of a particle due to Lorentz force is given by

$$R_i = \frac{q}{m}\left(E_i + \epsilon_{ijk}v_jB_k\right), \tag{2.46}$$

where m is the particle mass. Neglecting the collision term leads to the Vlasov equation given by

$$\frac{\partial f_s}{\partial t} + v_i \frac{\partial f_s}{\partial x_i} + \frac{q_s}{m_s} \left(E_i + \epsilon_{ijk} v_j B_k \right) \frac{\partial f_s}{\partial v_i} = 0. \tag{2.47}$$

The number density, $n_s(\mathbf{x}, t)$, is obtained by integrating the distribution function, $f_s(\mathbf{x}, \mathbf{v}, t)$, over the three dimensional velocity space

$$n_s(\mathbf{x}, t) = \int_{v_1=-\infty}^{\infty} \int_{v_2=-\infty}^{\infty} \int_{v_3=-\infty}^{\infty} f_s dv_1 dv_2 dv_3, \tag{2.48}$$

which can be represented in short as

$$n_s(\mathbf{x}, t) = \int f_s d^3 v, \tag{2.49}$$

where $d^3 v = dv_1 dv_2 dv_3$.

The average value of any physical quantity, $\langle \psi(\mathbf{x}, t) \rangle_s$, is obtained by integrating over the velocity space

$$\langle \psi(\mathbf{x}, t) \rangle_s = \frac{1}{n_s} \int \psi f_s d^3 v. \tag{2.50}$$

The solution of the kinetic equations is beyond the scope of this work. A simpler model is adopted for the plasma dynamics, namely the macroscopic fluid description. The macroscopic representation of the plasma fluid is valid when the collisions frequencies are much higher than the hydraulic frequencies and when length

scales are large compared to the molecular length scales. The macroscopic equations of plasma dynamics species can be obtained from the Boltzmann equation given in Equation (2.45) by taking its moments of various orders. This can be done most generally by multiplying Equation (2.45) by the general function, ψ, and integrating over the velocity space

$$\int \psi \left(\frac{\partial f_s}{\partial t} + v_i \frac{\partial f_s}{\partial x_i} + R_i \frac{\partial f_s}{\partial v_i} \right) d^3v = \int \psi \left(\frac{\partial f_s}{\partial t} \right)_{col.} d^3v. \tag{2.51}$$

The first term is given by

$$\begin{aligned} \int \psi \frac{\partial f_s}{\partial t} d^3v &= \int \frac{\partial \left(\psi f_s \right)}{\partial t} d^3v - \int f_s \frac{\partial \psi}{\partial t} d^3v \\ &= \frac{\partial \left(n_s \left\langle \psi \right\rangle_s \right)}{\partial t} - n_s \left\langle \frac{\partial \psi}{\partial t} \right\rangle_s, \end{aligned} \tag{2.52}$$

the second term is given by

$$\begin{aligned} \int \psi v_i \frac{\partial f_s}{\partial x_i} d^3v &= \int v_i \frac{\partial \left(\psi f_s \right)}{\partial x_i} d^3v - \int v_i f_s \frac{\partial \psi}{\partial x_i} d^3v \\ &= \frac{\partial \left(n \left\langle v_i \psi \right\rangle_s \right)}{\partial x_i} - n \left\langle v_i \frac{\partial \psi}{\partial x_i} \right\rangle_s, \end{aligned} \tag{2.53}$$

and the third term is given by

$$\begin{aligned} \int \psi R_i \frac{\partial f_s}{\partial v_i} d^3v &= \int R_i \frac{\partial \left(\psi f_s \right)}{\partial v_i} d^3v - \int R_i f_s \frac{\partial \psi}{\partial v_i} d^3v \\ &= \int \frac{\partial \left(R_i \psi f_s \right)}{\partial v_i} d^3v - \int \psi f_s \frac{\partial R_i}{\partial v_i} d^3v - \int R_i f_s \frac{\partial \psi}{\partial v_i} d^3v. \end{aligned} \tag{2.54}$$

Expanding the summation in the first term in the *r.h.s.* of Equation (2.54) and evaluating the integrals

$$\begin{aligned}\int \frac{\partial \left(R_i \psi f_s\right)}{\partial v_i} d^3v =& R_1 \psi f_s|_{-\infty}^{\infty} \int\int dv_2 dv_3 + R_2 \psi f_s|_{-\infty}^{\infty} \int\int dv_1 dv_3 \\ &+ R_3 \psi f_s|_{-\infty}^{\infty} \int\int dv_1 dv_2 \\ =& 0.\end{aligned} \tag{2.55}$$

By definition, f is assumed to go to zero at $\pm\infty$. This means there are no particles with infinite velocities. Considering the second term in the *r.h.s.* of Equation (2.54) and from Equation (2.46)

$$\frac{\partial R_i}{\partial v_i} = \frac{q}{m} \frac{\partial}{\partial v_i} \left(\epsilon_{ijk} v_j B_k\right) = \frac{q}{m} \epsilon_{ijk} \delta_{ij} B_k = 0. \tag{2.56}$$

Substituting Equations (2.55) and (2.56) into Equation (2.54)

$$\int \psi R_i \frac{\partial f_s}{\partial v_i} d^3v = -n_s \left\langle R_i \frac{\partial \psi}{\partial v_i} \right\rangle_s. \tag{2.57}$$

Substituting from Equations (2.52), (2.53), and (2.57) into Equation (2.51)

$$\begin{aligned}&\frac{\partial \left(n_s \left\langle \psi \right\rangle_s\right)}{\partial t} - n_s \left\langle \frac{\partial \psi}{\partial t} \right\rangle_s + \frac{\partial \left(n_s \left\langle v_i \psi \right\rangle_s\right)}{\partial x_i} \\ &- n_s \left\langle v_i \frac{\partial \psi}{\partial x_i} \right\rangle_s - n_s \left\langle R_i \frac{\partial \psi}{\partial v_i} \right\rangle_s = \int \psi \left(\frac{\partial f_s}{\partial t}\right)_{col.} d^3v.\end{aligned} \tag{2.58}$$

The substitution of ψ with the different moments will yield the different conservation laws in the macroscopic form as shown in the following subsections.

Splitting the velocity, v_i, into a mean component, $\langle v_i \rangle_s$, and a random component, $\tilde{v}_i$, defined by

$$\tilde{v}_i = v_i - \langle v_i \rangle_s \,, \tag{2.59}$$

allows the introduction of the partial species temperature

$$T_s \left(\mathbf{x}, t \right) = \frac{m_s}{3 \, k_b} \left\langle \tilde{v}_i \tilde{v}_i \right\rangle_s \,, \tag{2.60}$$

where k_b is the Boltzmann constant. The partial thermal energy is given by

$$e_s \left(\mathbf{x}, t \right) = \frac{m_s}{2} \left\langle \tilde{v}_i \tilde{v}_i \right\rangle_s \,, \tag{2.61}$$

and the partial stress tensor

$$\left(P_{ij} \right)_s \left(\mathbf{x}, t \right) = n_s \, m_s \left\langle \tilde{v}_i \tilde{v}_j \right\rangle_s = p_s \delta_{ij} - \left(\tau_{ij} \right)_s \,, \tag{2.62}$$

where $\left(\tau_{ij} \right)_s$ is the off-diagonal partial stress tensor and p_s is the partial pressure given by

$$p_s = n_s \, k_b \, T_s, \tag{2.63}$$

and the heat flux vector is given by

$$\left(h_j \right)_s \left(\mathbf{x}, t \right) = \frac{1}{2} n_s \, m_s \left\langle \tilde{v}_i \tilde{v}_i \tilde{v}_j \right\rangle_s \,. \tag{2.64}$$

Note that by averaging Equation (2.59) we get

$$\langle \tilde{v}_i \rangle_s = \langle v_i \rangle_s - \langle \langle v_i \rangle \rangle_s = \langle v_i \rangle_s - \langle v_i \rangle_s = 0. \tag{2.65}$$

2.2.1 Conservation of Mass

The conservation of mass equation is obtained by taking the zeroth moment of the Boltzmann equation. This can be accomplished by substituting $\psi = 1$ in Equation (2.58)

$$\frac{\partial n_s}{\partial t} + \frac{\partial \left(n_s \langle v_i \rangle_s \right)}{\partial x_i} = S^s_{col.}, \tag{2.66}$$

where

$$S^s_{col.} = \int \left(\frac{\partial f_s}{\partial t} \right)_{col.} d^3v, \tag{2.67}$$

is the collision mass source term. In the absence of collisions, the mass conservation equation reduces to

$$\frac{\partial n_s}{\partial t} + \frac{\partial \left(n_s \langle v_i \rangle_s \right)}{\partial x_i} = 0. \tag{2.68}$$

2.2.2 Conservation of Momentum

The conservation of momentum equation is obtained by taking the first velocity moment of the Boltzmann equation. This can be accomplished by substituting $\psi_j = m_s v_j$ in Equation (2.58). Since v_i, x_i, and t are independent variables, the terms with partial derivatives of ψ *w.r.t.* both x_i and t will yield zeros, and the term with partial

derivative *w.r.t.* v_i is given by

$$\left\langle R_i \frac{\partial (m v_j)}{\partial v_i} \right\rangle = \langle R_i m \delta_{ij} \rangle = m \langle R_j \rangle . \tag{2.69}$$

Substituting Equation (2.69) into Equation (2.58)

$$\frac{\partial \left(n_s m_s \langle v_j \rangle_s \right)}{\partial t} + \frac{\partial \left(n_s m_s \langle v_i v_j \rangle_s \right)}{\partial x_i} - n_s \, q_s \left(E_j + \epsilon_{jmn} \langle v_m \rangle_s B_n \right) = A^s_{j,col.}, \tag{2.70}$$

where

$$A^s_{j,col.} = \int m_s v_j \left(\frac{\partial f_s}{\partial t} \right)_{col.} d^3 v \tag{2.71}$$

is the change in momentum due to collisions.

Using Equations (2.62) and (2.66) in Equation (2.70) we get

$$\begin{aligned} n_s m_s \left(\frac{\partial \langle v_j \rangle_s}{\partial t} + \langle v_i \rangle_s \frac{\partial \langle v_j \rangle_s}{\partial x_i} \right) + \frac{\partial (P_{ij})_s}{\partial x_i} \\ - n_s \, q_s \left(E_j + \epsilon_{jmn} \langle v_m \rangle_s B_n \right) = A^s_{j,col.}. \end{aligned} \tag{2.72}$$

2.2.3 Conservation of Energy

The conservation of energy equation is obtained by taking the second velocity moment of the Boltzmann equation. This can be accomplished by substituting $\psi = \frac{1}{2} m v_j v_j$ in Equation (2.58). Similar to the momentum equation, all terms with partial derivatives of ψ *w.r.t.* either x_i or t will yield zeros, and the term with partial

derivative *w.r.t.* v_i is given by

$$\left\langle R_i \frac{\partial \left(\frac{1}{2} m v_j v_j\right)}{\partial v_i} \right\rangle = \left\langle R_i m v_j \delta_{ij} \right\rangle = m \left\langle R_i v_i \right\rangle . \tag{2.73}$$

Substituting from Equation (2.73) into Equation (2.58)

$$\frac{\partial}{\partial t}\left(n_s \frac{1}{2} m_s \left\langle v_i v_i \right\rangle_s\right) + \frac{\partial}{\partial x_i}\left(n_s \frac{1}{2} m_s \left\langle v_i v_j v_j \right\rangle_s\right) - n_s m_s \left\langle R_i v_i \right\rangle_s = M^s_{col.}, \tag{2.74}$$

where

$$M^s_{col.} = \int \frac{1}{2} m_s v_i v_i \left(\frac{\partial f_s}{\partial t}\right)_{col.} d^3 v \tag{2.75}$$

is the change in energy due to collisions.

2.3 One-Fluid Visco-Resistive Plasma Dynamics Equations

The different species of the plasma medium are treated as a single fluid in this approximation, *i.e.* the plasma medium is considered to be a conducting fluid with indistinguishable species. In order for this model to be accurate, the plasma fluid has to attain macroscopic neutrality and has to have non-relativistic speeds.

The total number density, n, and the total plasma density, ρ, are given by

$$n = \sum_{s=1}^{SP} n_s, \tag{2.76}$$

and

$$\rho = \sum_{s=1}^{SP} n_s m_s. \tag{2.77}$$

The fluid velocity, $\bar{\mathbf{v}}$, is defined such that the momentum of the plasma per unit volume stays the same from the kinetic analysis

$$\rho\bar{v}_i = \sum_{s=1}^{SP} n_s m_s \left\langle v_i \right\rangle_s . \tag{2.78}$$

Similar to Equation (2.59), the diffusion velocity associated with the mean mass velocity, $\acute{\mathbf{v}}$, is given by

$$\acute{v}_i = v_i - \bar{v}_i. \tag{2.79}$$

In order to convert Equation (2.58) from the species variable $\mathbf{v}$ to the mean mass variable $\acute{\mathbf{v}}$, the time, the spatial, and the velocity derivatives have to be converted as follows. Consider the time derivative

$$\frac{\partial}{\partial t} \Rightarrow \frac{\partial}{\partial t} + \frac{\partial \acute{v}_j}{\partial t}\frac{\partial}{\partial \acute{v}_j} = \frac{\partial}{\partial t} - \frac{\partial \bar{v}_j}{\partial t}\frac{\partial}{\partial \acute{v}_j}, \tag{2.80}$$

the spatial derivative

$$\frac{\partial}{\partial x_i} \Rightarrow \frac{\partial}{\partial x_i} + \frac{\partial \acute{v}_j}{\partial x_i}\frac{\partial}{\partial \acute{v}_j} = \frac{\partial}{\partial x_i} - \frac{\partial \bar{v}_j}{\partial x_i}\frac{\partial}{\partial \acute{v}_j}, \tag{2.81}$$

and the velocity derivative

$$\frac{\partial}{\partial v_i} \Rightarrow \frac{\partial \acute{v}_j}{\partial v_i}\frac{\partial}{\partial \acute{v}_j} = \delta_{ij}\frac{\partial}{\partial \acute{v}_j} = \frac{\partial}{\partial \acute{v}_i}. \tag{2.82}$$

Note that the mean quantities are not affected by the transformation since they are not a function of the velocity, $\mathbf{v}$. Furthermore, comparing $\langle \tilde{v}_i \rangle$, which is zero as in Equation (2.65), $\langle \acute{v}_i \rangle$ is not zero. However, taking the mass weighted summation over all the species of the average of Equation (2.79) we get

$$\sum_{s=1}^{SP} n_s m_s \langle \acute{v}_i \rangle_s = \sum_{s=1}^{SP} n_s m_s \langle v_i \rangle_s - \sum_{s=1}^{SP} n_s m_s \bar{v}_i. \tag{2.83}$$

Simplifying we get

$$\sum_{s=1}^{SP} n_s m_s \langle \acute{v}_i \rangle = 0. \tag{2.84}$$

Applying the transformation given in Equations (2.80), (2.81), and (2.82) to Equation (2.58) we get

$$\begin{aligned} &\frac{\partial \left(n_s \langle \psi \rangle_s \right)}{\partial t} + \frac{\partial \left(n_s \langle v_i \psi \rangle_s \right)}{\partial x_i} - n_s \left\langle \frac{\partial \psi}{\partial t} \right\rangle_s + n_s \left\langle \frac{\partial \bar{v}_j}{\partial t} \frac{\partial \psi}{\partial \acute{v}_j} \right\rangle_s \\ &- n_s \left\langle v_i \frac{\partial \psi}{\partial x_i} \right\rangle_s + n_s \left\langle v_i \frac{\partial \bar{v}_j}{\partial x_i} \frac{\partial \psi}{\partial \acute{v}_j} \right\rangle_s - n_s \left\langle R_i \frac{\partial \psi}{\partial \acute{v}_i} \right\rangle_s = \int \psi \left(\frac{\partial f_s}{\partial t} \right)_{col.} d^3 v. \end{aligned} \tag{2.85}$$

Substituting Equation (2.79) we get

$$\begin{aligned} &\frac{\partial \left(n_s \langle \psi \rangle_s \right)}{\partial t} + \frac{\partial \left(n_s \bar{v}_i \langle \psi \rangle_s \right)}{\partial x_i} + \frac{\partial \left(n_s \langle \acute{v}_i \psi \rangle_s \right)}{\partial x_i} - n_s \left\langle \frac{\partial \psi}{\partial t} \right\rangle_s + n_s \left\langle \frac{\partial \bar{v}_j}{\partial t} \frac{\partial \psi}{\partial \acute{v}_j} \right\rangle_s \\ &- n_s \bar{v}_i \left\langle \frac{\partial \psi}{\partial x_i} \right\rangle_s - n_s \left\langle \acute{v}_i \frac{\partial \psi}{\partial x_i} \right\rangle_s + n_s \bar{v}_i \frac{\partial \bar{v}_j}{\partial x_i} \left\langle \frac{\partial \psi}{\partial \acute{v}_j} \right\rangle_s + n_s \left\langle \acute{v}_i \frac{\partial \bar{v}_j}{\partial x_i} \frac{\partial \psi}{\partial \acute{v}_j} \right\rangle_s \\ &- n_s \left\langle R_i \frac{\partial \psi}{\partial \acute{v}_i} \right\rangle_s = \int \psi \left(\frac{\partial f_s}{\partial t} \right)_{col.} d^3 v. \end{aligned} \tag{2.86}$$

The total mass thermal energy of the plasma is given by

$$e = \frac{1}{\rho} \sum_{s=1}^{SP} \frac{1}{2} n_s m_s \left\langle \acute{v}_i \acute{v}_i \right\rangle , \tag{2.87}$$

and the total mass pressure tensor, $P(\mathbf{x}, t)$, is defined as

$$P_{ij} = \sum_{s=1}^{SP} n_s m_s \left\langle \acute{v}_i \acute{v}_j \right\rangle , \tag{2.88}$$

where $\left\langle \acute{v}_i \acute{v}_j \right\rangle$ is obtained from Equation (2.79) by

$$\left\langle \acute{v}_i \acute{v}_j \right\rangle = \left\langle \tilde{v}_i \tilde{v}_j \right\rangle + \left\langle \acute{v}_i \right\rangle \left\langle \acute{v}_j \right\rangle , \tag{2.89}$$

which simplifies Equation (2.88) to

$$P_{ij} = \sum_{s=1}^{SP} \left(P_s\right)_{ij} + \sum_{s=1}^{SP} n_s m_s \left\langle \acute{v}_i \right\rangle \left\langle \acute{v}_j \right\rangle . \tag{2.90}$$

The total mass heat flux is given by

$$h_j = \sum_{s=1}^{SP} \frac{1}{2} n_s \, m_s \left\langle \acute{v}_i \acute{v}_i \acute{v}_j \right\rangle_s . \tag{2.91}$$

2.3.1 Conservation of Mass

The species continuity equation is obtained from Equation (2.86) by substituting $\psi = 1$

$$\frac{\partial n_s}{\partial t} + \frac{\partial \left(n_s \bar{v}_i\right)}{\partial x_i} + \frac{\partial \left(n_s \left\langle \acute{v}_i \right\rangle_s\right)}{\partial x_i} = S^s_{col.}, \tag{2.92}$$

where $S^s_{col.}$ is given in Equation (2.67). The one-fluid plasma dynamics continuity equation is obtained by multiplying Equation (2.92) by m_s and summing over all the species leading to

$$\frac{\partial \rho}{\partial t} + \frac{\partial \left(\rho \bar{v}_i\right)}{\partial x_i} = 0. \tag{2.93}$$

The third term and the *r.h.s.* in Equation (2.92) vanish by summation.

2.3.2 Conservation of Momentum

The species momentum equation is obtained from Equation (2.86) by substituting $\psi_j = m_s \acute{v}_j$

$$\begin{aligned} &\frac{\partial \left(n_s m_s \left\langle \acute{v}_j \right\rangle_s\right)}{\partial t} + \frac{\partial \left(n_s m_s \bar{v}_i \left\langle \acute{v}_j \right\rangle_s\right)}{\partial x_i} + \frac{\partial \left(n_s m_s \left\langle \acute{v}_i \acute{v}_j \right\rangle_s\right)}{\partial x_i} \\ &+ n_s m_s \frac{\partial \bar{v}_j}{\partial t} + n_s m_s \bar{v}_i \frac{\partial \bar{v}_j}{\partial x_i} + n_s m_s \frac{\partial \bar{v}_j}{\partial x_i} \left\langle \acute{v}_i \right\rangle_s - n_s m_s \left\langle R_j \right\rangle_s = A^s_{j,col.}, \end{aligned} \tag{2.94}$$

where $A^s_{j,col.}$ is given in Equation (2.71). The one-fluid plasma dynamics momentum equation is obtained by summing Equation (2.94) over all the species leading to

$$\rho \frac{\partial \bar{v}_j}{\partial t} + \rho \bar{v}_i \frac{\partial \bar{v}_j}{\partial x_i} + \frac{\partial P_{ij}}{\partial x_i} - \sum_{s=1}^{SP} n_s m_s \left\langle R_j \right\rangle_s = 0, \tag{2.95}$$

where the first, the second, and the sixth terms vanish by summation, and the *r.h.s.* in Equation (2.94) also vanishes.

Substituting Equation (2.46) into the last term in Equation (2.95) we get

$$\sum_{s=1}^{SP} n_s m_s \left\langle R_i \right\rangle_s = \sum_{s=1}^{SP} n_s q_s \left(E_i + \epsilon_{ijk} \left\langle v_j \right\rangle_s B_k\right), \tag{2.96}$$

which using Equations (2.1) and (2.2) simplifies to

$$\sum_{s=1}^{SP} n_s m_s \langle R_i \rangle_s = \rho_e E_i + \epsilon_{ijk} J_j B_k. \tag{2.97}$$

From the macroscopic neutrality condition of the plasma medium, $\rho_e \approx 0$ for large scales, and the one fluid momentum conservation equation becomes

$$\rho \frac{\partial \bar{v}_j}{\partial t} + \rho \bar{v}_i \frac{\partial \bar{v}_j}{\partial x_i} + \frac{\partial P_{ij}}{\partial x_i} - \epsilon_{jmn} J_m B_n = 0. \tag{2.98}$$

Multiplying Equation (2.93) by $\bar{v}_j$ and adding to Equation (2.98) we get

$$\frac{\partial (\rho \bar{v}_j)}{\partial t} + \frac{\partial (\rho \bar{v}_i \bar{v}_j)}{\partial x_i} + \frac{\partial P_{ij}}{\partial x_i} - \epsilon_{jmn} J_m B_n = 0. \tag{2.99}$$

The pressure stress tensor, P_{ij}, given in Equation (2.90) is modeled by

$$P_{ij} = p\delta_{ij} - \tau_{ij}, \tag{2.100}$$

where p is the plasma pressure given by

$$p = \rho R T, \tag{2.101}$$

T is the temperature given by

$$T = \frac{e}{c_v}. \tag{2.102}$$

R and c_v are the gas constant and the heat capacity at constant volume, respectively. They are related to the heat capacity at constant pressure by

$$c_p = R + c_v, \tag{2.103}$$

and

$$\gamma = \frac{c_p}{c_v}. \tag{2.104}$$

The shear stress tensor, τ_{ij}, is given by

$$\tau_{ij} = 2\mu S_{ij} + \lambda \delta_{ij} S_{kk} \tag{2.105}$$

where μ is the viscosity coefficient and λ is the second coefficient of viscosity given by

$$\lambda = \frac{-2}{3}\mu. \tag{2.106}$$

The strain tensor, S_{ij}, is given by

$$S_{ij} = \frac{1}{2}\left(\frac{\partial \bar{v}_i}{\partial x_j} + \frac{\partial \bar{v}_j}{\partial x_i}\right). \tag{2.107}$$

To get Equation (2.99) into a conservative form, we consider the last term given by $\epsilon_{ijk}J_jB_k$ and substitute from Equations (2.25) and (2.20) we get

$$\begin{aligned}\epsilon_{ijk}J_jB_k =&\frac{1}{\mu^m}\epsilon_{ijk}\epsilon_{jmn}B_kB_{n,m} = \frac{1}{\mu^m}\left(\delta_{mk}\delta_{ni}-\delta_{mi}\delta_{nk}\right)B_kB_{n,m}\\ =&\frac{1}{\mu^m}\left(B_{i,k}B_k-B_{k,i}B_k\right) = \frac{1}{\mu^m}\left(\left(B_iB_k\right)_{,k}-\left(\frac{1}{2}B_iB_i\right)_{,k}\right),\end{aligned} \tag{2.108}$$

which can be simplified as

$$\epsilon_{ijk}J_jB_k = \Pi_{ki,k}, \tag{2.109}$$

where Π_{ij} is given by

$$\Pi_{ij} = \tau^m_{ij} - p^m\delta_{ij}. \tag{2.110}$$

The magnetic pressure, p^m, and the magnetic product stress tensor, τ^m_{ij}, are given by

$$p^m = \frac{1}{2\mu^m}B_iB_i \tag{2.111}$$

and

$$\tau^m_{ij} = \frac{1}{\mu^m}B_iB_j. \tag{2.112}$$

Substituting Equation (2.109) into Equation (2.99) we get the one-fluid plasma dynamics equation in the strong conservation from given by

$$\frac{\partial\left(\rho\bar{v}_j\right)}{\partial t}+\frac{\partial}{\partial x_i}\left(\rho\bar{v}_i\bar{v}_j+p\delta_{ij}-\Pi_{ij}\right)-\frac{\partial}{\partial x_i}\left(\tau_{ij}\right)=0. \tag{2.113}$$

2.3.3 Conservation of Energy

The species energy equation is obtained from Equation (2.86) by substituting $\psi = \frac{1}{2} m_s \acute{v}_j \acute{v}_j$

$$\begin{aligned}
&\frac{\partial}{\partial t}\left(\frac{1}{2} n_s m_s \left\langle \acute{v}_j \acute{v}_j \right\rangle_s\right) + \frac{\partial}{\partial x_i}\left(\frac{1}{2} n_s m_s \bar{v}_i \left\langle \acute{v}_j \acute{v}_j \right\rangle_s\right) \\
&+ \frac{\partial}{\partial x_i}\left(\frac{1}{2} n_s m_s \left\langle \acute{v}_i \acute{v}_j \acute{v}_j \right\rangle_s\right) + n_s m_s \frac{\partial \bar{v}_j}{\partial t}\left\langle \acute{v}_j \right\rangle_s + n_s m_s \bar{v}_i \frac{\partial \bar{v}_j}{\partial x_i}\left\langle \acute{v}_j \right\rangle_s \\
&+ n_s m_s \frac{\partial \bar{v}_j}{\partial x_i}\left\langle \acute{v}_i \acute{v}_j \right\rangle_s - n_s m_s \left\langle R_j \acute{v}_j \right\rangle_s = M^s_{col.},
\end{aligned} \tag{2.114}$$

where $M^s_{col.}$ is given in Equation (2.75). The one-fluid plasma dynamics energy equation is obtained by summing Equation (2.114) over all the species leading to

$$\frac{\partial \rho e}{\partial t} + \frac{\partial \left(\rho e \bar{v}_i\right)}{\partial x_i} + \frac{\partial h_i}{\partial x_i} + P_{ij}\frac{\partial \bar{v}_j}{\partial x_i} - \sum_{s=1}^{SP} n_s m_s \left\langle R_j \acute{v}_j \right\rangle_s = 0, \tag{2.115}$$

where the fourth and the fifth terms vanish by summation. The *r.h.s.* in Equation (2.114) vanishes as well. The heat flux, $\mathbf{h}$, is given by Fourier's law

$$h_i = -k\frac{\partial T}{\partial x_i} \tag{2.116}$$

where k is the heat conduction coefficient.

Substituting Equation (2.46) into the last term in Equation (2.115) we get

$$\sum_{s=1}^{SP} n_s m_s \left\langle R_i \acute{v}_i \right\rangle_s = \sum_{s=1}^{SP} n_s m_s \left(E_i \left\langle \acute{v}_i \right\rangle_s + \epsilon_{ijk} \left\langle v_j \acute{v}_i \right\rangle_s B_k\right), \tag{2.117}$$

and using Equation (2.79) we get

$$\begin{aligned}\sum_{s=1}^{SP} n_s m_s \left\langle R_i \acute{v}_i \right\rangle_s = &\sum_{s=1}^{SP} n_s m_s \left(E_i \left\langle v_i - \bar{v}_i \right\rangle_s + \epsilon_{ijk} \left\langle v_j \left(v_i - \bar{v}_i \right) \right\rangle_s B_k \right) \\ &\sum_{s=1}^{SP} n_s m_s \left(E_i \left\langle v_i \right\rangle_s - E_i \bar{v}_i + \epsilon_{ijk} \left(\left\langle v_j v_i \right\rangle_s - \left\langle v_j \right\rangle_s \bar{v}_i \right) B_k \right).\end{aligned} \tag{2.118}$$

The second term in Equation (2.118) vanishes due to the macroscopic neutrality of the plasma medium. The third term vanishes because it is a symmetric tensor, while the permutation tensor is anti-symmetric. Simplifying Equation eqrefeqn:onefluidenergy04 by using Equations (2.2) and (2.12) we get

$$\sum_{s=1}^{SP} n_s m_s \left\langle R_i \acute{v}_i \right\rangle_s = \eta J_i J_i. \tag{2.119}$$

Substituting into Equation (2.115) we get

$$\frac{\partial \left(\rho e \right)}{\partial t} + \frac{\partial \left(\rho e \bar{v}_i \right)}{\partial x_i} + \frac{\partial h_i}{\partial x_i} + P_{ij} \frac{\partial \bar{v}_j}{\partial x_i} - \eta J_i J_i = 0. \tag{2.120}$$

In order to arrive at a conservative form, we transform the energy equation into the total gas energy defined by

$$e_t = e + \frac{1}{2} \bar{v}_k \bar{v}_k, \tag{2.121}$$

and add Equation (2.120) to the dot product of Equation (2.99) with v_j and use Equation (2.12) to get

$$\frac{\partial\left(\rho e_t\right)}{\partial t}+\frac{\partial\left(\rho e_t \bar{v}_i\right)}{\partial x_i}+\frac{\partial h_i}{\partial x_i}+\frac{\partial\left(P_{ij}\bar{v}_j\right)}{\partial x_i}-J_iE_i=0. \tag{2.122}$$

Expanding the last term using Equation (2.25) we get

$$\begin{aligned} J_iE_i =&\frac{1}{\mu^m}\epsilon_{ijk}B_{k,j}E_i \\ =&\frac{1}{\mu^m}\epsilon_{ijk}\left(B_kE_i\right)_{,j}-\frac{1}{\mu^m}\epsilon_{ijk}B_kE_{i,j} \\ =&-\frac{1}{\mu^m}\epsilon_{jik}\left(E_iB_k\right)_{,j}+\frac{1}{\mu^m}B_k\epsilon_{kji}E_{i,j}. \end{aligned} \tag{2.123}$$

Using Equation (2.17) we get

$$J_iE_i=-\left(\frac{\partial}{\partial t}\left(\frac{B_iB_i}{2\mu^m}\right)+\frac{\partial}{\partial x_i}\left(\frac{\epsilon_{ijk}E_jB_k}{\mu^m}\right)\right), \tag{2.124}$$

and using Equation (2.12) we get

$$J_iE_i=-\left(\frac{\partial}{\partial t}\left(\frac{B_iB_i}{2\mu^m}\right)+\frac{\partial}{\partial x_i}\left(\frac{\epsilon_{ijk}E'_jB_k}{\mu^m}\right)-\frac{\partial}{\partial x_i}\left(\frac{1}{\mu^m}\epsilon_{ijk}\epsilon_{jmn}\bar{v}_mB_nB_k\right)\right). \tag{2.125}$$

Simplifying the last term we get

$$\begin{aligned} \frac{1}{\mu^m}\epsilon_{jki}\epsilon_{jmn}\bar{v}_mB_nB_k =&\frac{1}{\mu^m}\left(\delta_{km}\delta_{in}-\delta_{im}\delta_{kn}\right)\bar{v}_mB_nB_k \\ =&\frac{1}{\mu^m}\left(B_iB_k\bar{v}_k-B_kB_k\bar{v}_i\right) \\ =&\frac{1}{\mu^m}\left(B_iB_k-\frac{B_jB_j}{2}\delta_{ik}\right)\bar{v}_k-\frac{B_kB_k}{2\mu^m}\bar{v}_i. \end{aligned} \tag{2.126}$$

Using Equation (2.110) we get

$$\frac{1}{\mu^m}\epsilon_{jki}\epsilon_{jmn}\bar{v}_m B_n B_k = \Pi_{ik}\bar{v}_k - \frac{B_k B_k}{2\mu^m}\bar{v}_i, \tag{2.127}$$

and substituting into Equation (2.125) we get

$$J_i E_i = -\left(\frac{\partial}{\partial t}\left(\frac{B_i B_i}{2\mu^m}\right) + \frac{\partial}{\partial x_i}\left(\frac{B_k B_k}{2\mu^m}\bar{v}_i\right) - \frac{\partial}{\partial x_i}\left(\Pi_{ik}\bar{v}_k\right) + \frac{\partial}{\partial x_i}\left(\frac{\epsilon_{ijk}E'_j B_k}{\mu^m}\right)\right). \tag{2.128}$$

In order to get a conservative form, we define the total plasma energy as

$$e_t^m = e_t + \frac{B_i B_i}{2\rho\mu^m}, \tag{2.129}$$

and using Equations (2.100) and (2.128) into Equation (2.122), we get the energy equation of the one-fluid plasma dynamics in strong conservative form given by

$$\frac{\partial\left(\rho e_t^m\right)}{\partial t} + \frac{\partial}{\partial x_i}\left(\left(\rho e_t^m + p\right)\bar{v}_i - \Pi_{ik}\bar{v}_k\right) + \frac{\partial}{\partial x_i}\left(h_i + h_i^m - \tau_{ij}\bar{v}_j\right) = 0, \tag{2.130}$$

where h_i^m is the magnetic heating term given by

$$h_i^m = \frac{\epsilon_{ijk}E'_j B_k}{\mu^m}. \tag{2.131}$$

2.3.4 Conservation Variables and Vector Form

From this point forward, the mean fluid velocity symbol $\bar{v}_i$ is replaced by v_i. The conservation equations can be written in the vector form given by

$$\frac{\partial \mathbf{U}}{\partial t} + \frac{\partial \mathbf{F}_i}{\partial x_i} + \frac{\partial \mathbf{G}_i}{\partial x_i} = 0 \tag{2.132}$$

where $\mathbf{U}$, $\mathbf{F}_i = \mathbf{F}_i(\mathbf{U})$, and $\mathbf{G}_i = \mathbf{G}_i(\mathbf{U}, \mathbf{U}_{,j})$ are the conservative variables vector, convective flux vector, and the diffusive flux vector, respectively. These functional relations are characterized by introducing the following Jacobians:

$$\mathbf{a}_i = \frac{\partial \mathbf{F}_i}{\partial \mathbf{U}}, \qquad \mathbf{b}_i = \frac{\partial \mathbf{G}_i}{\partial \mathbf{U}}, \qquad \mathbf{c}_{ij} = \frac{\partial \mathbf{G}_i}{\partial \mathbf{U}_{,j}}. \tag{2.133}$$

The details of these Jacobians are discussed in Appendix A.

Comparing Equations (2.93), (2.113), (2.130), and (2.40) to Equation (2.132) we get

$$\mathbf{U} = \begin{bmatrix} U_1 \\ U_{1+j} \\ U_5 \\ U_{5+j} \end{bmatrix} = \begin{bmatrix} \rho \\ \rho v_j \\ \rho e_t^m \\ B_j \end{bmatrix}, \tag{2.134}$$

$$\mathbf{F}_i = \begin{bmatrix} \rho v_i \\ \rho v_i v_j + p\delta_{ij} - \Pi_{ij} \\ v_i(\rho e_t^m + p) - \Pi_{ik} v_k \\ v_i B_j - v_j B_i \end{bmatrix}, \tag{2.135}$$

$$\mathbf{G}_i = \begin{bmatrix} 0 \\ -\tau_{ij} \\ -\tau_{ik}v_k + h_i + h_i^m \\ -\frac{\eta}{\mu^m}B_{j,i} \end{bmatrix}. \tag{2.136}$$

2.3.5 Normalization and Non-Dimensional Quantities

The system of equations governing the one-fluid, visco-resistive plasma dynamics given in Equation (2.132) can be non-dimensionalized by the free-stream quantities given by

$$x_i = L_\infty \overset{*}{x}_i, \tag{2.137}$$

$$\rho = \rho_\infty \overset{*}{\rho}, \tag{2.138}$$

$$T = T_\infty \overset{*}{T}, \tag{2.139}$$

$$v_i = v_\infty \overset{*}{v}_i, \tag{2.140}$$

and

$$B_i = B_\infty \overset{*}{B}_i. \tag{2.141}$$

The rest of the dependent properties can be normalized as follows:

$$t = \frac{L_\infty}{v_\infty} \overset{*}{t}, \tag{2.142}$$

$$p = \rho_\infty v_\infty^2 \overset{*}{p}, \tag{2.143}$$

$$e_t^m = v_\infty^2 \overset{*}{e}_t^m, \tag{2.144}$$

$$\tau_{ij} = \rho_\infty v_\infty^2 \overset{*}{\tau}_{ij}, \tag{2.145}$$

$$S_{ij} = \frac{v_\infty}{L_\infty} \overset{*}{S}_{ij}, \tag{2.146}$$

$$h_i = \rho_\infty v_\infty^3 \overset{*}{h}_i, \tag{2.147}$$

$$\tau_{ij}^m = \rho_\infty v_\infty^2 \overset{*}{\tau}_{ij}^m, \tag{2.148}$$

$$h_i^m = \rho_\infty v_\infty^3 \overset{*}{h}_i^m, \tag{2.149}$$

$$E_i = v_\infty B_\infty \overset{*}{E}_i, \tag{2.150}$$

and

$$J_i = \frac{\rho_\infty v_\infty^2}{B_\infty L_\infty} \overset{*}{J}_i. \tag{2.151}$$

The equation of state, Equation (2.101), becomes

$$\rho_\infty v_\infty^2 \overset{*}{p} = \rho_\infty \overset{*}{\rho} R T_\infty \overset{*}{T}. \tag{2.152}$$

Simplifying we get

$$\overset{*}{p} = \overset{*}{\rho} \overset{*}{R} \overset{*}{T}, \tag{2.153}$$

where

$$\overset{*}{R} = \frac{1}{\gamma M_\infty^2}. \tag{2.154}$$

The free-stream Mach number, M_∞, is given by

$$M_\infty = \frac{v_\infty}{a_\infty}, \tag{2.155}$$

where a_∞ is the speed of the acoustic waves in the plasma medium given by

$$a_\infty = \sqrt{\gamma R T_\infty}. \tag{2.156}$$

The shear stress, Equation (2.105), becomes

$$\rho_\infty v_\infty^2 \overset{*}{\tau}_{ij} = 2\mu \frac{v_\infty}{L_\infty} \overset{*}{S}_{ij} + \lambda \delta_{ij} \frac{v_\infty}{L_\infty} \overset{*}{S}_{kk}, \tag{2.157}$$

simplifying we get

$$\overset{*}{\tau}_{ij} = 2\overset{*}{\mu} \overset{*}{S}_{ij} + \overset{*}{\lambda} \delta_{ij} \overset{*}{S}_{kk}, \tag{2.158}$$

where $\overset{*}{\mu}$ and $\overset{*}{\lambda}$ are given by

$$\overset{*}{\mu} = \frac{\mu}{\mu_\infty Re_\infty}, \tag{2.159}$$

and

$$\overset{*}{\lambda} = \frac{-2}{3} \overset{*}{\mu}. \tag{2.160}$$

The free-stream Reynolds number, Re_∞, is given by

$$Re_\infty = \frac{\rho_\infty v_\infty L_\infty}{\mu_\infty}. \tag{2.161}$$

From Fourier's law, Equation (2.116), we get

$$\rho_\infty v_\infty^3 \overset{*}{h}_i = -k \frac{T_\infty}{L_\infty} \frac{\partial \overset{*}{T}}{\partial \overset{*}{x}_i}, \tag{2.162}$$

simplifying

$$\overset{*}{h}_i = -\overset{*}{k} \frac{\partial \overset{*}{T}}{\partial \overset{*}{x}_i}, \tag{2.163}$$

where $\overset{*}{k}$ is given by

$$\overset{*}{k} = \begin{cases} \dfrac{1}{(\gamma-1)\, Re_\infty M_\infty^2 Pr} \left(\dfrac{\mu}{\mu_\infty}\right) & \text{if } Pr = \text{ const.} \\ \dfrac{1}{(\gamma-1)\, Re_\infty M_\infty^2 Pr_\infty} \left(\dfrac{k}{k_\infty}\right) & \text{if } Pr \neq \text{ const.} \end{cases} \tag{2.164}$$

the free-stream Prandtl number, Pr_∞, is given by

$$Pr_\infty = \frac{\mu_\infty c_p}{k_\infty}, \tag{2.165}$$

and the Peclet number, Pe, is given by

$$Pe = Re\, Pr. \tag{2.166}$$

From Ampere's law, Equation (2.25), we get

$$\frac{\rho_\infty v_\infty^2}{B_\infty L_\infty} \overset{*}{J}_i = \frac{1}{\mu^m} \frac{B_\infty}{L_\infty} \epsilon_{ijk} \overset{*}{B}_{k,j}, \tag{2.167}$$

simplifying

$$\overset{*}{J}_i = \frac{1}{\overset{*}{\mu}^m} \epsilon_{ijk} \overset{*}{B}_{k,j}, \tag{2.168}$$

where $\overset{*}{\mu}^m$ is given by

$$\overset{*}{\mu}^m = \left(M_\infty^m\right)^2. \tag{2.169}$$

The free-stream magnetic Mach number, M_∞^m, is given by

$$M_\infty^m = \frac{v_\infty}{\left(v_a\right)_\infty}, \tag{2.170}$$

where $\left(v_a\right)_\infty$ is the free-stream Alfvén wave speed given by

$$\left(v_a\right)_\infty = \frac{B_\infty}{\sqrt{\mu^m \rho_\infty}}. \tag{2.171}$$

From Ohm's law, Equation (2.12), we get

$$\eta \frac{\rho_\infty v_\infty^2}{B_\infty L_\infty} \overset{*}{J}_i = v_\infty B_\infty \left(\overset{*}{E}_i + \epsilon_{ijk} \overset{*}{v}_j \overset{*}{B}_k \right), \tag{2.172}$$

simplifying

$$\overset{*}{\eta} \overset{*}{J}_i = \overset{*}{E}_i + \epsilon_{ijk} \overset{*}{v}_j \overset{*}{B}_k, \tag{2.173}$$

where $\overset{*}{\eta}$ is given by

$$\overset{*}{\eta} = \frac{1}{\overset{*}{\sigma}} = \frac{1}{N_\infty}. \tag{2.174}$$

The magnetic interaction number, N_∞, is defined by

$$N_\infty = \frac{Rm_\infty}{(M_\infty^m)^2} = \frac{B_\infty^2 L_\infty}{\eta \rho_\infty v_\infty}, \tag{2.175}$$

where Rm_∞ is the magnetic Reynolds number given by

$$Rm_\infty = \frac{L_\infty v_\infty}{\lambda^m} = \frac{\mu_0^m L_\infty v_\infty}{\eta} = \sigma \mu^m L_\infty v_\infty. \tag{2.176}$$

The Lundquist number, S_L, is given by

$$S_L = \sqrt{Rm\, N}. \tag{2.177}$$

The magnetic/viscous interaction parameters are the Hartmann number, Ha, and the magnetic Prandtl number, Pm, given by

$$Ha = \sqrt{ReN} \tag{2.178}$$

and

$$Pm = \frac{Rm}{Re}. \tag{2.179}$$

Since all governing equations are normalized to have the same form, with only the constitutive properties being different, the non-dimensional notation, *, is dropped hereafter.

2.4 Simplification of Governing Equations

Neglecting the diffusive flux term, Equation (2.136), we get the ideal MHD equations for a compressible plasma medium. The full Navier-stokes equations, describing the compressible viscous Newtonian fluid flow with no body forces, no chemical reactions, and no heat sources can be obtained from Equations (2.134), (2.135), and (2.136) by dropping all the magnetic terms leading to

$$\mathbf{U} = \begin{bmatrix} \rho \\ \rho v_j \\ \rho e_t \end{bmatrix}, \tag{2.180}$$

$$\mathbf{F}_i = \begin{bmatrix} \rho v_i \\ \rho v_i v_j + p\delta_{ij} \\ v_i \left(\rho e_t + p\right) \end{bmatrix}, \tag{2.181}$$

$$\mathbf{G}_i = \begin{bmatrix} 0 \\ -\tau_{ij} \\ -\tau_{ik} v_k + h_i \end{bmatrix}. \tag{2.182}$$

The Sutherland's law can be employed to account for the temperature effects on viscosity

$$\mu = \frac{C_1 T^{1.5}}{C_2 + T}, \tag{2.183}$$

or

$$\frac{\mu}{\mu_\infty} = \frac{1 + C_2/T_\infty}{\overset{*}{T} + C_2/T_\infty} \overset{*}{T}^{1.5}. \tag{2.184}$$

The Sutherland's law can also be employed to account for the temperature effects on the thermal conductivity

$$k = \frac{C_3 T^{1.5}}{C_4 + T}. \tag{2.185}$$

or

$$\frac{k}{k_\infty} = \frac{1 + C_4/T_\infty}{\overset{*}{T} + C_4/T_\infty} \overset{*}{T}^{1.5}. \tag{2.186}$$

For air, the Sutherland's coefficients are given by

$$C_1 = 1.458 \times 10^{-6} Kg/m\, sec\, K^{\frac{1}{2}}$$

$$C_2 = 110.4K$$

$$C_3 = 2.495 \times 10^{-3} Kg/m\, sec^3\, K^{\frac{3}{2}}$$

$$C_4 = 194.0K.$$

Neglecting the diffusion term, Equation (2.182), in the Navier-Stokes equations we get the Euler equations.

CHAPTER 3

THE FLOWFIELD DEPENDENT VARIATION METHOD

In this chapter, the FDV method is introduced in detail along with its FEM implementation. To carry out the mathematical steps of the FDV method, the first and second order time derivatives of the conservation variables vector, $\mathbf{U}$, are necessary. The first order derivative is obtained by rewriting Equation (2.132) in the form

$$\frac{\partial \mathbf{U}}{\partial t} = -\frac{\partial \mathbf{F}_i}{\partial x_i} - \frac{\partial \mathbf{G}_i}{\partial x_i}. \tag{3.1}$$

The second order time derivative of $\mathbf{U}$ is obtained by taking the time derivative of Equation (3.1), interchanging the spatial and time derivatives, and using the Jacobians introduced in Equation (2.133):

$$\frac{\partial^2 \mathbf{U}}{\partial t^2} = \frac{\partial}{\partial x_i}\left((\mathbf{a}_i + \mathbf{b}_i)\left(\frac{\partial \mathbf{F}_j}{\partial x_j} + \frac{\partial \mathbf{G}_j}{\partial x_j}\right)\right) + \frac{\partial^2}{\partial x_i \partial x_j}\left(\mathbf{c}_{ij}\left(\frac{\partial \mathbf{F}_k}{\partial x_k} + \frac{\partial \mathbf{G}_k}{\partial x_k}\right)\right). \tag{3.2}$$

The FDV method is best summarized in the three steps given in Sections 3.1, 3.2, and 3.3. The finite element implementation of the FDV method is introduced in Section 3.4.

3.1 Special Taylor Series Expansion

Expanding $\mathbf{U}^{n+1}$ in a special form of Taylor series about $\mathbf{U}^n$ we get

$$\mathbf{U}^{n+1} = \mathbf{U}^n + \Delta t \frac{\partial \mathbf{U}^{n+s_a}}{\partial t} + \frac{\Delta t^2}{2} \frac{\partial^2 \mathbf{U}^{n+s_b}}{\partial t^2} + O\left(\Delta t^3\right) \tag{3.3}$$

where

$$\frac{\partial \mathbf{U}^{n+s_a}}{\partial t} = \frac{\partial \mathbf{U}^n}{\partial t} + s_a \frac{\partial \Delta \mathbf{U}^{n+1}}{\partial t} \qquad 0 \leq s_a \leq 1 \tag{3.4}$$

$$\frac{\partial^2 \mathbf{U}^{n+s_b}}{\partial t^2} = \frac{\partial^2 \mathbf{U}^n}{\partial t^2} + s_b \frac{\partial^2 \Delta \mathbf{U}^{n+1}}{\partial t^2} \qquad 0 \leq s_b \leq 1 \tag{3.5}$$

$$\Delta \mathbf{U}^{n+1} = \mathbf{U}^{n+1} - \mathbf{U}^n. \tag{3.6}$$

Substituting Equations (3.4)-(3.6) into Equation (3.3) we get

$$\Delta \mathbf{U}^{n+1} = \Delta t \left(\frac{\partial \mathbf{U}^n}{\partial t} + s_a \frac{\partial \Delta \mathbf{U}^{n+1}}{\partial t} \right) + \frac{\Delta t^2}{2} \left(\frac{\partial^2 \mathbf{U}^n}{\partial t^2} + s_b \frac{\partial^2 \Delta \mathbf{U}^{n+1}}{\partial t^2} \right) + O\left(\Delta t^3\right). \tag{3.7}$$

Expanding Equation (3.7) with the time derivatives given in Equations (3.1) and (3.2), and neglecting the product of the diffusion gradient Jacobian with the third order derivatives, we get

$$\begin{aligned} \Delta \mathbf{U}^{n+1} = & -\Delta t \left(\frac{\partial \mathbf{F}_i^n}{\partial x_i} + \frac{\partial \mathbf{G}_i^n}{\partial x_i} \right) - \Delta t s_a \left(\frac{\partial \Delta \mathbf{F}_i^{n+1}}{\partial x_i} + \frac{\partial \Delta \mathbf{G}_i^{n+1}}{\partial x_i} \right) \\ & + \frac{\Delta t^2}{2} \frac{\partial}{\partial x_i} \left((\mathbf{a}_i + \mathbf{b}_i) \left(\frac{\partial \mathbf{F}_j^n}{\partial x_j} + \frac{\partial \mathbf{G}_j^n}{\partial x_j} \right) \right) \\ & + \frac{\Delta t^2}{2} s_b \frac{\partial}{\partial x_i} \left((\mathbf{a}_i + \mathbf{b}_i) \left(\frac{\partial \Delta \mathbf{F}_j^{n+1}}{\partial x_j} + \frac{\partial \Delta \mathbf{G}_j^{n+1}}{\partial x_j} \right) \right). \end{aligned} \tag{3.8}$$

3.2 Introducing the FDV Parameters

In order to provide variations to the changes of convection and diffusion terms differently in accordance with the current flowfield situation, we reassign s_a and s_b as follows:

$$s_a \Delta \mathbf{F}_i \Rightarrow s_1 \Delta \mathbf{F}_i, \qquad s_a \Delta \mathbf{G}_i \Rightarrow s_3 \Delta \mathbf{G}_i \tag{3.9}$$

$$s_b \Delta \mathbf{F}_i \Rightarrow s_2 \Delta \mathbf{F}_i, \qquad s_b \Delta \mathbf{G}_i \Rightarrow s_4 \Delta \mathbf{G}_i. \tag{3.10}$$

s_1/s_2 and s_3/s_4 are the first/second order FDV parameters for convection and diffusion, respectively. These parameters gain their physical role through their calculation from the fluctuations in the appropriate flow variables, such as the Mach number or the magnetic Mach number for convection, and the Reynolds number or the magnetic Reynolds number for diffusion. The first order FDV parameters, s_1 and s_3, are flowfield dependent and their major role is to provide accuracy in physics, whereas the second order FDV parameters, s_2 and s_4, are assumed to be exponentially proportional to the first order parameters providing numerical stability in the solution process [31].

The convection FDV parameters are determined from the Mach number based on the speed of sound for fluids, or the Mach number based on the Alfvén velocity

for plasmas, and given by

$$s_1 = \begin{cases} \min(r,1) & r > \alpha \\ 0 & r < \alpha, M_{min} \neq 0 \\ 1 & M_{min} = 0 \end{cases} \tag{3.11}$$

$$s_2 = \frac{1}{2}\left(1 + s_1^{\eta}\right) \tag{3.12}$$

$$r = \sqrt{M_{max}^2 - M_{min}^2}/M_{min}$$

or

$$s_1 = \begin{cases} \min(r,1) & r > \alpha \\ 0 & r < \alpha, M_{min}^m \neq 0 \\ 1 & M_{min}^m = 0 \end{cases} \tag{3.13}$$

$$s_2 = \frac{1}{2}\left(1 + s_1^{\eta}\right) \tag{3.14}$$

$$r = \sqrt{\left(M_{max}^m\right)^2 - \left(M_{min}^m\right)^2}/M_{min}^m$$

whichever is larger. The diffusion FDV parameters are calculated using the Reynolds number, the Peclet number, or the magnetic Reynolds number and given by

$$s_3 = \begin{cases} \min(r, 1) & r > \alpha \\ 0 & r < \alpha, Re_{min} \neq 0 \\ 1 & Re_{min} = 0 \end{cases} \tag{3.15}$$

$$s_4 = \frac{1}{2}\left(1 + s_3^{\eta}\right) \tag{3.16}$$

$$r = \sqrt{Re_{max}^2 - Re_{min}^2}/Re_{min}$$

or

$$s_3 = \begin{cases} \min(r, 1) & r > \alpha \\ 0 & r < \alpha, Pe_{min} \neq 0 \\ 1 & Pe_{min} = 0 \end{cases} \tag{3.17}$$

$$s_4 = \frac{1}{2}\left(1 + s_3^{\eta}\right) \tag{3.18}$$

$$r = \sqrt{Pe_{max}^2 - Pe_{min}^2}/Pe_{min}$$

or

$$s_3 = \begin{cases} \min(r, 1) & r > \alpha \\ 0 & r < \alpha, Rm_{min} \neq 0 \\ 1 & Rm_{min} = 0 \end{cases} \tag{3.19}$$

$$s_4 = \frac{1}{2}\left(1 + s_3^{\eta}\right) \tag{3.20}$$

$$r = \sqrt{Rm_{max}^2 - Rm_{min}^2}/Rm_{min}$$

whichever is larger, where the maximum and minimum values are calculated between local element nodes, $0.05 < \eta < 0.2$, and the FDV parameters are to be updated at each time step. The primary goal of s_1 and s_3 is to provide the best possible solution accuracy in the regions of high gradients and discontinuities, whereas the goal from s_2 and s_4 is to provide the solution stability. Changing the flow regime changes the FDV parameters and adjusts the numerical scheme for the appropriate conditions.

3.3 The Residual Form

Rewriting Equation (3.8) in the residual form we get

$$\begin{aligned} \mathbf{R} =& \Delta\mathbf{U}^{n+1} + \Delta t\left(\frac{\partial \mathbf{F}_i^n}{\partial x_i} + \frac{\partial \mathbf{G}_i^n}{\partial x_i}\right) + \Delta t\left(s_1\frac{\partial \Delta\mathbf{F}_i^{n+1}}{\partial x_i} + s_3\frac{\partial \Delta\mathbf{G}_i^{n+1}}{\partial x_i}\right) \\ & - \frac{\Delta t^2}{2}\frac{\partial}{\partial x_i}\left((\mathbf{a}_i + \mathbf{b}_i)\left(\frac{\partial \mathbf{F}_j^n}{\partial x_j} + \frac{\partial \mathbf{G}_j^n}{\partial x_j}\right)\right) \\ & - \frac{\Delta t^2}{2}\frac{\partial}{\partial x_i}\left((\mathbf{a}_i + \mathbf{b}_i)\left(s_2\frac{\partial \Delta\mathbf{F}_j^{n+1}}{\partial x_j} + s_4\frac{\partial \Delta\mathbf{G}_j^{n+1}}{\partial x_j}\right)\right) = O\left(\Delta t^3\right). \end{aligned} \tag{3.21}$$

Substituting all the Δ terms with their Jacobian equivalents, and neglecting the diffusive gradient Jacobian product with the third order derivative, we get

$$\mathbf{R} = \Delta\mathbf{U}^{n+1} + \mathbf{D}_i^n \Delta\mathbf{U}_{,i}^{n+1} + \mathbf{E}_{ij}^n \Delta\mathbf{U}_{,ij}^{n+1} + \mathbf{Q}^n = O\left(\Delta t^3\right) \tag{3.22}$$

where

$$\mathbf{D}_i^n = \Delta t \left(s_1 \mathbf{a}_i + s_3 \mathbf{b}_i\right) \tag{3.23}$$

$$\mathbf{E}_{ij}^n = \Delta t s_3 \mathbf{c}_{ij} - \frac{\Delta t^2}{2} \left(\mathbf{a}_i + \mathbf{b}_i\right) \left(s_2 \mathbf{a}_j + s_4 \mathbf{b}_j\right) \tag{3.24}$$

$$\mathbf{Q}^n = \Delta t \left(\mathbf{F}_{i,i}^n + \mathbf{G}_{i,i}^n\right) - \frac{\Delta t^2}{2} \left(\mathbf{a}_i + \mathbf{b}_i\right) \left(\mathbf{F}_{j,ji}^n + \mathbf{G}_{j,ji}^n\right). \tag{3.25}$$

3.4 Finite Element Implementation

Since all the numerical stability mechanisms are already built-in into the FDV method, the FEM discretization via standard Galerkin method is sufficient;

$$\int_\Omega \Phi_\alpha R_r d\Omega = 0 \tag{3.26}$$

where Φ_α is a shape function. Applying the standard Galerkin method, Equation (3.26), to the residual given in Equation (3.22), integrating by parts, and arranging in a compact form, the element equations are given by

$$\left(A_{\alpha\beta rs}^n + B_{\alpha\beta rs}^n\right) \Delta U_{\beta s}^{n+1} = H_{\alpha r}^n + N_{\alpha r}^n \tag{3.27}$$

where

$$A^n_{\alpha\beta rs} = \int_\Omega \left(\Phi_\alpha \Phi_\beta \delta_{rs} - \Phi_{\alpha,i}\Phi_\beta D^n_{irs} - \Phi_{\alpha,i}\Phi_{\beta,j}E^n_{ijrs}\right) d\Omega \tag{3.28}$$

$$B^n_{\alpha\beta rs} = \int_\Gamma \left(\overset{*}{\Phi}_\alpha \overset{*}{\Phi}_\beta \overset{*}{D}{}^n_{irs} + \overset{*}{\Phi}_\alpha \overset{*}{\Phi}_{\beta,j} \overset{*}{E}{}^n_{ijrs}\right) n_i d\Gamma \tag{3.29}$$

$$H^n_{\alpha r} = \int_\Omega \left(\Delta t \Phi_{\alpha,i}\left(F^n_{ir} + G^n_{ir}\right) - \frac{\Delta t^2}{2}\Phi_{\alpha,i}\left(a_{irs} + b_{irs}\right)\left(F^n_{js,j} + G^n_{js,j}\right)\right) d\Omega \tag{3.30}$$

$$N^n_{\alpha r} = \int_\Gamma \left(-\Delta t \overset{*}{\Phi}_\alpha \left(\overset{*}{F}{}^n_{ir} + \overset{*}{G}{}^n_{ir}\right) + \frac{\Delta t^2}{2}\overset{*}{\Phi}_\alpha \left(a_{irs} + b_{irs}\right)\left(\overset{*}{F}{}^n_{js,j} + \overset{*}{G}{}^n_{js,j}\right)\right) n_i d\Gamma. \tag{3.31}$$

Equation (3.27) is referred to as the finite element equations. The superscript * is used for the contour variables. Neumann boundary conditions are easily accessible through the contour integrals, which cancel each other along the inter-element-faces insuring flux conservation. Dirichlet Boundary conditions are, also, very easy to enforce through the EBE data approach. One very interesting feature of FEMs, in general, is the automatic continuity of fluxes along the interfaces of any kind of elements. This is achieved by simply neglecting all contour integrals in the element equations.

In some special problems, such as the MHD shock tube and the Orszag-Tang vortex problems discussed in Sections 5.3.2 and 5.3.3, respectively, an extra term is added to Equation (3.27) for increased stability [32]. This term has the form

$$\int_\Omega \nu_d s_1 \Phi_{\alpha,i} U_{r,i} d\Omega,$$

which is the form of a classical artificial viscosity, and $0.005 \leq \nu_d \leq 0.01$.

Equation (3.27) is believed to include all the necessary numerical treatment to handle the different flow situations that could be encountered in the whole Mach number spectrum. This includes shock capturing for supersonic flows, as well as very low Mach number incompressible flows. A complete comparison between the FDV method, as a generalized scheme, and the other FEMs, FVMs, and FDMs, as special cases of FDV, is given in Chung [31].

CHAPTER 4

A GENERALIZED PARALLEL PROCESSING FRAMEWORK FOR UNSTRUCTURED HIGHER ORDER FINITE ELEMENT METHODS USING EBE-GMRES AND MPI

While implicit schemes have proved their superiority, in most cases, compared to their explicit counterparts in terms of numerical stability and accuracy the quest for their efficient parallelization is still ongoing. The main difficulty is the parallelization of the linear system solver. Direct solvers, like Gauss elimination, are considered as a good choice only for small finite element applications because of the associated computer needs. For practical finite element applications of large sizes, iteration-based matrix solvers are more computationally efficient. One of the most successful iterative solvers is the GMRES algorithm first introduced in Saad and Schultz [33]. This solver has the ability to work on general non-symmetric systems with superior performance compared to other conventional solvers.

Although GMRES is considered to be an effective iterative matrix solver, for large time steps and/or poor grids (*i.e.* discontinuous element sizes), the linear system becomes *"ill-conditioned"*. Such systems can slow the convergence of any iterative solver, and could cause convergence failure. Many preconditioning techniques have

been developed to improve the convergence of these systems [34, 35]. The basic idea is to carry out a transformation, which clusters the matrix bandwidth, and hence accelerates the convergence of both well-conditioned and ill-conditioned systems. The simplest form of these transformations is the diagonal preconditioner [31]. The incomplete LU (ILU) factorization is a more effective preconditioner when compared to the diagonal preconditioner in serial calculations.

Many of the system matrix entries are zeros because of the naturally unconnected nodes in the numerical grid. Different data structures can be adopted to reduce the computer memory needed in the system storage, including: sparse matrix [32,36], element-by-element (EBE) [37], and matrix free methods [38]. In this work we select the EBE data structure, in which assembly of the global matrix is not required. Hence, EBE data structure is a viable distributed memory model. The direct access to the element equations in the EBE data structure is effective in the application of different boundary conditions that may arise from the physics at hand.

Early research effort that indicated the potential of parallelized FEMs in CFD includes the work of Hughes and his co-workers [39–41] and [42]. The interested reader is referred to [43] for a good summary of the early progress in the parallel FEM research field. The recent literature is more diverse. Efficient parallelization of the ILU preconditioner is one of the main topics usually discussed. For brevity we only mention two publications including that of [44], which introduced a platform for parallel FEM applications in CFD based on distributed linear system generation and freeware parallel iterative solver libraries. Although the linear system is generated locally, a global sparse matrix is required for this framework. Reference [45] introduced

a parallel FEM implementation based on Lagrange multipliers and domain decomposition. In their framework, only the nodes shared between processors are used in the communication. However, the total number of equations increases with the number of processors.

A generalized framework for the efficient parallelization of implicit FEMs using domain decomposition through EBE data structure as a distributed memory model is introduced in this appendix. This framework is independent of the employed FEM scheme and can handle unstructured higher order grids as well as any number of equations per node without major modifications. The number of EBE-GMRES iterations and the number of total equations are independent of the number of processors used. The diagonal preconditioner is employed to avoid the inefficiencies and complexities associated with the parallelization of the ILU preconditioner [45–51].

The layout of this chapter is as follows. Section 4.1 introduces the framework and its various components; unstructured grids partitioning, conversion from linear grids to higher order grids, and the underlying distributed memory approach. Section 4.2 discusses in details the architecture of both the serial and parallel generalized solvers. Section 4.3 summarizes the serial EBE-GMRES iterative solver with a diagonal preconditioner and introduces the proposed parallel implementation in this research work. Different possible communication strategies are also discussed in this section. The parallel performance evaluation of the proposed framework is discussed in Section 4.4 indicating various factors affecting the parallel efficiency and speedup including: unstructured grids partitioning, higher order accuracy, and change of problem size.

4.1 The Generalized FEM Framework

The design of the proposed generalized FEM framework, shown on Figure 4.1, encapsulates all the details of the FEM scheme at hand as well as the set of equations in its most basic building block of the finite element equations. Changing the FEM scheme or solving for different physics with a different number of equations is totally independent of the solver architecture as discussed in Section 4.2. Grid generation, initialization, and post-processing of the simulation data are not discussed herein because they are specific to the physics at hand.

4.1.1 Unstructured Grid Partitioning

Consider the unstructured domain shown on Figure 4.2. Let

$$E = \{E^{(1)}, E^{(2)}, \cdots, E^{(NE)}\} \tag{4.1}$$

be a set of all non-overlapping elements in Ω, and NE be the total number of elements. In other words,

$$\bigcup_{e=1}^{NE} E^{(e)} = \Omega \tag{4.2}$$

such that,

$$E^{(i)} \cap E^{(j)} = \Gamma_{ij}, \quad \forall i \neq j, \quad E^{(i)}, E^{(j)} \in E \tag{4.3}$$

where Γ_{ij} is a node/line/area of intersection between neighboring 1D/2D/3D elements, respectively. This finite element grid data obtained from grid generation software are, in general, not optimized for parallel processing. Unstructured elements

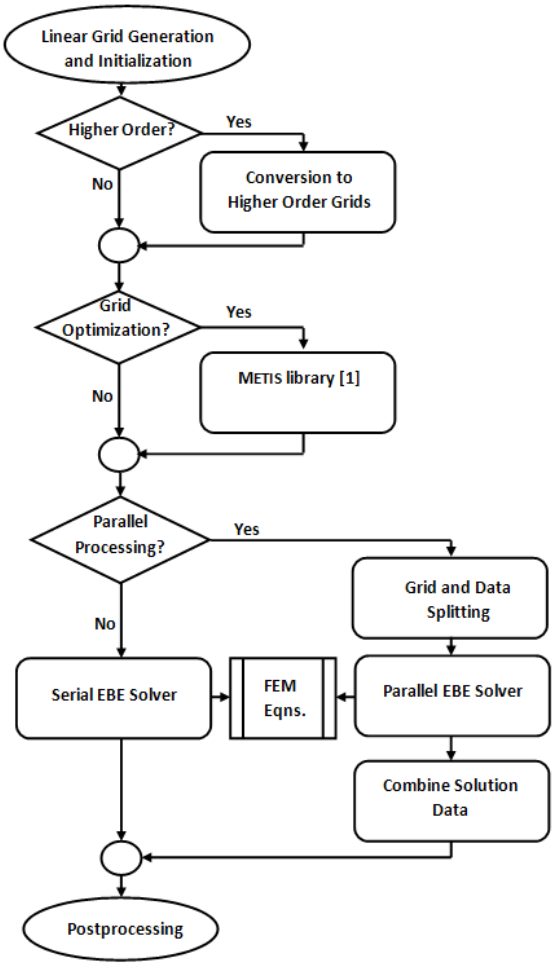

Figure 4.1 The proposed generalized FEM framework.

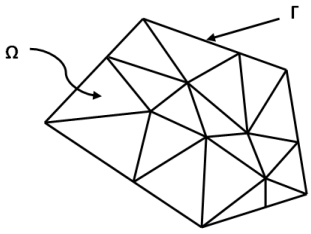

Figure 4.2 A general unstructured domain, Ω, with boundary Γ.

have to be divided into non-overlapping groups to minimize the parallel processing communication traffic.

One of the most successful unstructured grid partitioning packages is METIS [30]. This software package splits the elements' list, E, according to a preselected number of groups. Several optimization options can be used to fit the specific grid at hand including hybrid grid elements and multi-physics load balancing. The resulting sub-domains are optimized to have minimal boundaries for communication and the non-overlapping condition is strictly enforced.

4.1.2 Higher Order Grids

The generation of higher order finite element grids is not a standard option in commercially available software. The implementation of a software utility that converts linear grids into higher order seems to be a more viable alternative to ensure a straightforward integration with any commercially available grid generation software. Currently the proposed framework supports 1D/2D/3D elements with $\mathbf{C}^0$ continuity of two different families, namely; arbitrary higher order Lagrange polynomial elements, and linear/quadratic/cubic serendipity elements [52].

By definition, the serendipity elements have all the nodes on the edges. Hence, a unique segments list, S, exists between the linear grid nodes. Each element, $E^{(e)}$, can generate a set of line segment, $S^{(e)} = \{S_1^{(e)}, S_1^{(e)}, \cdots, S_{NL}^{(e)}\}$, where $NL = 4$ for 2D quadratic elements, and 12 for 3D hexahedral elements. The unique segments' list,

S, is given by

$$S = \bigcup_{e=1}^{NE} S^{(e)}. \tag{4.4}$$

Again, from the definition of the serendipity family of elements, all the new higher order nodes to be inserted are on S, and the data on Γ is to be updated as well. A utility program was constructed to convert the unstructured linear elements' data (2D or 3D) into the required higher order (quadratic or cubic). For example, Figure 4.3 shows a simple 2D linear grid and the corresponding higher order grids obtained by the proposed segments processing logic. The newly inserted higher order nodes are directly proportional to the corresponding unique segments, S, given in Table 4.1. The grid topology details, shown on Figure 4.3 and Table 4.1, is used throughout this appendix to provide a simple illustrative example.

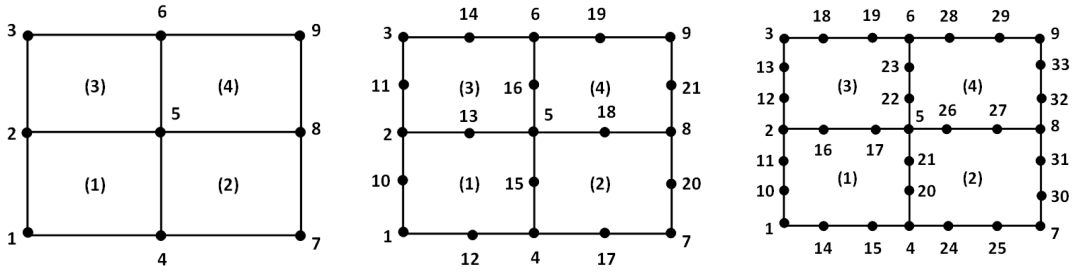

(a) (b) (c)

Figure 4.3 A sample 2D 2×2 grid showing the higher order grid conversion process using serendipity elements. (a) original linear grid, (b) quadratic, and (c) cubic.

A similar utility was also developed to convert 1D/2D/3D elements into Lagrange polynomial elements of arbitrary order of accuracy. The details of implementation for this utility is omitted for brevity. More element types (e.g. tetrahedrons

and prisms) can be treated with a similar logic. This facilitates the inclusion of a higher order hybrid element option capable of solving highly complicated flow fields, while preserving the order of accuracy and the continuity of the fluxes at the hybrid interfaces. It is worth noting that only FEMs can make such a claim in hybrid grids since fluxes are conserved naturally along the interfaces by neglecting the surface integrals in the element equations [31]. The sufficient number of Gauss quadrature points is selected during the run time according to the element order to preserve the level of accuracy attained by the shape function and minimize the work load [52].

Table 4.1 The unique segments' list, S, for the 2D linear grid shown on Figure 4.3(a).

Segment ID	Node 1	Node 2	Quadratic Nodes	Cubic Nodes
1	1	2	10	10, 11
2	2	3	11	12, 13
3	1	4	12	14, 15
4	2	5	13	16, 17
5	3	6	14	18, 19
6	4	5	15	20, 21
7	5	6	16	22, 23
8	4	7	17	24, 25
9	5	8	18	26, 27
10	6	9	19	28, 29
11	7	8	20	30, 31
12	8	9	21	32, 33

4.1.3 Distributed Memory Model Implementation

The finite element data structure on irregular grids is best maintained by a connectivity list, which is a list of the nodes' global numbers for each element. Let $N = \{N^1, N^2, \cdots, N^{NN}\}$ be an ordered set of all nodes in Ω, and NN be the number

of nodes. Each element can be defined by an ordered list given by

$$E_i^{(e)} = \Delta_{ij}^{(e)} N^j \tag{4.5}$$

where $\Delta_{ij}^{(e)}$ is a Boolean matrix with nonzero values only if local node i in element $E^{(e)}$ corresponds to global node j. As a logical consequence of that, all nodes in the numerical grid should be introduced in the connectivity list at least once. The domain decomposition of Ω is a straightforward task using this data structure, where the computational load can be balanced among the processors by equally distributing the elements. Unlike the multi-block data structure, common in the higher order FVMs, this FEM data structure can achieve nearly perfect balancing while solving for higher order elements on irregular grids.

Let ND be the number of sub-domains selected to divide Ω, and the list of the sub-domains is given by

$$\bigcup_{d=1}^{ND} \Omega^{[d]} = \Omega \tag{4.6}$$

such that

$$\Omega^{[i]} \cap \Omega^{[j]} = \bar{\Delta}_k^{[i,j]} N^k, \quad \forall i \neq j \tag{4.7}$$

where $\bar{\Delta}_k^{[i,j]}$ is a Boolean matrix with nonzero values only if global node k is shared between sub-domains $\Omega^{[i]}$ and $\Omega^{[j]}$.

Communication nodes, recognized by $\bar{\Delta}_k^{[i,j]}$, are linked across domains via their global indexing in N. The communication information is used in the EBE solution of the linear system as discussed in Section 4.3. The computer implementation of this

logic requires both global and local indexing of the nodes. Each processor is assigned the load of one sub-domain, i.e. $NP = ND$, where NP is the number of processors. Only the data relevant to each processor is stored on its local memory. A sample decomposition of the quadratic grid of Figure 4.3(b) into three sub-domains is shown on Figure 4.4. All the corresponding domain decomposition data can be extracted using $\bar{\Delta}_k^{[i,j]}$ shown in Table 4.2. Communication nodes, shown in Table 4.3, can also be recognized along with their different indexed values in each sub-domain.

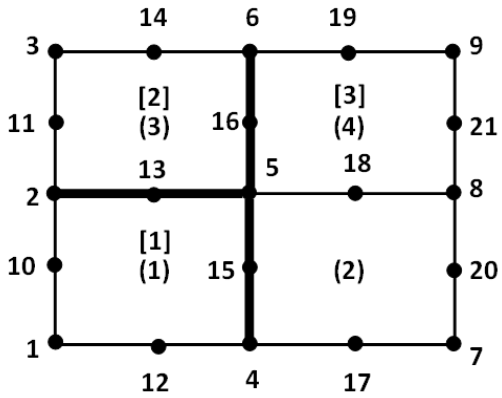

Figure 4.4 Domain decomposition of the quadratic grid shown on Figure 4.3(b) into three sub-domains.

It should be clear that this treatment is independent of the used FEM scheme and the system of equations to be solved. Fixing all the communication and the data traffic between processors to be nodal based facilitates future development without major modifications in the core of the parallel communications.

Table 4.2 Domain decomposition details for Figure 4.4.

Sub-Domain	Global Element	Local Element	Global Node	Local Node	Communication Node
1	1	1	1	1	No
			2	2	Yes
			4	3	Yes
			5	4	Yes
			10	5	No
			12	6	No
			13	7	Yes
			15	8	Yes
2	3	1	2	1	Yes
			3	2	No
			5	3	Yes
			6	4	Yes
			11	5	No
			13	6	Yes
			14	7	No
			16	8	Yes
3	2	1	4	1	Yes
			5	3	Yes
			7	9	No
			8	11	No
			15	2	Yes
			17	6	No
			18	7	No
			20	10	No
	4	2	5	3	Yes
			6	5	Yes
			8	11	No
			9	13	No
			16	4	Yes
			18	7	No
			19	8	No
			21	12	No

Table 4.3 Communication nodes' local indices for the quadratic grid given on Figure 4.4.

Communication Node	Global Node	Sub-Domain 1	Sub-Domain 2	Sub-Domain 3
1	2	2	1	—
2	4	3	—	1
3	5	4	3	3
4	6	—	4	5
5	13	7	6	—
6	15	8	—	2
7	16	—	8	4

4.2 Generalized Solver Architecture

All implicit FEM schemes result in a system of equations from the assembly of the element equations. This system is usually linear, or can be linearized in the form:

$$\mathbf{AX} = \mathbf{F} \tag{4.8}$$

where $\mathbf{A}$ is the global stiffness matrix of size $n \times n$, $\mathbf{F}$ is the right hand side vector of length n, and $\mathbf{X}$ is the unknowns vector of length n. By definition

$$n = \sum_{i=1}^{NN} NEQ_i$$

where NEQ_i is the number of unknowns at the i^{th} node. Rewriting Equation (4.8) in the EBE format gives [31]:

$$\bigcup_{e=1}^{NE} A_{\alpha\beta}^{(e)} X_{\beta}^{(e)} \hat{\Delta}_{\alpha i}^{(e)} = \bigcup_{e=1}^{NE} F_{\alpha}^{(e)} \hat{\Delta}_{\alpha i}^{(e)} \tag{4.9}$$

where $\hat{\Delta}_{\alpha i}^{(e)}$ is a Boolean matrix with nonzero values only if local unknown α in element $E^{(e)}$ corresponds to global unknown i. $\hat{\Delta}_{\alpha i}^{(e)}$ is identical to $\Delta_{ij}^{(e)}$ in one variable-per-node problems, and are directly related in general. The proposed parallel implementation can be written as an extension to Equation (4.9) as follows.

$$\bigcup_{p=1}^{NP}\left(\bigcup_{e=1}^{NE^{[p]}} A_{\alpha\beta}^{[p](e)} X_{\beta}^{[p](e)} \hat{\Delta}_{\alpha i}^{[p](e)}\right) \Delta_{ij}^{\prime[p]} = \bigcup_{p=1}^{NP}\left(\bigcup_{e=1}^{NE^{[p]}} F_{\alpha}^{[p](e)} \hat{\Delta}_{\alpha i}^{[p](e)}\right) \Delta_{ij}^{\prime[p]} \tag{4.10}$$

where the superscript $[p]$ is used to identify sub-domain data locally stored on the relevant processor, and $\Delta_{ij}^{\prime[p]}$ is a Boolean matrix with nonzero values only if local unknown i on processor $[p]$ corresponds to global unknown j. The information needed to extract $\Delta_{ij}^{\prime[p]}$ is contained in $\bar{\Delta}_{k}^{[i,j]}$.

Developing new serial/parallel solvers, Figure 4.5, comes down to the implementation of element equations using a FEM scheme of choice on a given set of equations. Virtually all computer programming needed in this process is serial in nature and compatible between serial and parallel solvers. Each processor in the parallel architecture, Figure 4.5(b), executes all the tasks assigned to serial processing, Figure 4.5(a). The main difference is that each processor in the parallel mode only carries out the calculations needed to generate the local EBE system corresponding to the sub-domain assigned to it. Whereas the serial solver carries out the calculations for the whole domain on one processor. All the necessary communication for the parallel architecture are encapsulated in the parallel EBE-GMRES solvers as discussed in Section 4.3. This approach allows the inclusion of more physics, new element types, and changing the FEM scheme with minimal impact on the parallel communications.

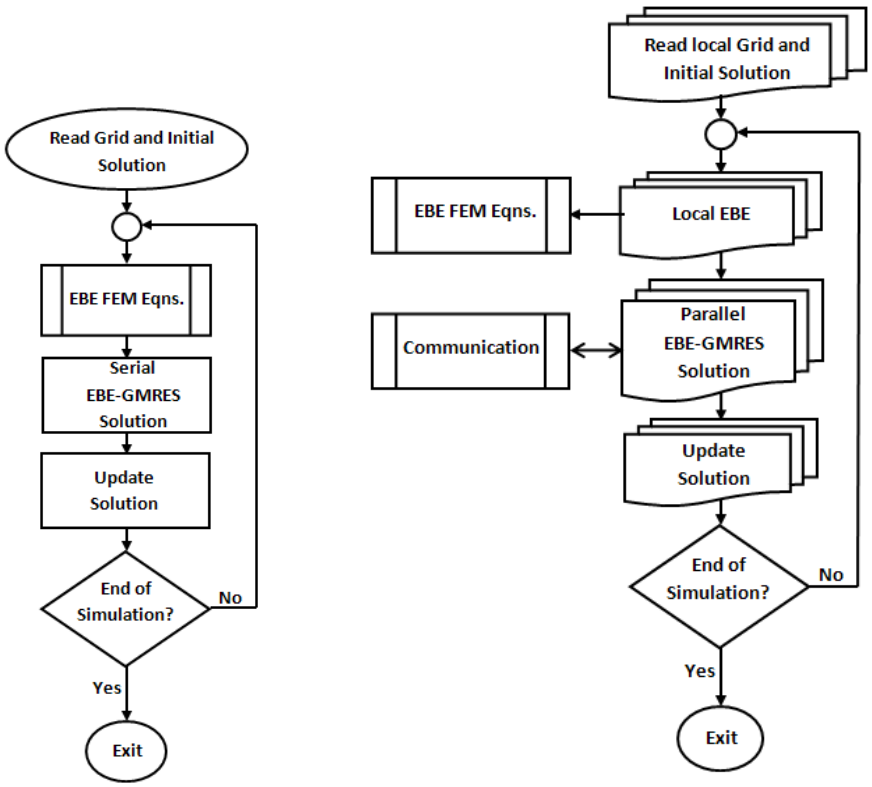

(a) serial solver. (b) parallel solver.

Figure 4.5 Generalized EBE-GMRES FEM framework layout. (a) serial solver in Equation (4.9) and (b) parallel solver in Equation (4.10).

It also allows for continuous improvement in the parallel communication technology, iterative matrix solver, and preconditioners with minimal effect on developed solvers.

During the EBE matrix population time the framework is nearly 100% parallel. The overall parallel efficiency is affected by the communication strategy during the linear system solution, which can be continuously improved. The computational time for obtaining the EBE matrices is usually larger than the time required to solve for the linear system. Therefore, the communication affects only a small portion of the computational time, whereas the larger part of the time is at nearly optimal paral-

lelization. Increasing the complexity of the physics to include more models, increases the number of variables at each node, which increases the size of the linear system. One could argue that, for well-posed problems, the computational load introduced with more equations in the EBE matrices population time is more significant than the increase in the problem size, which in turn could enhance the parallel efficiency of the solver.

4.3 EBE-GMRES

Algorithm 4.1 summarize a typical serial GMRES algorithm [31], and Algorithm 4.2 introduces the proposed parallel implementation. The details of the Q-R rotations used to skip the Hessenberg matrix inversion are omitted for brevity [31,32]. For the serial version, vectors D_i, X_i, and $\bar{E}_i$ could easily be switched back and forth between EBE and the assembled forms, whereas $A^{(e)}_{\alpha\beta}$ is never assembled according to the EBE approach. The parallel implementation utilizes EBE approach to keep data localized on each processor according to the distributed memory model. Neither the system matrix nor any vector is assembled across the processors. The contribution of the local elements, on each processor, to the communication nodes' variables on the boundaries, defined by Equation (4.7), is shared between relevant neighboring processors. Parallel exchange, of relevant nodal data only, occurs after each assembly of any vector from EBE to *"assembled"* format using information contained in $\Delta'^{[p]}_{ij}$ and according to the communication strategy. Communication is also necessary in any dot product process, where local results are summed across the processors taking into

account the repeated entries, again extracted from $\Delta_{ij}^{\prime[p]}$ along with their respective number of repetitions.

Algorithm 4.1 Serial EBE-GMRES iterative matrix solver with diagonal preconditioner.

Require: $A_{\alpha\beta}^{(e)}, F_i, X_i^0$

$D_i = \bigcup_{e=1}^{NE} A_{\alpha\alpha}^{(e)} \hat{\Delta}_{\alpha i}^{(e)}$

$F_i = \dfrac{F_i}{\sqrt{D_i}}$

$X_i = X_i^0 \sqrt{D_i}$

$A_{\alpha,\beta}^{(e)} = \dfrac{A_{\alpha,\beta}^{(e)}}{\sqrt{D_\alpha^{(e)} D_\beta^{(e)}}}$

repeat

$E_i^0 = F_i - \bigcup_{e=1}^{NE} A_{\alpha\beta}^{(e)} X_\beta^{(e)} \hat{\Delta}_{\alpha i}^{(e)}$

$\bar{E}_i^1 = \dfrac{E_i^0}{\|\mathbf{E}^0\|}$

for [**do**NK is the size of the Krylov space.]$k = 1$ to NK

$W_i = \bigcup_{e=1}^{NE} A_{\alpha\beta}^{(e)} \bar{E}_\beta^{(e),k} \hat{\Delta}_{\alpha i}^{(e)}$

for $m = 1$ to k **do**

$H(m,k) = W_i \bar{E}_i^m$

$W_i = W_i - H(m,k) \bar{E}_i^m$

end for

$H(k+1,k) = \|\mathbf{W}\|$

$\bar{E}_i^{k+1} = \dfrac{W_i}{H(k+1,k)}$

end for

$e_m = [\|\mathbf{E}^0\|, 0, 0, \cdots, 0]^{\mathrm{T}}$

$Y_k = H^{-1}(m,k) e_m$

$X_i = X_i + \bar{E}_i^k Y_k$

until $Y_{NK} \leq T$ ▷ T is the conversion tolerance

return $X_i = \dfrac{X_i}{\sqrt{D_i}}$

Algorithm 4.2 Parallel EBE-GMRES iterative matrix solver with diagonal preconditioner.

Require: $A_{\alpha\beta}^{[p](e)}, F_i^{[p]}, X_i^{[p],0}$

$D_i^{[p]} = \bigcup_{e=1}^{NE^{[p]}} A_{\alpha\alpha}^{[p](e)} \hat{\Delta}_{\alpha i}^{[p](e)}$

Parallel Communicate $D_i^{[p]}$

$F_i^{[p]} = \dfrac{F_i^{[p]}}{\sqrt{D_i^{[p]}}}$

$X_i^{[p]} = X_i^{[p],0} \sqrt{D_i^{[p]}}$

$A_{\alpha,\beta}^{[p](e)} = \dfrac{A_{\alpha,\beta}^{[p](e)}}{\sqrt{D_\alpha^{[p](e)} D_\beta^{[p](e)}}}$

repeat

$W^{[p]} = \bigcup_{e=1}^{NE^{[p]}} A_{\alpha\beta}^{[p](e)} X_\beta^{[p](e)} \hat{\Delta}_{\alpha i}^{[p](e)}$

Parallel Communicate $W^{[p]}$

$E_i^{[p],0} = F_i^{[p]} - W^{[p]}$

$\bar{E}_i^{[p],1} = \dfrac{E_i^{[p],0}}{\|\mathbf{E}^0\|}$

for $k = 1$ to NK **do**

$W_i^{[p]} = \bigcup_{e=1}^{NE^{[p]}} A_{\alpha\beta}^{[p](e)} \bar{E}_\beta^{[p](e),k} \hat{\Delta}_{\alpha i}^{[p](e)}$

Parallel Communicate $W_i^{[p]}$

for $m = 1$ to k **do**

$H^{[p]}(m,k) = W_i^{[p]} \bar{E}_i^{[p],m}$

Parallel Communicate $H^{[p]}(m,k)$

$W_i^{[p]} = W_i^{[p]} - H(m,k) \bar{E}_i^{[p],m}$

end for

$H(k+1,k) = \|\mathbf{W}\|$

$\bar{E}_i^{[p],k+1} = \dfrac{W_i^{[p]}}{H(k+1,k)}$

end for

Algorithm 4.2 (continued).

$e_m = [\|\mathbf{E}^0\|, 0, 0, \cdots, 0]^{\mathrm{T}}$
$Y_k = H^{-1}(m,k)e_m$
$X_i^{[p]} = X_i^{[p]} + \bar{E}_i^{[p],k} Y_k$
until $Y_{NK} \leq T$
return $X_i^{[p]} = \dfrac{X_i^{[p]}}{\sqrt{D_i^{[p]}}}$

4.3.1 Communication Strategies

Considering the results of Section 4.1.3, there are two possible strategies for the storage and handling of the communication data contained in $\Delta_{ij}^{\prime[p]}$, namely: Processor-to-Processor Communication List (PPCL), and Communication Nodes Global Numbering (CNGN). PPCL depends on scanning $\Delta_{ij}^{\prime[p]}$ to find the neighboring processors of every processor and identifying the communication nodes shared with each neighbor. During the parallel solution, all communications can be achieved via non-blocking MPI send/receive operations between neighbors.

For example, Table 4.4 shows the details of the communication map for the 2D grid decomposition given on Figure 4.4 using PPCL. The neighboring processors for each processor need to be ordered to complete the communication data necessary for the run time MPI calls, Table 4.5.

Table 4.4 PPCL summary of nodes IDs shared between processors for the grid given on Figure 4.4.

	Processor 1	Processor 2	Processor 3
Processor 1	—	$2, 5, 13$	$4, 5, 15$
Processor 2		—	$5, 6, 16$
Processor 3	sym.		—

Table 4.5 PPCL neighboring processors IDs for the grid decomposition of Figure 4.4.

	Neighbor 1	Neighbor 2
Processor 1	2	3
Processor 2	1	3
Processor 3	1	2

Table 4.6 Sample CNGN communication map summary for the grid decomposition of Figure 4.4.

	Local ID	Communication ID
Processor 1	$2, 3, 4, 7, 8$	$1, 2, 3, 5, 6$
Processor 2	$1, 3, 4, 6, 8$	$1, 3, 4, 5, 7$
Processor 3	$1, 3, 5, 2, 4$	$2, 3, 4, 6, 7$
Total		7

CNGN, on the other hand, places all the communication nodes in an ordered set and saves their respective local IDs on each processor. MPI all-reduce statements could be used in the run time to carry out the necessary communications.

For example, Table 4.6 shows the residing communication nodes on each processor and their local indexing for the same grid decomposition given on Figure 4.4. For this simple case, the two strategies could be compared easily. Examining Tables 4.4 and 4.6 shows that in both cases the number of shared nodes is the same as expected from Table 4.3. The main differences between the two strategies, during one communication instance are:

- PPCL will carry out six non-blocking send/receive MPI communications each with the size of 3 nodes' data (3 × NEQ × NByt), where $NByt$ is the number of bytes in the used arithmetic precision.

- CNGN will carry out a one all-reduce MPI statement with the traffic of 7 nodes' data among all processors.

Although for this simple case the communication traffic does not seem to be drastically different, CNGN has an inherent inferiority due to the traffic of the all-reduce communication statement. The results in Section 4.4.1 prove this fact. The ease of implementation stands to be the only advantage of CNGN over PPCL.

4.4 Parallel Performace

Table 4.7 Details of scaling analysis cases.

ID	NE	p	Comm.	METIS	$NN \times 10^6$	$n \times 10^6$	$\frac{NP_{Max}}{NP_{min}}$	$S_{total}\mid_{NP_{max}}$
7	99^3	1	PPCL	Yes	1	5	88/8	7.1
8	63^3	1	PPCL	Yes	0.26	1.31	88/2	31.8
9	63^3	1	CNGN	Yes	0.26	1.31	88/2	3.13
10	63^3	1	PPCL	No	0.26	1.31	88/2	8.7
11	31^3	1	PPCL	Yes	0.032	0.16	88/1	76
12	31^3	2	PPCL	Yes	0.12	0.64	88/2	31.7
13	31^3	3	PPCL	Yes	0.22	1.11	88/4	17.24

All scaling cases in Table 4.7 are tested using the CFD Lab cluster at the University of Alabama in Huntsville. This cluster has 45 nodes, each has a Dual-Core AMD Opteron™ $2GHz$ processors with $1MB$ cache memory per processor, sharing $2GB$ RAM memory, and running $x86-64$ Red Hat Enterprise Linux system.

The maximum number of processors used is $NP_{max} = 88$. A minimum number of processors, NP_{min}, for each case is selected such that the whole problem resides on the RAM memory only without using the swap system to avoid the associated significant time increase. All cases are tested with fully active nodes (i.e. two processors per node) except for the NP_{min} cases where only one processor is active on each node. The METIS package is used for grid decomposition in all cases except for Case 10. The scaling studies below are based on the average of the first 5 time steps from the initial solution of the lid-driven cavity problem discussed in Section 5.2.1.1. EBE matrix population time, t_{EBE}, and EBE-GMRES solver time, t_s, are normalized as follows:

$$t_{EBE} = \frac{1}{5 \times n} \sum_{i=1}^{5} t_{EBE}|_i$$

$$t_s = \frac{\sum_{i=1}^{5} t_s|_i}{n \times \sum_{i=1}^{5} r_i}$$

where $t_{EBE}|_i$, $t_s|_i$, and r_i are the wall-time for the EBE process, the wall time of the EBE-GMRES solver, and the number of GMRES iterations at the i^{th} time step, respectively. The total wall time is given by $t_{total} = t_{EBE} + t_s \times \sum_{i=1}^{5} r_i$, and the total CPU cost is $t_{total} \times NP$. The total speedup, S_{total}, is defined by

$$S_{total} = \frac{t_{total}|_{NP_{min}}}{t_{total}}$$

and the total parallel efficiency, η_{total}, is given by

$$\eta_{total} = \frac{S_{total}}{NP/NP_{min}} \times 100,$$

whereas the GMRES matrix solver speedup, S_{solver}, is defined by

$$S_{solver} = \frac{t_s|_{NP_{min}}}{t_s}$$

and the solver parallel efficiency, η_s, is given by

$$\eta_s = \frac{S_{solver}}{NP/NP_{min}} \times 100.$$

4.4.1 Effect of Communication Strategies

The performance of both communication strategies proposed in Section 4.3.1 is studied with Cases 8 and 9 and is shown on Figure 4.6. Since there is virtually no communication in the EBE part of the solver, t_{EBE} is the same for both cases. In the range $NP \geq 4$ the two communication strategies show similar trends, whereas the performance is totally different at $NP \geq 16$. It is clear that PPCL data communication is much more effective than CNGN. This is expected since MPI all-reduce calls in CNGN carry higher communication overheads than non-blocking send/receive operations used in PPCL. For $NP \geq 16$ any decrease in the total wall time from t_{EBE} is lost by the MPI traffic introduced by the CNGN strategy and t_{total} saturates. On the other hand PPCL is showing t_{total} to follow the same trend as t_{EBE} in the tested range, indicating better scalability.

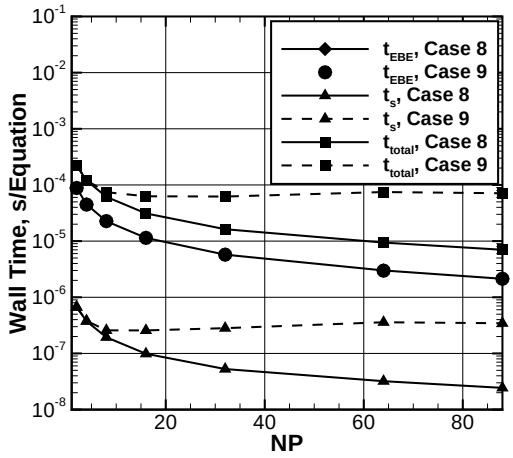

Figure 4.6 Comparison between different communication strategies.

4.4.2 Effect of Grid Partitioning Using Metis

Figure 4.7 shows typical partitioned 3D domain using the METIS package. The difference in the parallel performance of the optimized grid becomes clear for $NP \geq 32$ as shown on Figure 4.8(a). The wall time needed for every GMRES iteration in the non-optimized case, Case 10, virtually saturates in the range $32 \leq NP \leq 64$ and starts to increase beyond that. The optimized grid, Case 8, is not in *perfect* load balance as the non-optimized grid, Case 10, as shown on Figure 4.8(b). Nonetheless t_{EBE} is very close for the two cases indicating the load distribution of the optimized grids to be near the optimal load balancing performance. The observed GMRES solution time, t_s, proves that METIS is effective in reaching its optimization goals of minimizing the communication volume as well.

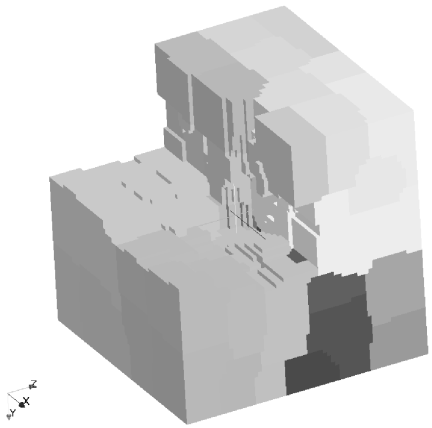

Figure 4.7 Surface contours colored by processor IDs for Case 8 at 88 sub-domains. Some sub-domains are removed to show the unstructured communication interface.

4.4.3 Effect of Higher Order Accuracy

Figure 4.9(a) shows the different cost associated with linear/quadratic/cubic grids using Cases 11/12/13, respectively. It is clear that a part of the cost difference is due to t_{EBE}, since higher order shape functions require more intensive integrations. However, the higher the order of the grid the higher the number of the communication nodes on the boundaries, hence increases the CPU cost. Nonetheless the cost of the higher order elements remains fairly constant up to the maximum number of processors tested. The super-linear trend noticed in Figure 4.9(b) for Case 11 is believed to be due to size of the problem which fits on the cache memory on two processors and up. The traffic cost increase for a higher number of processors, however, counters this effect. The higher order grids show an acceptable sub-linear performance.

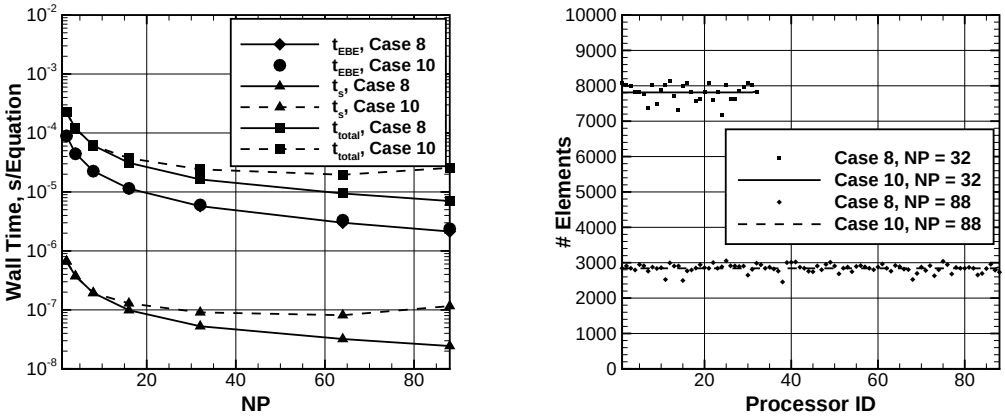

(a) (b)

Figure 4.8 Comparison between Cases 8 and 10 showing the effect of unstructured grid partitioning. (a) wall time comparison for different solver parts and (b) load distribution across all processors for the cases of 32 and 88 sub-domains.

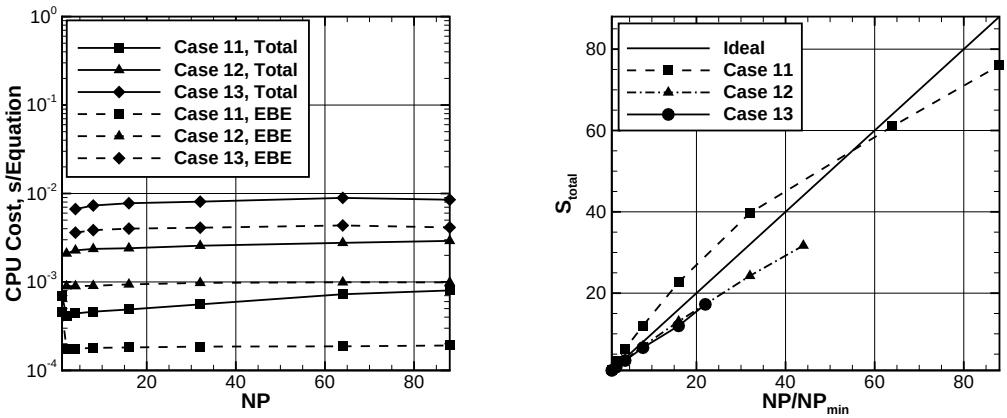

(a) (b)

Figure 4.9 Comparison between Cases 11, 12, and 13 showing the effect of higher order calculations. (a) wall time comparison for different solver parts and (b) speedup.

4.4.4 Effect of Problem Size

Figure 4.10(a) shows the EBE matrix population cost to be constant for any grid size and any number of processors. This trend proves that the EBE part of the solver is virtually 100% parallel. The total cost, however, increases with the number of processors used. This is due to the added cost in the MPI traffic for a higher number of processors associated with the increased sub-domains boundaries. Although PPCL communication is directed toward the neighboring processors only, the MPI overhead between high number of processors affects the total CPU cost in general. Also Figure 4.10(a) shows Case 7 to be more expensive than Case 8. This is to be expected since larger grids introduce higher number of nodes along the boundaries of the sub-domains which in turn increases the MPI traffic.

Figures 4.10(b) and 4.10(c) show the speedup and the parallel efficiency, respectively, of the EBE-GMRES matrix solver compared to the selected literature in Table 4.8. The cases of [45], [49], and [50] are closer to the number of equations of Case 8, whereas the case of [48] is closer to Case 7. It is clear that the proposed framework is efficient when compared to these available in the literature.

Table 4.8 Details of the research work used to evaluate the proposed framework.

Authors	$n \times 10^6$	$\frac{NP}{NP_{min}}$	S_{solver}	$\eta\%$
Rivera [45]	1.303	16/1	5.5	34
Behara [48]	4.85	64/6	6	57
Shen [49]	1	32/1	11.26	35
Staff [50]	1	12/1	8.6	71

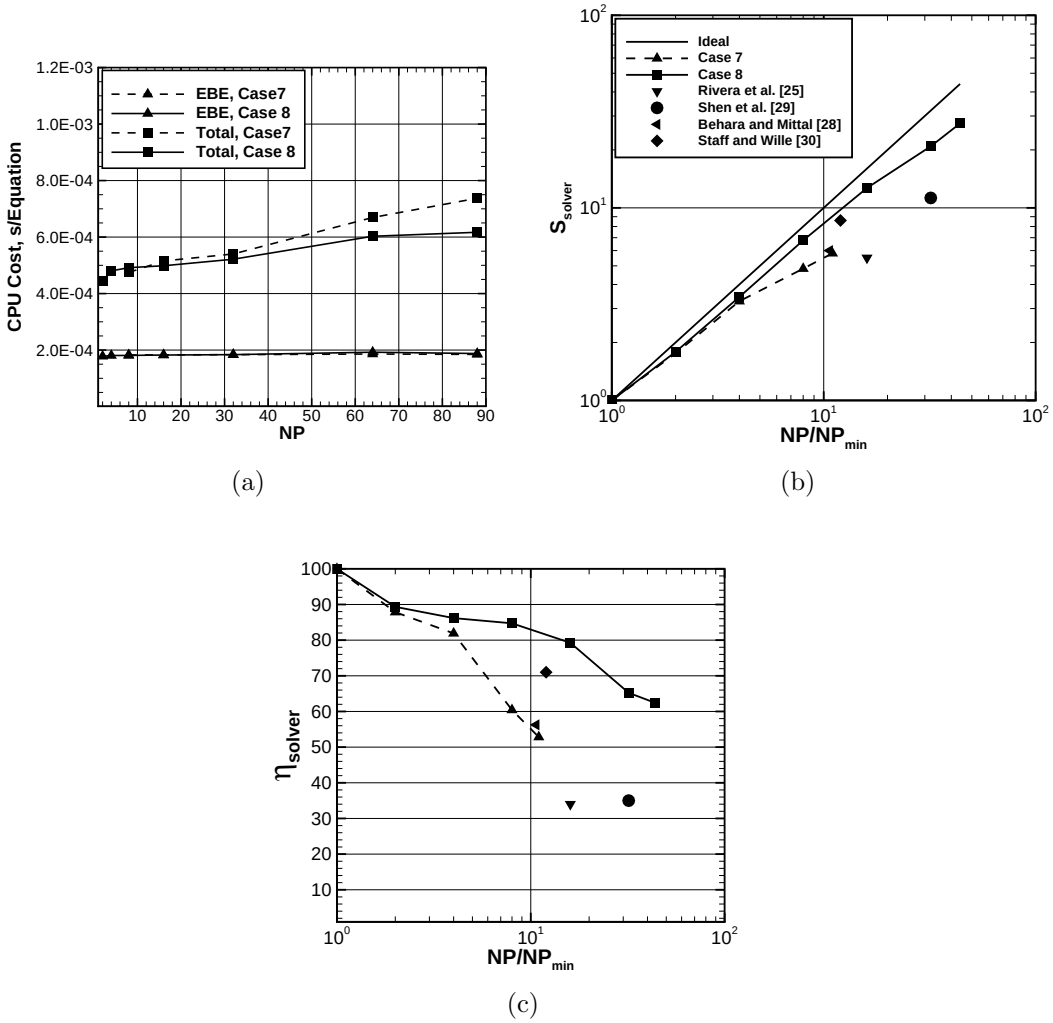

Figure 4.10 Comparison between Cases 7 and 8 showing the effect of grid size increase. (a) CPU cost in second per equation , (b) speedup and (c) parallel efficiency comparison with published literature.

CHAPTER 5

NUMERICAL VERIFICATIONS

In this chapter the developed FDV code is verified for different physics. The higher order accuracy is established via the MMS in Section 5.1. The fluid dynamics physics, including inviscid/viscous, compressible/incompressible, and subsonic/supersonic flows are verified through an extensive list of test cases in Section 5.2. The newly introduced extension of the FDV method to plasma physics is verified in Section 5.3.

5.1 Order of Accuracy Analysis

The MMS is used to investigate the order of accuracy of the developed framework. In this method, analytical functions of our choice are assumed for the primitive flow variables. Since these functions do not necessarily satisfy the governing equations, residual terms arise by substituting back these functions into the governing equations. Source terms are introduced to the original governing equations in order to analytically balance these residuals. The order of accuracy of the developed framework can be estimated from the analysis of the errors between its numerical solution and the imposed analytical solution. The manufactured solutions are usually smooth

and continuous sinusoidal functions in order to facilitate the error evaluation process. The analysis presented here is based on the test cases introduced by Roy et. al. [53].

In the interest of quantifying the numerical errors, the L_2 norm is defined by

$$L_2 = \sqrt{\frac{\sum_{i=1}^{NN} \left(\phi_i - \overset{*}{\phi}_i\right)^2}{NN}}, \tag{5.1}$$

whereas the L_∞ norm is given by

$$L_\infty = \max_{i=1}^{NN} |\phi_i - \overset{*}{\phi}_i|, \tag{5.2}$$

where ϕ is the computed solution of any of the variables, $\overset{*}{\phi}$ is the exact value of its corresponding manufactured solution, and NN is the number of nodes in the grid. The order of accuracy, np, is given at each grid level k by

$$np^k = \frac{ln\left(L_\alpha^{k+1}/L_\alpha^k\right)}{ln\left(r\right)}, \tag{5.3}$$

where r is the grid refinement factor, k is the fine grid level, $k+1$ is the coarse grid level, and L_α^k is a norm of our choice. Doubling the number of elements between levels $k+1$ and k makes $r = 2$.

The manufactured solutions are assumed of the form

$$\phi = a_0 + a_1 f_1\left(b_1 \pi x_1\right) + a_2 f_2\left(b_2 \pi x_2\right) + a_3 f_3\left(b_3 \pi x_1 x_2\right), \tag{5.4}$$

where a_i, b_i, and f_i are given in Table 5.1 for each primitive variable and for a 2D supersonic case. The numerical domain is set between $0 \leq x_1 \leq 1$ and $0 \leq x_2 \leq 1$, and uniform grids in both directions are used. The specific heat ratio and the universal gas constant are set to $\gamma = 1.4$ and $R = 287 J/KgK$, respectively. Figure 5.1 shows the contour plots of the manufactured solution for all the primitive variables. The corresponding source terms, shown on Figure 5.2, for the Euler system of equations are derived symbolically and converted to FORTRAN code using the MATLAB script given in Listing 5.1.

Table 5.2 summarizes the test cases used to investigate the order of accuracy of the developed FDV code for the 2D Euler equations. These test cases are selected to study the effect of refining the grid, by increasing the number of elements, NE, on different shape function polynomial orders, p. The supersonic inflow conditions are applied on boundaries $x_1 = 0$ and $x_2 = 0$, whereas the supersonic outflow conditions are used for boundaries $x_1 = 1$ and $x_2 = 1$. A steady state solution is obtained.

The L_2 and L_∞ norms and their corresponding orders of accuracy for all conservation variables are shown on Figures 5.3 to 5.6. The developed FDV code shows consistent behavior and a systematic increase in the order of accuracy for both norms, by increasing the polynomial orders. The observed relation between the order of accuracy, np, and the shape function polynomial order, p, is such that [52]

$$np \approx p + 1.$$

Table 5.1 Values of the pre-defined terms in the imposed manufactured solutions.

Variable	a_0	a_1	a_2	a_3	b_1	b_2	b_3	f_1	f_2	f_3
ρ	1	0.15	-0.1	0	1	0.5	0	sin	cos	cos
u_1	800	50	-30	0	1.5	0.6	0	sin	cos	cos
u_2	800	-75	40	0	0.5	2/3	0	cos	sin	cos
p	10^5	2×10^4	5×10^4	0	2	1	0	cos	sin	sin

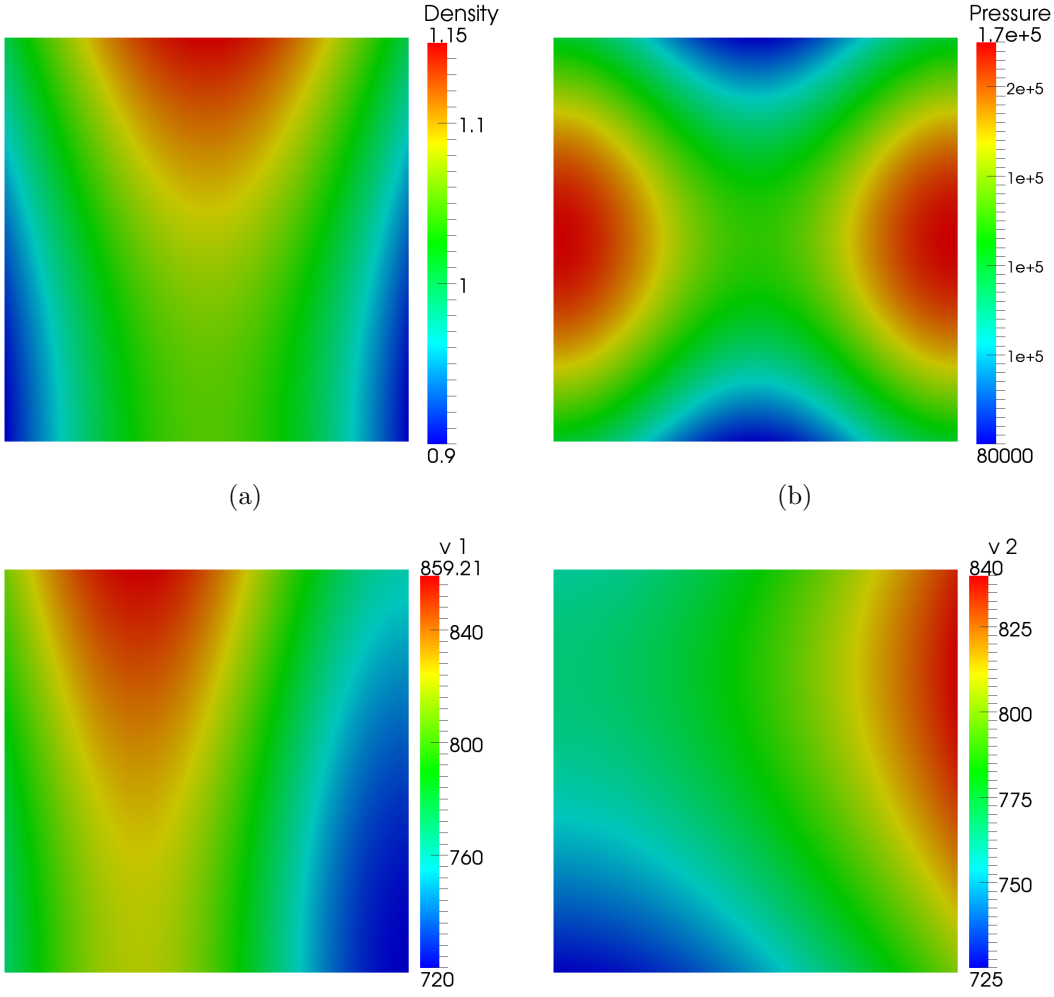

Figure 5.1 The assumed manufactured solutions employed to investigate the order of accuracy of the developed FDV code.

Listing 5.1 MATLAB script used to generate FORTRAN code for the MMS source terms.

```
clear all
clc

syms x y Rg g pii
syms r0 rx ry rxy arx ary arxy
syms u0 ux uy uxy aux auy auxy
syms v0 vx vy vxy avx avy avxy
syms p0 px py pxy apx apy apxy

r = r0+rx*sin(arx*pii*x)+ry*cos(ary*pii*y)+rxy*cos(arxy*pii*x*y);
u = u0+ux*sin(aux*pii*x)+uy*cos(auy*pii*y)+uxy*cos(auxy*pii*x*y);
v = v0+vx*cos(avx*pii*x)+vy*sin(avy*pii*y)+vxy*cos(avxy*pii*x*y);
p = p0+px*cos(apx*pii*x)+py*sin(apy*pii*y)+pxy*sin(apxy*pii*x*y);

t = p/(Rg*r);
e = 1.0/(g-1.0)*Rg*t;
et = e+(u*u+v*v)/2.0;

fm = diff(r*u,x)+diff(r*v,y);
fx = diff(r*u*u+p,x)+diff(r*v*u,y);
fy = diff(r*v*v+p,y)+diff(r*v*u,x);
fe = diff(r*u*et+p*u,x)+diff(r*v*et+p*v,y);

fmm = fortran(fm)
fxx = fortran(fx)
fyy = fortran(fy)
fee = fortran(fe)
```

Table 5.2 Method of manufactured solution cases.

Grid Level	$\frac{h}{h_{min}}$	NE	p
1	1	64^2	$1, 2, 3$
2	2	32^2	$1, 2, 3, 4, 5$
3	4	16^2	$1, 2, 3, 4, 5$
4	8	8^3	$1, 2, 3, 4, 5$

The estimated orders of accuracy makes the L_2 norm based order of accuracy to be more stable for coarse grids, *i.e.* higher h/h_{min} values, than the ones calculated from the L_∞ norm. This is believed to be due to the averaging nature of the L_2 norm. For fine grids, both norms behave as expected.

In the current FDV code, the higher order accuracy mode is available on straight sided numerical domains; *i.e.* no curved surfaces are allowed for higher order accuracy test cases.

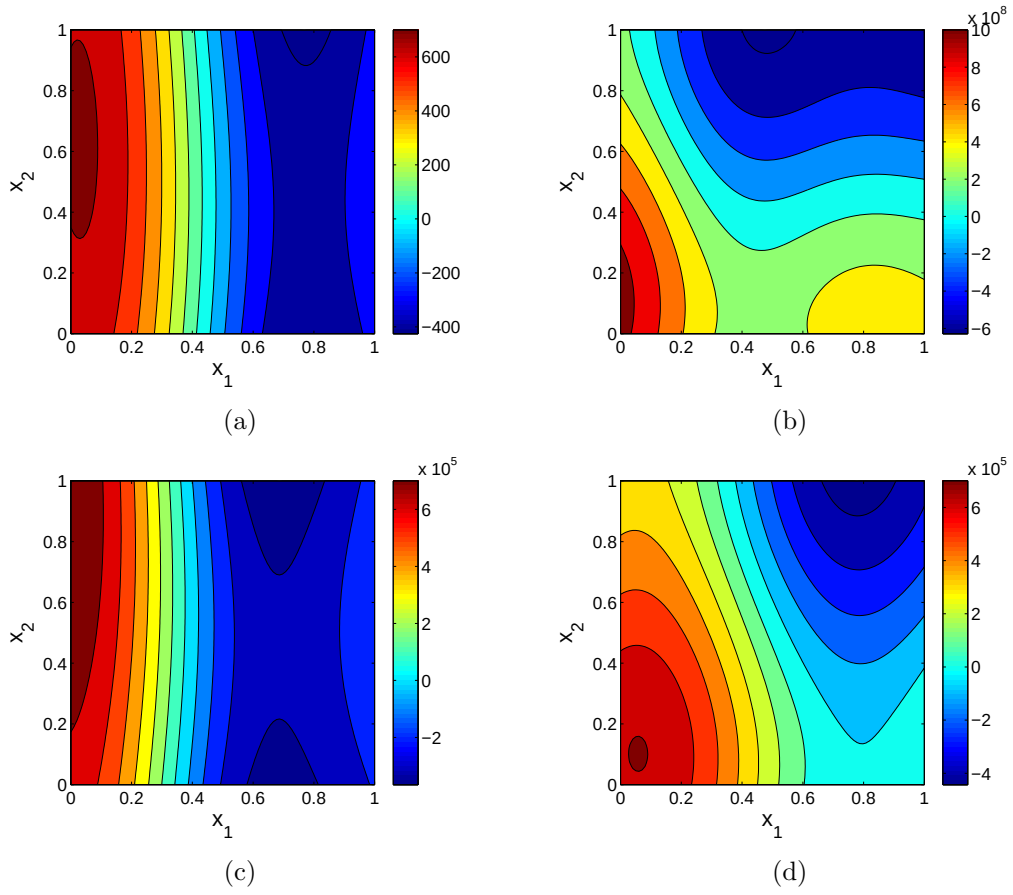

Figure 5.2 The resulting source terms from the imposed manufactured solutions. (a) mass equation source term, (b) energy equation source term, (c) axial momentum, x_1, equation source term, and (d) lateral momentum, x_2, equation source term.

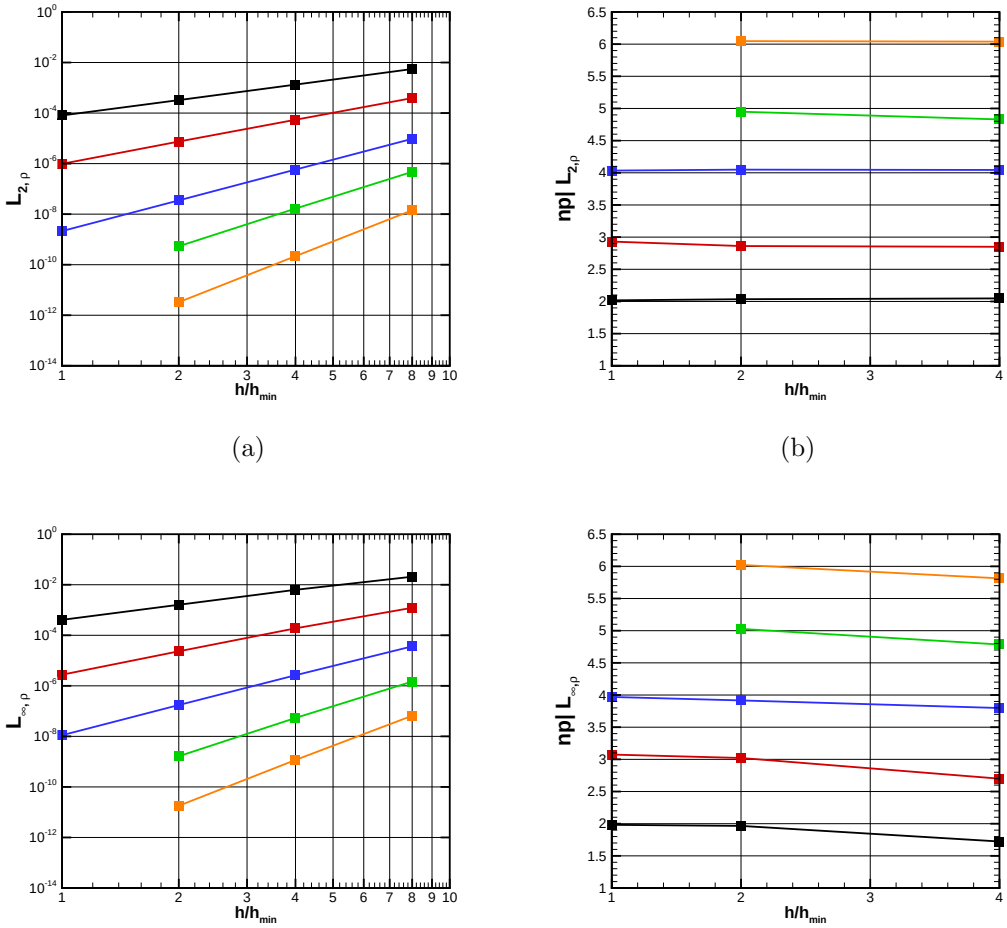

(a) (b)

(c) (d)

Figure 5.3 L_2 and L_∞ norms and their corresponding order of accuracies for the conservation variable ρ. — $p = 1$, — $p = 2$, — $p = 3$, — $p = 4$, — $p = 5$.

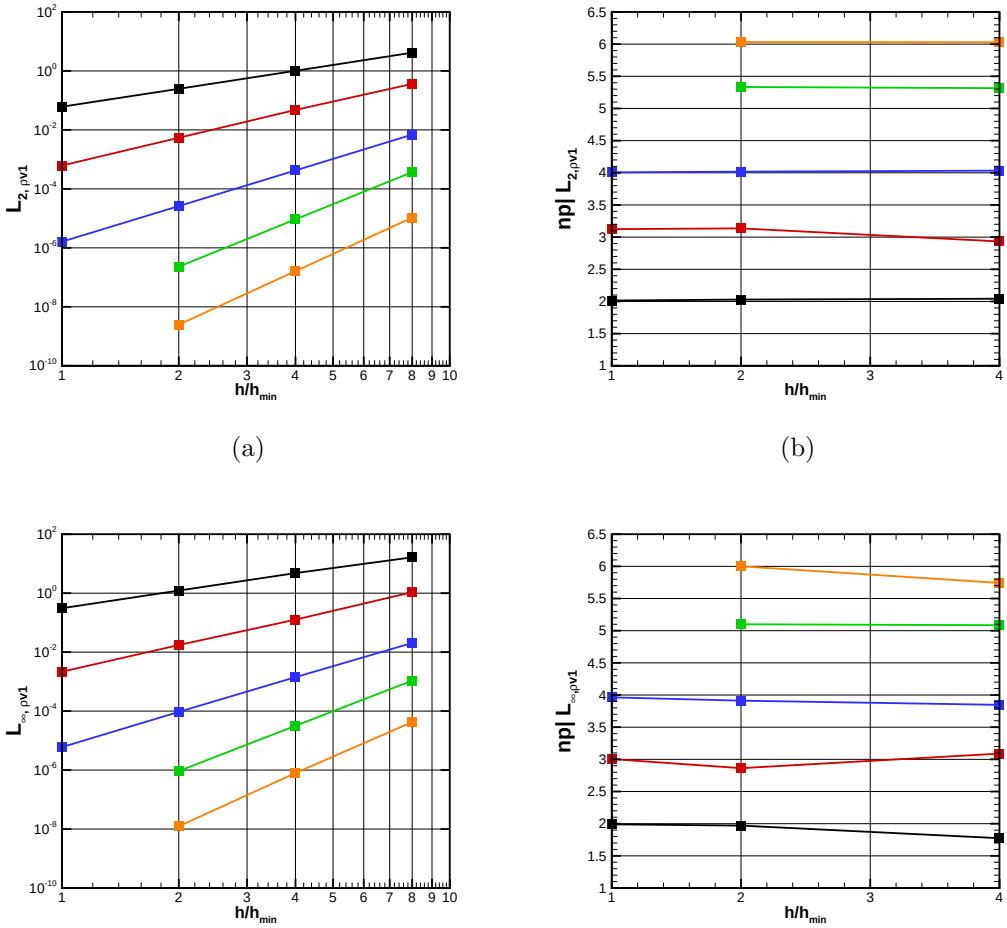

(a) (b)

(c) (d)

Figure 5.4 L_2 and L_∞ norms and their corresponding order of accuracies for the conservation variable ρv_1. — $p = 1$, — $p = 2$, — $p = 3$, — $p = 4$, — $p = 5$.

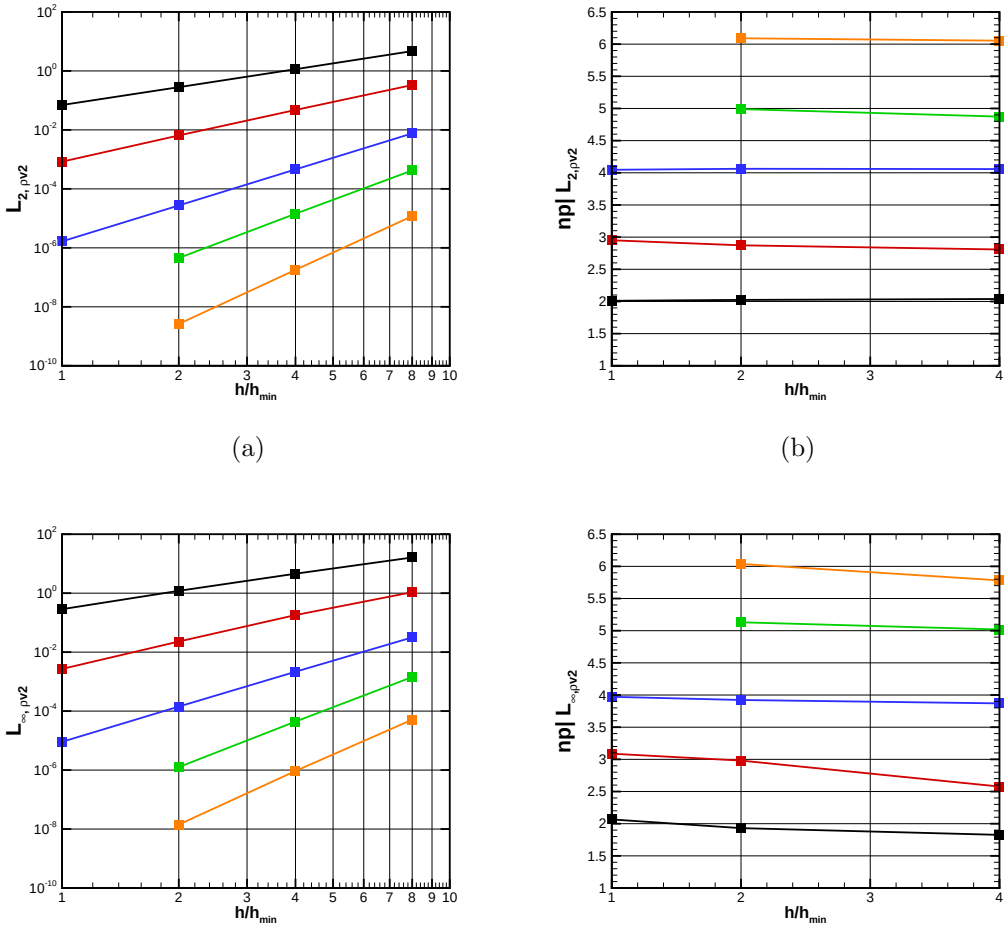

Figure 5.5 L_2 and L_∞ norms and their corresponding order of accuracies for the conservation variable ρv_2. — $p = 1$, — $p = 2$, — $p = 3$, — $p = 4$, — $p = 5$.

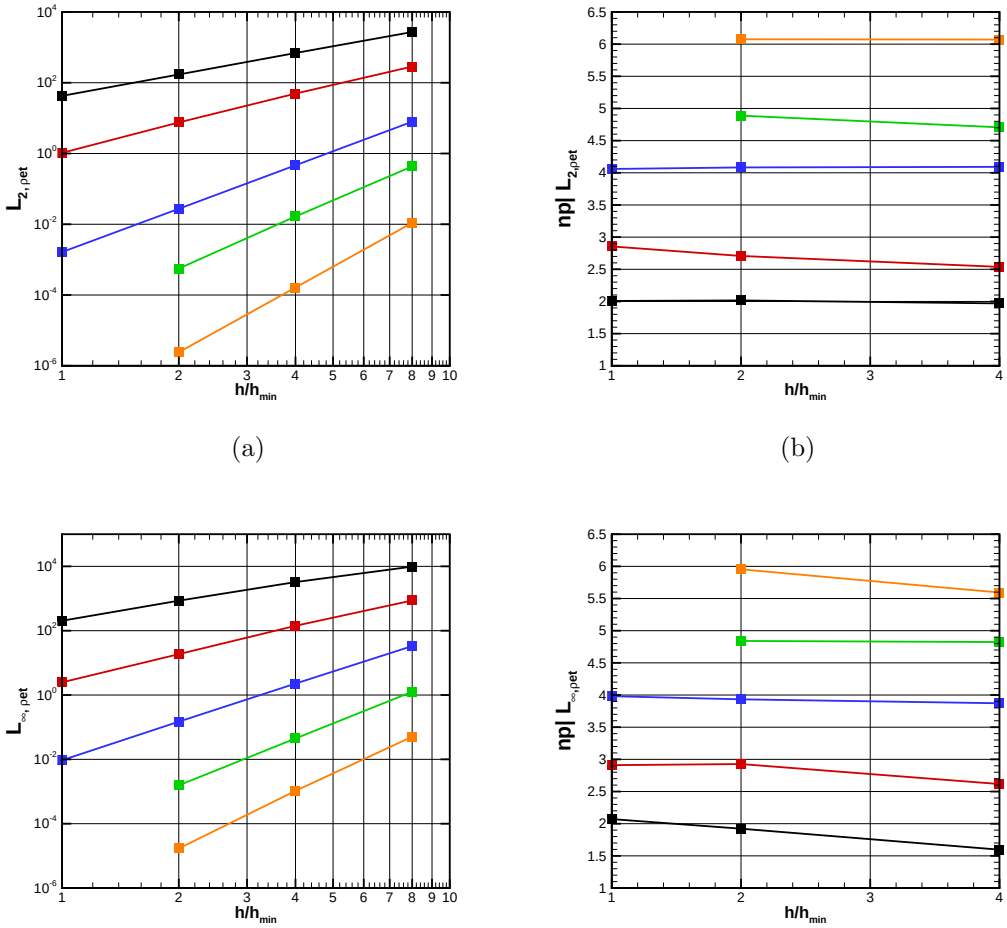

(a) (b)

(c) (d)

Figure 5.6 L_2 and L_∞ norms and their corresponding order of accuracies for the conservation variable ρe_t. — $p = 1$, — $p = 2$, — $p = 3$, — $p = 4$, — $p = 5$.

5.2 Fluid Dynamics Cases

The verification test cases of the fluid dynamics physics are split into two main categories: nearly incompressible flows introduced in Section 5.2.1, and compressible flows given in Section 5.2.2. Each section summarizes the information necessary to reproduce its relevant cases. The details of the grid as well as the free stream conditions and the boundary conditions are provided. Comparisons with available literature are used extensively to verify the developed FDV solver.

5.2.1 Incompressible Flow Problems

Two incompressible flow cases are reported herein. The classical 2D and 3D lid-driven cavity problems are discussed in Section 5.2.1.1, whereas the backward-facing step flow at low Reynolds numbers is introduced in Section 5.2.1.2. The lid-driven cavity test case was also used in Chapter 4 to study the parallel performance of the developed finite element framework.

5.2.1.1 Lid-Driven Cavity

Using the FDV scheme and the complete Navier-Stokes equations, several lid-driven cavity flow cases are solved at the incompressible limit [54]. Figure 5.7 shows a schematic of the cavity flow and Table 5.3 summarizes the analyzed cases at $M = 0.05$ to approach the incompressible flow regime. All walls are no-slip adiabatic walls and the numerical grid is uniformly discretized. Higher order grids are obtained from a utility program developed based on Section 4.1.2. The solution domain is initialized

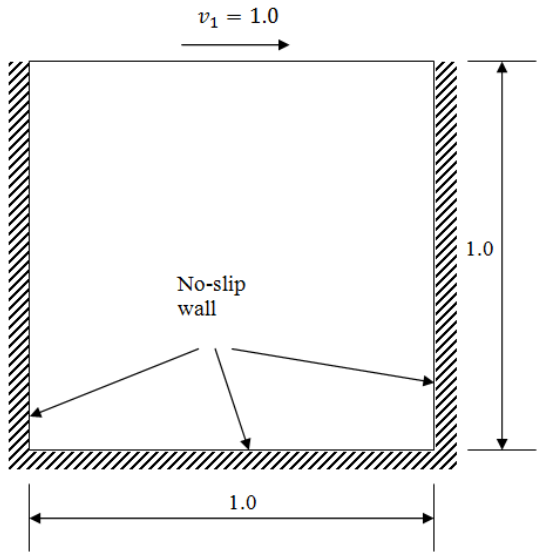

Figure 5.7 A Schematic of the lid-driven cavity domain.

Table 5.3 Studied lid-driven cavity cases.

ID	Dim.	NE	Grid Order	NN	n	Re
1	2D	127^2	1	16,384	65,536	1,000
2	2D	127^2	2	48,896	195,584	1,000
3	2D	127^2	3	81,408	325,632	1,000
4	2D	255^2	1	65,536	262,144	1,000
5	2D	255^2	2	196,096	784,384	1,000
6	2D	255^2	3	326,656	1,306,624	1,000
7	2D	255^2	1	65,536	262,144	5,000
8	2D	255^2	2	196,096	784,384	5,000
9	3D	15^3	2	15,616	78,080	1,000
10	3D	15^3	3	27,136	135,680	1,000
11	3D	31^3	2	128,000	640,000	1,000
12	3D	63^3	1	262,144	1,310,720	1,000
13	3D	127^3	1	2,097,152	10,485,760	1,000

with a stagnant flow field inside the cavity and the lid speed is set to 1.0 in the axial, x_1, direction. The Reynolds number used in this problem is based on the cavity side length. A solution is considered to be in steady state when the root-mean-square change $d \approx O\left(10^{-10}\right)$, where d is defined by

$$d = \sqrt{\frac{1}{n} \sum_{i=1}^{NN} \sum_{j=1}^{NEQ_i} \left(\Delta U_j^{n+1} \big|_i \right)^2}.$$

The steady state solutions of Cases 1 and 7 are shown on Figures 5.8 and 5.9, respectively. Case 1 shows one main vortex in the middle of the cavity due to the rotation of the flow and two secondary vortices residing at each of the lower corners. Whereas, the solution of Case 7 shows two more vortices at the lower right corner and the upper left corner. Another difference is the intensified main vortex strength in Case 7. The reason for both differences is the higher Re of Case 7. The added instability in the flow by increasing Re results in the new vortices. The lower viscosity effect of the higher Re also intensifies the main vortex by thinning the near wall boundary effect. The core of the main vortex also becomes smaller due to the same reason. Similar effects are clear on the secondary vortices leading to increasing their sizes in the higher Re case.

The FDV parameters mimic the structure of the flowfield almost exactly. The regions of higher s_1 and s_3 values are the near wall, the shear layers and the centers of the vortices. These phenomena are emphasized through the FDV parameters. Since this problem is nearly incompressible, the two FDV parameters associated with both convection and diffusion maintain almost the same distribution.

The 2D solution of the FDV method for Cases 1–8 match the results of Erturk et al. [55] and Ghia et al. [56] as shown on Figure 5.10. The higher order approximations give *better* results, although all cases are considered satisfactory in comparison with the published literature as shown on Figures 5.11, 5.12, and 5.13.

The 3D solution of Case 13 is shown on Figure 5.14. The results of Cases 9–13 are in good agreement with the computational results of Lo et al. [57] as shown on Figure 5.15. The cubic 15^3 elements grid of Case 9 shows some discrepancies, Figure 5.16, due to its significantly low number of elements. Nonetheless, the solution is reasonable given the savings in CPU time and memory as shown on Table 5.3. This is evident when compared to the solution of Case 12. That is the quadratic grid of the 15^3 elements Case 9 is comparable, for the most part, to that of the linear grid of the 63^3 elements Case 12. Whereas the cubic grid of the 15^3 elements Case 10 is comparable to the quadratic grid of the 31^3 elements Case 11 and the linear grid of the 127^3 elements Case 13. Hence, Cases 10 and 11 are achieving compression ratios in the order of 1/100 and 6/100 compared to Case 13 as can be calculated from Table 5.3. Where the compression ratio, b, is defined by

$$b = \frac{n_{higher\ order}}{n_{linear}}.$$

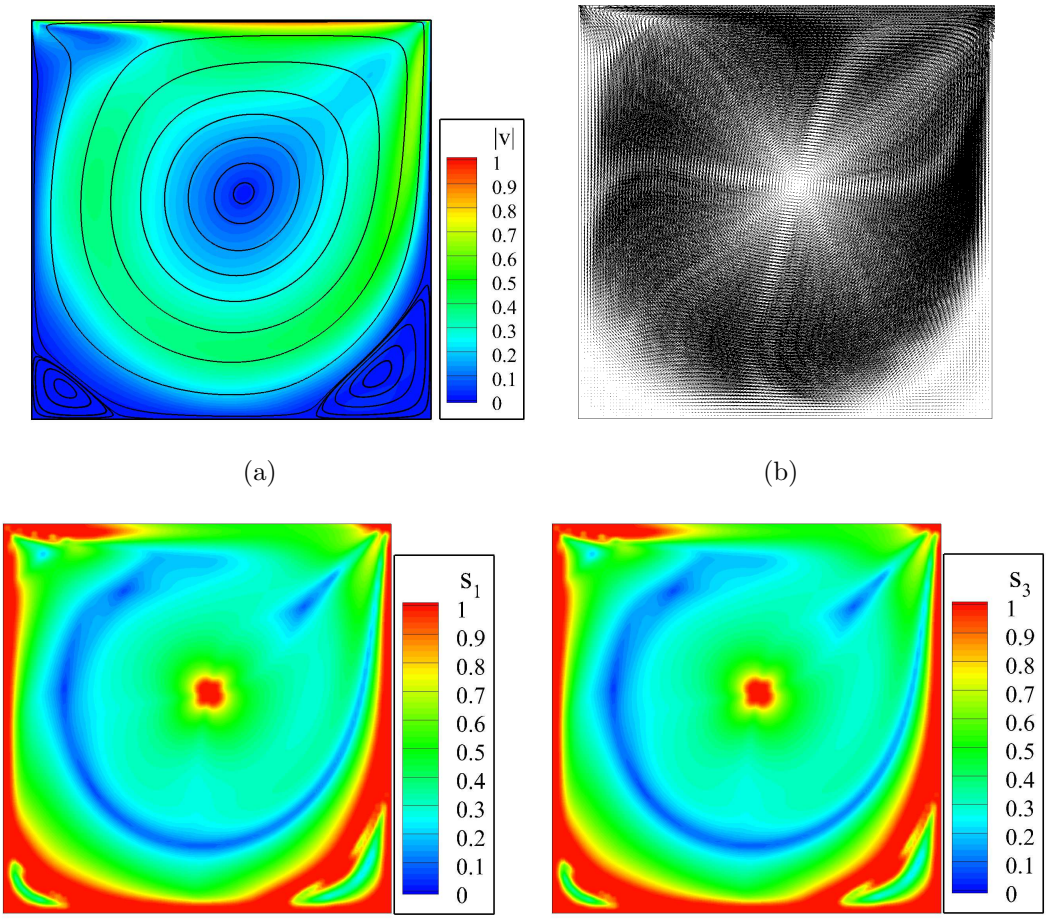

Figure 5.8 2D lid-driven cavity solution at $Re = 1{,}000$ using Case 1. (a) streamlines and contours of the normalized velocity magnitude, (b) velocity vector field, and (c) and (d) FDV parameters.

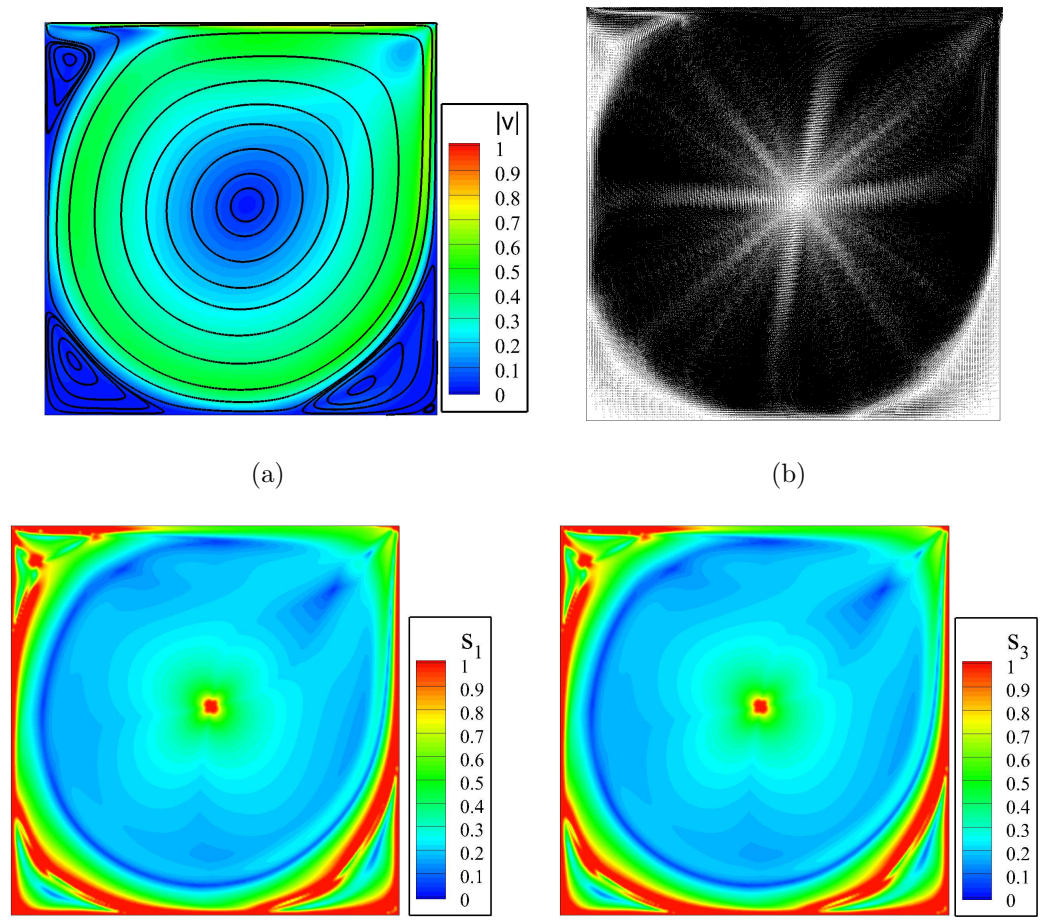

Figure 5.9 2D lid-driven cavity solution at $Re = 5{,}000$ using Case 7. (a) streamlines and contours of the normalized velocity magnitude, (b) velocity vector field, and (c) and (d) FDV parameters.

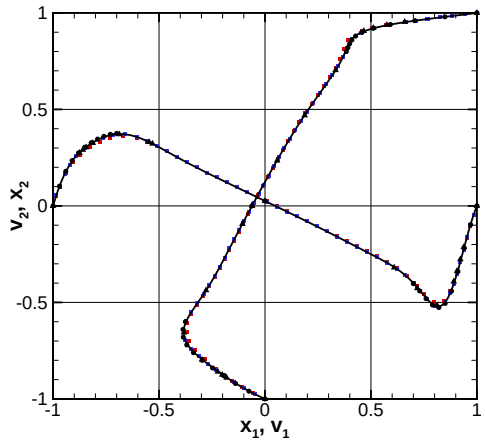

(a) ■ Case 1, ■ Case 2, —— Case 3, • Erturk et al. [55], and ▲ Ghia et al. [56]

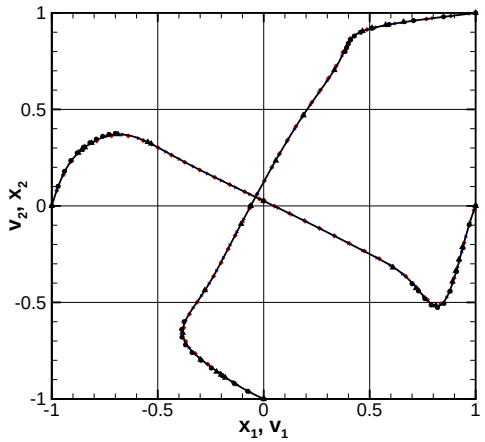

(b) ♦ Case 4, ▶ Case 5, —— Case 6, • Erturk et al. [55], and ▲ Ghia et al. [56]

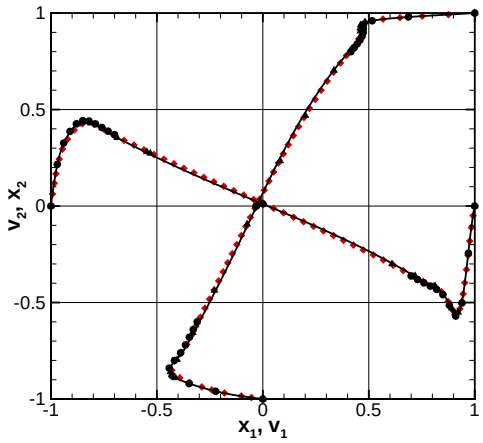

(c) ♦ Case 7, —— Case 8, • Erturk et al. [55], and ▲ Ghia et al. [56]

Figure 5.10 Comparison of the FDV solution of the 2D lid-driven cavity problem to published literature. (a) Cases 1–3, (b) Cases 4–6, and (c) Cases 7–8.

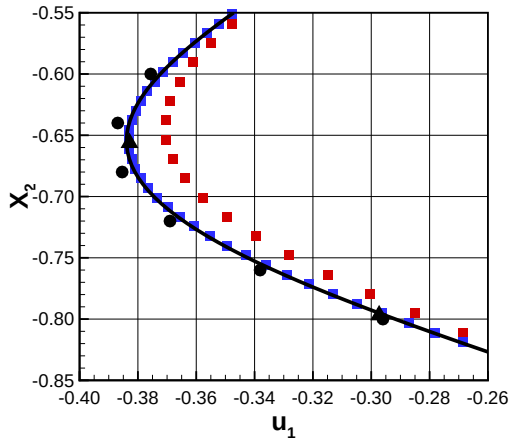

(a) v_1, lower-vertical-midsection.

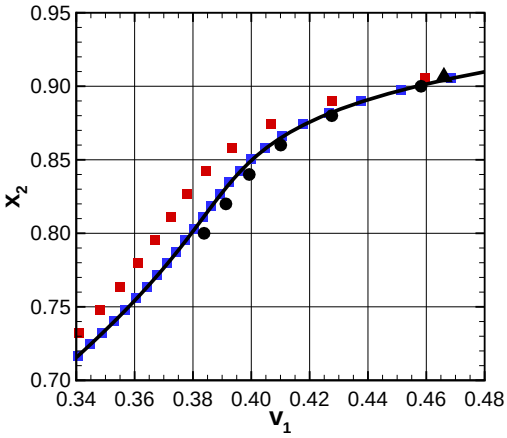

(b) v_1, upper-vertical-midsection.

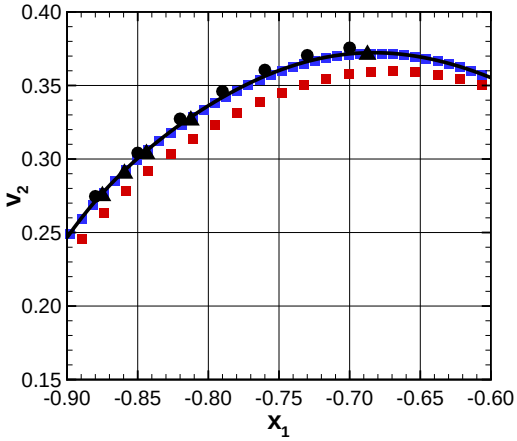

(c) v_2, left-horizontal-midsection.

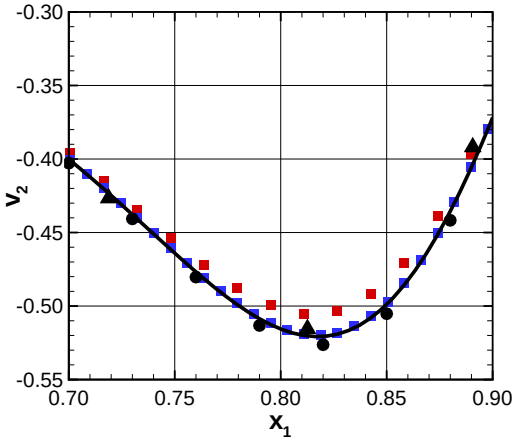

(d) v_2, right-horizontal-midsection.

Figure 5.11 First close up view of the comparison of the FDV solution of the 2D lid-driven cavity problem to published literature. ■ Case 1, ■ Case 2, —— Case 3, • Erturk et al. [55], and ▲ Ghia et al. [56] .

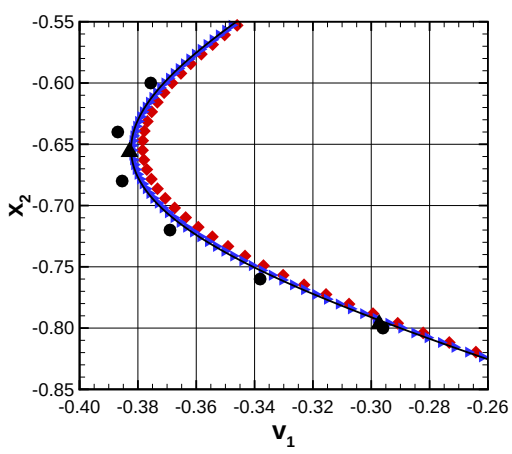

(a) v_1, lower-vertical-midsection.

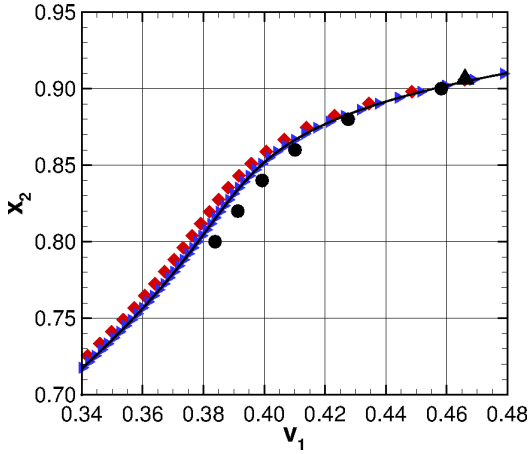

(b) v_1, upper-vertical-midsection.

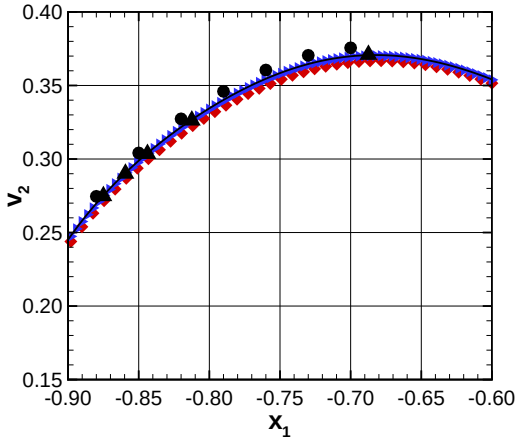

(c) v_2, left-horizontal-midsection.

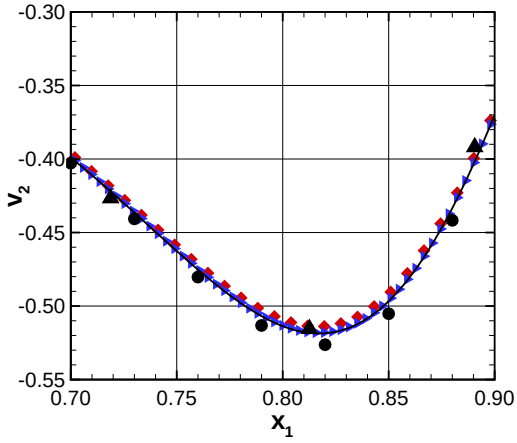

(d) v_2, right-horizontal-midsection.

Figure 5.12 Second close up view of the comparison of the FDV solution of the 2D lid-driven cavity problem to published literature. ♦ Case 4, ▶ Case 5, — Case 6, • Erturk et al. [55], and ▲ Ghia et al. [56] .

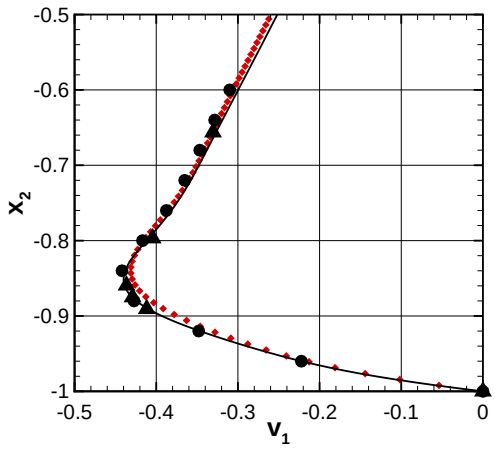

(a) v_1, lower-vertical-midsection.

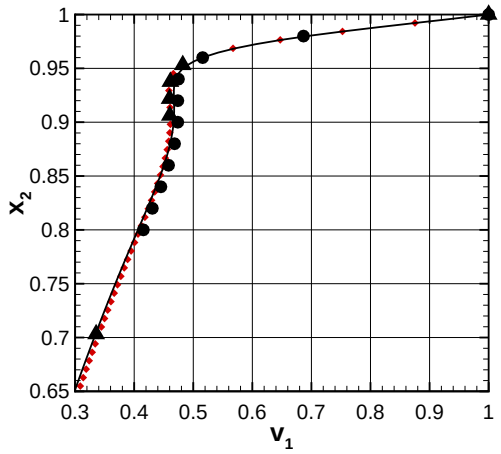

(b) v_1, upper-vertical-midsection.

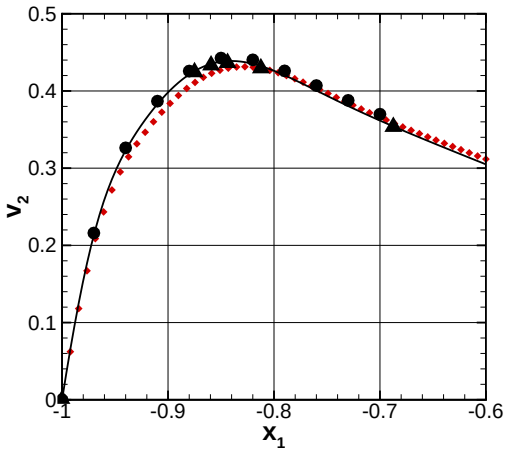

(c) v_2, left-horizontal-midsection.

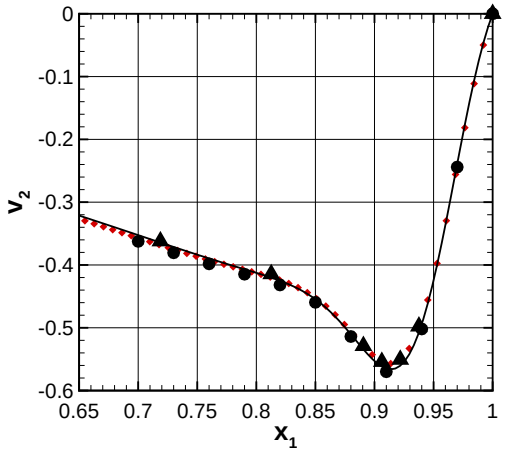

(d) v_2, right-horizontal-midsection.

Figure 5.13 Third close up view of the comparison of the FDV solution of the 2D lid-driven cavity problem to published literature. ♦ Case 7, — Case 8, • Erturk et al. [55], and ▲ Ghia et al. [56] .

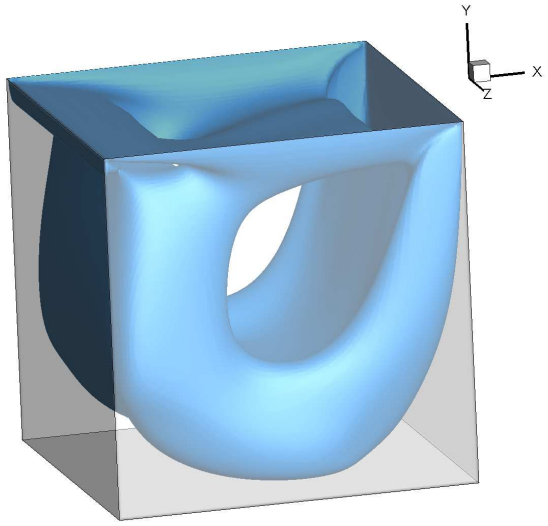

Figure 5.14 Iso-surface of the normalized velocity magnitude $v = 0.13$ for the 3D lid-driven cavity problem using Case 13.

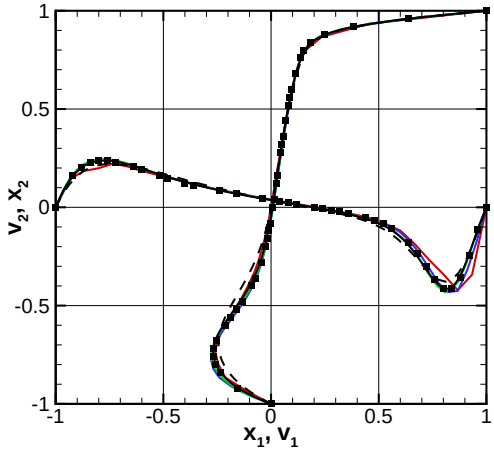

Figure 5.15 Comparison of the FDV solution of the 3D lid-driven cavity problem to published literature at $Re = 1000$ using Cases 9–13. — Case 9, — Case 10, — Case 11, --- Case 12, — Case 13, and ■ Lo et al. [57].

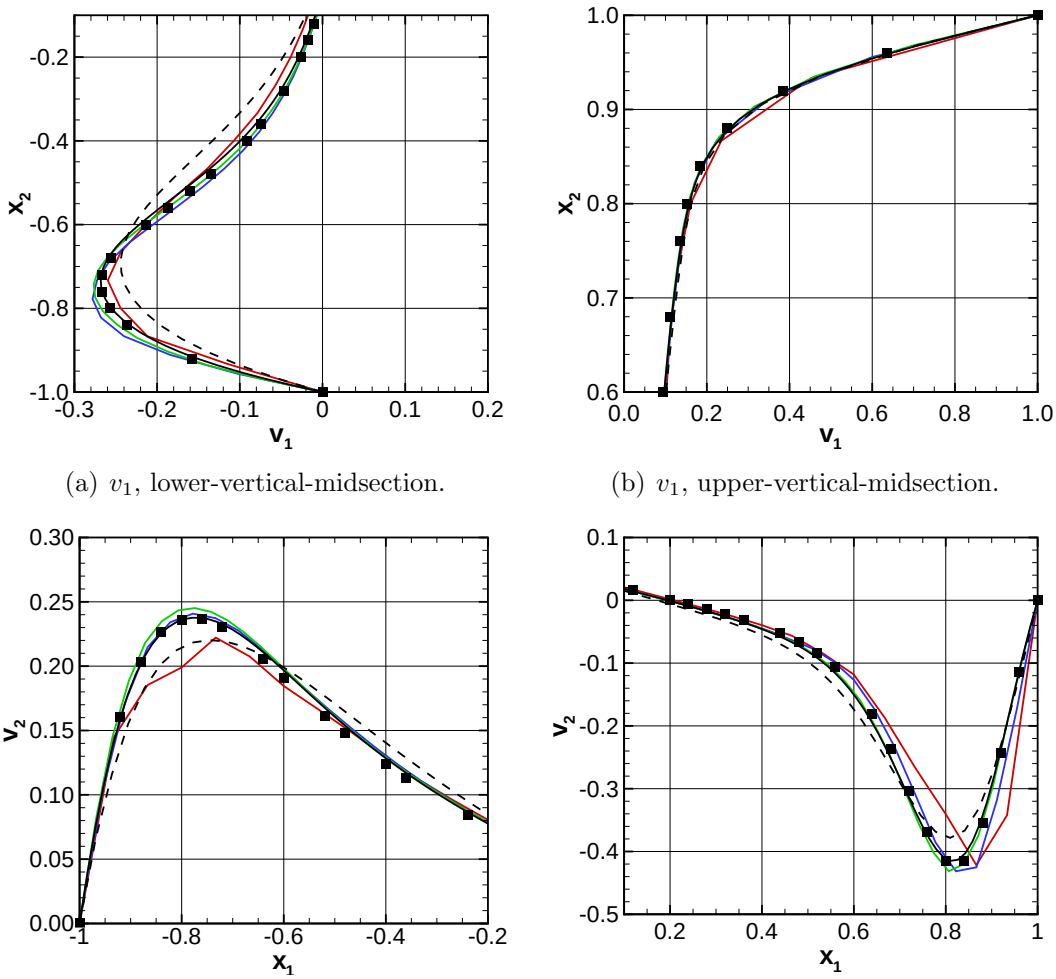

(a) v_1, lower-vertical-midsection.

(b) v_1, upper-vertical-midsection.

(c) v_2, left-horizontal-midsection.

(d) v_2, right-horizontal-midsection.

Figure 5.16 Close up view of the comparison of the FDV solution of the 3D lid-driven cavity problem to published literature at $Re = 1000$ using Cases 9–13. — Case 9, — Case 10, — Case 11, - - - Case 12, — Case 13, and ■ Lo et al. [57].

5.2.1.2 Backward-Facing Step

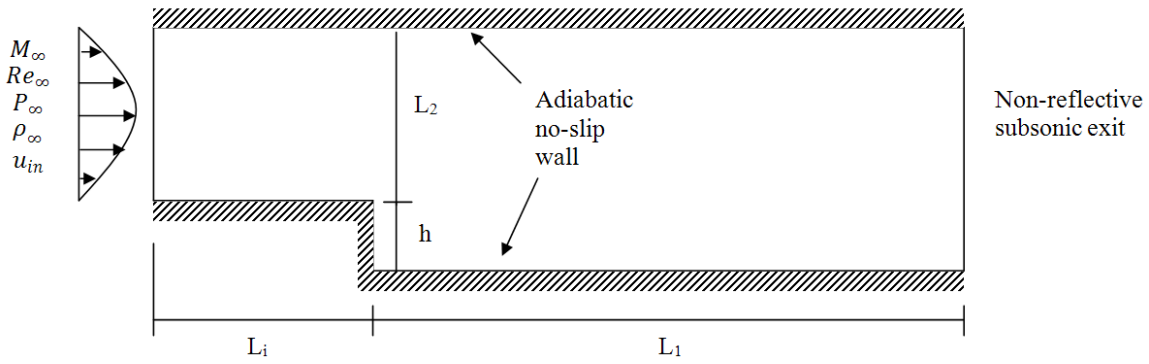

Figure 5.17 A schematic of the backward-facing step problem.

The 2D backward-facing step benchmark is studied at the incompressible limit, $M = 0.05$, in details to demonstrate the ability of the developed FDV method in capturing the physics of flow separation at different Reynolds numbers, $Re = 600, 800$. The step height is fixed at $h = 1$ and the other length scales are fixed as $L_i = 20h$, $L_1 = 100h$, and $L_2 = h$. Where L_i, L_1, and L_2 are the domain extension before the step, after the step, and the domain height above the step, respectively, as shown on Figure 5.17. This case is selected to match the 2D simulations done by Gartling [58] and Erturk [59]. A laminar parabolic profile is used at the inlet to fix the inlet mass flow rate according to the relation given by

$$v_1(0, x_2) = \frac{4}{L_2^2} (x_2 - h) (L_2 - (x_2 - h)) .$$

The inlet density is fixed to 1.0 and the inlet temperature is initialized to be 1.0. Inlet stagnation conditions are used to initialize the rest of the domain. The adiabatic wall boundary condition is used for the no-slip walls and non-reflective subsonic boundary condition is imposed at the exit. The grid is uniform 50 elements per h in the x_2 direction. The grid before the step is uniform 500 elements in the x_1 direction and uniform 2,500 elements after the step. The total number of nodes is 278,050.

Figures 5.18 and 5.19 show the same flow structures found in Erturk [59]. For both Reynolds numbers the selected backward-facing step generates two vortices resulting from the flow separation. The first vortex is just at the step, lower vortex, and the second is an upper wall vortex immediately following the lower vortex with a possible overlap distance. The width of both vortices and the start position of the upper vortex are functions of the Reynolds number. To verify the obtained solution, the width of the lower vortex, w_l, the start of the upper vortex, x_{us}, and its width, w_u, are compared to Erturk [59] as shown in Table 5.4.

The two solutions agree, for the most part. The differences are believed to be due to two main reasons. The first reason is the difference in the after step channel length, L_1, between the two solutions. This effect is discussed in [59] where the author argued for the extreme sensitivity of the results to the size and configuration of the solution domain. The second reason is the fact that Erturk [59] solves the incompressible form of the Navier-Stokes equations. To appreciate this effect we consider the velocity profiles development.

Figure 5.20 shows the velocity profile development for the $Re = 800$ case. Throughout the pre-step channel, the solution preserves the parabolic axial velocity

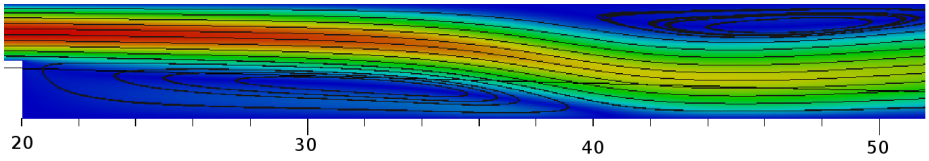

(a)

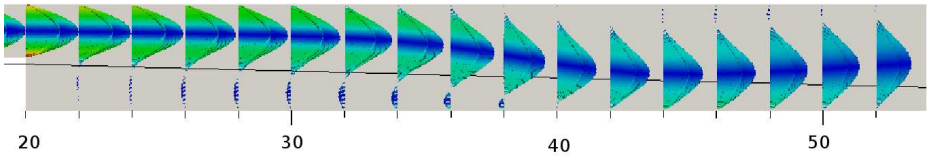

(b)

Figure 5.18 2D FDV solution of the backward-facing step at $Re = 600$. (a) flowfield streamlines and velocity contours, (b) flowfield velocity vector field colored by the vorticity magnitude.

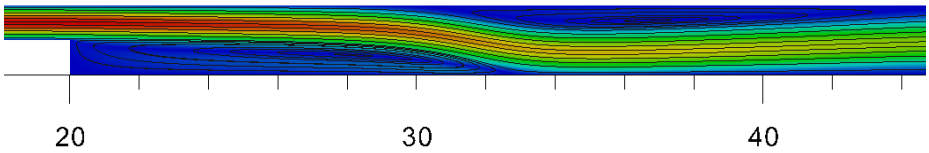

(a)

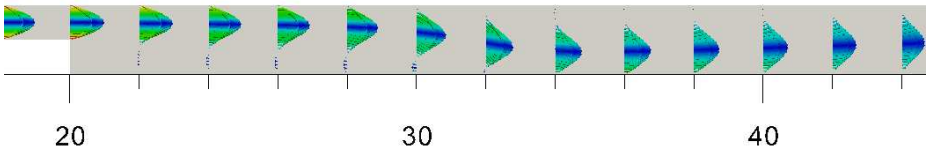

(b)

Figure 5.19 2D FDV solution of the backward-facing step at $Re = 800$. (a) flowfield streamlines and velocity contours, (b) flowfield velocity vector field colored by the vorticity magnitude.

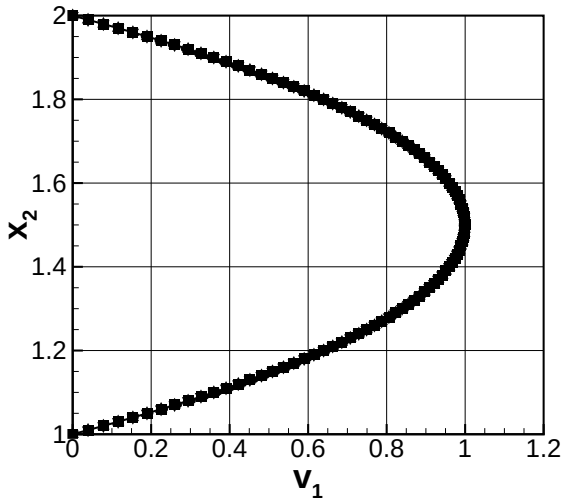

(a) —— $x_1 = 0$, ■ $x_1 = 5$, ▲ $x_1 = 10$, ▼ $x_1 = 15$, and • $x_1 = 20$.

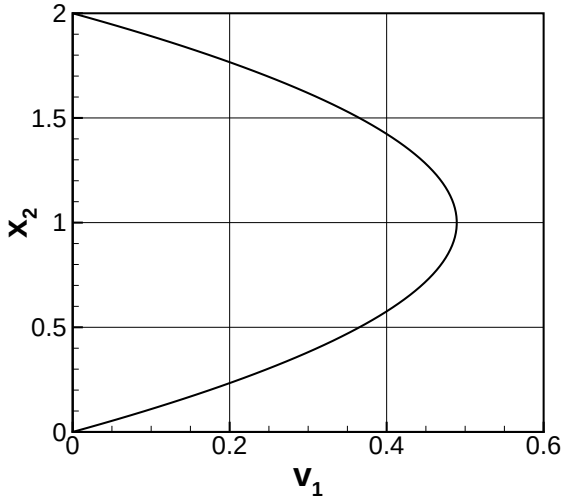

(b)

Figure 5.20 Velocity profiles development for the 2D backward-facing step solution at $Re = 800$. (a) inlet sections and (b) exit section.

Table 5.4 Comparison between the 2D FDV solution and published literature for the flow structures dimensions.

Case	w_l	x_{us}	w_u
FDV at $Re = 600$	10.364	28.425	8.997
Erturk [59] at $Re = 600$	10.444	28.722	6.521
FDV at $Re = 800$	12.5	30.2	15.24
Erturk [59] at $Re = 800$	11.982	29.646	10.346

profile as expected, Figure 5.20(a). At the exit section, $x_1 = L_i + L_1 = 120$, the solution develops to become parabolic again such that the outlet mass flow rate is the same as the one imposed by the inlet boundary conditions. Integrating the mass flow rate per unit depth at the inlet gives

$$\dot{m}_{in} = \int_{x_2=h}^{h+L_2} \rho(0, x_2) v_1(0, x_2) dx_2 = \frac{2}{3} Kg/s.$$

Similarly, integrating the outlet mass flow rate gives $\dot{m}_{out} = 0.666602 Kg/s$. Which establishes a numerical error in the order of $O\left(10^{-5}\right)$. To appreciate the change in the density introduced by using the compressible form of the Navier-Stokes equations in the solution, the mass flow rate integration is carried with the outlet density assumed to 1.0 as the inlet gives error in the order of $O\left(10^{-2}\right)$.

Figure 5.21 shows comparisons between the obtained solution at $Re = 800$ and Erturk [59] using the line plots of both the axial and lateral velocity components at $x_1 = 26$, $x_1 = 34$, and $x_1 = 50$. The differences between the two solutions are again believed to be due to the main two reasons mentioned above.

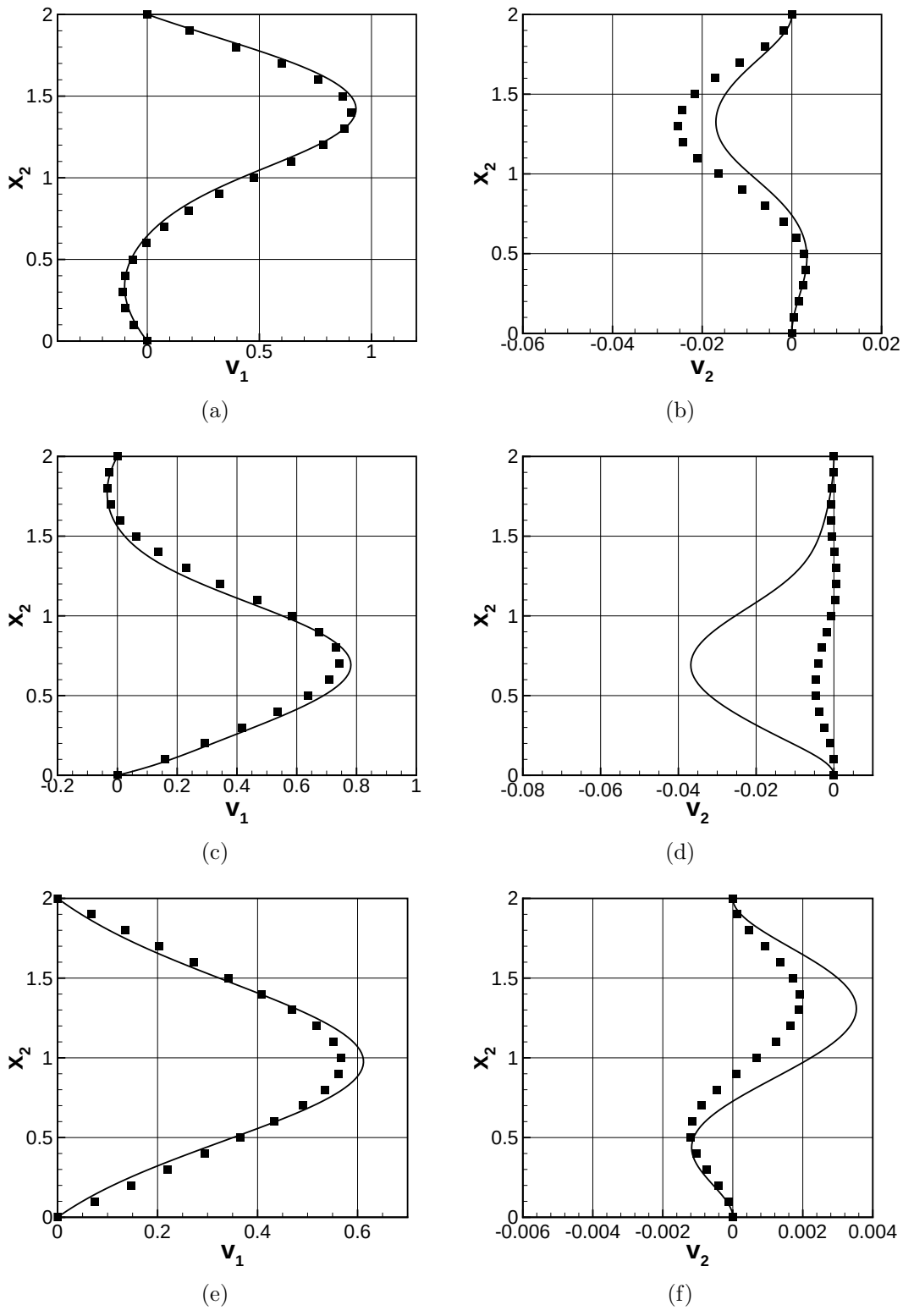

Figure 5.21 Verification of the 2D backward-facing step at $Re = 800$. (a) and (b) $x_1 = 26$, (c) and (d) $x_1 = 34$, and (e) and (f) $x_1 = 50$. —— FDV solution and ■ Erturk [59].

5.2.2 Compressible Flow Problems

Compressible flows are driven by wave phenomena. These waves stem from the ability of the fluid particles to come closer to each other at high pressures and to relax away from each other at lower pressures. The generated phenomena is the familiar acoustic waves. In supersonic flows, discontinuities are inevitable in the flow field.

Five test cases are selected to verify the developed FDV solver in handling the compressible flow physics. The smooth acoustic pulse test case is introduced in Section 5.2.2.1, where the effect of the grid resolution and the order of accuracy on the quality of the solution is studied in comparison with the available analytical solution. A shock tube problem is compared to the analytical Riemann solution in Section 5.2.2.2. The role of the FDV parameters in this problem solution is discussed. A supersonic flat plate problem at $M_\infty = 3$ is solved for both 2D and 3D in Section 5.2.2.3. The solution is compared to published literature, and the role of the FDV parameters is emphasized. Similar to the flat plate, a supersonic compression corner is analyzed for both 2D and 3D at two different Mach numbers, $M_\infty = 3$ and 4. Comparisons with available literature is used for verification.

5.2.2.1 Acoustic Pulse

The isentropic acoustic pulse problem of initial amplitude 1% is analyzed to establish the ability of the developed FDV framework to accurately simulate the acoustic waves. The details of the problem and its analytical solution are given in Tam

et al. [60]. The domain is a 2D square with an edge side 1.0 and a uniformly discretized grid. The flowfield is initialized with a stagnant flow and a symmetric exponential pressure pulse in the center of the domain, Figure 5.22, added to a constant pressure field. The temperature of the domain is initialized to be a constant and the density is calculated from the equation of state. The flow variables are normalized such that the initial pressure and temperature are both 1.0. The characteristic boundary condition is used for all domain boundaries. The details of the analyzed cases are given in Table 5.5. These cases are selected to study the effect of grid size, time step, and higher order accuracy.

Table 5.5 Studied acoustic pulse cases.

ID	NE	Order	Δt
1	255^2	1	10^{-5}
2	127^2	1	10^{-5}
3	127^2	1	10^{-4}
4	127^2	3	10^{-5}

Figure 5.23 shows the pressure contours of the solution obtained by the developed FDV framework using Case 1. The acoustic pulse propagates in the 2D domain maintaining its symmetric structure in the form of a two concentric circles; an overshoot and an under shoot. The developed FDV solver is able to capture the solution accurately as shown on Figure 5.24. Good agreement is obtained in both phase and amplitude.

Figure 5.25(a) shows a comparison between Cases 1–3 and the analytical solution. The smaller grid of Case 2, for the same time step, shows Gibbs type errors

compared to the higher grid of Case 1. However, the same grid at a larger time step, Case 3, shows a solution free of the Gibbs type oscillations, although more dissipative. The linear solution appears to be more dissipative than the cubic solution as expected, Figure 5.25(b). It also shows a small phase lag at the last time instant shown. The cubic grid, however, shows a better solution that matches the analytical solution.

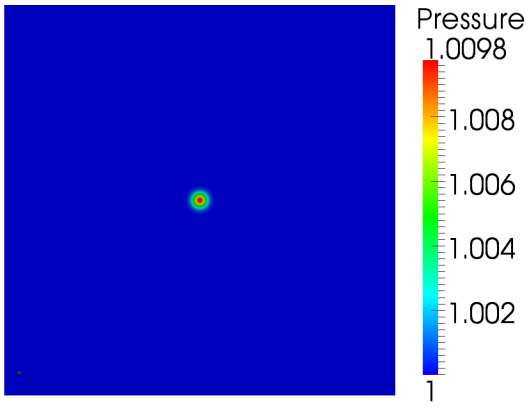

(a)

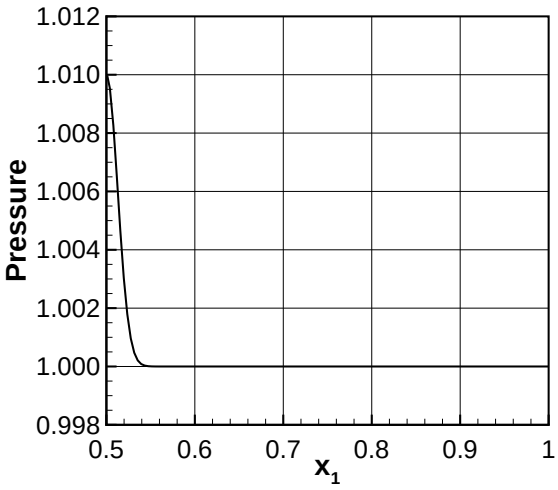

(b)

Figure 5.22 2D acoustic pulse initial pressure. (a) contours and (b) line plot.

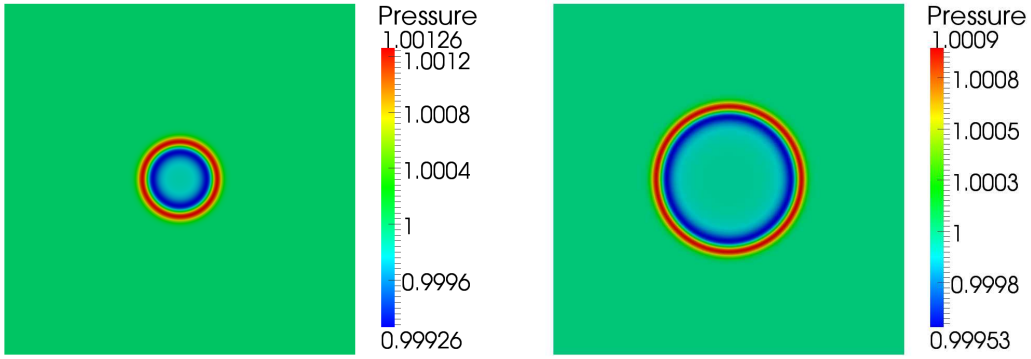

(a) $t = 0.05s$ (b) $t = 0.10s$

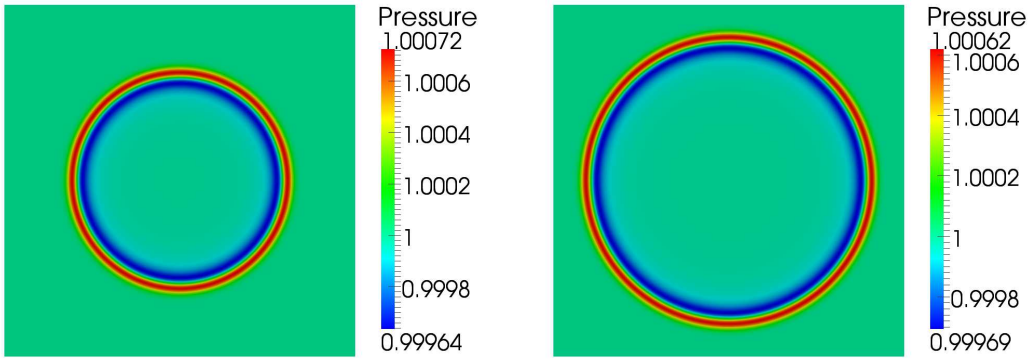

(c) $t = 0.15s$ (d) $t = 0.20s$

Figure 5.23 2D acoustic pulse FDV solution using Case 1.

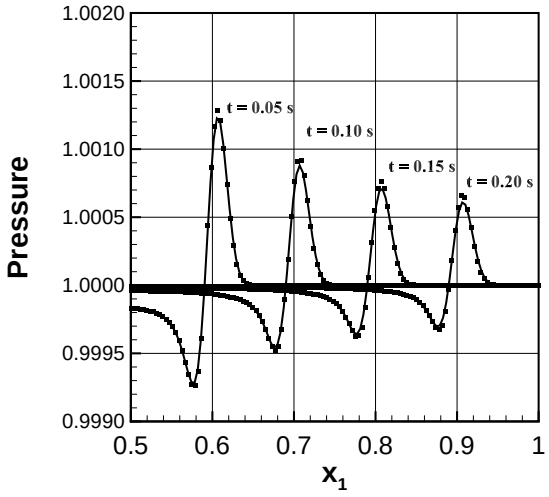

Figure 5.24 Comparison of the 2D acoustic pulse FDV solution to the analytical solution given in Tam et al. [60]. ■ analytical solution and —— Case 1.

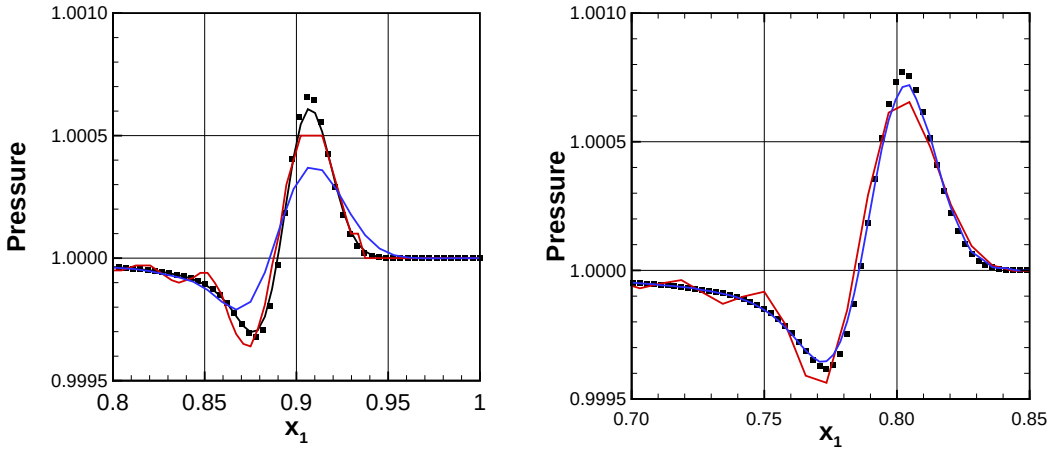

(a) ■ analytical solution, —— Case 1, —— Case 2, and —— Case 3 at $t = 0.20s$.

(b) ■ analytical solution, —— Case 2, and —— Case 4 at $t = 0.13s$.

Figure 5.25 Effects of the grid resolution, time step, and higher order accuracy on the FDV solution of the 2D acoustic pulse.

5.2.2.2 Shock Tube

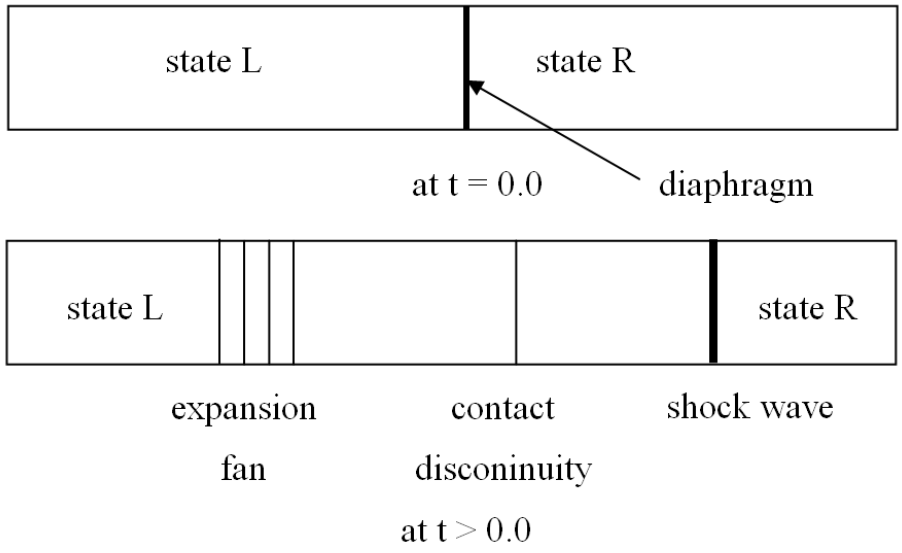

Figure 5.26 A schematic of the shock tube domain.

The inviscid compressible shock tube is a classical Riemann problem. Initially, there is a diaphragm that separates two different gases at rest and each has different pressure and density. Upstream state L is defined by p_L and ρ_L, and downstream state R is defined by p_R and ρ_R. Suddenly this diaphragm is removed generating a shock wave, a contact discontinuity, and an expansion fan as shown on Figure 5.26. The analytical solution of this problem can be found in typical gasdynamics text books [61].

This problem is essentially one dimensional, and the one dimensional FDV Euler equations flow solver is employed. The computational domain is set to 1.0 and discretized by 1001 equally spaced nodes. The boundary conditions are set to characteristic inflow on the left and characteristic outflow on the right. A constant

time step of $0.5ms$ is used, which gives a CFL number close to 0.5 at the beginning of the solution. The initial conditions are set to a stagnant flow with $p_L = 1.0$, $\rho_L = 1.0$, $p_R = 0.1$, and $\rho_R = 0.125$.

The comparison between the numerical and exact solutions for density, pressure, and Mach number are shown on Figures 5.27(a), 5.27(b), and 5.27(c), respectively. The FDV method is able to accurately simulate the propagation of the different non-linear wave phenomena existing in this problem. This is emphasized through the FDV parameter, s_1, shown on Figure 5.27(d). For the regions with stagnant flow on both sides of the solution domain, s_1 is kept close to 1.0 assuring the stability of the solution. In the regions with constant properties and a non-zero velocity, s_1 is kept close to zero for accuracy. At the shock and the contact discontinuity s_1 increases adequately to establish the necessary stability according to the FDV scheme.

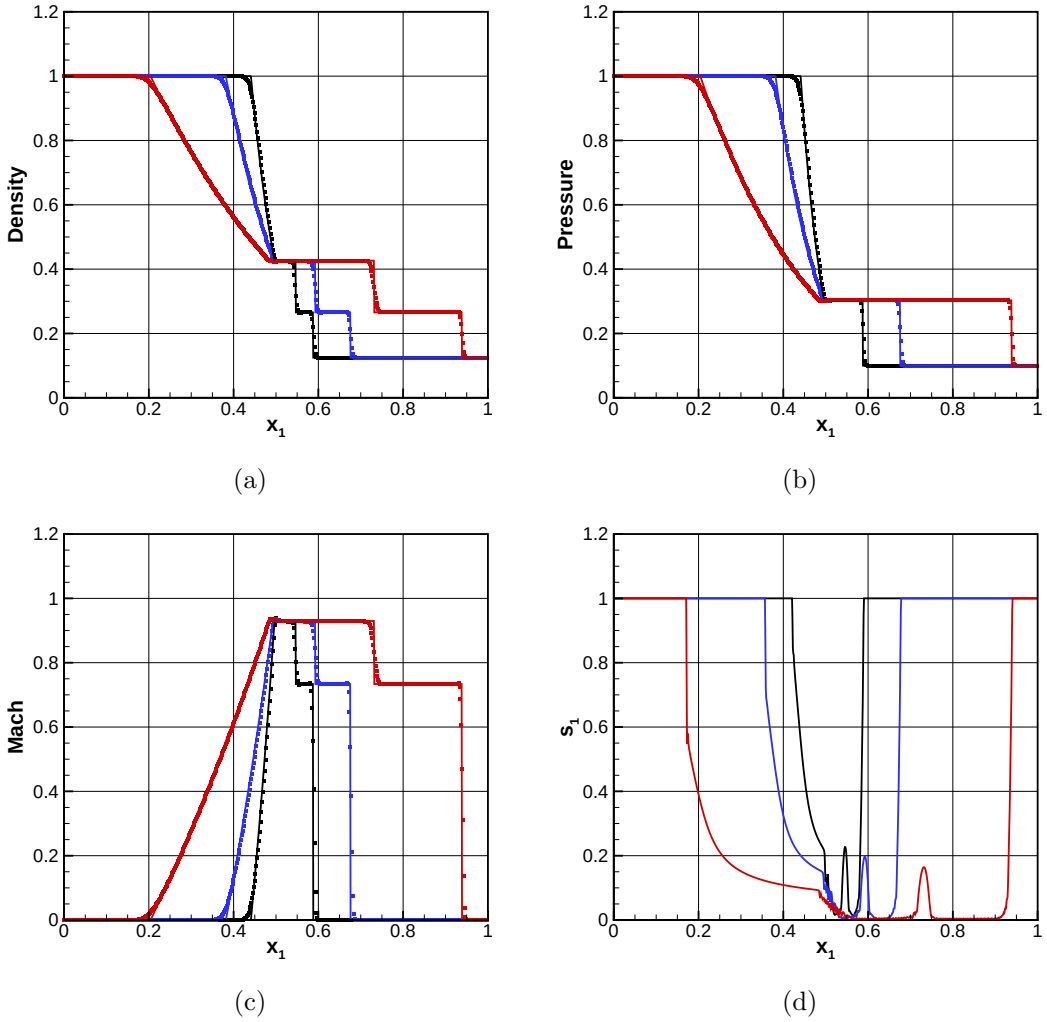

Figure 5.27 FDV solution of a 1D shock tube problem. ■, ■, and ■ FDV solution at $t = 0.05s$, $t = 0.10s$, and $t = 0.25s$, respectively. ——, ——, and —— are the analytical solution at the same time steps.

5.2.2.3 Supersonic Flat Plate

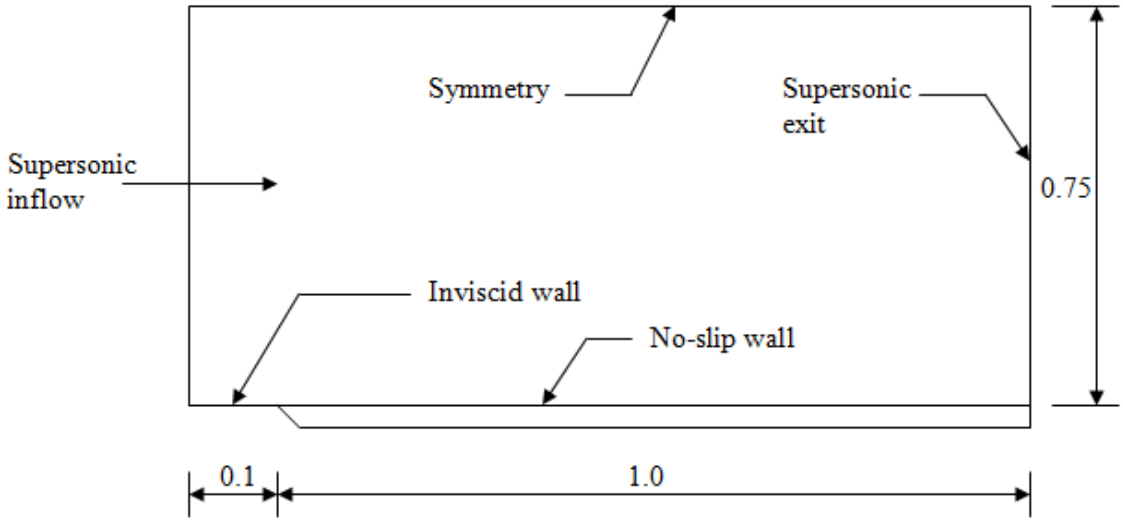

Figure 5.28 A schematic of the flat plate domain.

The flat plate domain, shown on Figure 5.28, is solved using the complete Navier-Stokes equations FDV solver at $M_\infty = 3.0, Re_L = 1000, Pr = 0.72, \gamma = 1.4, T_\infty = 216.67K$, with both 2D and 3D numerical grids shown on Figure 5.29. The 2D grid is set to 96×64 nodes, whereas the 3D grid is set to $74 \times 51 \times 68$ nodes with transverse length of 1.0 in the x_3 direction. The grid is uniformly discretized in both axial, x_1, and transverse, x_3, directions. It expands exponentially from the wall in the lateral, x_2, direction according to the relation given by [31]

$$\frac{x_2}{h} = \frac{(\beta+1) - (\beta-1)\left(\frac{(\beta+1)}{(\beta-1)}\right)^{1-\eta}}{\left(\frac{(\beta+1)}{(\beta-1)}\right)^{1-\eta} + 1}, \tag{5.5}$$

where η is the normalized transverse coordinates and β is the expansion ratio. For the 2D and 3D cases $\beta = 1.3$ and $\beta = 1.1$ are used, respecively.

The inlet flow conditions are normalized such that the axial velocity, the density, and the temperature are set to 1.0. The inlet conditions are supersonic and all variables are fixed. The outlet conditions are set to supersonic outlet and the no-slip wall is set to isothermal conditions with temperature equal to the stagnation temperature of the free stream. For the 3D case the periodic boundary condition is used for the transverse direction. The domain is initialized with the stagnation conditions of the inlet flow. These cases are selected to approach the results of Carter [62] and Heard [63].

Figures 5.30 and 5.31 show the FDV steady state solution for the 2D and the 3D cases, respectively. The supersonic flow generates a leading-edge shock wave due to the existence of the plate. The no-slip condition generates a boundary layer near the wall. In this case, the free-stream is supersonic as well as the flow after the oblique shock and far from the wall. The flow inside the boundary layer is mainly subsonic compressible and it goes to nearly incompressible in the near wall vicinity as shown on Figure 5.30(a).

The FDV method is able to capture all the physics involved. The density contours, shown on Figures 5.30(b) and 5.31(a), are nearly constant inside the boundary layer as expected. It exhibits a sudden increases across the shock wave and then expands to the after oblique shock conditions over the boundary layer. The pressure contours on the other hand, shown on Figures 5.30(c) and 5.31(b), change along the flat. Similar to the density, the pressure increases across the shock wave and it ex-

pands due to the existence of the boundary layer. Small numerical noise is noticed due to the leading edge singularity. The finer 2D mesh showed better leading edge resolution. The 3D solution proves that this problem is essentially 2D due to its laminar nature which does not lead to any 3D structures.

Figures 5.32 and 5.33 show the contours of the FDV parameters for the 2D and 3D cases, respectively. In this supersonic case the convection FDV parameter, s_1, shows a different behavior from the diffusion FDV parameter, s_3. Both s_1 and s_3 are high in the shock region and near the wall to provide the needed stability and accuracy. s_3 has an extra high region near the leading edge to emphasis the diffusive interactions between the supersonic flow after the oblique shock and the boundary layer and ensure accurate solution for this mixed region. The shock wave and the boundary layer are visible in Figure 5.34 through the vector field.

To verify the FDV method's results for the supersonic flat plate problem, Figures 5.35 and 5.36 compare the obtained solution to Carter's [62] through line plots along $x_1|_{x_2=0}$ and $x_2|_{x_1=1}$, respectively. Figures 5.35(a) and 5.35(b) show good agreement for both the skin friction coefficient, c_f, and wall pressure. The effect of the leading edge singularity is evident in both plots, although it does not affect the rest of the solution. Figure 5.36(a), 5.36(b), and 5.36(c) confirm the agreement between both solutions. A comparison with the single precision outputs of Heard [63] for both the 2D and the 3D cases showed differences of the order $O(10^{-8})$, which is expected; since the obtained results are in double precision format.

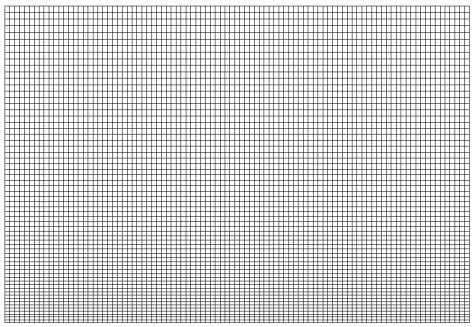

(a) 2D

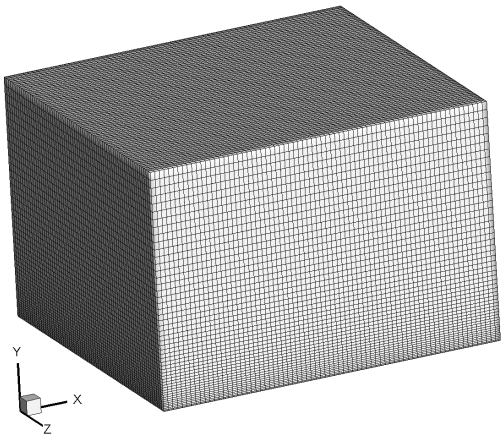

(b) 3D

Figure 5.29 Numerical grids of the flat plate problems.

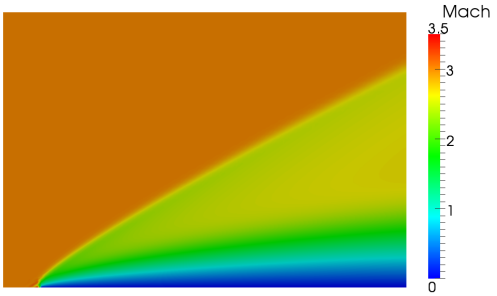

(a)

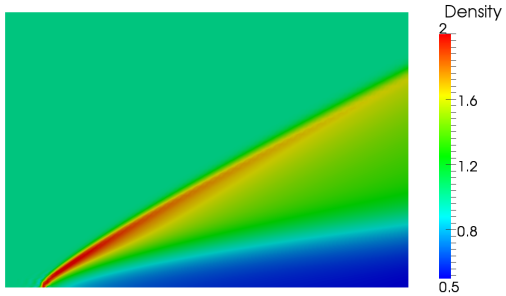

(b)

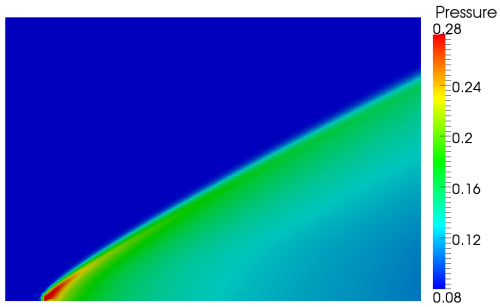

(c)

Figure 5.30 FDV solution of the 2D flat plate problem.

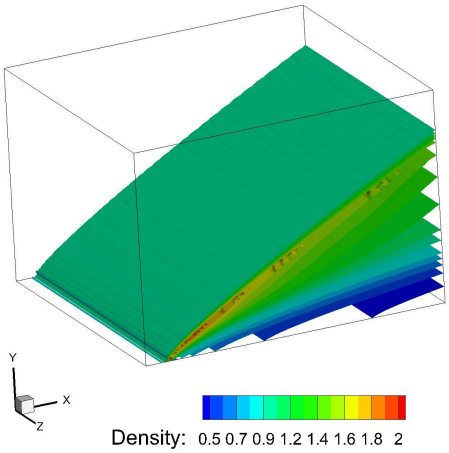

(a)

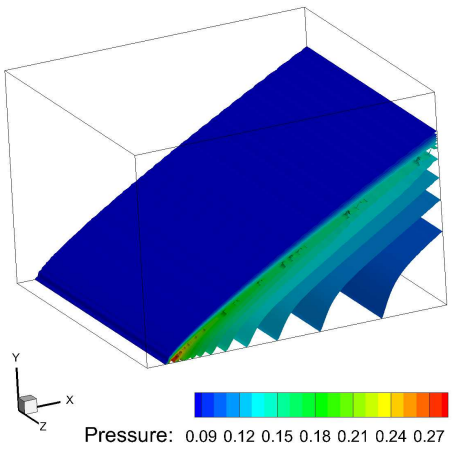

(b)

Figure 5.31 FDV solution of the 3D flat plate problem.

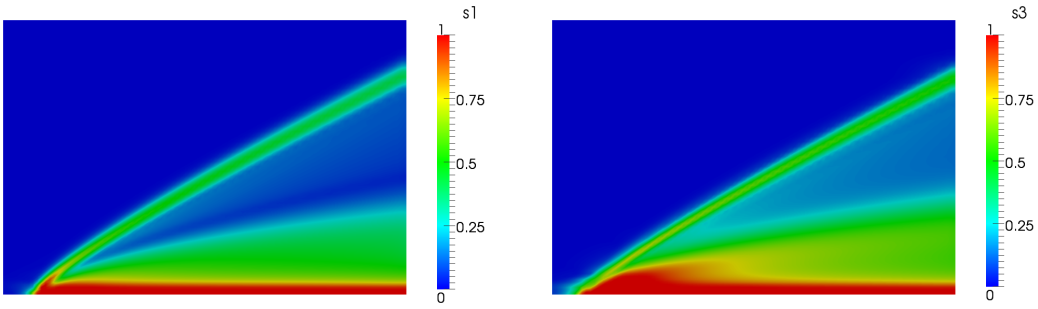

(a) (b)

Figure 5.32 FDV parameters for the 2D flat plate problem.

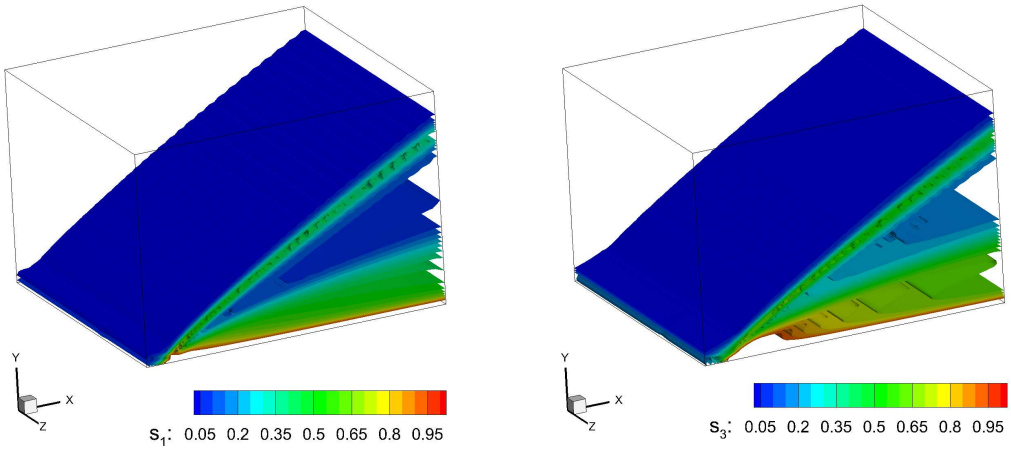

(a) (b)

Figure 5.33 FDV parameters for the 3D flat plate problem.

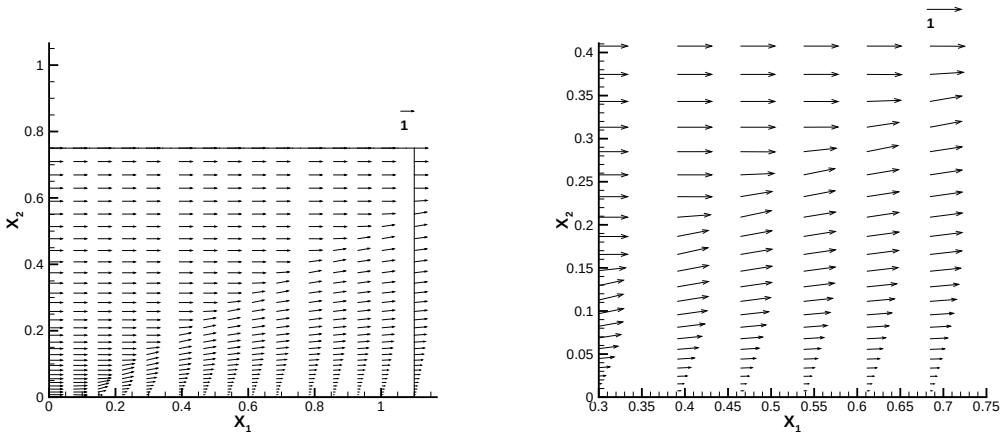

(a) (b)

Figure 5.34 Velocity vector field for the 2D flat plate problem. (a) all domain and (b) close-up view.

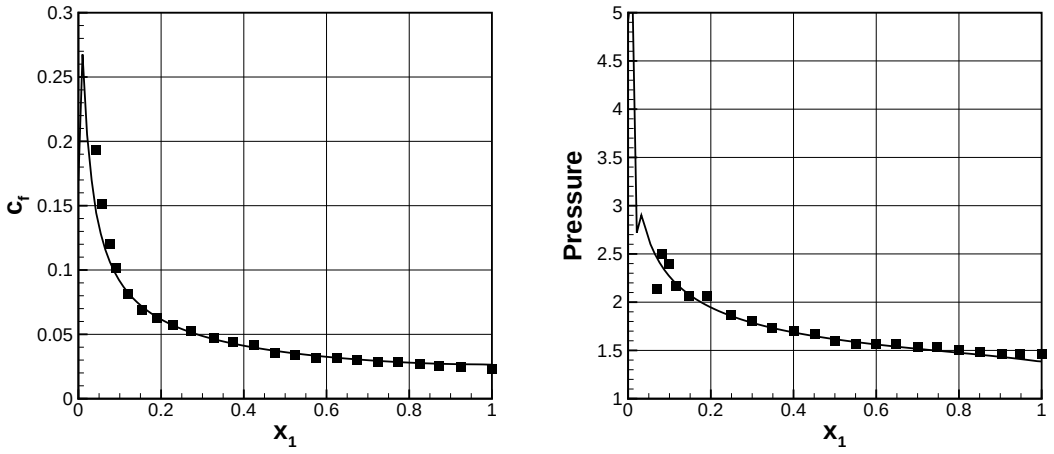

(a) (b)

Figure 5.35 Verification of the FDV results for the flat plate problem; x_1 profiles. — FDV and ■ Carter [62].

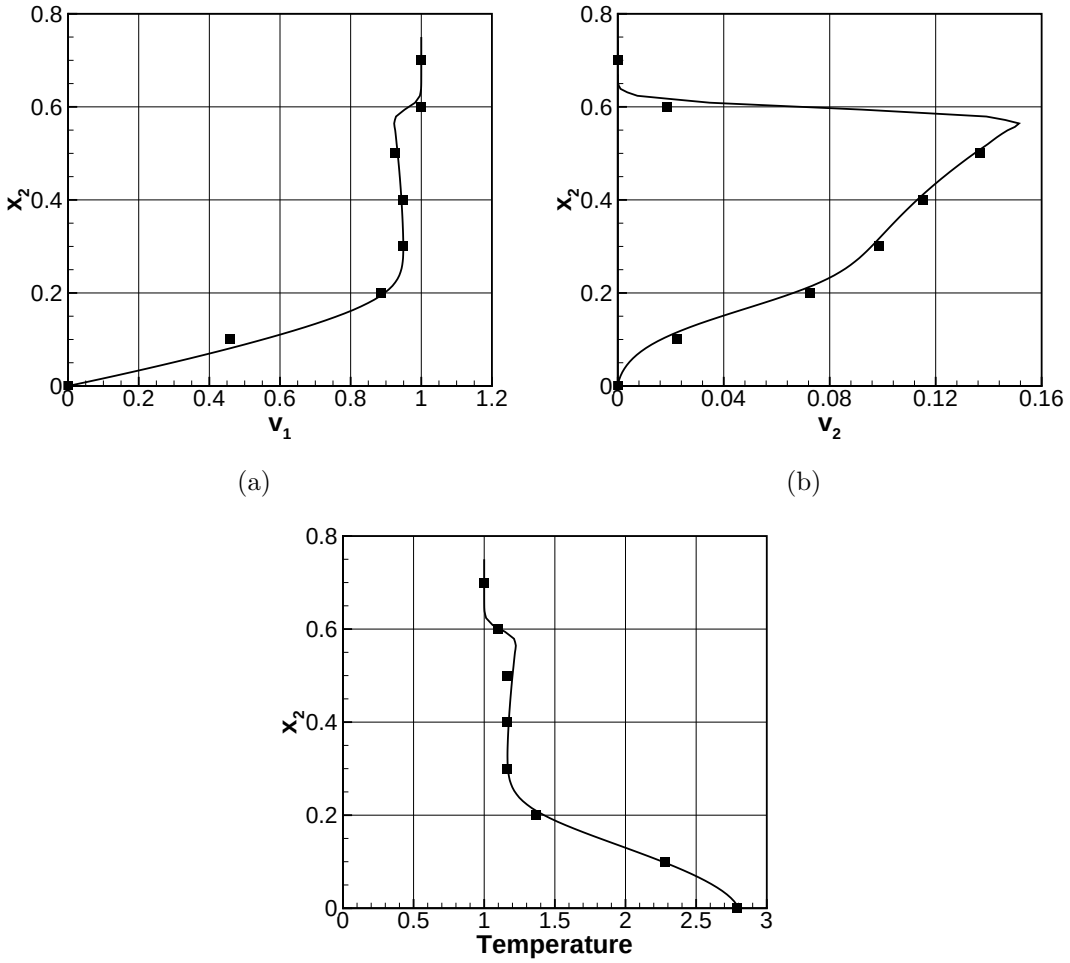

(a) (b)

(c)

Figure 5.36 Verification of the FDV results for the flat plate problem; x_2 profiles at $x_1 = 1$. —— FDV and ■ Carter [62].

5.2.2.4 Supersonic Compression Corner

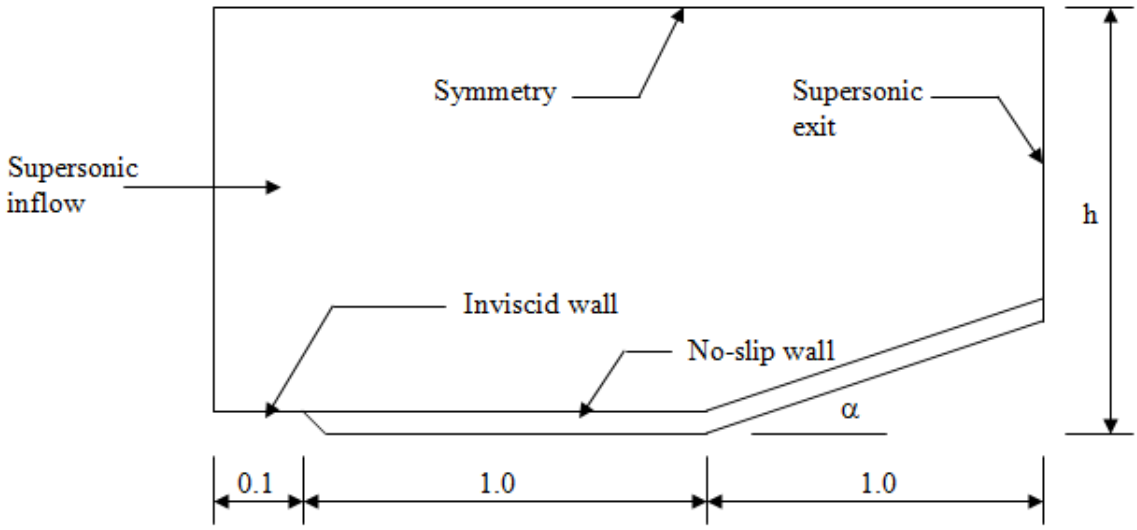

Figure 5.37 A schematic of the compression corner domain.

The compression corner domain, shown on Figure 5.37, is solved using the Navier-Stokes equations FDV flow solver at two different conditions, namely:

- $M_\infty = 3.0$, $Re_L = 16800.0$, and $T_\infty = 216.67K$.
- $M_\infty = 4.0$, $Re_L = 68000.0$, and $T_\infty = 48.887K$.

The two cases are solved using 2D grids at $Pr = 0.72$, $\gamma = 1.4$, and $\alpha = 10.0^o$. Only the first case is solved in 3D at the same 2D conditions. The 3D case is set to have a no-slip wall on one of the third dimension boundaries, $x_3 = 0$. This wall starts with the leading edge of the compression corner. The other third dimension boundary, $x_3 = h$, is inviscid. The height of the 2D solution domain of the first case is set to $h = 1.0$, whereas for the second case $h = 0.7$. The height of the solution domain

in the 3D case is $h = 0.6$. These conditions are selected to match the conditions of Lewis [64], Carter [62], and Heard [63].

The grid is uniformly discretized in the axial, x_1, direction and expands exponentially from the wall in both the lateral and the transverse directions, x_2 and x_3, with 1.1 expansion ratio according to the relationship given in Equation (5.5). The numerical grid nodes are 169×104 for the 2D cases, Figure 5.38, and $89 \times 41 \times 41$ for the 3D case, Figure 5.39.

All the no-slip walls are isothermal with the wall temperature, T_w, fixed at the stagnation temperature for the first case and given by

$$\frac{T_w}{T_\infty} = 1 + \frac{\gamma - 1}{2} M_\infty^2.$$

Whereas for the second case, the wall temperature is fixed at

$$\frac{T_w}{T_\infty} = 1 + \frac{\gamma - 1}{2} \sqrt{Pr} M_\infty^2,$$

as given by Carter [62].

The inlet flow conditions are normalized such that the axial velocity, the density, and the temperature are set to 1.0. The inlet conditions are supersonic and all variables are fixed. The outlet conditions are set to supersonic outlet. The domain is initialized with the stagnation conditions of the inlet flow.

For the 2D cases, shown on Figures 5.40 and 5.41, the supersonic flow generates a leading-edge shock wave and an oblique shock wave due to the existence of

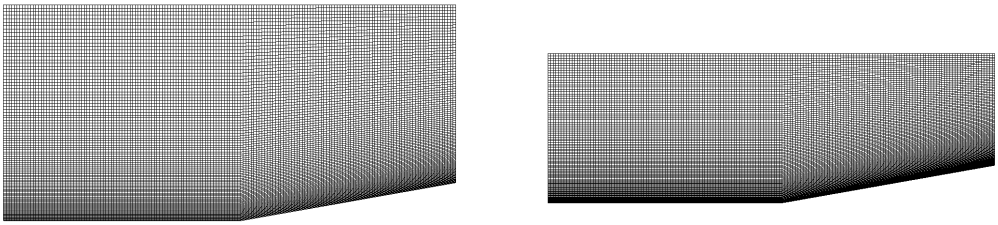

(a) $M_\infty = 3$ (b) $M_\infty = 4$

Figure 5.38 The numerical grids of the 2D compression corner problems.

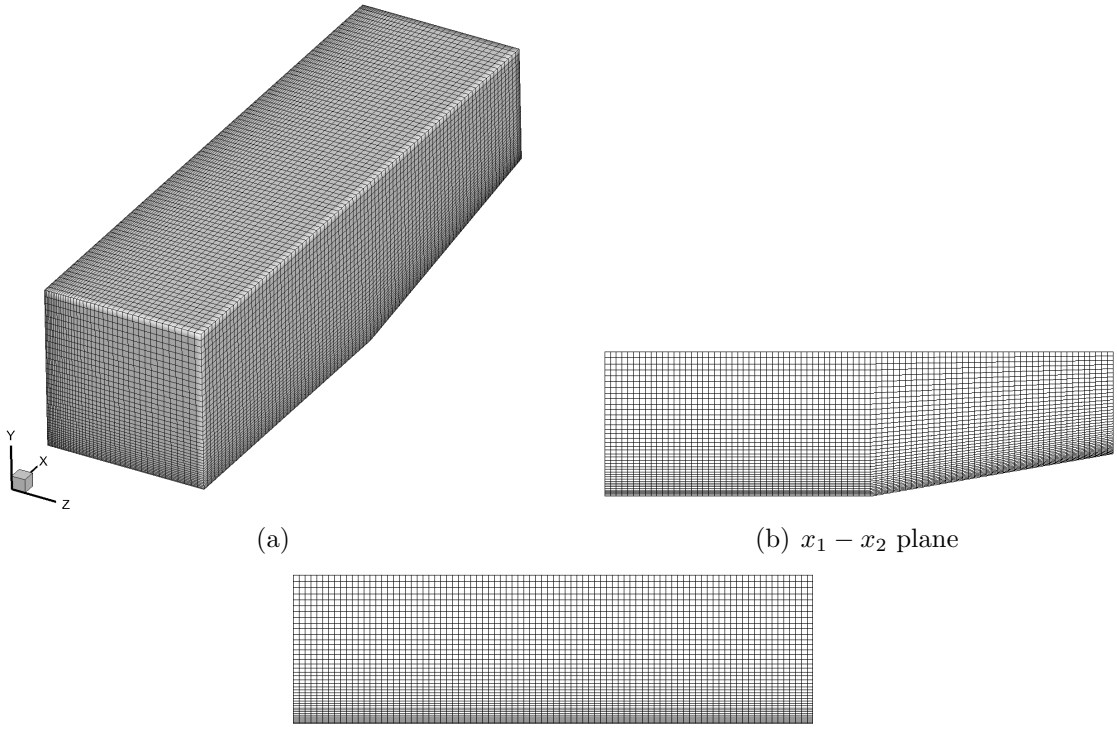

(a) (b) $x_1 - x_2$ plane

(c) $x_1 - x_3$ plane

Figure 5.39 The numerical grid of the 3D compression corner problem.

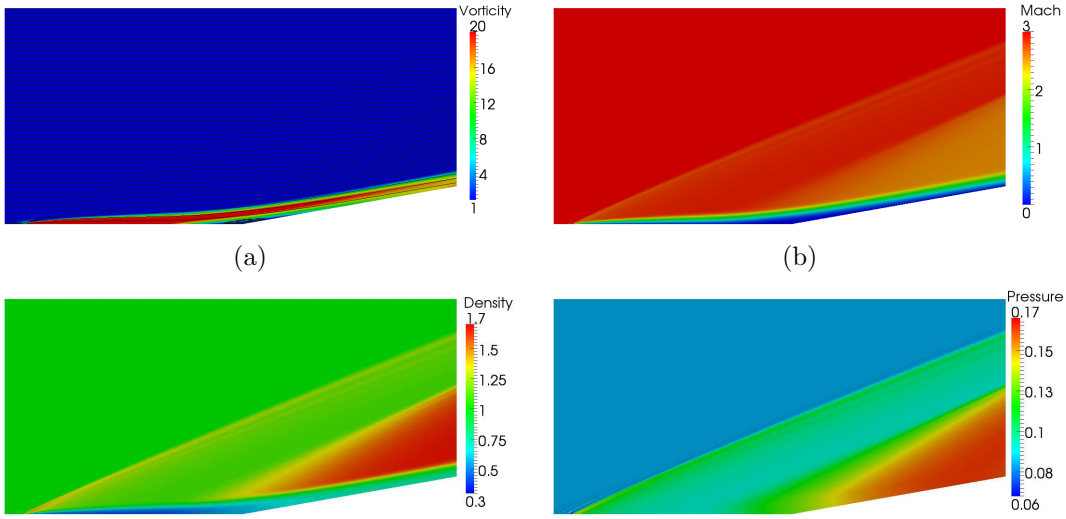

Figure 5.40 Steady state FDV solution for the 2D compression corner problem at $M_\infty = 3$.

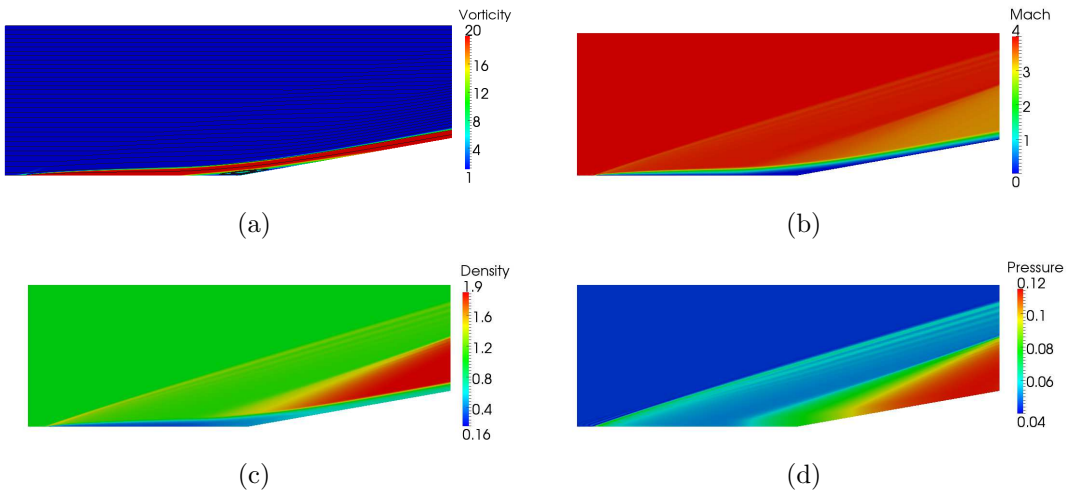

Figure 5.41 Steady state FDV solution for the 2D compression corner problem at $M_\infty = 4$.

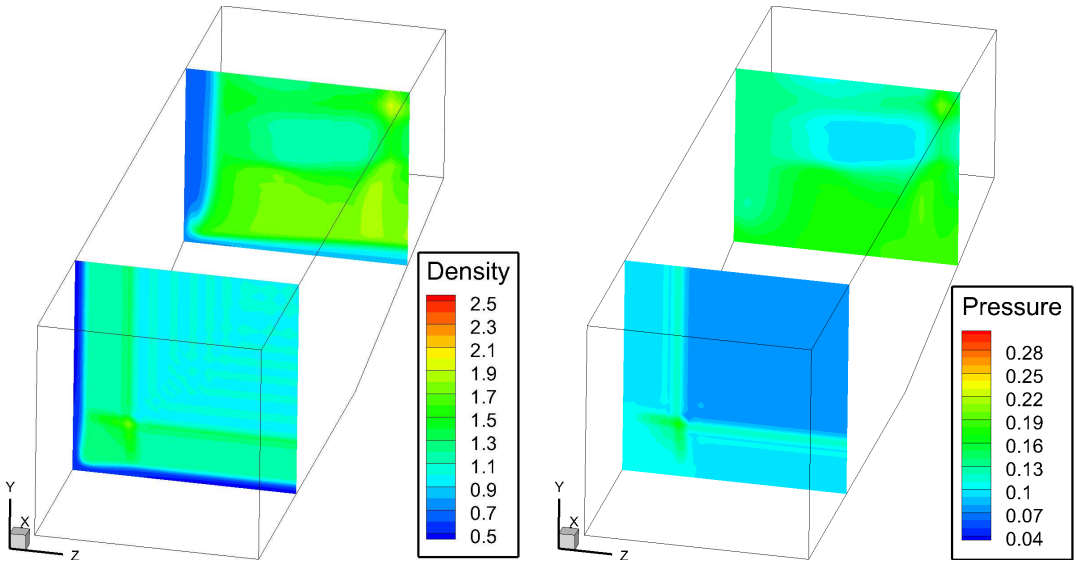

Figure 5.42 FDV solution of the 3D compression corner problem.

the compression corner. The no-slip condition generates a boundary layer near the wall. At the compression corner the flow separates generating a recirculation bubble as shown on Figures 5.40(a) and 5.41(a). The flow outside the boundary layer is irrotational supersonic, and the flow inside the boundary layer is mainly subsonic compressible and it goes to nearly incompressible in the near wall vicinity as shown on Figures 5.40(b) and 5.41(b). The difference in the Mach numbers changes the leading edge shock wave angle as well as the compression shock at the corner. The higher the Mach number the stronger the shock waves.

The leading edge shock wave has similar effects on the density and the pressure contours, Figures 5.40(c), 5.41(c), 5.40(d), and 5.41(d), to those found in the supersonic flat plate problem discussed in Section 5.2.2.3. The elevated no-slip wall at the corner causes the supersonic flow to change its direction, which in turn generates a

shock wave in the free stream. Inside the boundary layer the flow is subsonic and the compression corner originates as a gradual pressure increase. The gradual pressure waves coalesce to generate the oblique shock wave outside the boundary layer. This adverse pressure gradient is believed to be the reason for the separation bubble residing around the compression corner.

The 3D case, shown on Figure 5.42, has flow features similar to those found in the 2D case . The wall in the transverse, x_3, direction generates another leading edge shock normal to the original one found in the 2D solution. The interaction between the two leading edge shocks and the compression corner shock wave is visualized by showing the contours of both density and pressure at two cross-sections; $x_1 = 0.4292$ and 1.69.

The FDV parameters for the 2D cases, Figure 5.43–5.44, and the 3D case, Figure 5.45, mimic the flow and insure the accurate calculations of the different phenomena. All results are verified against the single precision outputs of Heard [63]. Results are compared with Carter [62] on Figure 5.46 and with Lewis [64] on Figure 5.47. The obtained solution matches very well the wall pressure and skin friction coefficient of the numerical solution given in Carter [62]. However, the wall pressure calculated by the FDV solver at the $M_\infty = 4$ is higher than the measured pressure of Lewis [64]. This difference is believed to be due to the possible partial dissociation at high velocities.

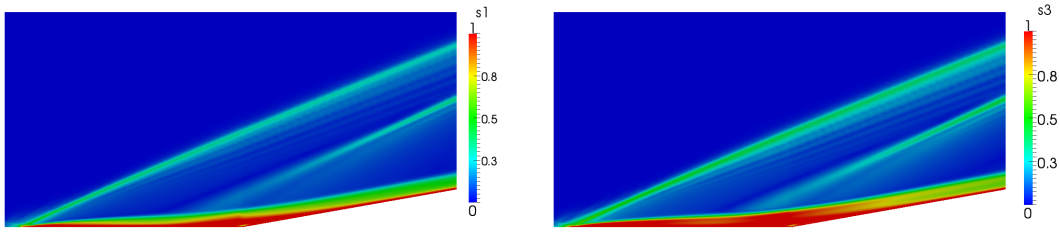

(a) (b)

Figure 5.43 FDV parameters for the 2D compression corner problem at $M_\infty = 3$.

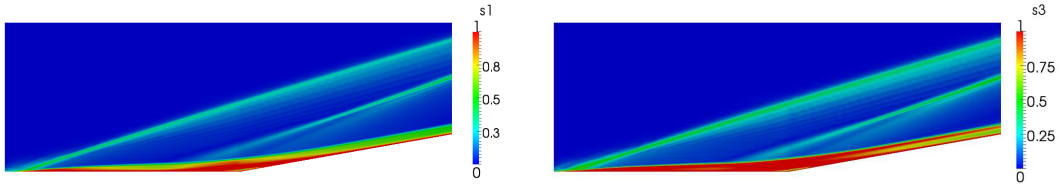

(a) (b)

Figure 5.44 FDV parameters for the 2D compression corner problem at $M_\infty = 4$.

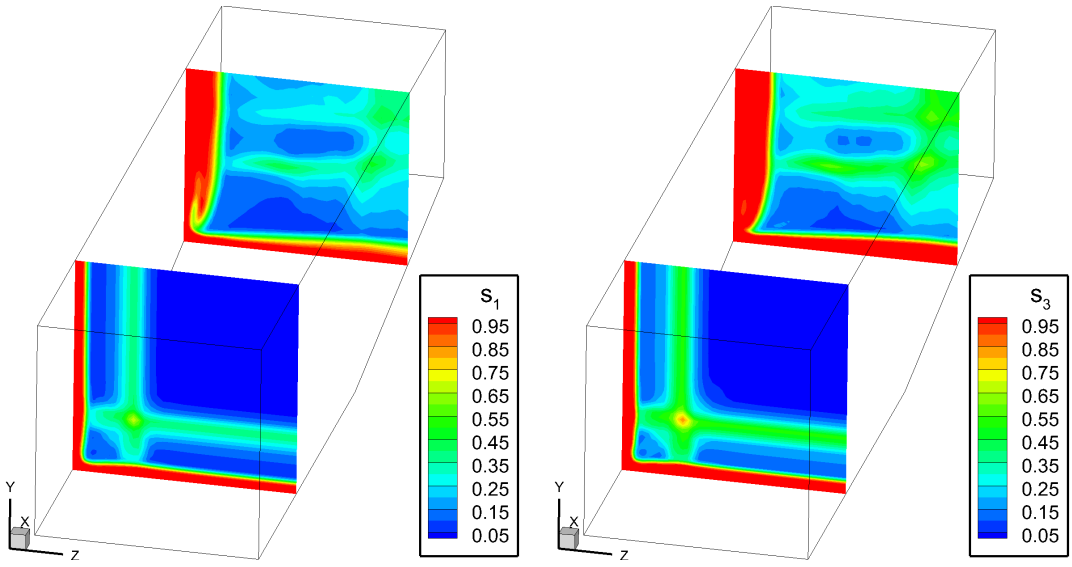

(a) (b)

Figure 5.45 FDV parameters for the 3D compression corner problem.

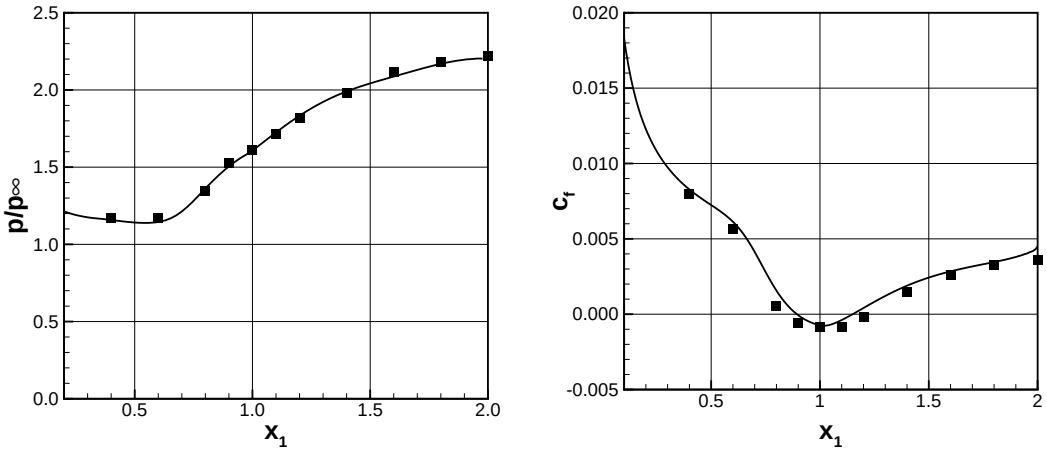

(a) (b)

Figure 5.46 Validation of the FDV results for the compression corner problem at $M_\infty = 3$. —— FDV and ■ Carter [62].

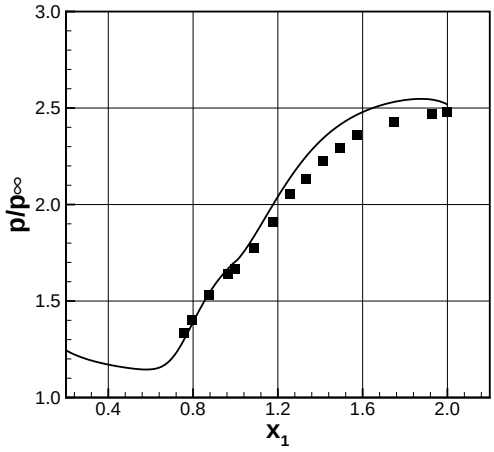

Figure 5.47 Validation of the FDV results for the compression corner problem at $M_\infty = 4$. —— FDV and ■ Lewis [64].

5.3 Plasma Dynamics Cases

Three test cases are selected to establish the FDV method's ability to accurately predict the physics of the one-fluid plasma dynamics in this section. These cases range in complexity from the non-linear exact solution for the ideal MHD equations of the smooth Alfvén wave discussed in Section 5.3.1 to shock wave and discontinuity governed physics of the MHD shock tube and the Orszag-Tang vortex flow investigated in Sections 5.3.2 and 5.3.3, respectively. The numerical setup details necessary for the reproduction of these test cases are summarized along with the relevant grid configurations. Analytical solutions, grid refinement, and published literature are used, whenever possible, to verify the developed FDV plasma dynamics solver.

5.3.1 Smooth Alfvén Wave

The non-linear circularly polarized smooth Alfvén wave is solved using the developed FDV solver and the ideal MHD equations discussed in Section 2.4. This problem is 2D and it is solved by a 3D solver using one-element-depth in the transverse, x_3, direction. Periodic boundary conditions are used along all faces to generate a self-repeating wave for verification purposes. The Alfvén wave propagation angle and distance are selected to be $\alpha = \pi/4$ and $L = 1.0$, respectively. This makes the length of the domain in the axial, L_1, and the lateral, L_2, directions to be

$$L_1 = \frac{L}{\cos\alpha} = \sqrt{2},$$

and

$$L_2 = \frac{L}{\sin\alpha} = \sqrt{2}.$$

The length of the domain in the transverse direction, L_3, is selected such that the generated hexahedral elements are all cubes.

The domain is initialized with the smooth Alfvén wave conditions given in Li and Xu [65]:

$$\rho = 1, \qquad u_{\parallel} = 0, \qquad u_{\perp} = 0.1\sin 2\pi\beta, \qquad u_3 = 0.1\cos 2\pi\beta,$$

$$p = 0.1, \qquad B_{\parallel} = 1, \qquad B_{\perp} = u_{\perp}, \qquad B_3 = u_3,$$

where $\beta = x_1\cos\alpha + x_2\sin\alpha$, and $\parallel$ and $\perp$ denote the parallel and the normal directions to the wave propagation angle, respectively. Figure 5.48 shows the Alfvén wave initial solution. The specific heat ratio is set to $\gamma = 5/3$, and the fluid free stream Mach number is chosen to be $M_\infty = 1/\sqrt{\gamma}$. The free stream magnetic Mach number is set to $M_\infty^m = 1.0$.

Table 5.6 Studied Alfvén wave cases.

ID	NE	$Order$	NN	NN for $x_1 - x_2$ face
1	$63^2 \times 1$	1	8,192	4,096
2	$21^2 \times 1$	3	16,384	4,096

Two cases are solved, Table 5.6, at constant time step, $\Delta t = 0.005s$, with the same number of nodes for the $x_1 - x_2$ face. These simulations are carried out to $t = 10s$ in order to quantify the numerical dissipation introduced by the FDV method

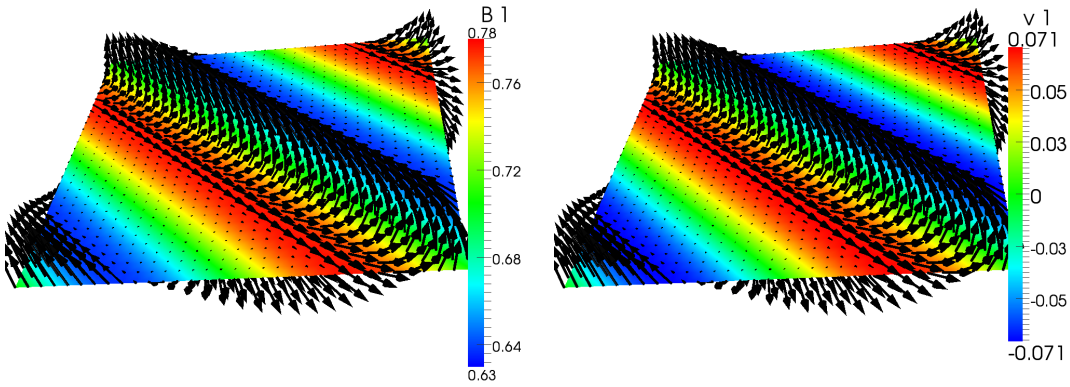

(a) (b)

Figure 5.48 Initial conditions of the Alfvén wave problem. (a) contours of B_1 and **J** vector field, and (b) contours of v_1 and **v** vector field.

to the Alfvén wave phenomena. Any differences found in the solution are expected to be a direct manifestation of the higher order shape function effect on the accuracy of the solver.

The axial component of the magnetic field, B_1, is shown on Figure 5.49(a) as an example of the other sinusoidal varying quantities. The FDV method is able to capture the propagation of the Alfvén wave in both cases. The waves are repeated every integer time step as expected analytically. The phase angles of all the different variables are preserved throughout the simulation.

The effect of the numerical dissipation is negligible for small durations as can be seen on Figure 5.49(b). The solution of the higher order case, Case 2, is showing a slightly superior performance to the linear case, Case 1, at later simulation times. This effect is important for long integration times.

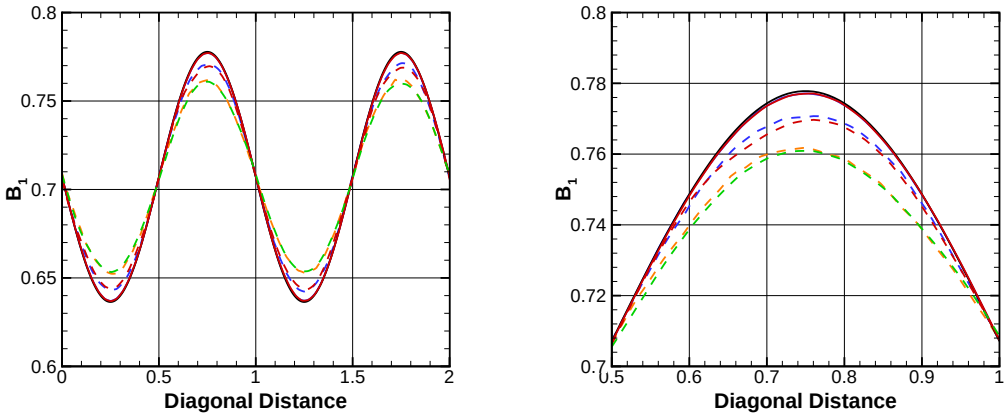

(a) (b)

Figure 5.49 The FDV method's solution of the Alfvén wave problem. —— initialization at $t = 0.0s$, —— Case 1 at $t = 1.0s$, —— Case 2 at $t = 1.0s$, - - - Case 1 at $t = 5.0s$, - - - Case 2 at $t = 5.0s$, - - - Case 1 at $t = 10.0s$, and - - - Case 2 at $t = 10.0s$.

5.3.2 Ideal MHD Shock Tube

The non-strictly hyperbolic system of equations of the ideal MHD makes the wave phenomena to be more complicated than the non-magnetic flows of the Euler equations. The simple Riemann problem of the shock tube is no exception. The analytical solution of such a problem does not exist, in general, and approximate solutions are the only tool [66, 67].

In order to obtain a solution valid in the 1D shock tube geometry given in Figure 5.26, the axial component of the magnetic field has to stay constant throughout the shock tube. The full 3D solver is used, and the number of elements in both the lateral, x_2, and the transverse, x_3, are set to one element. The effect of changing the number of elements in the axial direction, x_1, is studied. Periodic boundary conditions are used along all faces except the ones perpendicular to x_1. The solution along the faces perpendicular to x_1 are fixed to the left, L, and right, R, conditions.

The generated wave phenomena in the ideal 1D MHD shock tube problem depend on the initial conditions introduced in the domain [66]. In the most general case, the solution may exhibit as many as seven different waves; two fast shock waves or rarefaction waves, two slow shock waves or rarefaction waves, two rotational discontinuities, and one contact discontinuity.

Table 5.7 summarizes the left and right conditions for two different cases of the ideal 1D MHD shock tube. These two cases are selected to match the ones solved by Ryu and Jones [67]. Case 1 is a non-rotational problem, which is integrated to

Table 5.7 Studied MHD shock tube cases.

Property	Case 1		Case 2	
	L	R	L	R
ρ	1	1	1.08	1
p	20	1	0.95	1
v_1	10	-10	1.2	0
v_2	0	0	0.01	0
v_3	0	0	0.5	0
B_1	$\frac{5}{\sqrt{4\pi}}$	$\frac{5}{\sqrt{4\pi}}$	$\frac{2}{\sqrt{4\pi}}$	$\frac{2}{\sqrt{4\pi}}$
B_2	$\frac{5}{\sqrt{4\pi}}$	$\frac{5}{\sqrt{4\pi}}$	$\frac{3.6}{\sqrt{4\pi}}$	$\frac{4}{\sqrt{4\pi}}$
B_3	0	0	$\frac{2}{\sqrt{4\pi}}$	$\frac{2}{\sqrt{4\pi}}$

Table 5.8 MHD shock tube grids.

Grid	NE	dt
G1	$250 \times 1 \times 1$	4×10^{-5}
G2	$500 \times 1 \times 1$	2×10^{-5}
G3	$1000 \times 1 \times 1$	10^{-5}

$t = 0.08s$. Whereas Case 2 is a rotational problem, and it is integrated to $t = 0.2s$. Each of those cases is solved on the three different grids summarized in Table 5.8.

Case 1 should exhibit a pair of fast moving shocks in each direction, a contact discontinuity, a slow moving shock moving right, and a slow rarefaction wave moving left. On the other hand, Case 2 should show a pair of fast moving shocks in each direction, a pair of slow moving shocks in each direction, a pair of rotational discontinuities on each direction, and a contact discontinuity.

The results of Case 1 using G3 are compared to Ryu and Jones [67] on Figures 5.50, 5.51, and 5.52. The different nonlinear wave phenomena involved in this case is well captured by the developed FDV solver. The plasma pressure, shown on Figure 5.50(a), shows the presence of the Gibbs type errors near the two fast shocks without affecting the rest of the solution. The contact discontinuity is only visible in the plasma density shown on Figure 5.50(b). The axial magnetic field component, shown on Figure 5.51(b), stays constant as anticipated. Although Figure 5.51(a) shows the axial velocity component to only change due to the pair of the fast shocks, the pair of slow waves do have minor effects. The pair of fast waves, as well as the pair of the slow waves, are visible on the lateral, x_2, velocity and magnetic field components as shown on Figures 5.52(a) and 5.52(b), respectively.

The effect of increasing the number of elements in the axial, x_1 direction on the contact discontinuity is shown on Figure 5.53(a), and on the shock wave phenomena shown on Figure 5.53(b). As expected, the denser grids resulted in sharper singularities. The five different waves involved in this case are clearly visible in the response of the FDV parameter, s_1, shown on Figure 5.54.

Similar to Case 1, the results of Case 2 using G3 are compared to Ryu and Jones [67] on Figures 5.55, 5.56, 5.57, and 5.58. Again, the contact discontinuity is only visible in the plasma density, shown on Figure 5.55(b). The rest of the plasma properties show the effects of the two pairs of fast and slow shock waves, as well as, the two rotational discontinuities. Only the axial component of the magnetic field, B_1 remains constant throughout the shock tube as shown on Figure 5.56(b). High resolution grids make all the plasma flow singularities sharper as shown on Figure 5.59.

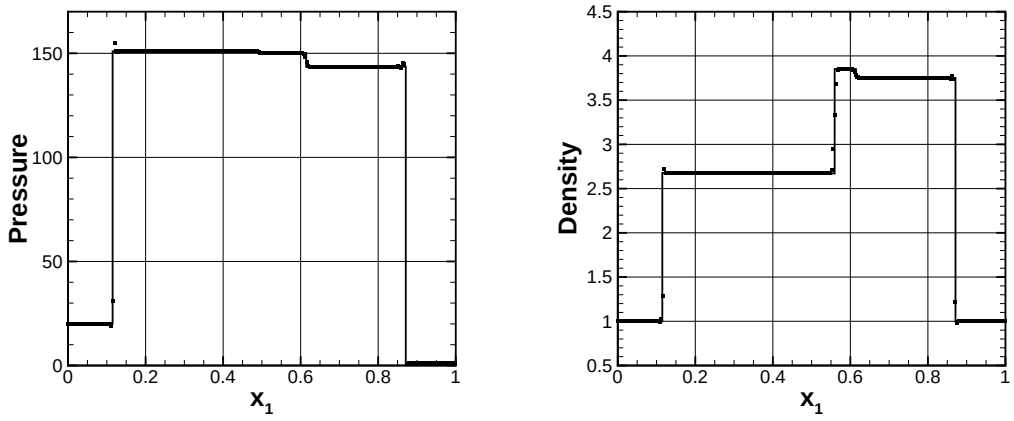

(a) (b)

Figure 5.50 The FDV method's solution of the non-rotational MHD shock tube case; pressure and density. —— Ryu et al. [67] and ■ FDV solution.

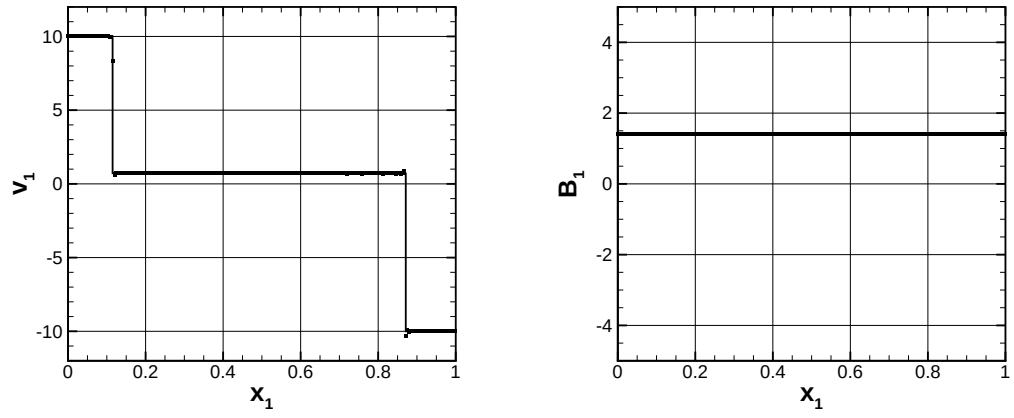

(a) (b)

Figure 5.51 The FDV method's solution of the non-rotational MHD shock tube case; axial velocity and magnetic field components. —— Ryu et al. [67] and ■ FDV solution.

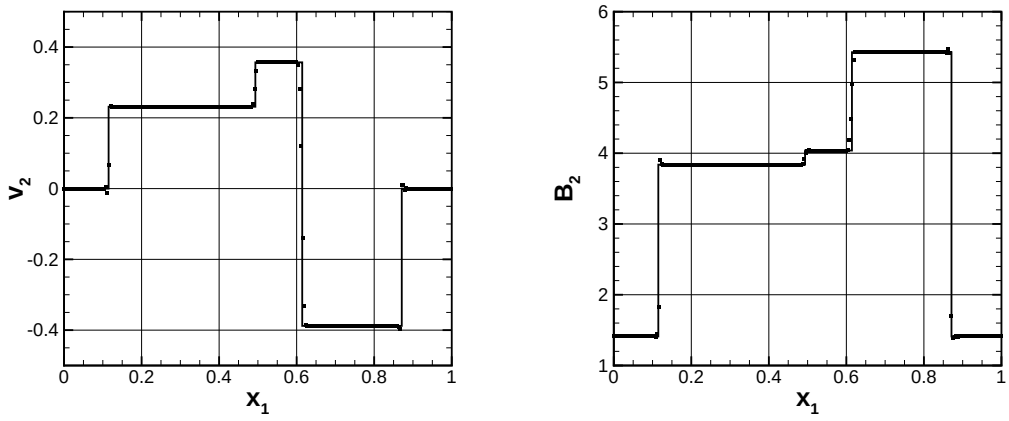

(a) (b)

Figure 5.52 The FDV method's solution of the non-rotational MHD shock tube case; lateral velocity and magnetic field components. — Ryu et al. [67] and ■ FDV solution.

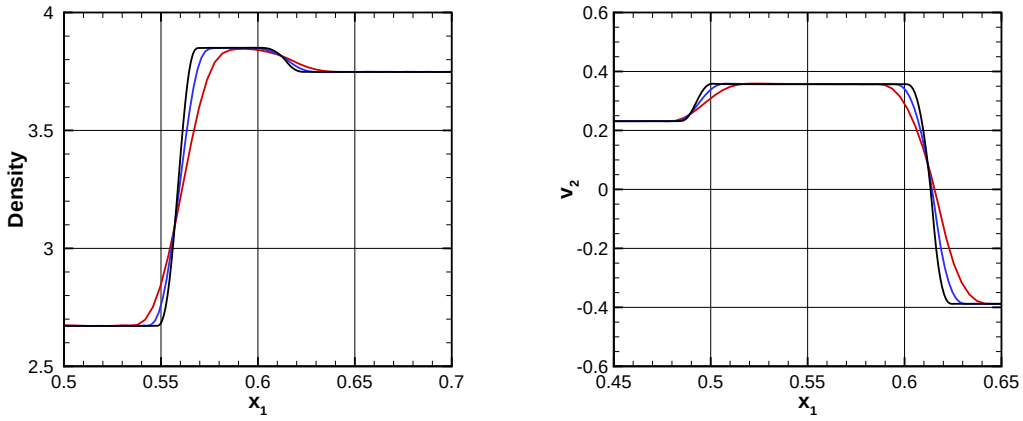

(a) (b)

Figure 5.53 The FDV method's solution of the non-rotational MHD shock tube case; grid resolution effects. — $NE = 250$, — $NE = 500$, and — $NE = 1000$.

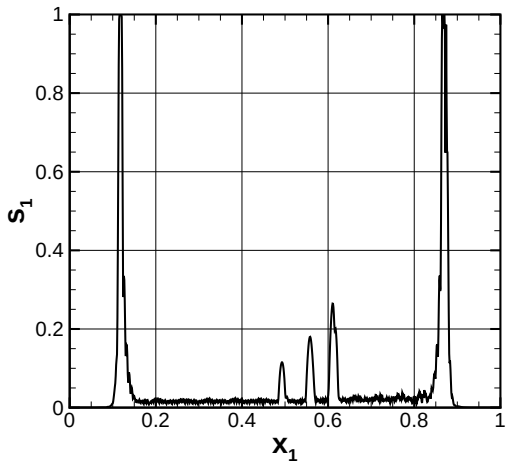

Figure 5.54 The FDV method's solution of the non-rotational MHD shock tube case; FDV parameter s_1.

The seven different waves involved in this case are clearly visible on the response of the FDV parameter, s_1, shown on Figure 5.60.

The developed FDV solver is able to capture all the physics involved in the two cases analyzed in this section. Increasing the grid resolution resulted in sharper singularities. The role of the FDV parameters established in the fluid dynamics cases is extended to plasma dynamics and its relevant wave phenomena; higher values of the FDV parameters are used near the different plasma flow singularities to maintain the solution stability and accuracy.

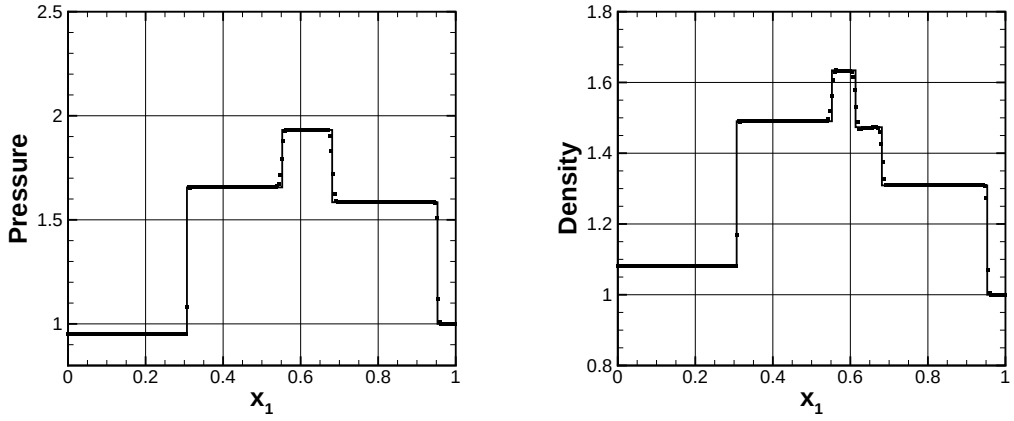

(a) (b)

Figure 5.55 The FDV method's solution of the rotational MHD shock tube case; plasma pressure and density. —— Ryu et al. [67] and ■ FDV solution.

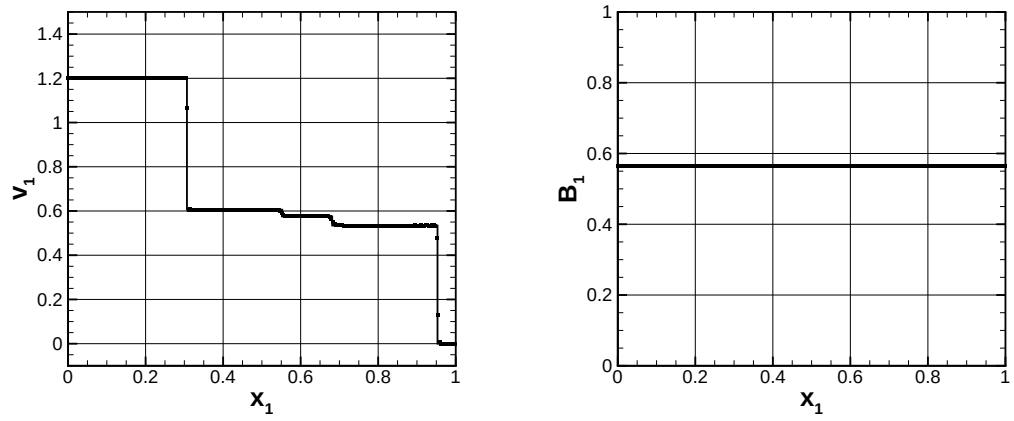

(a) (b)

Figure 5.56 The FDV method's solution of the rotational MHD shock tube case; axial velocity and magnetic field components. —— Ryu et al. [67] and ■ FDV solution.

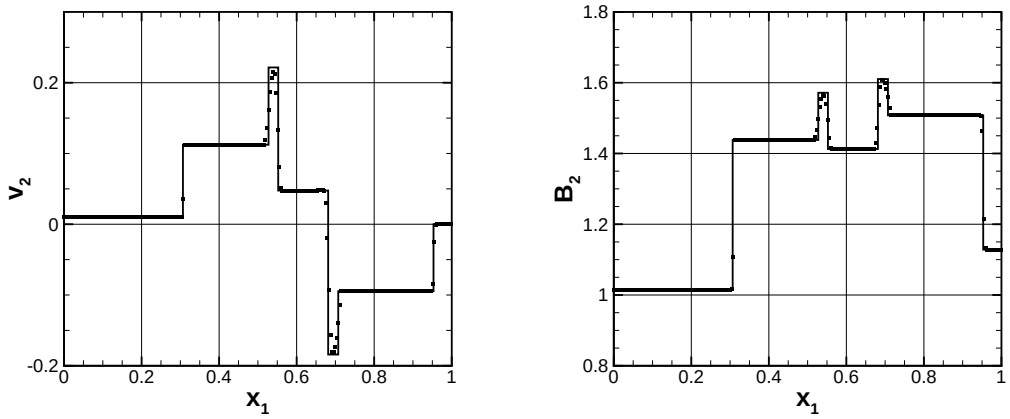

(a) (b)

Figure 5.57 The FDV method's solution of the rotational MHD shock tube case; lateral velocity and magnetic field components.

—— Ryu et al. [67] and ■ FDV solution.

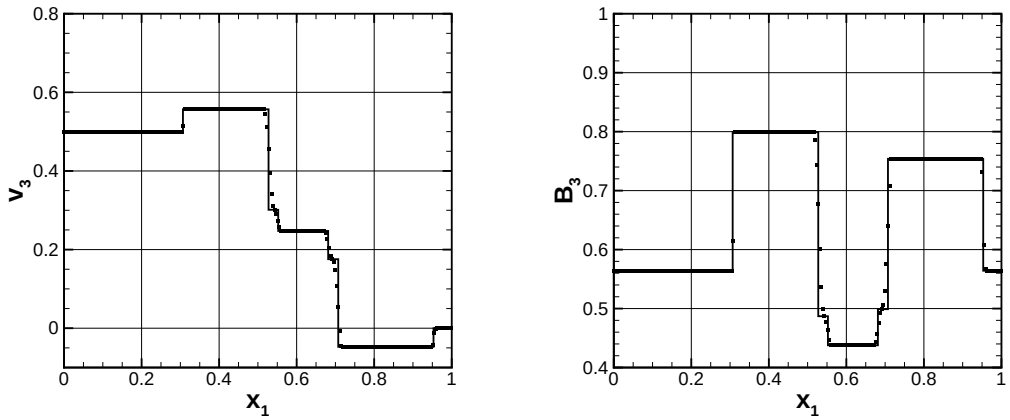

(a) (b)

Figure 5.58 The FDV method's solution of the rotational MHD shock tube case; transverse velocity and magnetic field components. —— Ryu et al. [67] and ■ FDV solution.

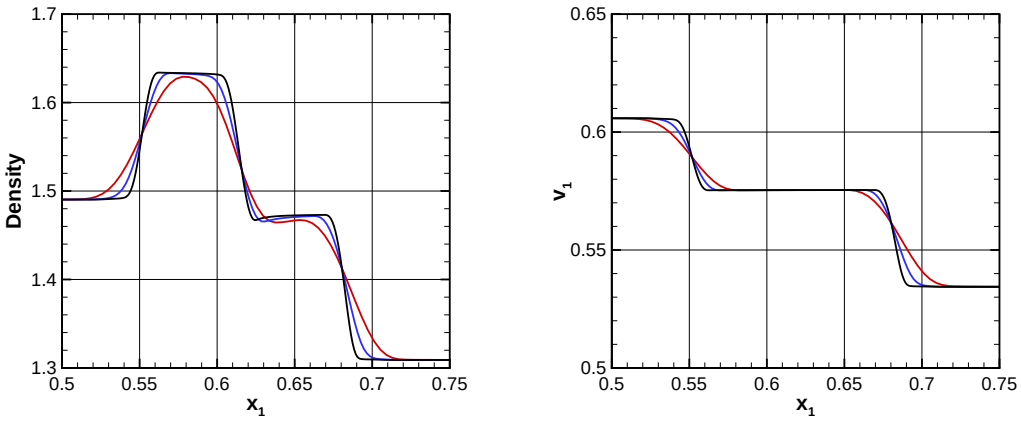

(a) (b)

Figure 5.59 The FDV method's solution of the rotational MHD shock tube case; grid resolution effects. — $NE = 250$, — $NE = 500$, and — $NE = 1000$.

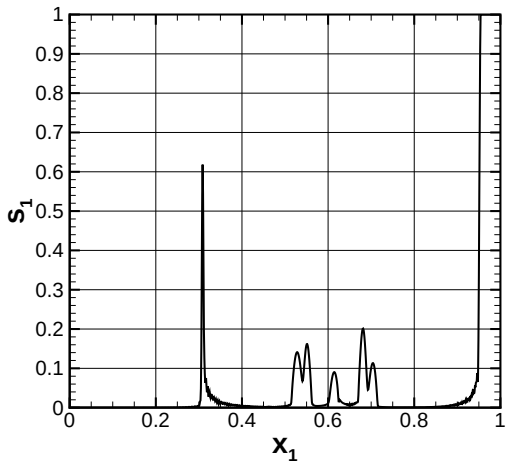

Figure 5.60 The FDV method's solution of the rotational MHD shock tube case; FDV parameter s_1.

5.3.3 Orszag-Tang Vortex

One of the most challenging test cases for any ideal MHD solver is the Orszag-Tang vortex problem. The numerical domain is a 2D square of 1.0 edge length and one-element-depth in the transverse, x_3, direction. The full 3D solver is used for this problem. Periodic boundary conditions are applied in all directions. The domain is initialized with constant density and pressure fields, and smooth sinusoidal velocity and magnetic fields as given in Li and Xu [65]:

$$\rho = \gamma^2, \qquad u_1 = -\sin 2\pi x_2, \qquad u_2 = \sin 2\pi x_1, \qquad u_3 = 0,$$

$$p = \gamma, \qquad B_1 = -\sin 2\pi x_2, \qquad B_2 = \sin 4\pi x_1, \qquad B_3 = 0,$$

where $\gamma = 5/3$ is used. The magnitudes of the initial velocity and magnetic fields are shown on Figure 5.61. The fluid free stream Mach number is chosen to be $M_\infty = 1/\sqrt{\gamma}$, and the free stream magnetic Mach number is set to $M_\infty^m = 1.0$. The domain is discretized with a uniformly distributed grid in both the axial, x_1, and the lateral, x_2, directions. The length of the domain in the transverse direction, x_3, is set to create cubical hexahedral elements.

Table 5.9 Studied Orszag-Tang vortex cases.

ID	NE	$Order$	NN	$\Delta t, s$
1	$128^2 \times 1$	1	33,282	10^{-3}
2	$256^2 \times 1$	1	132,098	5×10^{-4}

The interactions between the magnetic and the velocity fields intensify with time through wave phenomena. These interactions lead to generation of shock waves in both fields. The generated shock waves exist in both large and small scale structures. The newly generated structures, in turn, lead to yet finer structures. The highly non-linear solution, especially at later stages, is dependent on the grid resolution used and the inherent numerical dissipation introduced by the scheme. Table 5.9 summarizes the two cases used to investigate the FDV method's ability to simulate this complicated problem.

The initially constant density and pressure fields undergo dramatic changes as shown on Figures 5.62 and 5.63, respectively. The generated sharp shock waves are captured very well by the solution at earlier times as shown on Figures 5.62(a) and 5.63(a). The numerical dissipation effect is clear on Figures 5.62(b) and 5.63(b). If accurate solutions at later times are needed, the grid resolution has to be increased accordingly.

The generated shock structures are visible through the velocity field and the magnetic field, shown on Figure 5.64(a) and 5.64(b), respectively. The electric current, shown on Figure 5.65(a), has a clear effect on the variation of first order FDV parameter, s_1, shown on Figure 5.65(b). This leads to the conclusion that in the FDV selection for the critical phenomena to base stability upon, the magnetic field variation is chosen for the most part.

Figure 5.66 shows the effect of grid refinement on the axial component of the magnetic field, B_1, and a comparison between the obtained FDV solution and the solution of Waagan et al. [68] at $t = 0.5s$. The plot is along the lateral, x_2, axes at

$x_1 = 0.428$. The developed FDV solver is able to capture the physics involved in this complex problem.

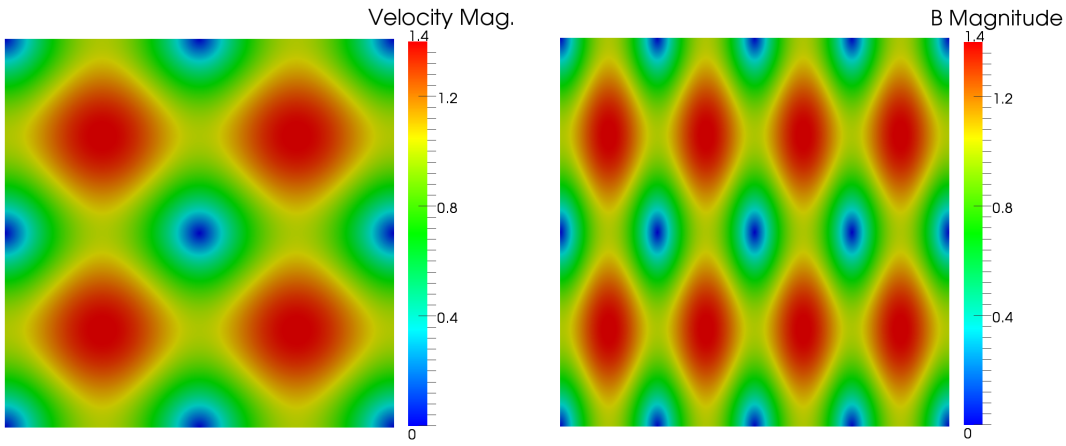

(a) (b)

Figure 5.61 Initial conditions of the Orszag-Tang problem.

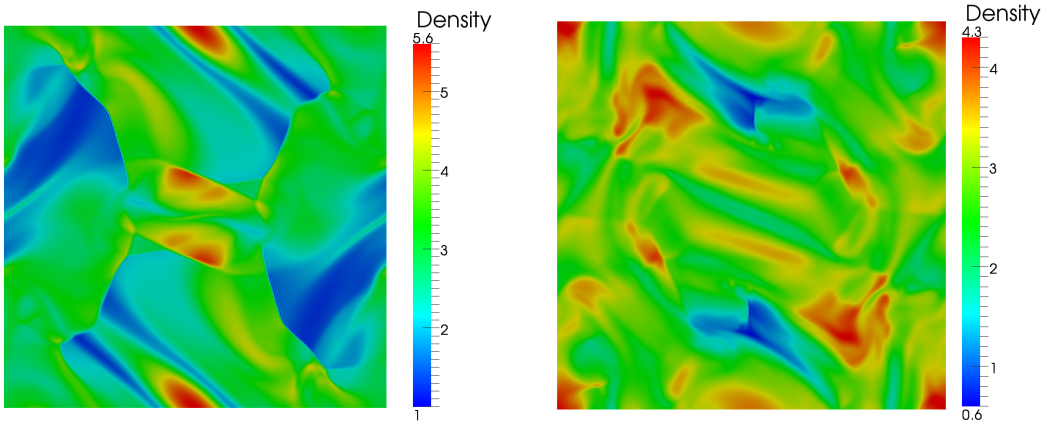

(a) $t = 0.5s$ (b) $t = 1.0s$

Figure 5.62 The FDV method's solution of the Orszag-Tang problem; plasma density contours.

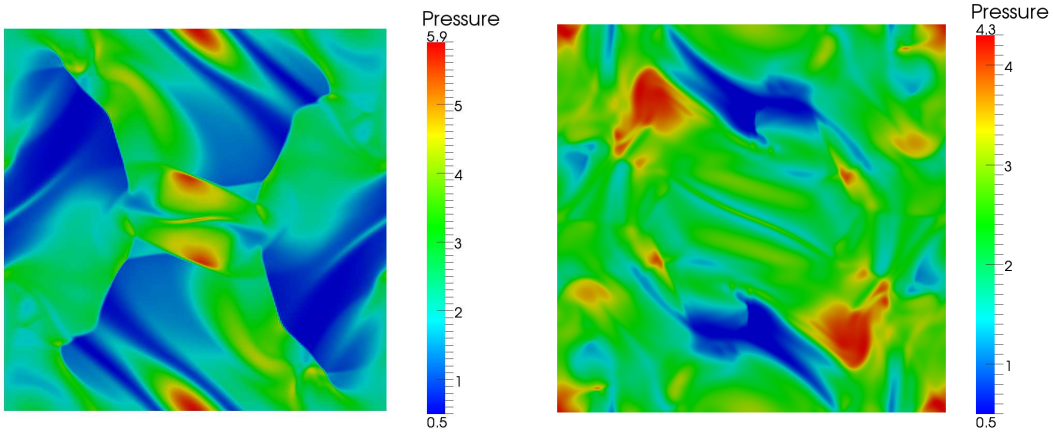

(a) $t = 0.5s$ (b) $t = 1.0s$

Figure 5.63 The FDV method's solution of the Orszag-Tang problem; plasma pressure contours.

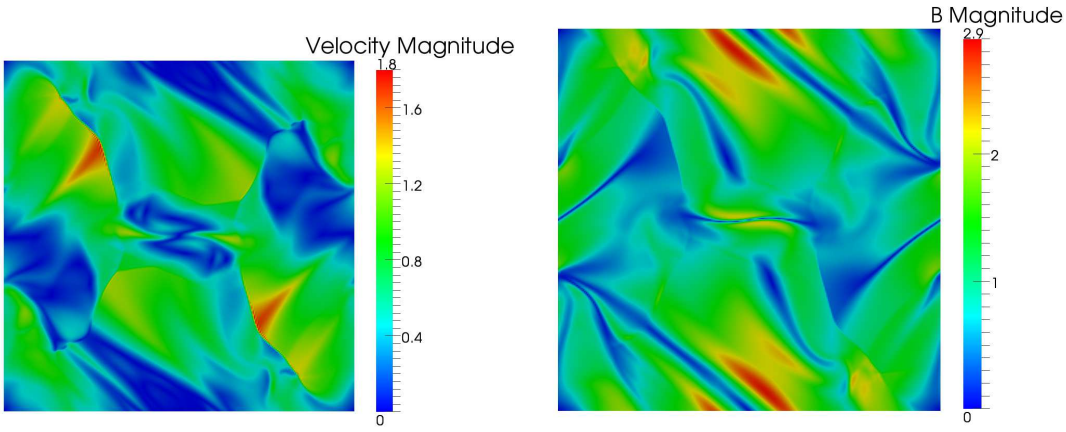

(a) (b)

Figure 5.64 The FDV method's solution of the Orszag-Tang problem at $t = 0.5s$; velocity field and magnetic field contours.

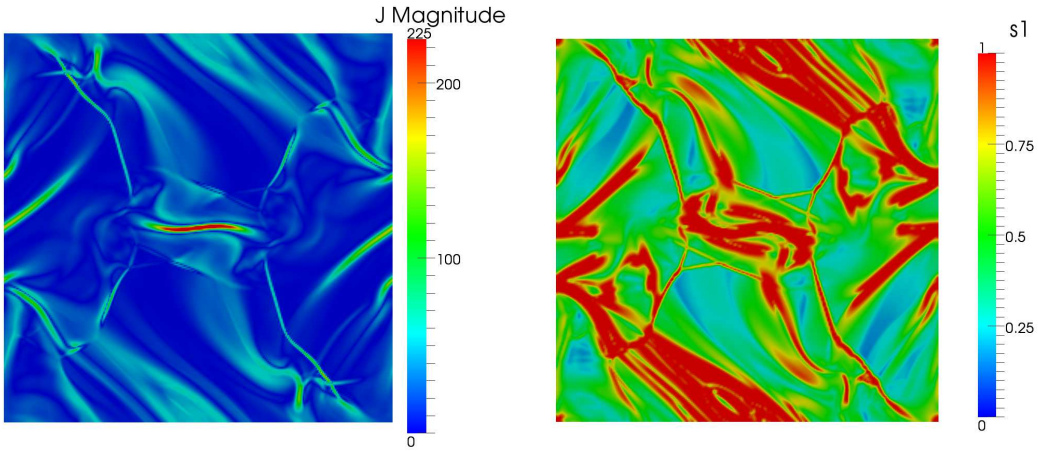

(a) (b)

Figure 5.65 The FDV method's solution of the Orszag-Tang problem at $t = 0.5s$; electric current and s_1 contours.

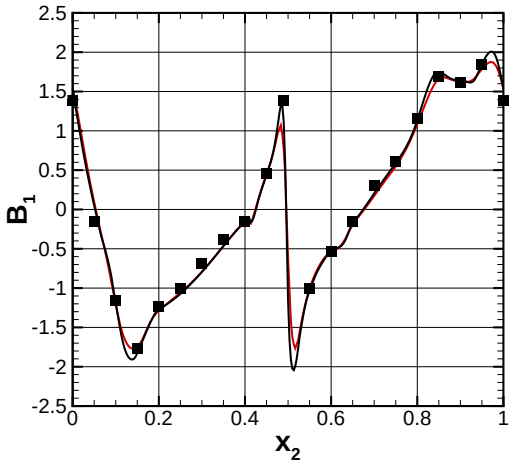

Figure 5.66 Comparison of the FDV method's solution of the Orszag-Tang vortex problem $t = 0.5s$ and $x_1 = 0.428$. — Case 1, — Case 2, and ■ Waagan et al. [68].

CHAPTER 6

ISOTROPIC AND ANISOTROPIC FREELY DECAYING TURBULENCE

The problem of homogeneous, isotropic, freely decaying turbulence is a fundamental problem for verifying any numerical scheme in turbulent flow simulations. In isotropic turbulence, the flow is free of all complexities such as shock waves, wall effects, and inhomogeneous boundary conditions. This makes isotropic turbulence particularly suitable for investigating the ability of FDV in simulating flow turbulence.

The focus of this dissertation is to study the effects of an imposed background magnetic field of constant intensity on an initially isotropic turbulent velocity field. Such a scenario is representative of one-fluid plasma dynamics simulations. The interactions between the applied magnetic field and the turbulent velocity field offer a great deal of insight into the inherent non-linearity of this problem.

For all cases considered in this chapter, the flow domain is initialized with a divergence-free random velocity field and constant density and temperature fields. A turbulent kinetic energy spectrum is imposed on the velocity field, and the turbulence intensity is a problem input. For the anisotropic cases, the magnetic field is initialized

to be of constant strength, B_0, directed along the axial, x_1, direction. The simulation domain is a periodic cubic box of size 2π.

The 3D velocity field is initialized to be a random velocity field in the physical space and is then transformed to the spectral space to enforce the divergence-free condition along with an initial power spectrum profile. The resulting velocity field is then transformed from the spectral space back to the physical space. The initial power spectrum, $E(\kappa)$, was set to the form given in Samtaney et al. [69]:

$$E(\kappa) = A\,\kappa^4\,\exp\left(-2\kappa^2/\kappa_0^2\right), \tag{6.1}$$

where κ is the wave number, κ_0 is the wave number at which the energy spectrum peaks, and A is a constant to control the initial turbulent kinetic energy.

This chapter is organized as follows. The flow statistics necessary for the analysis of both the isotropic and the anisotropic freely decaying turbulence are introduced in Section 6.1, along with a brief description of their physical meanings. Section 6.2 gives a quantitative analysis of the numerical dissipation and dispersion errors inherent to the numerical discretization scheme. Finally, Sections 6.3 and 6.4 introduce the numerical simulations of the isotropic and anisotropic flow problems, respectively, using the developed FDV code.

6.1 Flow Statistics

The problems of freely decaying isotropic and anisotropic turbulence are initialized with a physical divergence-free random velocity field of zero field average.

This simplifies the calculation of the velocity field statistics. The root-mean-square ($r.m.s.$) component of the fluctuating velocity field is defined by

$$v'^2 = \frac{1}{3}\left\langle v_1^2 + v_2^2 + v_3^2 \right\rangle, \tag{6.2}$$

where $\langle \cdots \rangle$ is an instantaneous volume average obtained by integrating over all the elements and the prime notation is used to identify the $r.m.s.$ quantities. The turbulent kinetic energy, TKE, and the viscous dissipation, ϵ, are given by

$$TKE = \frac{3}{2}v'^2, \tag{6.3}$$

and

$$\epsilon = \left\langle \frac{\tau_{ij}}{\rho}\frac{\partial v_i}{\partial x_j} \right\rangle, \tag{6.4}$$

respectively.

Similarly, the $r.m.s.$ fluctuating magnetic field is given by

$$b'^2 = \frac{1}{3}\left\langle (b_1 - B_0)^2 + b_2^2 + b_3^2 \right\rangle, \tag{6.5}$$

where B_0 is the initial magnetic field in the axial, x_1, direction. The turbulent magnetic energy, TME, is given by

$$TME = \frac{3}{2}b'^2. \tag{6.6}$$

The Taylor micro-scale, λ, and its Reynolds number, Re_λ, are defined by

$$\lambda^2 = \frac{3v'^2}{\left\langle \left(\frac{\partial v_1}{\partial x_1}\right)^2 + \left(\frac{\partial v_2}{\partial x_2}\right)^2 + \left(\frac{\partial v_3}{\partial x_3}\right)^2 \right\rangle}, \tag{6.7}$$

and

$$Re_\lambda = \frac{v'\lambda \langle \rho \rangle}{\langle \mu \rangle}, \tag{6.8}$$

respectively. The Kolmogorov micro-scale, η, and the longitudinal integral length scale, L_f, are given by

$$\eta = \frac{\langle \mu/\rho \rangle^{3/4}}{\epsilon^{1/4}}, \tag{6.9}$$

and

$$L_f = \frac{\pi}{2v'^2} \int_0^\infty E(\kappa)\, d\kappa, \tag{6.10}$$

respectively. The turbulent Mach number, M_t, is given by

$$M_t = \sqrt{3}\frac{v'}{\langle a \rangle}, \tag{6.11}$$

where a is the speed of sound.

The vorticity field enstrophy, Ω_v, and the velocity field helicity, H_v, are defined by

$$\Omega_v = \frac{1}{2} \int \omega_i \omega_i \, d^3x, \tag{6.12}$$

and

$$H_v = \int v_i \omega_i \, d^3x, \tag{6.13}$$

respectively, where ω_i is the flow vorticity given by

$$\omega_i = \epsilon_{ijk} v_{k,j}. \tag{6.14}$$

The magnetic enstrophy, Ω_m, and the modified magnetic helicity, H_m, are defined by

$$\Omega_m = \frac{1}{2\mu_0^m} \int \epsilon_{ijk}\epsilon_{imn}\, B_{k,j} B_{n,m}\, d^3x, \tag{6.15}$$

and

$$H_m = \int \epsilon_{ijk} B_i B_{k,j}\, d^3x, \tag{6.16}$$

respectively. The cross magnetic helicity, H_{vm}, is given by

$$H_{vm} = \int v_i B_i\, d^3x. \tag{6.17}$$

Another important interaction quantity between the magnetic field and the velocity field is the Lorentz work, W_L, given by

$$W_L = \int \epsilon_{ijk}\, v_i J_j B_k\, d^3x, \tag{6.18}$$

where the Lorentz force is defined in Equation (2.7).

The Q-criterion, Q, used to visualize the coherent turbulent flow structures is given by

$$Q = \frac{1}{2}\left(R_{ij}R_{ij} - S_{ij}S_{ij}\right), \tag{6.19}$$

where R_{ij} is the velocity rotation tensor given by

$$R_{ij} = \frac{1}{2}\left(\frac{\partial v_i}{\partial x_j} - \frac{\partial v_j}{\partial x_i}\right). \tag{6.20}$$

A normalized time scale, t', is defined by

$$t' = \frac{\epsilon_0 t}{TKE_0}, \tag{6.21}$$

where the subscript 0 denotes the initial conditions at $t = 0$.

6.2 Quantification of Numerical Errors

Application of numerical schemes such as the FEM, FDM, and FVM to solve non-linear partial differential equations results in solutions that deviate from the exact solution. These deviations, called numerical errors, can be broadly classified into the dissipative and dispersive errors [31, 52, 70]. In Chapter 5, the Method of Manufactured Solutions (MMS) was used to quantify the deviation of the numerical solution from an exact manufactured solution. However, in that analysis, the numerical errors were not specifically split into the dissipative and dispersive errors. The classification of numerical errors into the the dissipative and dispersive errors and their quantification are presented in this chapter.

To quantify dispersion errors, the Lagrange polynomial shape functions are used in conjunction with the Fourier transform of the first-order spatial derivative in Section 6.2.1. The dissipation errors are quantified in Section 6.2.2 through numerical

simulations of the inviscid isotropic turbulence using the Euler equations discussed in Section 2.4.

6.2.1 Dispersion Errors

Dispersion error analysis of the FEMs is not straightforward due to the inter-element connectivity of the shape functions. The principal difficulty is that the spatial differencing stencil is difficult to extract from the FEM system matrix, unlike FDM and FVM. The formal procedure of the dispersion error quantification in FEM is outlined in Thompson and Pinsky [71]. In this method, a model wave equation is employed and its solution is obtained by imposing a wave-rich solution. The resulting FEM approximation is tested for any missing wave numbers. The accuracy of the solution is measured by the wave number at which the solution starts deteriorating.

In the FDM literature, the dispersion errors are quantified by applying Fourier transform of the spatial differencing stencils as discussed in Tam and Webb [60]. In this technique, the first-order spatial derivative can be used for error quantification purposes. Consider the general spatial differencing stencil of the first order derivative of a 1D function $\psi(x)$ at the i^{th} node on a uniform grid, which can be written as

$$\left(\frac{\partial \psi(x)}{\partial x}\right)_i \simeq \frac{1}{\Delta x} \sum_{j=-N}^{M} a_j \psi_{i+j}, \tag{6.22}$$

where x is the continuous 1D coordinate, Δx is the uniform grid spacing, a_j is the difference scheme stencil, and M and N are the number of values of ψ to the right and the left of node i, respectively. Writing Equation (6.22) in terms of the continuous

coordinate x we get

$$\frac{\partial \psi(x)}{\partial x} \simeq \frac{1}{\Delta x} \sum_{j=-N}^{M} a_j \psi(x + j\Delta x). \tag{6.23}$$

The Fourier transform of any general 1D function $\psi(x)$ is given by

$$\tilde{\psi}(\alpha) = \frac{1}{2\pi} \int_{-\infty}^{\infty} \psi(x) e^{(-\imath\alpha x)} dx, \tag{6.24}$$

where α is the wave number. Following the same procedure outlined in Tam and Webb [60], the Fourier transform of Equation (6.23) becomes

$$\imath\alpha\tilde{\psi} \simeq \left(\frac{1}{\Delta x} \sum_{j=-N}^{M} a_j e^{\imath\alpha j \Delta x} \right) \tilde{\psi}. \tag{6.25}$$

Comparing the two sides, the effective wave number, $\tilde{\alpha}$, from the approximate derivative stencil becomes

$$\tilde{\alpha} = \frac{-\imath}{\Delta x} \sum_{j=-N}^{M} a_j e^{\imath\alpha j \Delta x}, \tag{6.26}$$

where $\Delta x\tilde{\alpha}$ becomes a periodic complex function of $\Delta x\alpha$ with a period of 2π. The special case of $N = M$ makes $\Delta x\tilde{\alpha}$ a real function.

Equation (6.26) can be written in the FEM context by substituting the difference stencil, a_j, by the derivatives of the shape functions in the natural element coordinates:

$$\tilde{\alpha} = \frac{-2\imath}{p} \sum_{j=1}^{p+1} \frac{\partial L_j^p}{\partial x} e^{\imath\alpha x_j}, \tag{6.27}$$

where p is the Lagrange polynomial order, $-1 \leq x \leq 1$ is the natural element coordinate, and L_j^p is the p^{th} order Lagrange polynomial shape function introduced in

Appendix B. Odd order shape functions contain even number of nodes resulting in complex $\tilde{\alpha}$ at all the element nodes. To arrive at real values of $\tilde{\alpha}$, only even order shape functions are considered. The mid-nodes of an element are tested for their $\tilde{\alpha}$ characteristics.

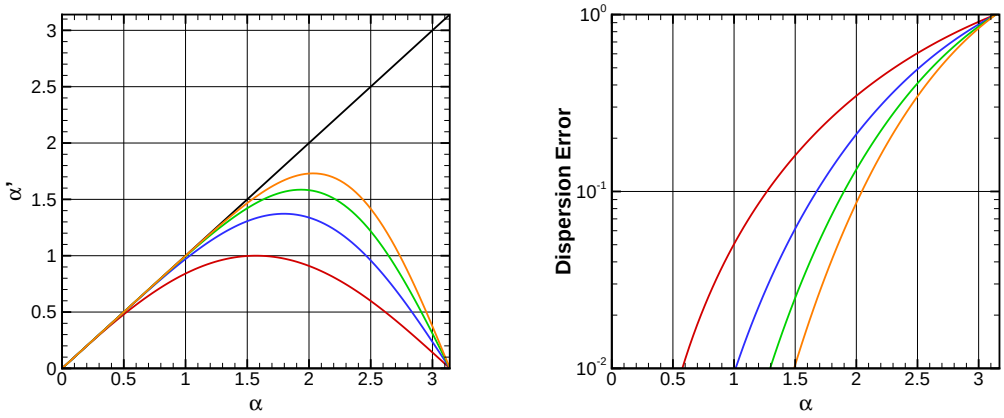

(a) (b)

Figure 6.1 Quantification of the dispersion errors introduced by the Lagrange polynomials family of elements. — optimal, — $p = 2$, — $p = 4$, — $p = 6$, — $p = 8$.

Figure 6.1(a) shows a systematic improvement in the effective wave number of the FEM scheme with an increase in the order of the Lagrange polynomial shape functions. The deviation of the effective wave number, $\tilde{\alpha}$, from the exact wave number is delayed as the polynomial order, p, increases. Figure 6.1(b) shows the dispersion error, defined as the deviation from the optimal response, $\tilde{\alpha} = \alpha$. Taking 2% to be the error limit, the second-order Lagrange polynomial, for example, shows a cut-off at $\tilde{\alpha}|_{2\%} = 0.72$. This means that this polynomial order can resolve wave lengths of $\lambda|_{2\%} \geq 8.7$, *i.e.* about one quarter of a wave within the element length. Table 6.1

summarizes the results of the Lagrange polynomial family of shape functions for 2% cut-off error.

Table 6.1 Details of the dispersion error analysis for 2% cut-off error limit.

p	$\tilde{\alpha}\|_{2\%}$	$\lambda\|_{2\%}$	NE per wave length
2	0.72	8.7	4.35
4	1.16	5.4	2.7
6	1.43	4.4	2.2
8	1.63	3.9	1.95

6.2.2 Dissipation Errors

In order to quantify the turbulent kinetic energy dissipated due to the dissipation error, several simulations were carried out for the inviscid isotropic turbulence problem using the Euler equations. Since the Euler equations are inviscid, any loss in the turbulent kinetic energy will be due to the numerical dissipation error inherent to the FDV method.

Table 6.2 summarizes the details of the five cases under consideration. These cases were selected to investigate the effects on the solution of the shape function order, p, the time step size, Δt, and the FDV parameter, s_1. All the cases were initialized with an *r.m.s.* fluctuating velocity of unity, *i.e.* $v_0' = 1$, and the number of grid nodes is held constant at 64^3. Ideally, in the absence of dissipative errors, the fluctuating *r.m.s.* velocity should remain constant during the simulation. The actual dissipation error of the FDV scheme is measured by the deviation from this optimal scenario.

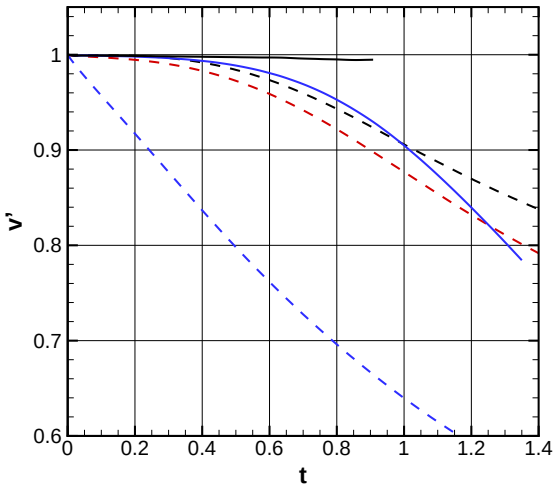

Figure 6.2 Effect of the numerical dissipation from the FDV method on the turbulent velocity fluctuation. --- Case 1, — Case 2, --- Case 3, --- Case 4, and — Case 5.

Table 6.2 Details of the dissipation error analysis cases.

ID	NE	Order	NN	s_1	Δt
1	63^3	1	64^3	0	10^{-3}
2	63^3	1	64^3	0	10^{-4}
3	21^3	3	64^3	0	10^{-3}
4	21^3	3	64^3	FDV	10^{-3}
5	21^3	3	64^3	0	10^{-4}

Figure 6.2 shows the time evolution of the *r.m.s.* fluctuating velocity, v', for these cases. From Figure 6.2, the lower order cases 1 and 2 show greater numerical dissipation compared to the the higher order cases 3 and 5. This establishes the need for higher order solutions in turbulent flow problems using the FDV method. For a given spatial discretization, *i.e.* for a given number of elements and polynomial order, the role of time step, Δt, can be crucial. The important role that the time step plays in the FDV formulation can be seen by comparing cases 1 and 2, and cases 3 and 5,

respectively. It is evident that a higher time step results in higher dissipation errors. The differences between cases 3 and 4 illustrate the role of the FDV parameter, s_1. It is clear that the parameter s_1 plays a dissipative role, as intended in the original FDV method. However, the dissipation error introduced by s_1 is much smaller than that introduced by either the lower order shape functions or the larger time step.

6.3 Freely Decaying Isotropic Turbulence

Table 6.3 Details of the freely decaying isotropic turbulence cases.

ID	NE	Order	NN	n	Re_λ	Δt
1	63^3	1	262,144	1,250,235	50	10^{-4}
2	63^3	1	262,144	1,250,235	100	10^{-4}
3	127^3	1	2,097,152	10,241,915	50	10^{-3}
4	31^3	2	128,000	595,820	50	10^{-3}
5	31^3	3	223,232	1,042,685	50	10^{-3}

For all the cases indicated in Table 6.3, the energy spectrum given by Equation (6.1) is used to initialize the isotropic turbulence with $\kappa_0 = 8$, $A = 0.00013$. This energy spectrum is applied in the wave number range $4 \leq \kappa \leq 8$ and the initial turbulent Mach number $M_t = 0.018$. The cases in Table 6.3 were chosen to study the effects of varying the Taylor micro-scale Reynolds number, Re_λ, and the polynomial order of the shape functions. The FDV-based full Navier-Stokes equations solver is employed to carry out the computations.

Figure 6.3 shows the time evolution of the energy spectrum at different time instances during the simulation. The turbulent kinetic energy, originally initialized between wave numbers 4 and 8, has now been distributed to the whole wave number spectrum. With increasing time, the energy spectrum is progressively dissipated. At both Re_λ of 50 and 100, the $\kappa^{-5/3}$ dependence of the energy spectrum in the inertia subrange is evident.

The flow field statistics, shown in Figure 6.4, exhibit trends consistent with the problem of decaying isotropic turbulence. The turbulent kinetic energy decreases

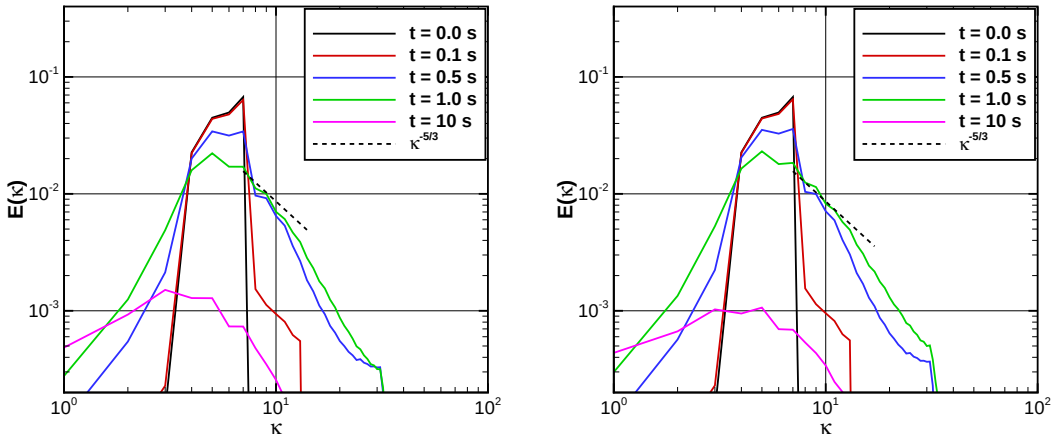

(a) (b)

Figure 6.3 Time evolution of the energy spectrum for different Taylor micro-scale Reynolds number. (a) Case 1 with $Re_\lambda = 50$ and (b) Case 2 with $Re_\lambda = 100$.

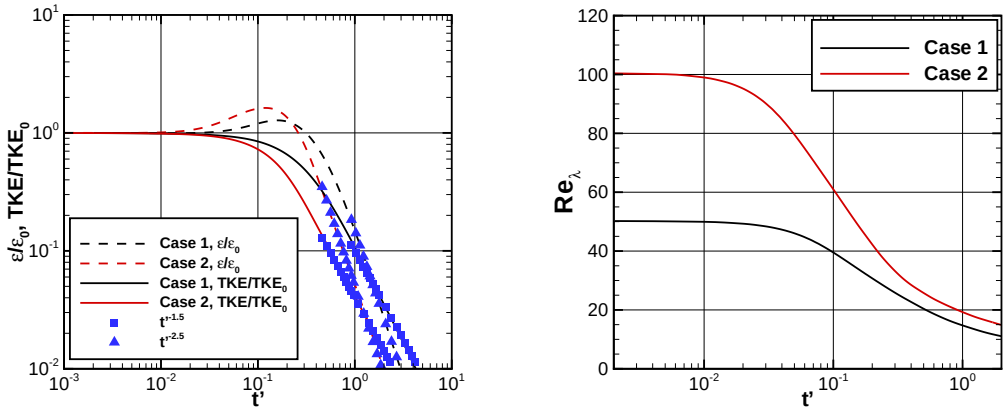

(a) (b)

Figure 6.4 Comparison between Cases 1 and 2 statistics evolution with time. (a) turbulence kinetic energy and viscous dissipation and (b) Taylor micro-scale Reynolds number, Re_λ.

monotonically with time, while the dissipation rate increases initially and then decays monotonically as shown on Figure 6.4(a). Theoretically, the kinetic energy decay should be $\sim t'^{-n}$, whereas the dissipation rate decay should follow $\sim t'^{-(n+1)}$ [72]. It was indeed observed that for both of the cases studied $n \approx 1.5$. Figure 6.4(b) shows that Re_λ decreases monotonically with time. The peak in the dissipation rate in Figure 6.4(a) and the minimum in the Kolmogorov length scale in Figures 6.5(a) are both due to the initial distribution of the turbulent kinetic energy from the pre-specified range, $4 \leq \kappa \leq 8$, to the higher wave numbers. The initial increase in the dissipation rate is accompanied by an initial decrease in both Kolmogorov micro-scale, η, and the longitudinal integral length scale, L_f. Subsequent to the distribution of energy across the entire wave number spectrum, the dissipation rate decays monotonically, which is accompanied by a monotonic increase in both η and L_f. The monotonic increase for the length scales coincides with the monotonic decrease of the dissipation. The higher Reynolds number case experiences quicker dissipation of turbulent kinetic energy due to the increased integral length scale L_f (note that the dissipation rate $\epsilon \sim v'^3/L_f$). It is to be noted that the Kolmogorov length scale *eta* is related to the dissipation rate through $\eta = (\nu^3/\epsilon)^{1/4}$, which explains the minimum in η when there is a maximum in ϵ.

The turbulent structures, shown in Figure 6.6, indicate that Case 2 ($Re_\lambda = 100$) has a broader range of turbulent length scales when compared to Case 1 ($Re_\lambda = 50$). The temporal evolution of the turbulent structures for case 3 is shown in Figure 6.7. It is clear from Figure 6.7(a) that at time $t = 0$ there is only a limited number of length scales as determined by the wave number range in which the energy spec-

trum was initialized. The distribution of energy from the initial wave number range to the entire wave number spectrum results in an increased range of length scales, as seen in Figure 6.7(b). However, with further progress in time, there is a decay in turbulent kinetic energy, which is manifested as the reduced number of turbulent length scales at time $t = 10.0s$ in Figure 6.7(c).

The effects of the higher order elements on the turbulent kinetic energy dissipation rate are shown on Figure 6.8(a). The cubic grid of Case 5 seems to have more effective wave numbers than Cases 3 and 4. In fact, the cubic grid of Case 5 precedes Case 3 which has ten times higher number of nodes, Table 6.3. That is the higher peak of Case 5 indicates the spread of the turbulent energy into more wave numbers than those of the other cases. Case 4 with the 31^3 quadratic elements grid seems to have about the same effective wave numbers span as Case 3 with the 127^3 linear elements grid. Remarkably, however, Figure 6.8(b) shows that the *r.m.s.* fluctuating velocity v' is nearly the same for all three cases 3, 4 and 5.

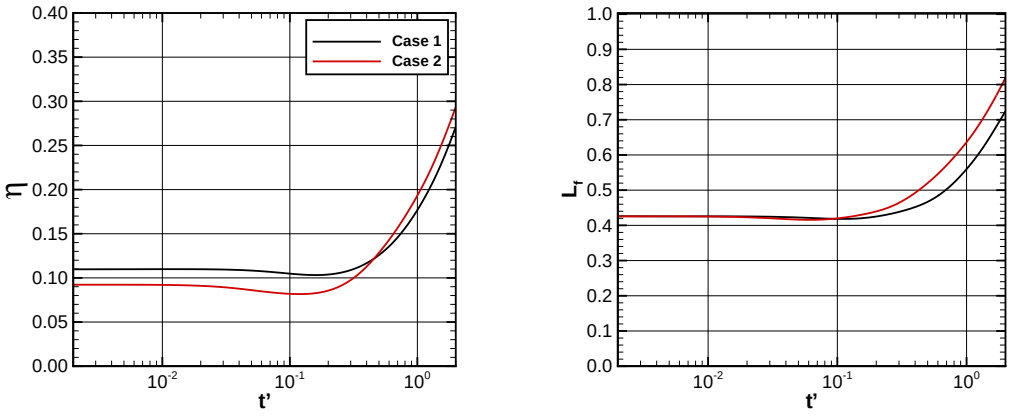

(a) (b)

Figure 6.5 Higher Reynolds number effect on length scales statistics. (a) Kolmogorov length scale, η, and (b) longitudinal length scale, L_f.

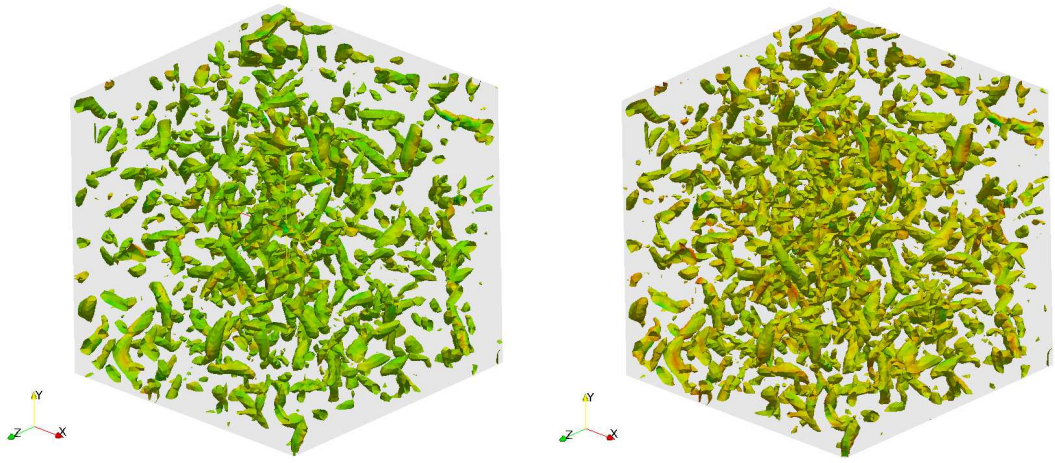

(a) (b)

Figure 6.6 Higher Reynolds number effect on turbulent flow structures visualized at $t = 1.0s$ by the Q-criterion iso-surfaces and colored by the vorticity magnitude. (a) Case 1 with $Re_\lambda = 50$ and (b) Case 2 with $Re_\lambda = 100$.

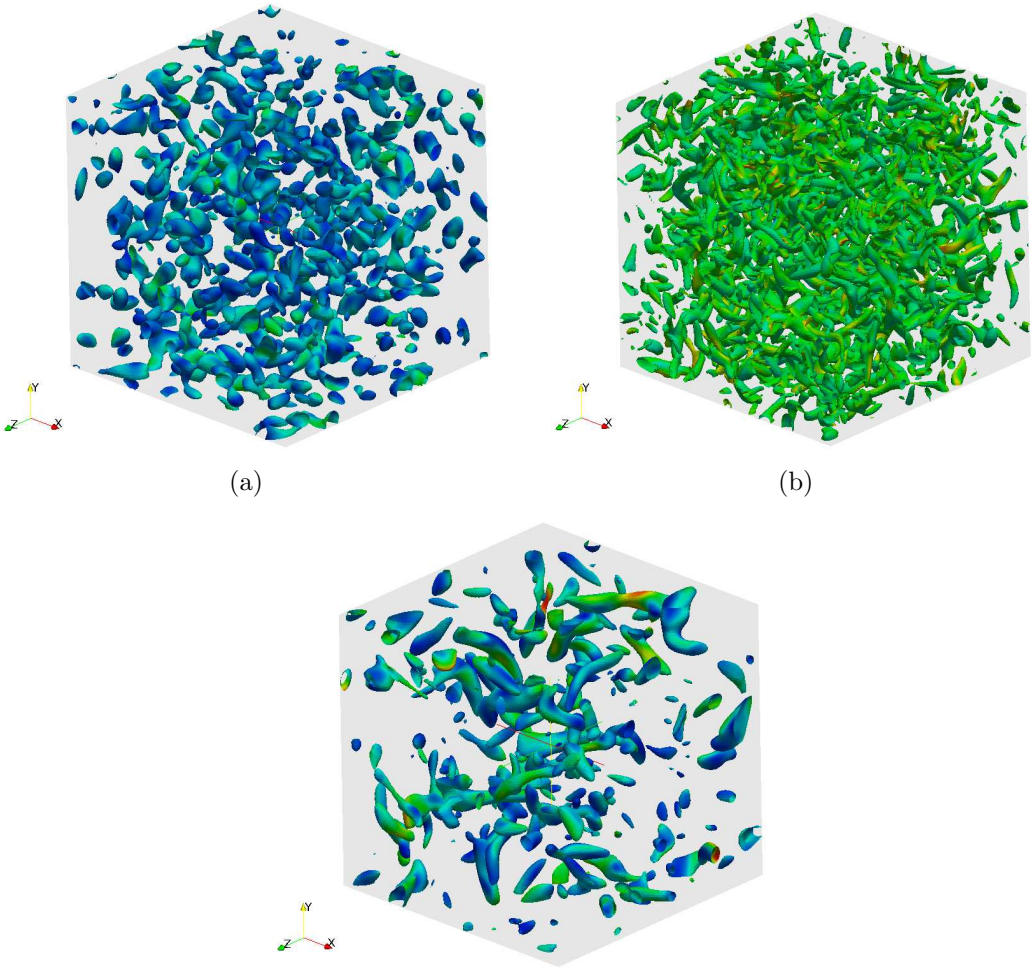

(a) (b)

(c)

Figure 6.7 Time progress of the turbulent flow structures of Case 3 visualized by the Q-criterion iso-surfaces and colored by the vorticity magnitude. (a) $t = 0.0s$, (b) $t = 1.0s$, and (c) $t = 10.0s$.

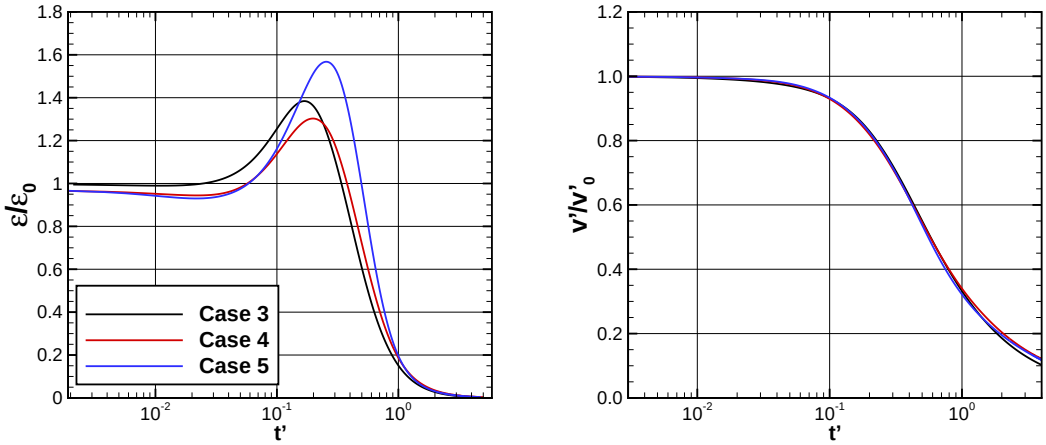

(a) (b)

Figure 6.8 Effect of the different grids orders/sizes of Cases 3–5 on the flow statistics. (a) viscous dissipation and (b) velocity fluctuation.

6.4 Freely Decaying Anisotropic MHD Turbulence

Table 6.4 Details of the freely decaying anisotropic turbulence cases.

ID	NE	Order	NN	n	B_0	Δt
1	21^3	3	262,144	2,000,376	2	5×10^{-4}
2	21^3	3	262,144	2,000,376	4	5×10^{-4}
3	21^3	3	262,144	1,250,235	NS	5×10^{-4}

The cases used to investigate the application of the FDV code to simulate MHD turbulence are summarized in Table 6.4. These cases were selected to study the effects of a spatially uniform magnetic field of strength, B_0, on a turbulent flow. The first two cases were simulated using the one-fluid plasma dynamics FDV solver, whereas the third case was simulated using the Navier-Stokes FDV solver. In order to balance the requirements of the numerical order of accuracy and of the computational resources the third order polynomials and $NE = 21^3$ were chosen.

For all the cases studied, the initial Taylor micro-scale Reynolds number and the initial turbulent Mach number are set to $Re_\lambda = 50$ and $M_t = 0.018$, respectively. The initial magnetic Reynolds number and the magnetic Mach number are set to $Re^m = Re_\lambda$ and $M^m = 1.0$, respectively. The initial turbulent kinetic energy is distributed in the wave number range $1 \leq \kappa \leq 10$. The wavelength at which the peak in the turbulent kinetic energy occurs is set to $\kappa_0 = 8$, and the constant A is chosen such that the initial *r.m.s.* fluctuating velocity is $v_0' = 1$.

The results obtained from these simulations are presented in the subsections that follow. Based on the flow visualization at various stages of the simulation, a

qualitative discussion of the results is given in Section 6.4.1. In Section 6.4.2, a detailed energy budget analysis is presented along with other important turbulence statistics.

6.4.1 Qualitative Descriptions

The initial conditions for all three cases are identical. A qualitative picture of the initial conditions is presented through the iso-surface contours of vorticity, Q-criterion and magnetic field in Figure 6.9. The initial turbulent flow field is visualized in Figures 6.9(a) and 6.9(b) through the iso-contours of vorticity and Q-criterion, while the initial magnetic field is visualized in Figure 6.9(c). For Cases 1 and 2, the initially uniform magnetic field, B_0, has only non-zero one component in the axial, x_1, direction, as shown in Figure 6.9(c).

Figure 6.10 visualizes the turbulent flow structures through the iso-contours of the vorticity and the Q-criterion for the three cases under consideration in this study. These contours are shown at time $t = 6$s, which is near the end of the simulation. The imposed magnetic field has a significant effect on the development of the turbulent flow structures for Cases 1 and 2. Figures 6.10(a)–(d) indicate that the flow structures are very nearly aligned with the direction of the magnetic field. This alignment with the magnetic field results in a more 2D-like flow structures, which is more prominent for Case 2 because of the stronger magnetic field. These findings are consistent with the studies of [73, 74]. Turbulent structures for Case 3, where there is no imposed magnetic field, demonstrate no directional preference as shown in Figures 6.10(e)–(f).

The effects of the initial magnetic field strength on the subsequent evolution of the magnetic field are shown in Figures 6.11 and 6.12. The high strength magnetic field of Case 2 did not allow for the magnetic lines to *"wrinkle"* as much as Case 1 did, as shown on Figures 6.11(a) and 6.11(c). As a result, greater electric current is generated in Case 1 than Case 2 as shown on Figures 6.12(a) and 6.12(a). It is also clear from Figures 6.11 that the wrinkled magnetic field is nearly restored to its original 1D state as the turbulence decays progressively with time. The electric current generated due to the wrinkling of the magnetic field also drops as shown in Figures 6.12(b) and 6.12(d).

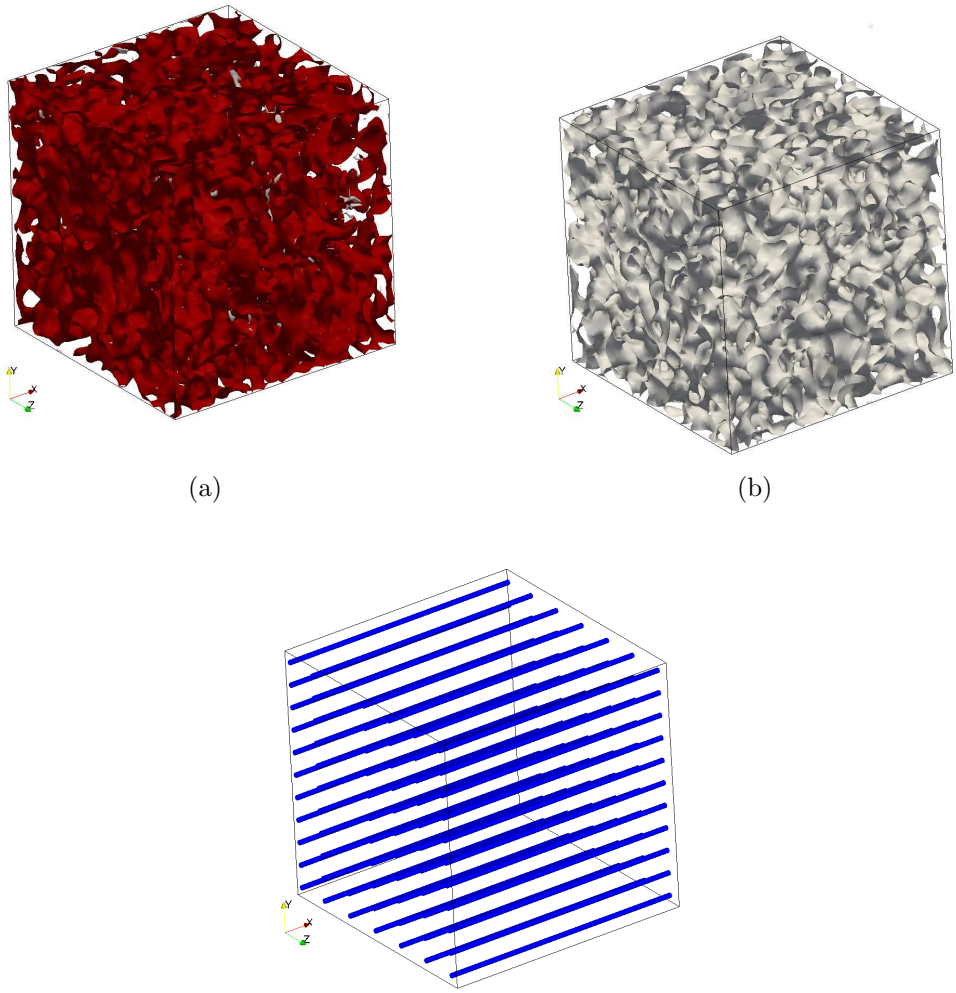

(a) (b)

(c)

Figure 6.9 Initial conditions of the anisotropic freely decaying turbulence cases. (a) Vorticity iso-surfaces, (b) Q-criterion iso-surfaces, and (c) magnetic field lines.

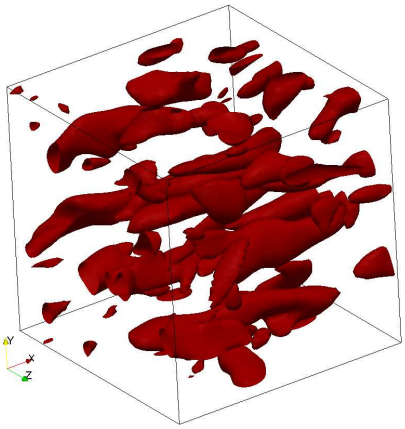

(a) Case 1 vorticity iso-surfaces.

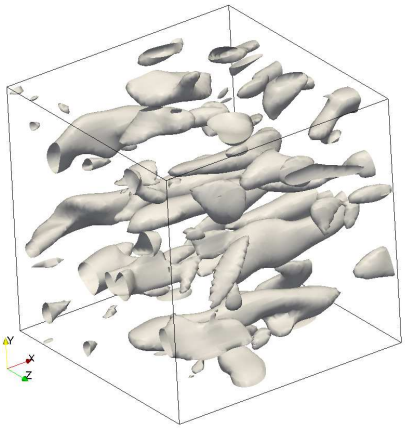

(b) Case 1 Q-criterion iso-surfaces.

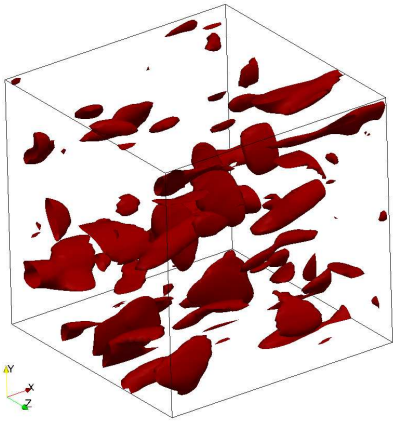

(c) Case 2 vorticity iso-surfaces.

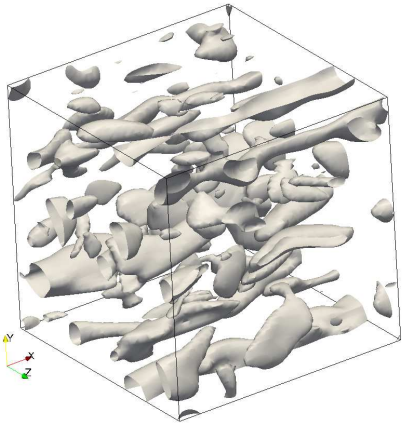

(d) Case 2 Q-criterion iso-surfaces.

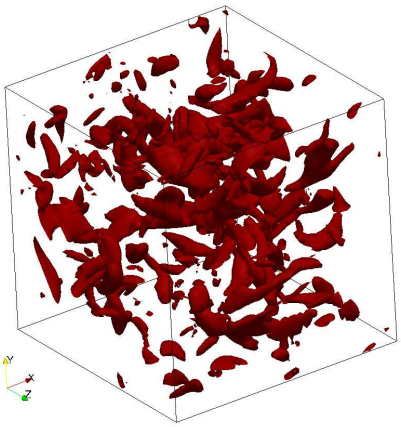

(e) Case 3 vorticity iso-surfaces.

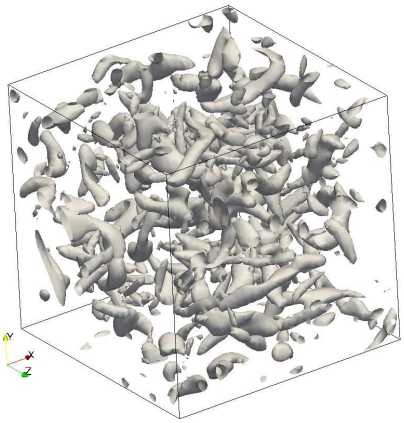

(f) Case 3 Q-criterion iso-surfaces.

Figure 6.10 Turbulent flow structures visualized at $t = 6.0s$.

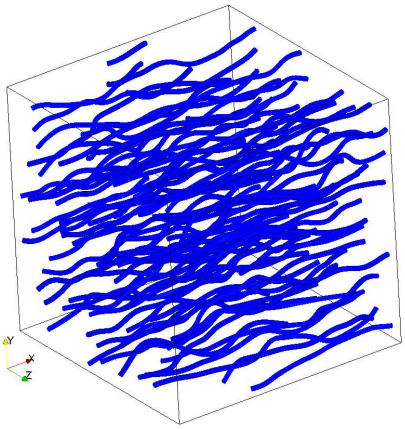

(a) Case 1 at $t = 0.5s$.

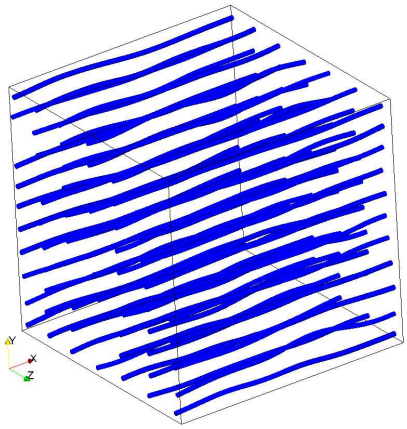

(b) Case 1 at $t = 6.0s$.

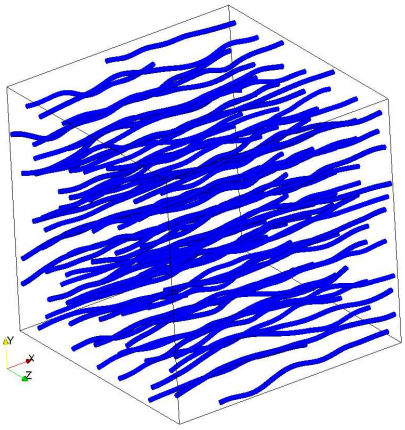

(c) Case 2 at $t = 0.5s$.

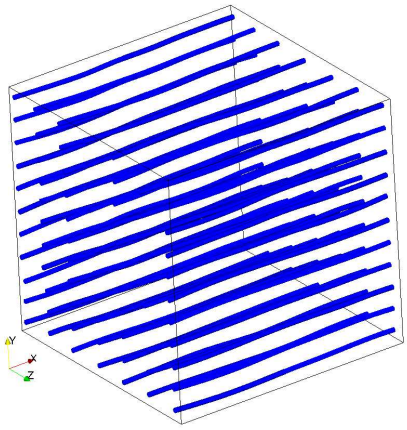

(d) Case 2 at $t = 6.0s$.

Figure 6.11 Magnetic field lines visualized at different times.

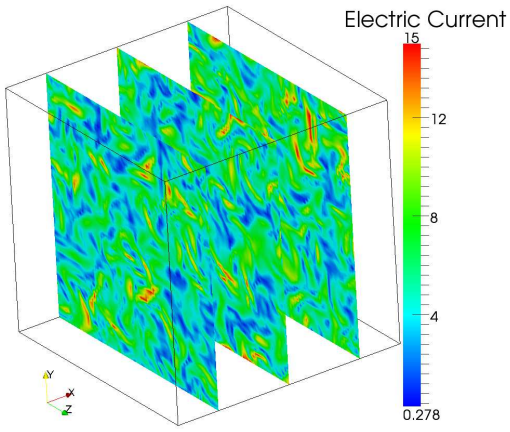

(a) Case 1 at $t = 0.5s$.

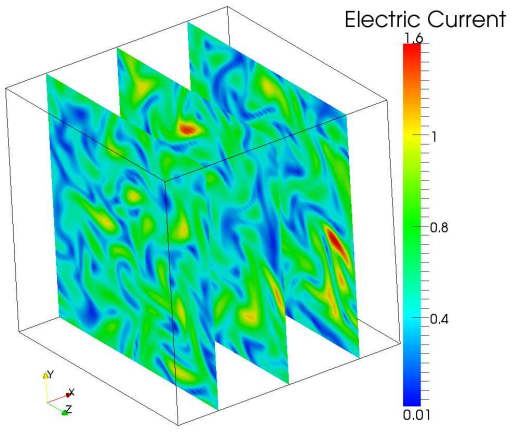

(b) Case 1 at $t = 6.0s$.

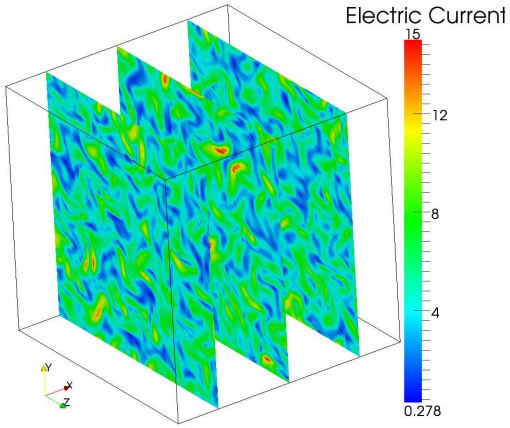

(c) Case 2 at $t = 0.5s$.

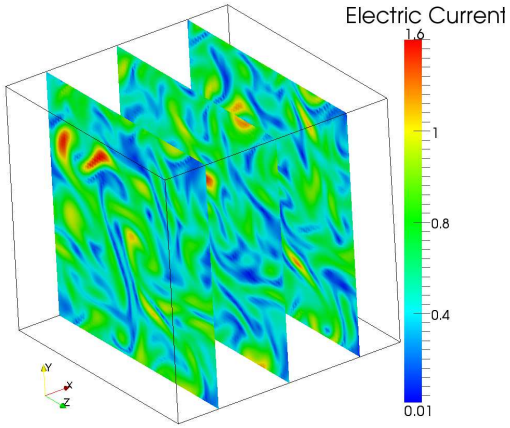

(d) Case 2 at $t = 6.0s$.

Figure 6.12 Electric current contours visualized at different times.

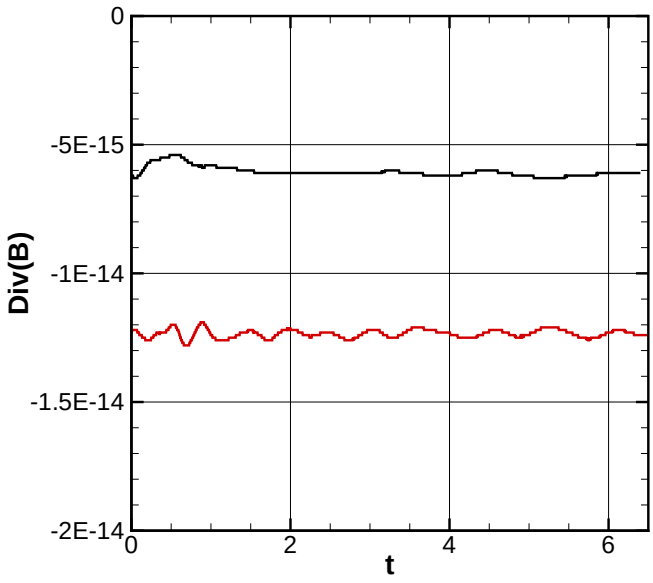

Figure 6.13 Hysteresis of the magnetic field divergence. —— Case 1 and —— Case 2.

In order to ensure that the divergence-free magnetic field constraint is satisfied during the simulations, as required by Equation (2.34), the time hysteresis of the divergence of the magnetic field averaged over the entire simulation volume is shown in Figure 6.13. It can be seen that the divergence of the magnetic field for cases 1 and 2 is $O(10^{-15})$-$O(10^{-14})$, which for all practical purposes can be considered as satisfying the divergence-free magnetic field constraint. There are two principal reasons for the divergence-free magnetic field obtained in the simulations. First, the initial magnetic field itself is divergence free. Second, this criterion is also implicitly incorporated into the governing equations as shown in Chapter 2.

Figure 6.14 shows the effects of the magnetic field strength on both the velocity and the magnetic fields components in the center of the numerical domain. It is

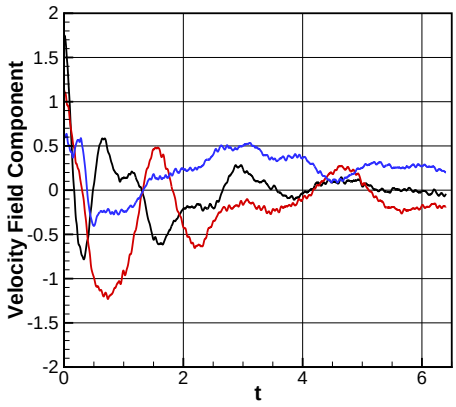

(a) Case 1 — v_1, — v_2, and — v_3.

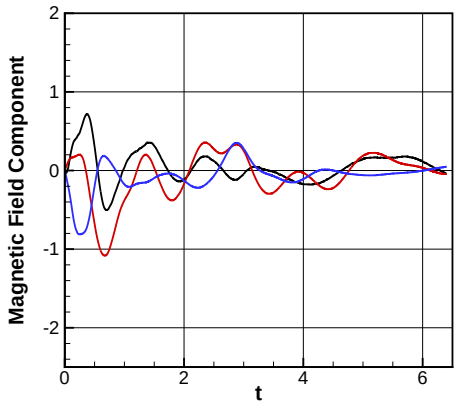

(b) Case 1 — b_1, — b_2, and — b_3.

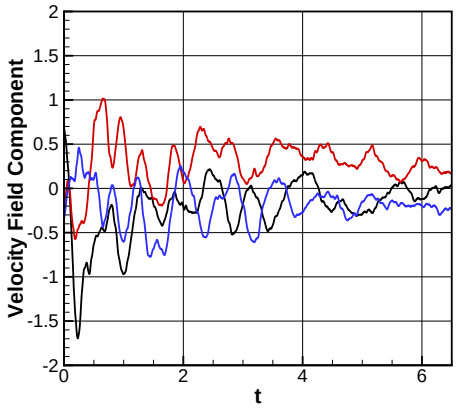

(c) Case 2.

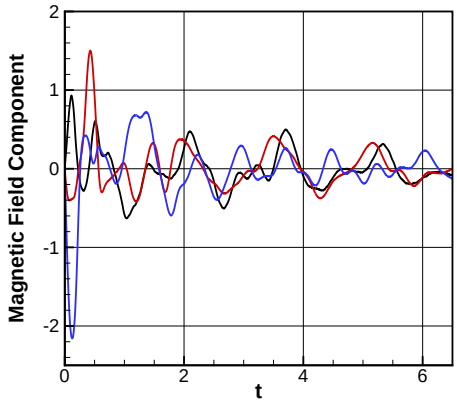

(d) Case 2.

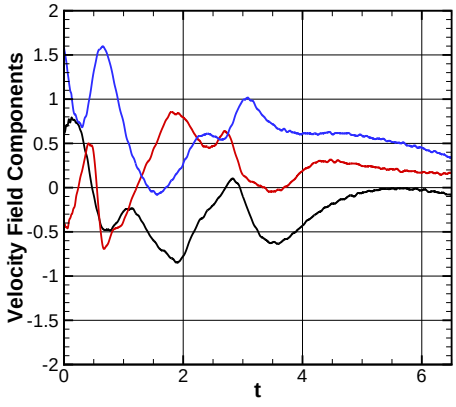

(e) Case 3.

Figure 6.14 Hysteresis of a probe attached to a node in the center of the domain.

evident that the presence of an external magnetic field in Cases 1 and 2 results in a more complex time hysteresis for the velocity field components. Also, the hysteresis for Case 1 shows more subtle variations compared to that for Case 2. The interactions between the imposed magnetic field and the turbulent flow are discussed in the next subsection.

6.4.2 Energy Budget and Flow Statistics

The turbulent kinetic energy budget for the cases with the magnetic field is fundamentally different from that of the Navier-Stokes hydrodynamics, as shown in Figure 6.15. As time progresses, the turbulent kinetic energy for both Cases 1 and 2 shows a pulsating behavior. Initially, there is an increase in the turbulent magnetic energy, which can be attributed to the transfer of energy from the turbulent flow field to the magnetic field. The subsequent pulsations in the turbulent kinetic and magnetic energies are of opposite sign, suggesting a reversal of the energy transfer process. That is, the energy transfer is now occurring from the magnetic field to the turbulent flow field. It is also seen that the pulsation frequency is higher for the case with the higher initial magnetic field strength. In fact, for case 2, the pulsation frequency is twice that for case 1, as is the case for their respective initial magnetic field strengths. Also plotted in Figure 6.15 is the Lorentz work term, which also shows a pulsating behavior after the initial transients. These findings are consistent with those in Richard et. al. [75].

In order to understand the effects of the magnetic field on the turbulence statistics and to shed light on the interactions between the magnetic and flow fields,

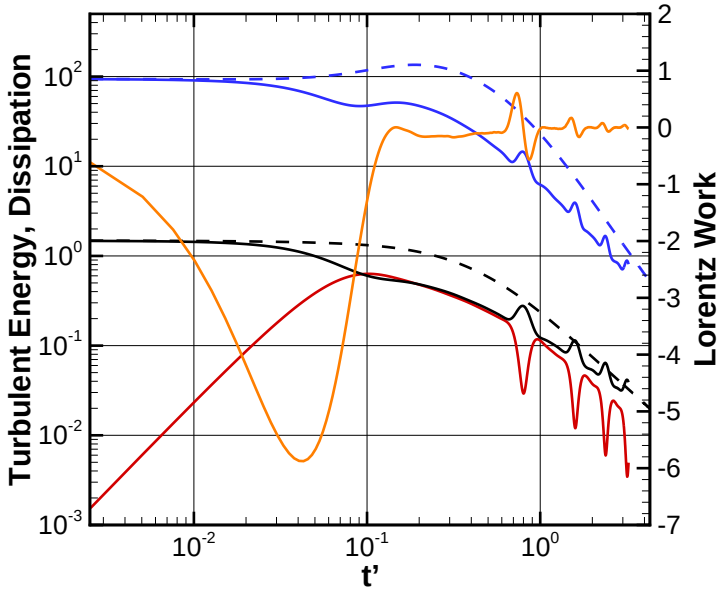

(a) Case 1

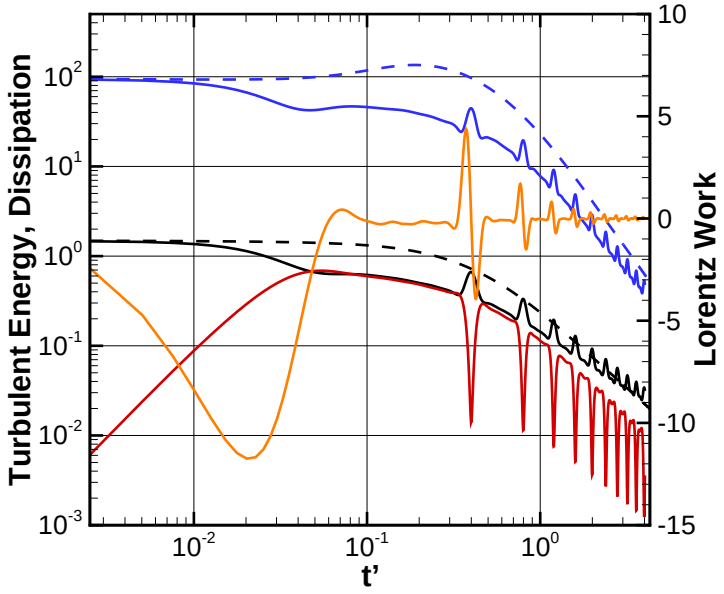

(b) Case 2

Figure 6.15 Effects of the magnetic field strength on the energy budget. Case 3 --- ϵ and --- TKE, Cases 1 or 2 — ϵ, — TKE, — TME, and — W_L.

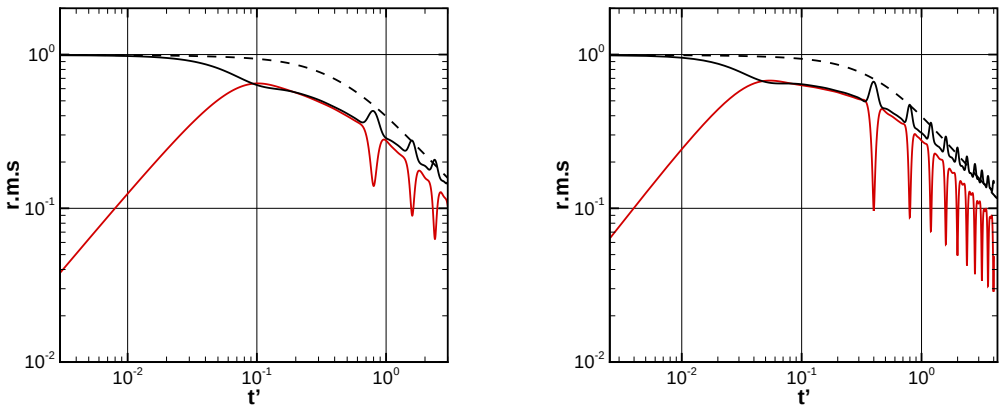

(a) Case 1 (b) Case 2

Figure 6.16 Effects of the magnetic field strength on the velocity and the magnetic fields fluctuations. Case 3. --- v', and Cases 1 or 2 —— v', and —— b'.

the *r.m.s.* statistics of the velocity and magnetic field fluctuations are shown in Figure 6.17. Since the magnetic field is applied along the axial, x_1, direction, one expects that the three components of *r.m.s.* fluctuating velocity will not be identical, as would be the case in the absence of the magnetic field. This is indeed the case in Figure 6.17. It is evident that the axial component of the *r.m.s.* fluctuating velocity, $\langle v_1 v_1 \rangle$, is greater than the other two components, $\langle v_2 v_2 \rangle$ and $\langle v_3 v_3 \rangle$. Correspondingly, the x_1 component of the *r.m.s.* fluctuating magnetic field, $\langle b_1 b_1 \rangle$, is lower than the other two components, $\langle b_2 b_2 \rangle$ and $\langle b_3 b_3 \rangle$. These trends are indicative of the anisotropy resulting from the external magnetic field.

The effects of the magnetic field on the temporal evolution of the Taylor micro-scale Reynolds number, Re_λ is shown in Figure 6.18(a). Also included in Figure 6.18(a) is the temporal evolution of Re_λ for the case with no imposed magnetic

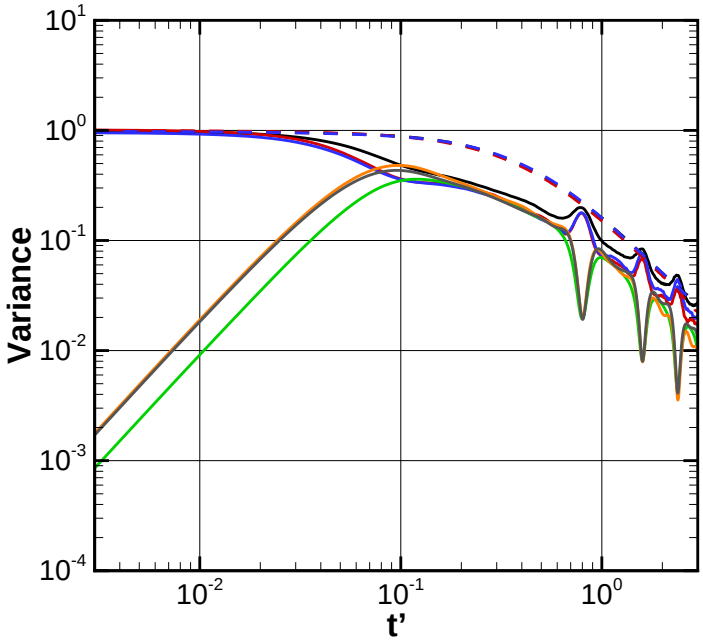

(a) Case 1

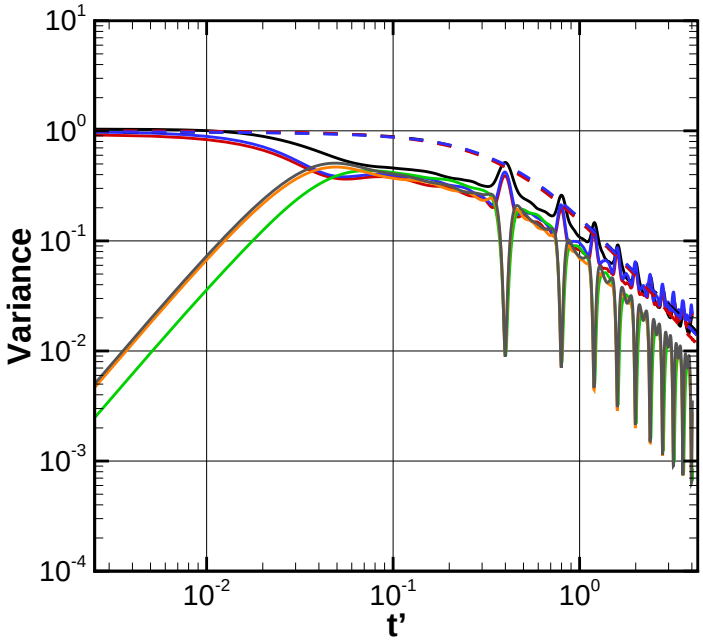

(b) Case 2

Figure 6.17 Effects of the magnetic field strength on the flow variances. Case 3 --- $\langle v_1 v_1 \rangle$, --- $\langle v_2 v_2 \rangle$, and --- $\langle v_3 v_3 \rangle$, Cases 1 or 2 — $\langle v_1 v_1 \rangle$, — $\langle v_2 v_2 \rangle$, — $\langle v_3 v_3 \rangle$, — $\langle b_1 b_1 \rangle$, — $\langle b_2 b_2 \rangle$, and — $\langle b_3 b_3 \rangle$.

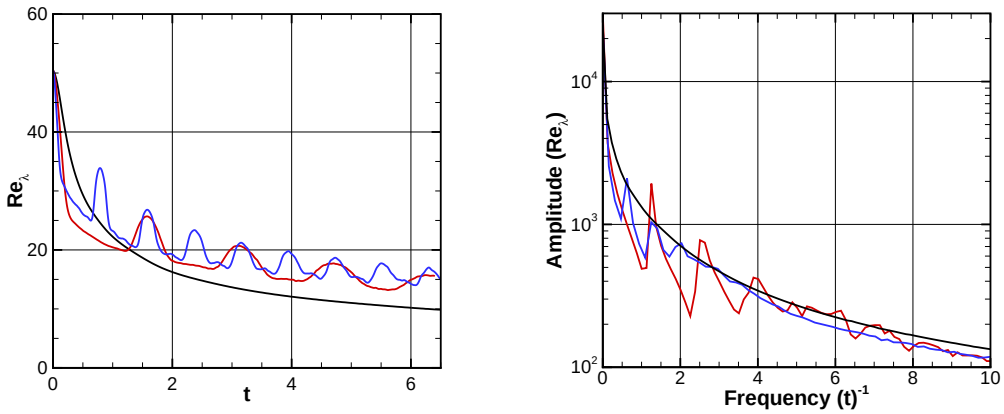

(a) (b)

Figure 6.18 Effect of background magnetic field strength on the Taylor micro-scale Reynolds number. — Case 1, — Case 2, and — Case 3.

field. Overall, Re_λ decreases with time due to the continuous decay of the turbulent kinetic energy. However, the temporal decay of Re_λ shows a pulsating behavior for the cases with the magnetic field. Also, the frequency of pulsation for Case 1 is exactly half that of Case 2, which is also the case with their respective magnetic field strengths. Also shown in Figure 6.18(b) is the Fourier transform of Re_λ. The peaks in the Fourier transform of Re_λ that correspond to the pulsation frequency of Re_λ are evident. The pulsation frequency corresponds to the frequency of the Alfvén wave. This can be understood as follows. It can be said that the initial transfer of energy from the turbulent flow field to the magnetic field via the Lorentz force has initiated an Alfvén wave disturbance in the magnetic field. This disturbance, which travels at the Alfvén wave speed, results in the pulsating behavior of both the flow and the magnetic fields. These findings are consistent with the study of [74].

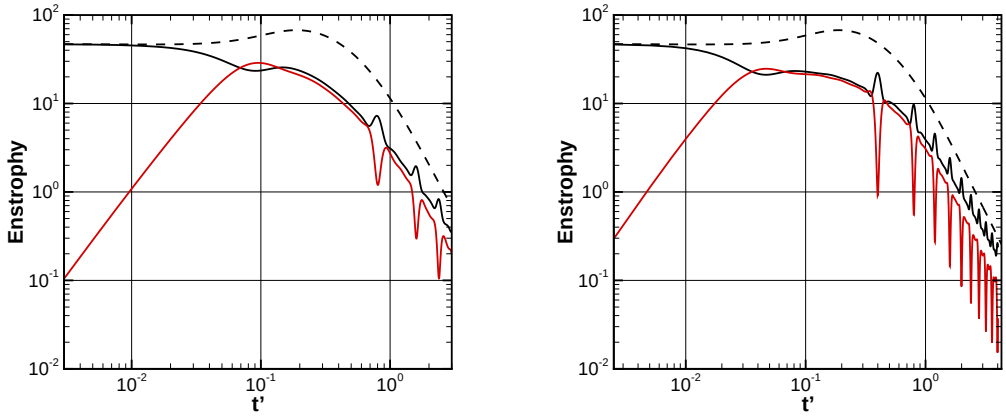

(a) Case 1 (b) Case 2

Figure 6.19 Effect of background magnetic field strength on the velocity field enstrophy and magnetic field enstrophy. Case 3 --- Ω_v and Cases 1 or 2 — Ω_v, and — Ω_m.

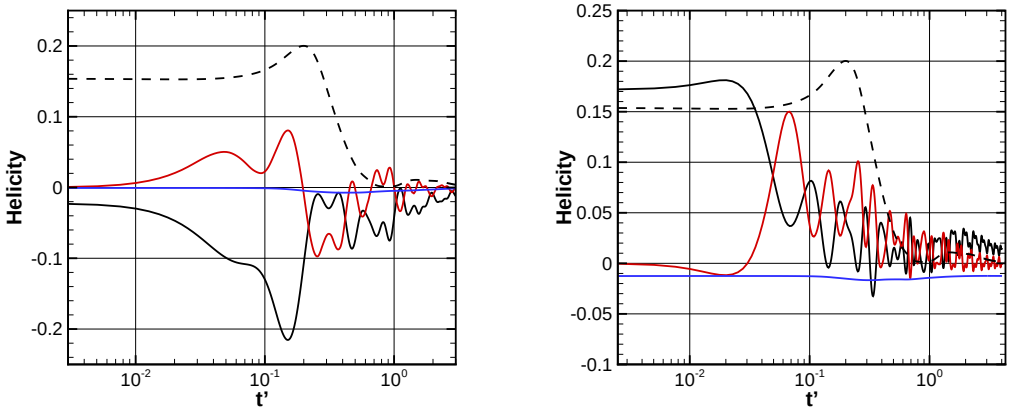

(a) Case 1 (b) Case 2

Figure 6.20 Effect of background magnetic field strength on the velocity field helicity, modified magnetic helicity, and cross magnetic helicity. Case 3 --- H_v and Cases 1 or 2 — H_v, — H_m, and — H_{vm}.

The enstrophies of velocity and magnetic field are shown in Figure 6.20. Also shown is the enstrophy of velocity for the case with no magnetic field. For case 3, there is an initial increase in the enstrophy before it begins to decrease monotonically. The initial increase in enstrophy can be attributed to the distribution of energy from the initial narrow wave number spectrum to the entire wave number spectrum. The subsequent decrease in enstrophy is due to the monotonic decay in the turbulent kinetic energy. For the cases with the external magnetic field, the enstrophy trends are different from the above. Initially, there is a decrease in the velocity enstrophy, with a corresponding increase in the enstrophy of the magnetic field. This is due to the transfer of energy from the turbulent flow field to the magnetic field. One also notices the pulsations in both the velocity and magnetic field enstrophies, which were evident in the other statistics as well. Finally, the temporal evolution of the velocity helicity, magnetic field helicity and the velocity-magnetic field cross helicity, H_v, H_m and H_{vm} respectively, are shown in Figure 6.20. It is clear that the cross helicity stays almost constant as suggested by Davidson [74].

CHAPTER 7

CONCLUSIONS

In this dissertation, an extension of the FDV method to the plasma physics is implemented. The governing equations for the one-fluid plasma dynamics are formulated from the fundamental principles into the vector form suitable for the FDV method. The various formulas necessary for the calculation of the FDV parameters relevant to plasma dynamics are introduced. The Jacobian terms of the flux vectors have been introduced as well.

A parallel framework for the arbitrarily higher order unstructured finite element computations is developed and thoroughly tested. This framework utilized the EBE data structure to store the linear system and to satisfy the distributed memory model. A parallel GMRES algorithm has been introduced to solve the linear system in the EBE format. The parallel communications are carried out using the MPI library. The efficiency of this framework have been documented in this dissertation. The utilization of the METIS package is proved effective in load balancing. The effects of different communication strategies, order of accuracy, and the problem size have been studied and documented. Comparisons with published literature proved the parallel scalability of the developed code.

The order of accuracy of the developed code has been established using the MMS. A systematic increase in the order of the spatial accuracy has been obtained with the increase of the Lagrange polynomial orders. This study used the L_2 and the L_∞ norms. The spacial accuracy is found to be approximately equal to the polynomial order plus one.

Several fluid dynamics test cases (2D and 3D) have been studied to verify the developed code in all flow regimes: incompressible, subsonic, and supersonic. All test cases showed good agreement with available literature and analytical solutions. The higher order grids proved their effectiveness in obtaining the most accurate solutions with the minimum number of nodes. The FDV parameters were always able to mimic the flow situation to provide stable and accurate solutions for all flow regimes.

The newly implemented extension of the FDV method to the plasma dynamics has been verified using three test cases. All cases showed good agreement with the published literature results. The first test case is the non-linear circularly polarized smooth Alfvén wave. This cases confirmed the ability of the FDV method to simulate accurately the Alfvén wave phenomena, which is predominant in this case. Higher order solutions proved more accurate in long simulations. The second test case is ideal MHD shock tube. This case established the ability of the FDV method to effectively resolve the different wave phenomena involved in plasma dynamics including: fast/slow shock waves, contact discontinuities, and fast/slow rotational discontinuities. The FDV parameters extended their role that was observed in the fluid dynamics cases by mimicking the solution domain to supply the flowfield with the necessary stability while maintaining the accuracy. The third test case is the Orszag-Tang vortex. This

case established the ability of the FDV method in resolving complex interactions between the velocity and the magnetic fields; which lead to strong shock waves in both fields as well as the pressure and the density fields.

Finally, the FDV method has been studied for the first time in turbulent flow simulations through the problems of isotropic and anisotropic turbulence. The effects of the the higher order grids and time step size on the dissipation and dispersion errors are studied in details. The higher order polynomial shape functions are proved necessary for achieving the desired level of accuracy along with carefully selected time step sizes.

Several test cases are selected for the problem of freely decaying isotropic turbulence. These problems studied the effects of increasing the Taylor micro-scale Reynolds number, the higher order grids, grid sizes, the time step sizes, and higher turbulent Mach numbers. All the results and the turbulent flow statistics are consistent with the literature.

The problem of freely decaying anisotropic magnetic turbulence was also studied. The effects of the background magnetic field strength were investigated in detail. The analysis was based upon both qualitative descriptions and turbulent energy budget. The turbulent kinetic energy is found to be fundamentally different from that of the Navier-Stokes hydrodynamics. Pulsating behavior in both the turbulent kinetic energy and the turbulent magnetic energy was observed. The pulsation is due to the initial transfer of the turbulent energy from the velocity field to the magnetic field. Which generated an Alfvén wave. The pulsating frequency was found directly proportional to the background magnetic field strength. All the results are found consistent

with available literature proving the ability of the implemented extension of the FDV method to accurately resolve the physics of the one-fluid plasma dynamics.

APPENDICES

APPENDIX A

FLUX JACOBIANS AND FLUX GRADIENTS

The flux vectors Jacobians; namely $\mathbf{a}_i$, $\mathbf{b}_i$, and $\mathbf{c}_{ij}$, defined in Equation (2.133), are necessary for the FDV method's calculations. The first step to obtain these Jacobians is to write the convection flux, $\mathbf{F}_i$, given in Equation (2.135) and the diffusion flux, $\mathbf{G}_i$, given in Equation (2.136) in terms of the conservation variables, $\mathbf{U}$, given in Equation (2.134) and their gradients, $\mathbf{U}_{,i}$, . The second step is to differentiate these fluxes *w.r.t.* $\mathbf{U}$ and $\mathbf{U}_{,i}$.

The flux gradients, $\mathbf{F}_{i,i}$ and $\mathbf{G}_{i,i}$, are also required as shown in Equation (3.27). To preserve the order of accuracy imposed by the assumed shape function, the flux gradients have to be written as functions of the conservation variables and their gradients.

However, the explicit expansion of the flux Jacobians and the flux gradients in terms of the conservation variables and their gradients results in lengthy terms. Therefore, the derivation process adopted here employ an implicit differentiation technique.

Section A.1 introduces the gradients and the Jacobians of the various physical properties appearing in the fluxes. Section A.2 shows the details of the flux Jacobians

and the flux gradients for the visco-resistive plasma dynamics equations. However, the Jacobian terms for the Navier-Stokes equations are simpler and the explicit representation is well known. The details of the Navier-Stokes Jacobians are summarized in Section A.3. In the next subsections, the counters i, j, k, n, and m run from one to three, whereas the counters r and s run from one to eight.

A.1 Physical Properties Jacobians and Gradients

The convection and the diffusion fluxes contain several physical properties that are, in general, non-linear functions of the conservation variables. The mathematical effort required to derive the flux Jacobians and the flux gradients, as well as the computer implementation complexity for the resulting expressions, are greatly simplified by differentiating these terms implicitly.

To this end, the listing of the derivatives of the different physical properties included in the flux vectors are introduced below. Each property is written in terms of the conservation variables, and the necessary Jacobian and gradient differentiations are carried out. Table A.1 summerizes all the physical properties that appear in the differentiation properties, and the actual listing is given next.

- Magnetic Pressure

$$p^m = \frac{1}{2\mu^m} B_k B_k = \frac{1}{2\mu^m} U_{5+k} U_{5+k}$$

$$p^m_{,i} = \frac{1}{\mu^m} U_{5+k} U_{5+k,i}$$

$$p^m_{,ij} = \frac{1}{\mu^m} \left(U_{5+k,j} U_{5+k,i} + U_{5+k} U_{5+k,ij} \right)$$

Table A.1 List of the required physical properties gradients and Jacobians for implicit differentiation.

p^m	$p^m_{,i}$	$p^m_{,ij}$	$\frac{\partial p^m}{\partial U_r}$	$\frac{\partial p^m_{,i}}{\partial U_r}$	$\frac{\partial p^m_{,i}}{\partial U_{r,k}}$
τ^m_{ij}	$\tau^m_{ij,k}$	$\frac{\partial \tau^m_{ij}}{\partial U_r}$			
Πij^m	$\Pi^m_{ij,k}$	$\frac{\partial \Pi^m_{ij}}{\partial U_r}$			
J_i	$J_{i,j}$	$\frac{\partial J_i}{\partial U_r}$	$\frac{\partial J_i}{\partial U_{r,k}}$		
h^m_i	$h^m_{i,j}$	$\frac{\partial h^m_i}{\partial U_r}$	$\frac{\partial h^m_i}{\partial U_{r,k}}$		
p	$p_{,i}$	$p_{,ij}$	$\frac{\partial p}{\partial U_r}$	$\frac{\partial p_{,i}}{\partial U_r}$	$\frac{\partial p_{,i}}{\partial U_{r,j}}$
T	$T_{,i}$	$T_{,ij}$	$\frac{\partial T_{,i}}{\partial U_r}$	$\frac{\partial T_{,i}}{\partial U_{r,j}}$	
v_i	$v_{i,j}$	$v_{i,jk}$	$\frac{\partial v_{i,j}}{\partial U_r}$	$\frac{\partial v_{i,j}}{\partial U_{r,k}}$	
ε_{ij}	$\varepsilon_{ij,k}$	$\frac{\partial \varepsilon_{ij}}{\partial U_r}$	$\frac{\partial \varepsilon_{ij}}{\partial U_{r,k}}$		
τij	$\tau ij,k$	$\frac{\partial \tau ij}{\partial U_r}$	$\frac{\partial \tau ij}{\partial U_{r,k}}$		
h_i	$h_{i,j}$	$\frac{\partial h_i}{\partial U_r}$	$\frac{\partial h_i}{\partial U_{r,k}}$		

$$\frac{\partial p^m}{\partial U_{1-5}} = 0$$
$$\frac{\partial p^m}{\partial U_{5+j}} = \frac{1}{\mu^m} U_{5+j}$$
$$\frac{\partial p^m_{,i}}{\partial U_{1-5}} = 0$$
$$\frac{\partial p^m_{,i}}{\partial U_{5+j}} = \frac{1}{\mu^m} U_{5+j,i}$$
$$\frac{\partial p^m_{,i}}{\partial U_{1-5,k}} = 0$$
$$\frac{\partial p^m_{,i}}{\partial U_{5+j,k}} = \frac{1}{\mu^m} U_{5+j} \delta_{ik}$$

- Magnetic Product Stress Tensor

$$\tau^m_{ij} = \frac{1}{\mu^m} B_i B_j = \frac{1}{\mu^m} U_{5+i} U_{5+j}$$
$$\tau^m_{ij,k} = \frac{1}{\mu^m} \left(U_{5+i} U_{5+j,k} + U_{5+j} U_{5+i,k} \right)$$
$$\frac{\partial \tau^m_{ij}}{\partial U_{1-5}} = 0$$
$$\frac{\partial \tau^m_{ij}}{\partial U_{5+k}} = \frac{1}{\mu^m} \left(U_{5+i} \delta_{jk} + U_{5+j} \delta_{ik} \right)$$

- Maxwell Stress Tensor

$$\Pi_{ij} = \tau^m_{ij} - p^m \delta_{ij}$$

$$\Pi_{ij,k} = \tau^m_{ij,k} - p^m_{,k} \delta_{ij}$$
$$\frac{\partial \Pi_{ij}}{\partial U_{1-5}} = 0$$
$$\frac{\partial \Pi_{ij}}{\partial U_{5+k}} = \frac{\partial \tau^m_{ij}}{\partial U_{5+k}} - \frac{\partial p^m}{\partial U_{5+k}} \delta_{ij}$$

- Electric Current Density

$$J_i = \frac{1}{\mu^m}\epsilon_{ijk}B_{k,j} = \frac{1}{\mu^m}\epsilon_{ijk}U_{5+k,j}$$

$$J_{i,j} = \frac{1}{\mu^m}\epsilon_{imn}U_{5+n,mj}$$

$$\frac{\partial J_i}{\partial U_r} = 0$$

$$\frac{\partial J_i}{\partial U_{1-5,k}} = 0$$

$$\frac{\partial J_i}{\partial U_{5+j,k}} = \frac{1}{\mu^m}\epsilon_{ikj}$$

- Magnetic Heating Flux

$$h_i^m = \lambda^m\epsilon_{ijk}J_jB_k = \lambda^m\epsilon_{ijk}J_jU_{5+k}$$

$$h_{i,j}^m = \lambda^m\epsilon_{imn}\left(J_{m,j}U_{5+n} + J_mU_{5+n,j}\right)$$

$$\frac{\partial h_i^m}{\partial U_{1-5}} = 0$$

$$\frac{\partial h_i^m}{\partial U_{5+j}} = \lambda^m\epsilon_{ikj}J_k$$

$$\frac{\partial h_i^m}{\partial U_{1-5,k}} = 0$$

$$\frac{\partial h_i^m}{\partial U_{5+j,k}} = \lambda^m\epsilon_{imn}\frac{\partial J_m}{\partial U_{5+j,k}}U_{5+n}$$

- Pressure

$$p = (\gamma-1)\left(U_5 - \frac{U_2^2+U_3^2+U_4^2}{2U_1} - p^m\right)$$

$$p_{,i} = (\gamma-1)\left(U_{5,i} - \frac{U_2U_{2,i}+U_3U_{3,i}+U_4U_{4,i}}{U_1} + \frac{U_2^2+U_3^2+U_4^2}{2U_1^2}U_{1,i} - p_{,i}^m\right)$$

$$p_{,ij} = (\gamma-1)\left[U_{5,ij} - \frac{U_2U_{2,ij}+U_3U_{3,ij}+U_4U_{4,ij}}{U_1}\right.$$

$$
\begin{aligned}
&-\frac{U_{2,j}U_{2,i}+U_{3,j}U_{3,i}+U_{4,j}U_{4,i}}{U_1}\\
&+\frac{U_2^2+U_3^2+U_4^2}{U_1^2}\left(\frac{1}{2}U_{1,ij}-\frac{1}{U_1}U_{1,i}U_{1,j}\right)\\
&+\frac{U_2U_{2,i}+U_3U_{3,i}+U_4U_{4,i}}{U_1^2}U_{1,j}\\
&+\frac{U_2U_{2,j}+U_3U_{3,j}+U_4U_{4,j}}{U_1^2}U_{1,i}-p^m_{,ij}\Bigg]
\end{aligned}
$$

$$\frac{\partial p}{\partial U_1}=(\gamma-1)\,\frac{U_2^2+U_3^2+U_4^2}{2U_1^2}$$

$$\frac{\partial p}{\partial U_{1+j}}=(1-\gamma)\,\frac{U_{1+j}}{U_1}$$

$$\frac{\partial p}{\partial U_5}=\gamma-1$$

$$\frac{\partial p}{\partial U_{5+j}}=(1-\gamma)\,\frac{\partial p^m}{\partial U_{5+j}}$$

$$\frac{\partial p_{,i}}{\partial U_1}=\frac{\gamma-1}{U_1^2}\left(U_2U_{2,i}+U_3U_{3,i}+U_4U_{4,i}-\frac{U_2^2+U_3^2+U_4^2}{U_1}U_{1,i}\right)$$

$$\frac{\partial p_{,i}}{\partial U_{1+j}}=\frac{\gamma-1}{U_1}\left(-U_{1+j,i}+\frac{U_{1+j}}{U_1}U_{1,i}\right)$$

$$\frac{\partial p_{,i}}{\partial U_5}=0$$

$$\frac{\partial p_{,i}}{\partial U_{5+j}}=(1-\gamma)\,\frac{\partial p^m_{,i}}{\partial U_{5+j}}$$

$$\frac{\partial p_{,i}}{\partial U_{1,j}}=\frac{\gamma-1}{2U_1^2}\left(U_2^2+U_3^2+U_4^2\right)\delta_{ij}$$

$$\frac{\partial p_{,i}}{\partial U_{1+j,k}}=\frac{1-\gamma}{U_1}U_{1+j}\delta_{ik}$$

$$\frac{\partial p_{,i}}{\partial U_{5,j}}=(\gamma-1)\,\delta_{ij}$$

$$\frac{\partial p_{,i}}{\partial U_{5+j,k}}=(1-\gamma)\,\frac{\partial p^m_{,i}}{\partial U_{5+j,k}}$$

- Temeprature

$$T = \frac{p}{RU_1}$$
$$T_{,i} = \frac{1}{RU_1}\left(p_{,i} - \frac{p}{U_1}U_{1,i}\right)$$
$$T_{,ij} = \frac{1}{RU_1}\left(p_{,ij} - \frac{1}{U_1}\left(p_{,i}U_{1,j} + p_{,j}U_{1,i} + pU_{1,ij}\right) + \frac{2p}{U_1^2}U_{1,i}U_{1,j}\right)$$
$$\frac{\partial T_{,i}}{\partial U_1} = \frac{1}{RU_1}\left(\frac{\partial p_{,i}}{\partial U_1} - \frac{1}{U_1}\left(p_{,i} + U_{1,i}\frac{\partial p}{\partial U_1}\right) + \frac{2p}{U_1^2}U_{1,i}\right)$$
$$\frac{\partial T_{,i}}{\partial U_{1+j}} = \frac{1}{RU_1}\left(\frac{\partial p_{,i}}{\partial U_{1+j}} - \frac{U_{1,i}}{U_1}\frac{\partial p}{\partial U_{1+j}}\right)$$
$$\frac{\partial T_{,i}}{\partial U_5} = \frac{1}{RU_1}\left(\frac{\partial p_{,i}}{\partial U_5} - \frac{U_{1,i}}{U_1}\frac{\partial p}{\partial U_5}\right)$$
$$\frac{\partial T_{,i}}{\partial U_{5+j}} = \frac{1}{RU_1}\left(\frac{\partial p_{,i}}{\partial U_{5+j}} - \frac{U_{1,i}}{U_1}\frac{\partial p}{\partial U_{5+j}}\right)$$
$$\frac{\partial T_{,i}}{\partial U_{1,j}} = \frac{1}{RU_1}\left(\frac{\partial p_{,i}}{\partial U_{1,j}} - \frac{p}{U_1}\delta_{ij}\right)$$
$$\frac{\partial T_{,i}}{\partial U_{1+j,k}} = \frac{1}{RU_1}\frac{\partial p_{,i}}{\partial U_{1+j,k}}$$
$$\frac{\partial T_{,i}}{\partial U_{5,j}} = \frac{1}{RU_1}\frac{\partial p_{,i}}{\partial U_{5,j}}$$
$$\frac{\partial T_{,i}}{\partial U_{5+j,k}} = \frac{1}{RU_1}\frac{\partial p_{,i}}{\partial U_{5+j,k}}$$

- Velocity

$$v_i = \frac{U_{1+i}}{U_1}$$
$$v_{i,j} = \frac{1}{U_1}\left(U_{1+i,j} - \frac{U_{1+i}}{U_1}U_{1,j}\right)$$
$$v_{i,jk} = \frac{1}{U_1}\left(U_{1+i,jk} - \frac{1}{U_1}\left(U_{1+i,j}U_{1,k} + U_{1+i,k}U_{1,j} + U_{1+i}U_{1,jk}\right) + 2\frac{U_{1+i}}{U_1^2}U_{1,j}U_{1,k}\right)$$
$$\frac{\partial v_{i,j}}{\partial U_1} = \frac{1}{U_1^2}\left(-U_{1+i,j} + 2\frac{U_{1+i}}{U_1}U_{1,j}\right)$$
$$\frac{\partial v_{i,j}}{\partial U_{1+k}} = \frac{-\delta_{ik}}{U_1^2}U_{1,j}$$

$$\frac{\partial v_{i,j}}{\partial U_{5-5+k}} = 0$$
$$\frac{\partial v_{i,j}}{\partial U_{1,k}} = -\frac{U_{1+i}}{U_1^2}\delta_{jk}$$
$$\frac{\partial v_{i,j}}{\partial U_{1+n,k}} = \frac{1}{U_1}\delta_{ni}\delta_{jk}$$
$$\frac{\partial v_{i,j}}{\partial U_{5-5+n,k}} = 0$$

- Strain Tensor

$$\varepsilon_{ij} = \frac{1}{2}\left(v_{i,j} + v_{j,i}\right)$$
$$\varepsilon_{ij,k} = \frac{1}{2}\left(v_{i,jk} + v_{j,ik}\right)$$
$$\frac{\partial \varepsilon_{ij}}{\partial U_r} = \frac{1}{2}\left(\frac{\partial v_{i,j}}{\partial U_r} + \frac{\partial v_{j,i}}{\partial U_r}\right)$$
$$\frac{\partial \varepsilon_{ij}}{\partial U_{r,k}} = \frac{1}{2}\left(\frac{\partial v_{i,j}}{\partial U_{r,k}} + \frac{\partial v_{j,i}}{\partial U_{r,k}}\right)$$

- Stress Tensor

$$\tau_{ij} = 2\mu\varepsilon_{ij} + \lambda\delta_{ij}\varepsilon_{nn}$$

$$\tau_{ij,k} = 2\mu\varepsilon_{ij,k} + \lambda\delta_{ij}\varepsilon_{nn,k}$$
$$\frac{\partial \tau_{ij}}{\partial U_r} = 2\mu\frac{\partial \varepsilon_{ij}}{\partial U_r} + \lambda\delta_{ij}\frac{\partial \varepsilon_{nn}}{\partial U_r}$$
$$\frac{\partial \tau_{ij}}{\partial U_{r,k}} = 2\mu\frac{\partial \varepsilon_{ij}}{\partial U_{r,k}} + \lambda\delta_{ij}\frac{\partial \varepsilon_{nn}}{\partial U_{r,k}}$$

- Convective Heat Flux

$$h_i = -kT_{,i}$$

$$h_{i,j} = -kT_{,ij}$$

$$\frac{\partial h_i}{\partial U_r} = -k\frac{\partial T_{,i}}{\partial U_r}$$
$$\frac{\partial h_i}{\partial U_{r,k}} = -k\frac{\partial T_{,i}}{\partial U_{r,k}}$$

A.2 Visco-resistive Plasma Dynamics Jacobians and Gradients

The convection and diffusion flux vectors, given in Equations (2.135) and (2.136), respectively, are written in terms of the conservation variables as follows:

$$F_{ir} = \begin{bmatrix} U_{1+i} \\ \dfrac{U_{1+i}U_{1+j}}{U_1} + p\delta_{ij} - \Pi_{ij} \\ \dfrac{U_{1+i}}{U_1}\left(U_5 + p\right) - \Pi_{ik}\dfrac{U_{1+k}}{U_1} \\ \dfrac{1}{U_1}\left(U_{1+i}U_{5+j} - U_{1+j}U_{5+i}\right) \end{bmatrix}, \tag{A.1}$$

and

$$G_{ir} = \begin{bmatrix} 0 \\ -\tau_{ij} \\ -\tau_{ik}\dfrac{U_{1+k}}{U_1} + h_i + h_i^m \\ -\lambda^m U_{5+j,i} \end{bmatrix}. \tag{A.2}$$

Taking the gradient of both fluxes we get

$$F_{ir,k} = \begin{bmatrix} U_{1+i,k} \\ \dfrac{1}{U_1}\left(U_{1+i,k}U_{1+j} + U_{1+i}U_{1+j,k} - \dfrac{U_{1+i}U_{1+j}}{U_1}U_{1,k}\right) + p_{,k}\delta_{ij} - \Pi_{ij,k} \\ F_{i\,5,k} \\ F_{i\,5+j,k} \end{bmatrix}, \tag{A.3}$$

where

$$F_{i\,5,k} = \frac{1}{U_1}\left[U_{1+i}\left(U_{5,k} + p_{,k}\right) + \left(U_5 + p\right)\left(U_{1+i,k} - \frac{U_{1+i}}{U_1}U_{1,k}\right) - U_{1+j,k}\Pi_{ji} - U_{1+j}\Pi_{ji,k} + \frac{U_{1+j}}{U_1}\Pi_{ji}U_{1,k}\right], \tag{A.4}$$

$$F_{i\,5+j,k} = \frac{1}{U_1}\left[U_{1+i,k}U_{5+j} + U_{1+i}U_{5+j,k} - U_{1+j,k}U_{5+i} - U_{1+j}U_{5+i,k} - \frac{1}{U_1}\left(U_{1+i}U_{5+j} - U_{1+j}U_{5+i}\right)U_{1,k}\right], \tag{A.5}$$

and

$$G_{ir,k} = \begin{bmatrix} 0 \\ -\tau_{ij,k} \\ -\dfrac{1}{U_1}\left(U_{1+j,k}\tau_{ij} + U_{1+j}\tau_{ij,k} - \dfrac{U_{1+j}}{U_1}\tau_{ij}U_{1,k}\right) + h_{i,k} + h^m_{i,k} \\ -\lambda^m U_{5+j,ik} \end{bmatrix}. \tag{A.6}$$

The respective Jacobians for both the convection and diffusion fluxes are given in Tables A.2, A.3, and A.4.

Table A.2 Visco-resistive Plasma Dynamics a_{irs} Jacobian.

0	δ_{ik}	0	0
$a^i_{1+j\,1}$	$a^i_{1+j\,1+k}$	$a^i_{1+j\,5}$	$a^i_{1+j\,5+k}$
$a^i_{5\,1}$	$a^i_{5\,1+k}$	$a^i_{5\,5}$	$a^i_{5\,5+k}$
$a^i_{5+j\,1}$	$a^i_{5+j\,1+k}$	0	$a^i_{5+j\,5+k}$

$$
\begin{aligned}
a^i_{1+j\,1} =& -\frac{U_{1+i}U_{1+j}}{U_1^2} + \delta_{ij}\frac{\partial p}{\partial U_1} \\
a^i_{1+j\,1+k} =& \frac{1}{U_1}\left(U_{1+i}\delta_{jk} + U_{1+j}\delta_{ik}\right) + \delta_{ij}\frac{\partial p}{\partial U_{1+k}} \\
a^i_{1+j\,5} =& \delta_{ij}\frac{\partial p}{\partial U_5} \\
a^i_{1+j\,5+k} =& \delta_{ij}\frac{\partial p}{\partial U_{5+k}} - \frac{\partial \Pi_{ji}}{\partial U_{5+k}} \\
a^i_{5\,1} =& -\frac{U_{1+i}}{U_1^2}\left(U_5 + p\right) + \frac{U_{1+i}}{U_1}\frac{\partial p}{\partial U_1} + \frac{U_{1+n}}{U_1^2}\Pi_{ni} \\
a^i_{5\,1+k} =& \frac{\delta_{ik}}{U_1}\left(U_5 + p\right) + \frac{U_{1+i}}{U_1}\frac{\partial p}{\partial U_{1+k}} - \frac{\Pi_{ki}}{U_1} \\
a^i_{5\,5} =& \frac{U_{1+i}}{U_1} + \frac{U_{1+i}}{U_1}\frac{\partial p}{\partial U_5} \\
a^i_{5\,5+k} =& \frac{U_{1+i}}{U_1}\frac{\partial p}{\partial U_{5+k}} - \frac{U_{1+n}}{U_1}\frac{\partial \Pi_{ni}}{\partial U_{5+k}} \\
a^i_{5+j\,1} =& -\frac{1}{U_1^2}\left(U_{1+i}U_{5+j} - U_{1+j}U_{5+i}\right) \\
a^i_{5+j\,1+k} =& \frac{1}{U_1}\left(\delta_{ik}U_{5+j} - \delta_{jk}U_{5+i}\right) \\
a^i_{5+j\,5+k} =& \frac{1}{U_1}\left(\delta_{jk}U_{1+i} - \delta_{ik}U_{1+j}\right)
\end{aligned}
$$

Table A.3 Visco-resistive Plasma Dynamics b_{irs} Jacobian.

0	0	0	0
$-\dfrac{\partial \tau_{ji}}{\partial U_1}$	$-\dfrac{\partial \tau_{ji}}{\partial U_{1+k}}$	0	0
$b^i_{5\,1}$	$b^i_{5\,1+k}$	$b^i_{5\,5}$	$\dfrac{\partial h_i}{\partial U_{5+k}} + \dfrac{\partial h^m_i}{\partial U_{5+k}}$
0	0	0	0

$$
\begin{aligned}
b^i_{5\,1} =& \frac{U_{1+n}}{U_1^2}\tau_{ni} - \frac{U_{1+n}}{U_1}\frac{\partial \tau_{ni}}{\partial U_1} + \frac{\partial h_i}{\partial U_1} \\
b^i_{5\,1+k} =& -\frac{\tau_{ki}}{U_1} - \frac{U_{1+n}}{U_1}\frac{\partial \tau_{ni}}{\partial U_{1+k}} + \frac{\partial h_i}{\partial U_{1+k}} \\
b^i_{5\,5} =& -\frac{U_{1+n}}{U_1}\frac{\partial \tau_{ni}}{\partial U_5} + \frac{\partial h_i}{\partial U_5}
\end{aligned}
$$

Table A.4 Visco-resistive Plasma Dynamics c_{ijrs} Jacobian.

0	0	0	0
$-\dfrac{\partial \tau_{ni}}{\partial U_{1,j}}$	$-\dfrac{\partial \tau_{ni}}{\partial U_{1+k,j}}$	0	0
$c^i_{5\,1}$	$c^i_{5\,1+k}$	$\dfrac{\partial h_i}{\partial U_{5,j}}$	$\dfrac{\partial h_i}{\partial U_{5+k,j}} + \dfrac{\partial h^m_i}{\partial U_{5+k,j}}$
0	0	0	$-\lambda^m \delta_{js}\delta_{ik}$

$$
\begin{aligned}
c^i_{5\,1} =& -\frac{U_{1+n}}{U_1}\frac{\partial \tau_{ni}}{\partial U_{1,j}} + \frac{\partial h_i}{\partial U_{1,j}} \\
c^i_{5\,1+k} =& -\frac{U_{1+n}}{U_1}\frac{\partial \tau_{ni}}{\partial U_{1+k,j}} + \frac{\partial h_i}{\partial U_{1+k,j}}
\end{aligned}
$$

A.3 Navier-Stokes Jacobians

The Navier-Stokes fluxes given in Equations (2.181) and (2.182) contain fewer terms. The explicit expansion of their respective Jacobians is given in Tables A.5 to A.19.

Table A.5 Navier-Stokes $\mathbf{a}_1$ Jacobian.

0	1	0	0	0
a_{21}^1	$(3-\gamma)\,v_1$	$(1-\gamma)\,v_2$	$(1-\gamma)\,v_3$	$(\gamma-1)$
$-v_1v_2$	v_2	v_1	0	0
$-v_1v_3$	v_3	0	v_1	0
a_{51}^1	a_{52}^1	$(1-\gamma)\,v_1v_2$	$(1-\gamma)\,v_1v_3$	γv_1

$$
\begin{aligned}
a_{21}^1 =& \frac{1}{2}\left((\gamma-3)\,v_1^2+(\gamma-1)\left(v_2^2+v_3^2\right)\right)\\
a_{51}^1 =& -v_1\left((1-\gamma)\left(v_1^2+v_2^2+v_3^2\right)+\gamma e_t\right)\\
a_{52}^1 =& \gamma e_t+\frac{1-\gamma}{2}\left(3v_1^2+v_2^2+v_3^2\right)
\end{aligned}
$$

Table A.6 Navier-Stokes $\mathbf{a}_2$ Jacobian.

0	0	1	0	0
$-v_1v_2$	v_2	v_1	0	0
a_{31}^2	$(1-\gamma)\,v_1$	$(3-\gamma)\,v_2$	$(1-\gamma)\,v_3$	$(\gamma-1)$
$-v_2v_3$	0	v_3	v_2	0
a_{51}^2	$(1-\gamma)\,v_1v_2$	a_{53}^2	$(1-\gamma)\,v_2v_3$	γv_2

$$
\begin{aligned}
a_{31}^2 =& \frac{1}{2}\left((\gamma-3)\,v_2^2+(\gamma-1)\left(v_1^2+v_3^2\right)\right)\\
a_{51}^2 =& -v_2\left((1-\gamma)\left(v_1^2+v_2^2+v_3^2\right)+\gamma e_t\right)\\
a_{53}^2 =& \gamma e_t+\frac{1-\gamma}{2}\left(v_1^2+3v_2^2+v_3^2\right)
\end{aligned}
$$

Table A.7 Navier-Stokes $\mathbf{a}_3$ Jacobian.

0	0	0	1	0
$-v_1 v_3$	v_3	0	v_1	0
$-v_2 v_3$	0	v_3	v_2	0
a^3_{41}	$(1-\gamma)\, v_1$	$(1-\gamma)\, v_2$	$(3-\gamma)\, v_3$	$(\gamma-1)$
a^3_{51}	$(1-\gamma)\, v_1 v_3$	$(1-\gamma)\, v_2 v_3$	a^3_{54}	γv_3

$$
\begin{aligned}
a^3_{41} =& \frac{1}{2}\left((\gamma-3)\, v_3^2 + (\gamma-1)\left(v_1^2 + v_2^2\right)\right) \\
a^3_{51} =& -v_3\left((1-\gamma)\left(v_1^2 + v_2^2 + v_3^2\right) + \gamma e_t\right) \\
a^3_{54} =& \gamma e_t + \frac{1-\gamma}{2}\left(v_1^2 + v_2^2 + 3v_3^2\right)
\end{aligned}
$$

Table A.8 Navier-Stokes $\mathbf{b}_1$ Jacobian.

0	0	0	0	0
b^1_{21}	$\frac{\mu_R \rho_{,1}}{\rho^2}$	$\frac{\lambda \rho_{,2}}{\rho^2}$	$\frac{\lambda \rho_{,3}}{\rho^2}$	0
b^1_{31}	$\frac{\mu \rho_{,2}}{\rho^2}$	$\frac{\mu \rho_{,1}}{\rho^2}$	0	0
b^1_{41}	$\frac{\mu \rho_{,3}}{\rho^2}$	0	$\frac{\mu \rho_{,1}}{\rho^2}$	0
b^1_{51}	b^1_{52}	b^1_{53}	b^1_{54}	$\frac{k \rho_{,1}}{\rho^2 c_v}$

$$
\begin{aligned}
b^1_{21} =& \frac{1}{\rho^2}\left(\mu_R l_{,1} + \lambda\left(m_{,2} + n_{,3}\right) + \mu_R\left(-2v_1\rho_{,1} + v_2\rho_{,2} + v_3\rho_{,3}\right)\right) \\
b^1_{31} =& \frac{\mu}{\rho^2}\left(l_{,2} + m_{,1} - 2\left(v_1\rho_{,2} + v_2\rho_{,1}\right)\right) \\
b^1_{41} =& \frac{\mu}{\rho^2}\left(l_{,3} + n_{,1} - 2\left(v_1\rho_{,3} + v_3\rho_{,1}\right)\right) \\
b^1_{51} =& v_1 b^1_{21} + v_2 b^1_{31} + v_3 b^1_{41} + \frac{1}{\rho}\left(v_1\tau_{11} + v_2\tau_{12} + v_3\tau_{13}\right) \\
& - \frac{k}{\rho^2 c_v}\left(-e_{,1} + \rho_{,1}\left(2e_t - 3\left(v_1^2 + v_2^2 + v_3^2\right)\right) + 2\left(v_1 l_{,1} + v_2 m_{,1} + v_3 n_{,1}\right)\right) \\
b^1_{52} =& v_1 b^1_{22} + v_2 b^1_{32} + v_3 b^1_{42} - \frac{\tau_{11}}{\rho} - \frac{k}{\rho^2 c_v}\left(2v_1\rho_{,1} - l_{,1}\right) \\
b^1_{53} =& v_1 b^1_{23} + v_2 b^1_{33} + v_3 b^1_{43} - \frac{\tau_{12}}{\rho} - \frac{k}{\rho^2 c_v}\left(2v_2\rho_{,1} - m_{,1}\right) \\
b^1_{54} =& v_1 b^1_{24} + v_2 b^1_{34} + v_3 b^1_{44} - \frac{\tau_{13}}{\rho} - \frac{k}{\rho^2 c_v}\left(2v_3\rho_{,1} - n_{,1}\right) \\
\mu_R =& 2\mu + \lambda
\end{aligned}
$$

Table A.9 Navier-Stokes $\mathbf{b}_2$ Jacobian.

0	0	0	0	0
b^1_{31}	b^1_{32}	b^1_{33}	0	0
b^2_{31}	$\frac{\lambda\rho_{,1}}{\rho^2}$	$\frac{\mu_R\rho_{,2}}{\rho^2}$	$\frac{\lambda\rho_{,3}}{\rho^2}$	0
b^2_{41}	0	$\frac{\mu\rho_{,3}}{\rho^2}$	$\frac{\mu\rho_{,2}}{\rho^2}$	0
b^2_{51}	b^2_{52}	b^2_{53}	b^2_{54}	$\frac{k\rho_{,2}}{\rho^2 c_v}$

$$
\begin{aligned}
b^2_{31} =& \frac{1}{\rho^2}\left(\mu_R m_{,2} + \lambda\left(l_{,1} + n_{,3}\right) + \mu_R\left(v_1\rho_{,1} - 2v_2\rho_{,2} + v_3\rho_{,3}\right)\right)\\
b^2_{41} =& \frac{\mu}{\rho^2}\left(m_{,3} + n_{,2} - 2\left(v_2\rho_{,3} + v_3\rho_{,1}\right)\right)\\
b^2_{51} =& v_1 b^2_{21} + v_2 b^2_{31} + v_3 b^2_{41} + \frac{1}{\rho}\left(v_1\tau_{21} + v_2\tau_{22} + v_3\tau_{23}\right)\\
&- \frac{k}{\rho^2 c_v}\left(-e_{,2} + \rho_{,2}\left(2e_t - 3\left(v_1^2 + v_2^2 + v_3^2\right)\right) + 2\left(v_1 l_{,2} + v_2 m_{,2} + v_3 n_{,2}\right)\right)\\
b^2_{52} =& v_1 b^2_{22} + v_2 b^2_{32} + v_3 b^2_{42} - \frac{\tau_{21}}{\rho} - \frac{k}{\rho^2 c_v}\left(2v_1\rho_{,2} - l_{,2}\right)\\
b^2_{53} =& v_1 b^2_{23} + v_2 b^2_{33} + v_3 b^2_{43} - \frac{\tau_{22}}{\rho} - \frac{k}{\rho^2 c_v}\left(2v_2\rho_{,2} - m_{,2}\right)\\
b^2_{54} =& v_1 b^2_{24} + v_2 b^2_{34} + v_3 b^2_{44} - \frac{\tau_{23}}{\rho} - \frac{k}{\rho^2 c_v}\left(2v_3\rho_{,2} - n_{,2}\right)
\end{aligned}
$$

Table A.10 Navier-Stokes $\mathbf{b}_3$ Jacobian.

0	0	0	0	0
b^1_{41}	b^1_{42}	0	b^1_{44}	0
b^2_{41}	0	b^2_{43}	b^2_{44}	0
b^3_{41}	$\dfrac{\lambda\rho_{,1}}{\rho^2}$	$\dfrac{\lambda\rho_{,2}}{\rho^2}$	$\dfrac{\mu_R\rho_{,3}}{\rho^2}$	0
b^3_{51}	b^3_{52}	b^3_{53}	b^3_{54}	$\dfrac{k\rho_{,3}}{\rho^2 c_v}$

$$
\begin{aligned}
b^3_{41} =& \frac{1}{\rho^2}\left(\mu_R n_{,3} + \lambda\left(l_{,1} + m_{,2}\right) + \mu_R\left(v_1\rho_{,1} + v_2\rho_{,2} - 2v_3\rho_{,3}\right)\right)\\
b^3_{51} =& v_1 b^3_{21} + v_2 b^3_{31} + v_3 b^3_{41} + \frac{1}{\rho}\left(v_1\tau_{31} + v_2\tau_{32} + v_3\tau_{33}\right)\\
&- \frac{k}{\rho^2 c_v}\left(-e_{,3} + \rho_{,3}\left(2e_t - 3\left(v_1^2 + v_2^2 + v_3^2\right)\right) + 2\left(v_1 l_{,3} + v_2 m_{,3} + v_3 n_{,3}\right)\right)\\
b^3_{52} =& v_1 b^3_{22} + v_2 b^3_{32} + v_3 b^3_{42} - \frac{\tau_{31}}{\rho} - \frac{k}{\rho^2 c_v}\left(2v_1\rho_{,3} - l_{,3}\right)\\
b^3_{53} =& v_1 b^3_{23} + v_2 b^3_{33} + v_3 b^3_{43} - \frac{\tau_{32}}{\rho} - \frac{k}{\rho^2 c_v}\left(2v_2\rho_{,3} - m_{,3}\right)\\
b^3_{54} =& v_1 b^3_{24} + v_2 b^3_{34} + v_3 b^3_{44} - \frac{\tau_{33}}{\rho} - \frac{k}{\rho^2 c_v}\left(2v_3\rho_{,3} - n_{,3}\right)
\end{aligned}
$$

Table A.11 Navier-Stokes $\mathbf{c}_{11}$ Jacobian.

0	0	0	0	0
$\dfrac{\mu_R v_1}{\rho}$	$\dfrac{-\mu_R}{\rho}$	0	0	0
$\dfrac{\mu v_2}{\rho}$	0	$\dfrac{-\mu}{\rho}$	0	0
$\dfrac{\mu v_3}{\rho}$	0	0	$\dfrac{-\mu}{\rho}$	0
c^{11}_{51}	$v_1\left(c^{11}_{22} + \dfrac{k}{c_v\rho}\right)$	$v_2\left(c^{11}_{33} + \dfrac{k}{c_v\rho}\right)$	$v_3\left(c^{11}_{44} + \dfrac{k}{c_v\rho}\right)$	$\dfrac{-k}{c_v\rho}$

$$
c^{11}_{51} = v_1 c^{11}_{21} + v_2 c^{11}_{31} + v_3 c^{11}_{41} + \frac{k}{c_v\rho}\left(e_t - \left(v_1^2 + v_2^2 + v_3^2\right)\right)
$$

Table A.12 Navier-Stokes $\mathbf{c}_{12}$ Jacobian.

0	0	0	0	0
$\frac{\lambda v_2}{\rho}$	0	$\frac{-\lambda}{\rho}$	0	0
$\frac{\mu v_1}{\rho}$	$\frac{-\mu}{\rho}$	0	0	0
0	0	0	0	0
$(\mu+\lambda)\frac{v_1 v_2}{\rho}$	$\frac{-\mu v_2}{\rho}$	$\frac{-\lambda v_1}{\rho}$	0	0

Table A.13 Navier-Stokes $\mathbf{c}_{13}$ Jacobian.

0	0	0	0	0
$\frac{\lambda v_3}{\rho}$	0	0	$\frac{-\lambda}{\rho}$	0
0	0	0	0	0
$\frac{\mu v_1}{\rho}$	$\frac{-\mu}{\rho}$	0	0	0
$(\mu+\lambda)\frac{v_1 v_3}{\rho}$	$\frac{-\mu v_3}{\rho}$	0	$\frac{-\lambda v_1}{\rho}$	0

Table A.14 Navier-Stokes $\mathbf{c}_{21}$ Jacobian.

0	0	0	0	0
$\frac{\mu v_2}{\rho}$	0	$\frac{-\mu}{\rho}$	0	0
$\frac{\lambda v_1}{\rho}$	$\frac{-\lambda}{\rho}$	0	0	0
0	0	0	0	0
$(\mu+\lambda)\frac{v_2 v_1}{\rho}$	$\frac{-\lambda v_2}{\rho}$	$\frac{-\mu v_1}{\rho}$	0	0

Table A.15 Navier-Stokes $\mathbf{c}_{22}$ Jacobian.

0	0	0	0	0
$\frac{\mu v_1}{\rho}$	$\frac{-\mu}{\rho}$	0	0	0
$\frac{\mu_R v_2}{\rho}$	0	$\frac{-\mu_R}{\rho}$	0	0
$\frac{\mu v_3}{\rho}$	0	0	$\frac{-\mu}{\rho}$	0
c_{51}^{22}	$v_1\left(c_{22}^{22}+\frac{k}{c_v\rho}\right)$	$v_2\left(c_{33}^{22}+\frac{k}{c_v\rho}\right)$	$v_3\left(c_{44}^{22}+\frac{k}{c_v\rho}\right)$	$\frac{-k}{c_v\rho}$

$$c_{51}^{22} = v_1 c_{21}^{22} + v_2 c_{31}^{22} + v_3 c_{41}^{22} + \frac{k}{c_v \rho}\left(e_t - \left(v_1^2 + v_2^2 + v_3^2\right)\right)$$

Table A.16 Navier-Stokes $\mathbf{c}_{23}$ Jacobian.

0	0	0	0	0
0	0	0	0	0
$\frac{\lambda v_3}{\rho}$	0	0	$\frac{-\lambda}{\rho}$	0
$\frac{\mu v_2}{\rho}$	0	$\frac{-\mu}{\rho}$	0	0
$(\mu+\lambda)\frac{v_2 v_3}{\rho}$	0	$\frac{-\mu v_3}{\rho}$	$\frac{-\lambda v_2}{\rho}$	0

Table A.17 Navier-Stokes $\mathbf{c}_{31}$ Jacobian.

0	0	0	0	0
$\frac{\mu v_3}{\rho}$	0	0	$\frac{-\mu}{\rho}$	0
0	0	0	0	0
$\frac{\lambda v_1}{\rho}$	$\frac{-\lambda}{\rho}$	0	0	0
$(\mu+\lambda)\frac{v_3 v_1}{\rho}$	$\frac{-\lambda v_3}{\rho}$	0	$\frac{-\mu v_1}{\rho}$	0

Table A.18 Navier-Stokes $\mathbf{c}_{32}$ Jacobian.

0	0	0	0	0
0	0	0	0	0
$\frac{\mu v_3}{\rho}$	0	0	$\frac{-\mu}{\rho}$	0
$\frac{\lambda v_2}{\rho}$	0	$\frac{-\lambda}{\rho}$	0	0
$(\mu+\lambda)\frac{v_3 v_2}{\rho}$	0	$\frac{-\lambda v_3}{\rho}$	$\frac{-\mu v_2}{\rho}$	0

Table A.19 Navier-Stokes $\mathbf{c}_{33}$ Jacobian.

0	0	0	0	0
$\frac{\mu v_1}{\rho}$	$\frac{-\mu}{\rho}$	0	0	0
$\frac{\mu v_2}{\rho}$	0	$\frac{-\mu}{\rho}$	0	0
$\frac{\mu_R v_3}{\rho}$	0	0	$\frac{-\mu_R}{\rho}$	0
c_{51}^{33}	$v_1\left(c_{22}^{33}+\frac{k}{c_v\rho}\right)$	$v_2\left(c_{33}^{33}+\frac{k}{c_v\rho}\right)$	$v_3\left(c_{44}^{33}+\frac{k}{c_v\rho}\right)$	$\frac{-k}{c_v\rho}$

$$c_{51}^{33} = v_1 c_{21}^{33} + v_2 c_{31}^{33} + v_3 c_{41}^{33} + \frac{k}{c_v\rho}\left(e_t - \left(v_1^2+v_2^2+v_3^2\right)\right)$$

APPENDIX B

SHAPE FUNCTIONS AND METRIC CALCULATIONS

The shape functions (also called trial functions) module is one of the most important parts of any finite element computer implementation. The selection of the type of elements is also a critical decision especially when higher order calculations are required. Incomplete polynomial elements, like serendipity elements, are not suitable for such a task. Their missing modes will, in general, show shortcomings in complex physical phenomena like turbulence and acoustics.

In this work the Lagrange polynomial elements are selected for 1/2/3D calculations. The elements geometry is generated to be linear, then converted to the desired higher order. The conversion is accomplished by pre-processing of the grid and inserting new nodes within the originally linear elements. The newly inserted nodes are placed such that they best represent their numbering position by linear interpolation of the original nodes. In this setup, the elements geometry is always linear and the variables are of higher order. The developed computer implementation allows for arbitrary choice of the higher order accuracy.

Any newly inserted node between neighboring elements is checked for uniqueness. This is ensured via dissolving the grid into its building blocks. For 1D geome-

tries, the grid is converted to a list of segments connecting neighboring nodes, and for 2D geometries, a list of surfaces is also generated along with the list of segments. For 3D geometries, lists of segments, surfaces, and volumes are processed.

In this appendix the necessary mathematics for the shape functions and metric calculations are introduced. The details of the Lagrange polynomial family of elements is explained in Section B.1, and Section B.2 introduces the metric calculations needed for the derivative calculations in the finite element equations.

B.1 Lagrange Polynomial Family of Elements

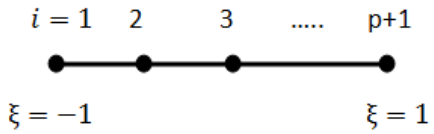

Figure B.1 Higher order 1D Lagrange element.

Consider the 1D element given in Figure B.1. The Lagrange polynomials, given by [52]:

$$L_i^p(\xi) = \prod_{\substack{m=1 \\ m \neq i}}^{p+1} \frac{\xi - \xi_m}{\xi_i - \xi_m}, \tag{B.1}$$

can be used in finite element calculations. Where p is the polynomial order, ξ is the natural coordinate of the 1D element, and i is the nodes index.

Differentiating the Lagrange polynomial given in Equation B.1 *w.r.t.* ξ we get

$$\frac{\partial L_i^p}{\partial \xi}(\xi) = \sum_{\substack{n=1 \\ n \neq i}}^{p+1} \frac{1}{\xi_i - \xi_n} \prod_{\substack{m=1 \\ m \neq i \\ m \neq n}}^{p+1} \frac{\xi - \xi_m}{\xi_i - \xi_m}. \tag{B.2}$$

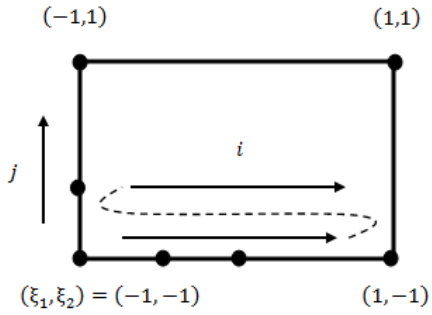

Figure B.2 Higher order 2D Lagrange element.

The shape functions of the higher order 2D Lagrange element, shown on Figure B.2, are given from Equation B.1 by

$$L_{ij}^{pp}(\xi_1, \xi_2) = L_i^p(\xi_1) L_j^p(\xi_2). \tag{B.3}$$

The same higher order polynomial of degree p is chosen for both of the 2D coordinates. The derivatives can be calculated by

$$\frac{\partial L_{ij}^{pp}}{\partial \xi_1}(\xi_1, \xi_2) = \frac{\partial L_i^p(\xi_1)}{\partial \xi_1} L_j^p(\xi_2), \tag{B.4}$$

and

$$\frac{\partial L_{ij}^{pp}}{\partial \xi_2}(\xi_1, \xi_2) = L_i^p(\xi_1) \frac{\partial L_j^p(\xi_2)}{\partial \xi_2}. \tag{B.5}$$

Similarly for 3D Lagrange elements, the shape functions and their derivatives are given by

$$L_{ijk}^{ppp}(\xi_1, \xi_2, \xi_3) = L_i^p(\xi_1) L_j^p(\xi_2) L_k^p(\xi_3), \tag{B.6}$$

$$\frac{\partial L_{ijk}^{ppp}}{\partial \xi_1}(\xi_1, \xi_2, \xi_3) = \frac{\partial L_i^p(\xi_1)}{\partial \xi_1} L_j^p(\xi_2) L_k^p(\xi_3), \tag{B.7}$$

$$\frac{\partial L_{ijk}^{ppp}}{\partial \xi_2}(\xi_1, \xi_2, \xi_3) = L_i^p(\xi_1) \frac{\partial L_j^p(\xi_2)}{\partial \xi_2} L_k^p(\xi_3), \tag{B.8}$$

and

$$\frac{\partial L_{ijk}^{ppp}}{\partial \xi_3}(\xi_1, \xi_2, \xi_3) = L_i^p(\xi_1) L_j^p(\xi_2) \frac{\partial L_k^p(\xi_3)}{\partial \xi_3}. \tag{B.9}$$

Again the same polynomial order, p, is assumed for all of the 3D coordinates.

B.2 Derivative Terms Calculation

Since the shape functions are written as functions of the natural coordinates, a metric Jacobian is necessary for derivatives calculations. Consider the derivative of the general variable u *w.r.t.* the natural coordinates system ξ_i given by

$$\frac{\partial u}{\partial \xi_i} = J_{ij} \frac{\partial u}{\partial x_j}, \tag{B.10}$$

where x_i is the system of real spacial coordinates, and J_{ji} is the metric Jacobian given by

$$J_{ij} = \frac{\partial x_j}{\partial \xi_i}. \tag{B.11}$$

In order to obtain the derivatives *w.r.t.* the x_i spacial coordinates system, an inversion of J_{ij} needs to be calculated.

$$\frac{\partial u}{\partial x_i} = J_{ij}^{-1} \frac{\partial u}{\partial \xi_j}, \tag{B.12}$$

where J_{ij}^{-1} is the inverse Jacobian. For 1D grids the metric Jacobian is a scalar and the calculation of the inverse is trivial. Whereas for 2D (3D) cases, the metric Jacobian is a 2×2 (3×3) matrix. Cramer's rule is one of the direct methods for calculating the inverse of such small rank matrices.

APPENDIX C

BOUNDARY CONDITIONS IMPLEMENTATION

Different application problems require different boundary conditions depending on their nature. The boundary conditions necessary for a certain application problem can be determined based on the involved physics, *i.e.* the set of equations governing the problem, and the flow situation at hand. Efficient implementation of these different boundary conditions is a crucial step in developing any computational tool. This is especially important for higher order methods where numerical accuracy of the boundary conditions can affect adversely on the accuracy of the solution domain. In order to preserve the solution accuracy, the boundary conditions implementation has to be at least of the same order of accuracy has the internal domain approximation. The implementation has also to be general enough to be able to include all possible flow situations that might rise up in the studied applications.

All the test cases introduced in this dissertation for the one-fluid plasma dynamics and the two problems of the freely decaying isotropic and anisotropic turbulence required the periodic boundary conditions. The test cases of the fluid dynamics verification discussed in Section 5.2 required a more comprehensive list of boundary

conditions. To this end, the discussion in this appendix is limited to the boundary conditions of the full Navier-Stokes equations introduced in Section 2.4.

An extension to the work of Poinsot and Lele [76] to the arbitrarily higher order implicit finite element applications is introduced in this appendix. Poinsot and Lele [76] formulated the boundary conditions of the Navier-Stokes equations from a mathematical and physical point of view. Then they implemented their formulation in the FDM/FVM context. To extend Poinsot and Lele [76] formulation into the implicit finite element context, while preserving the order of accuracy of the solution, one has to base all derivatives on the used shape functions.

To this end, the conservation variables has to be transformed to the characteristic variables. This can be done according to the analysis given in Hirsch [70]:

$$\delta \mathbf{W} = \mathbf{P}^{-1} \delta \mathbf{U}, \tag{C.1}$$

where $\mathbf{U}$, $\mathbf{W}$, and $\mathbf{P}^{-1}$ are the conservation variables vector, the characteristic variables vector, and the conversion matrix, respectively.

For example, the non-reflective subsonic outflow boundary condition is given in Poinsot and Lele [76] by

$$\frac{\partial W_1}{\partial x_n} = K \left(p - p_\infty \right), \tag{C.2}$$

where x_n is the normal direction tot he boundary, K is a constant, and p_∞ is the back pressure imposed in the far stream. Using Equation (C.1), this can be written as:

$$\left(P^{-1}\right)_1 \frac{\partial U}{\partial x_n} = K\left(p - p_\infty\right), \tag{C.3}$$

which can be used in the system matrix instead of the energy equation for all the nodes on the subsonic outflow boundary. Note that in this formulation, the boundary conditions are written *w.r.t.* to the conservation variable which conserves the order of accuracy of the solution.

REFERENCES

[1] J. L. Williams and A. F. Alhajji. The coming energy crisis? `http://www.wtrg.com/EnergyCrisis/index.html`, February 2003.

[2] John Wesson. *Tokamaks*. Clarendon Press-Oxford, third edition, 2004.

[3] Hans Peter Goedbloed and Stefaan Poedts. *Principles of Magnetohydrodynamics, with Applications to Laboratory and Astrophysical Plasmas*. Cambridge University Press, 2004.

[4] H. Weller and H. G. Weller. A high-order arbitrarily unstructured finite-volume model of the global atmosphere: Tests solving the shallow-water equations. *International Journal for Numerical Methods in Fluids*, 56:1589–1596, 2008.

[5] Z. J. Wang and Y. Liu. Spectral (finite) volume method for conservation laws on unstructured grids III: One dimensional systems and partition optimization. *Journal of Scientific Computing*, 20(1):137–157, 2004.

[6] Ionut Porumbel. *Large Eddy Simulation of bluff body stabilized premixed and partially premixed combustion*. PhD thesis in aerospace engineering, Georgia Institute of Technology, 2006.

[7] P. Colella, M. Dorr, J. Hittinger, D. F. Martin, and P. McCorquodale. High-order finite-volume adaptive methods on locally rectangular grids. *J. Phy.: Conference Series*, 180, 2009.

[8] Volker John and Gunar Matthies. Higher-order finite element discretizations in a benchmark problem for incompressible flows. *nt. j. num. meth. fluids*, 37:885–903, 2001.

[9] Z. Yosibash, R. M. Kirby, K. Myers, B. Szabo, and G. Karniadakis. High-order finite elements for fluid-structure interaction problems. *Int. J. Num. Meth. Fluids*, 56:1589–1596, 2008.

[10] D. L. Bonhaus. *A higher order accurate finite element method for viscous compressible flows*. PhD thesis in aerospace and ocean engineering, Virginia Polytechnic Institute and State University, 1998.

[11] R. Lohner, K. Morgan, and O. C. Zienkiewiez. The solution of non linear hyperbolic equation systems by the finite element method. *Int. J. Num. Meth. Fluids*, 4:1043–1063, 1984.

[12] J. Donea. A Taylor Galerkin method for convective transport problems. *Int. J. Numer. Meth. Eng.*, 20:101–119, 1984.

[13] J. T. Oden, T. Strouboulis, and P. Devloo. Adaptive finite element methods for high speed compressible flows. *Int. J. Num. Meth. Fluids*, 7:1211–1228, 1987.

[14] J. F. Polk and P. P. Lynn. A least squares finite element approach to unsteady gas dynamics. *Int. J. Num. Meth. Eng.*, 12:3–10, 1978.

[15] H. Nguyen and J. Reynen. A space-time least square finite element scheme for advection diffusion equations. *Comp. Meth. Appl. Mech. Eng.*, 42:331–342, 1984.

[16] B. N. Jiang and L. A. Povinelli. Least squares finite element method for fluid dynamics. *Comp. Meth. Appl. Mech. Eng.*, 81(3):13–37, 1990.

[17] A. L. Brooks and T. J. R. Hughes. Streamline upwind Petrov-Galerkin formulations for convection dominated flows with particular emphasis on the incompressible Navier-Stokes equations. *Comp. Meth. Appl. Mech. Eng.*, 32:199–259, 1982.

[18] F. Shakib, T. J. R. Hughes, and Z. Johan. A new finite element formulation for computational fluid dynamics: X. the compressible Euler and Navier-Stokes equations. *Comp. Meth. Appl. Mech. Eng.*, 89:141–219, 1991.

[19] T. J. R. Hughes and M. Mallet. A new finite element formulation for computational fluid dynamics: IV. a discontinuity capturing operator for multidimensional advective diffusive systems. *Comp. Meth. Appl. Mech. Eng.*, 58(3):329–339, 1986.

[20] T. J. Chung. Transitions and interactions of inviscid/viscous, compressible/incompressible and laminar/turbulent flows. *Int. J. Numer. Meth. Fluids*, 31:223–246, 1999.

[21] G. Schunk, F. Gunabal, G. Heard, and T. J. Chung. Unified CFD methods via flowfield-dependent variation theory. In *Proceedings of AIAA 30th Fluid Dyn. Conf.*, pages AIAA Paper 99–3715, Norfolk, Virginia, 1999.

[22] K. T. Yoon and T. J. Chung. Three dimensional mixed explicit-implicit generalized Galerkin spectral elements methods for high speed turbulent compressible flows. *Comp. Meth. Appl. Mech. Eng.*, 135:343–367, 1996.

[23] K. T. Yoon, S. Y. Moon, S. A. Garcia, G. W. Heard, and T. J. Chung. Flowfield-dependent mixed explicit (FDMEI) methods for high and low speed and compressible and incompressible flows. *Comp. Meth. Appl. Mech. Eng.*, 151:75–104, 1998.

[24] A. A. Megahed, M. W. El-Mallah, and B. Girgis. A modified flowfield dependent variation method applied to the compressible Euler flow equations. In *Proceedings of 8th Int. Con. Fluid Dyn. and Prop.*, pages ICFDP8–EG–102, Sharm El-Sheikh, Egypt, 2006.

[25] S. Y. Moon, C. H. Sohn, and C. W. Lee. Applications of a flowfield-dependent mixed explicit-implicit (FDMEI) method to heat and fluid dynamics problems. *Numr. Heat Transfer*, 39:389–404, 2001.

[26] F. Canabal. *Suppression of the ignition overpressure generated by launch vehicles*. PhD Thesis in Mechanical Engineering, University of Alabama in Huntsville, 2004.

[27] F. Canabal and A. Frendi. Study of the ignition over-pressure suppression technique by water addition. *Spacecraft and Rockets*, 43(4):853–865, 2006.

[28] G. A. Richardson and T. J. Chung. Computational relativistic astrophysics using the flow field-dependent variation theory. *The Astrophysical Journal Supplement Series*, 139:539563, 2002.

[29] G. A. Richardson, J. T. Cassibry, T. J. Chung, and S. T. Wu. Finite element form of fdv for widely varying flowfields. *Journal of Computational Physics*, 229:145167, 2010.

[30] G. Karypis and V. Kumar. *METIS: unstructured graph partitioning and sparse matrix ordering system*. Technical Report, Department of Computer Science, University of Minnesota, 1995.

[31] T. J. Chung. *Computational Fluid Dynamics*. Cambridge University Press, 2002.

[32] B. Girgis. Flowfield dependent variation method applied to compressible euler flow equations. Masters thesis in engineering mathematics and physics, Cairo University, 2007.

[33] Y. Saad and M. H. Schultz. Gmres: a generalized minimal residual algorithm for solving nonsymmetric linear systems. *SIAM J. Sci Statist. Comput.*, 7(3):856–869, 1986.

[34] Y. Saad. Preconditioning techniques for indefinite and nonsymmertic linear systems. *J. Comput. Appl. Math.*, 24:89–105, 1988.

[35] Y. Saad. *Iterative Methods for Sparse Linear Systems*. SIAM, Philadelphia, PA, 2nd edition, 2003.

[36] J. Shadid, S. Hutchinson, G. Hennigan, H. Moffat, K. Devine, and A. G. Salinger. Efficient parallel computation of unstructured finite element reacting flow simulations. *Parallel Computing*, 23:1307–1325, 1997.

[37] T. J. R. Hughes, I. Levit, and J. Winget. An element-by-element implicit algorithm for heat conduction. *ASCE J. Engrg. Mech. Div.*, 74:271–287, 1983.

[38] Z. Johan and T.J.R. Hughes. A globally convergent matrix-free algorithm for implicit time-marching schemes arising in finite element analysis in fluids. *Comput. Methods App. Mech. Engrg.*, 87(2-3):281–304, 1991.

[39] Z. Johan, K.K. Mathur, S.L. Johnsson, and T.J.R. Hughes. An efficient communication strategy for finite element methods on the Connection Machine CM-5 system. *Comput. Methods Appl. Mech Engrg.*, 113:363–387, 1994.

[40] Z. Johan, K.K. Mathur, S.L. Johnsson, and T.J.R. Hughes. Scalability of finite element applications on distributed-memory parallel computers. *Comput. Methods Appl. Mech Engrg.*, 119:61–72, 1994.

[41] Z. Johan, K.K. Mathur, S.L. Johnsson, and T.J.R. Hughes. A case study in parallel computation: Viscous flow around an onera m6 wing. *Int. J. Numer. Methods Fluids*, 21:877–884, 1995.

[42] T. E. Tezduyar, S. Aliabadi, M. Behr, A. Johnson, and S. Mittal. Parallel finite-element computation of 3d flows. *Computer*, 26:27–36, 1993.

[43] T. E. Tezduyar and A. Sameh. Parallel finite element computations in fluid mechanics. *Comput. Methods Appl. Mech. Engrg.*, 195:1872–1884, 2006.

[44] A. Tezuka, J. Matsumoto, T. Suzuki, and K. Matsubara. A platform for parallel cfd fem computations. *Int. J. Comput. Fluid Dyn.*, 19(3):235–242, 2005.

[45] C. A. Rivera, M. Heniche, R. Glowinski, and P. A. Tanguy. Parallel finite elment simulations of incompressible viscous fluid flow by domain decomposition with lagrange multipliers. *Journal of Computational Physics*, 229:5123–5143, 2010.

[46] M. Sosonkina and Y. Saad. Using the parallel algebraic recursive multilevel solver in modern physical applications. *Future Generation Computer Systems*, 20:489–500, 2004.

[47] Pascal Henon and Yousef Saad. A parallel multistage ILU factorization based on a hierarchical graph decomposition. *SIAM Journal on Scientific Computing*, 28(6):2266–2293, 2006.

[48] S. Behara and S. Mittal. Parallel finite element computation of incompressible flows. *Parallel Comput.*, 35:195–212, 2009.

[49] Chi Shen, Jun Zhang, and Kai Wang. Distributed block independent set algorithms and parallel multilevel ilu preconditioners. *Journal of Parallel and Distributed Computing*, 65(3):331–346, 2005.

[50] O. Staff and S. Wille. Parallel ILU preconditioning and parallel mesh adaptation with load balancing for general domain decompositions for the Navier-Stokes equations. *Int. J. Numer. Methods Fluids*, 47:1301–1306, 2005.

[51] Takeshi Iwashita, Yuuichi Nakanishi, and Masaaki Shimasaki. Comparison criteria for parallel orderings in ILU preconditioning. *SIAM Journal on Scientific Computing*, 26(4):1234–1260, 2005.

[52] O. C. Zienkiewicz, R. L. Taylor, and J. Z. Zhu. *The Finite Element Method: Its Basis and Fundamentals*. Elsevier, sixth edition, 2005.

[53] C. J. Roy, C. C. Nelson, T. M. Smith, and C. C. Ober. Verification of euler/navier-stokes codes using method of manufactured solutions. *Int. J. Numer. Meth. Fluids*, 44:599–620, 2004.

[54] A. Frendi and B. Girgis. A High Order Accuracy Computational Tool for Unsteady Turbulent Flows and Acoustics. NASA SBIR Phase I: Contract Num. NNX-11CD-05P, Final Report, Septemper 2011.

[55] E. Erturk, T. C. Corke, and C. Gökçöl. Numerical solutions of 2-d steady incompressible driven cavity flow at high Reynolds numbers. *Int. J. Numer. Meth. Fluids*, 48:747 – 774, 2005.

[56] U. Ghia, K. N. Ghia, and C. T. Shin. High-Re solutions for incompressible flow using the Navier-Stokes equations and a multigrid method. *J. Comput. Phys.*, 48(3):387 – 411, 1982.

[57] D. C. Lo, K. Murugesan, and D. L. Young. Numerical solution of the three-dimensional velocity-vorticity navier-stokes equations by finite difference method. *Int. J. Num. Meth. Fluids*, 47:1469–1487, 2005.

[58] David K. Gartling. A test problem for outflow boundary conditions – flow over a backward-facing step. *Int. J. Numer. Meth. Fluids*, 11:953 – 967, 1990.

[59] E. Erturk. Numerical solutions of 2-d steady incompressible flow over a backward-facing step, Part I: High Reynolds number solutions. *Computers and Fluids*, 37:633 – 655, 2008.

[60] C. Tam and J. Webb. Dispersion-relation-preserving finite difference schemes for computational acoustics. *J. Comput. Physics*, 107:262–281, 1993.

[61] John D. Anderson. *Modern Compressible Flow; with Historical Perspective*. McGraw-Hill, third edition, 2004.

[62] James E. Carter. Numerical solutions of the Navier-Stokes equations for the supersonic laminar flow over a two-dimensional compression corner. Technical report, Langley Research Center, Hampton, VA 23365, July 1972.

[63] G. W. Heard. *Flowfield-Dependent Variation (FDV) method for compressible, incompressible, viscous, and inviscid flow interactions with FDV adaptive mesh refinements and parallel processing*. PhD dissertation, The University of Alabama in Huntsville, 2007.

[64] John Eldon Lewis. *Experimental investigation of supersonic laminar, two-dimensional boundary layer separation in a compression corner with and without cooling*. PhD thesis in aeronautics, California Institute of Technology, 1967.

[65] F. Li and L. Xu. Arbitrary order exactly divergence-free central discontinuous Galerkin methods for ideal MHD equations. *Journal of Computational Physics*, 231:2655–2675, March 2012.

[66] Wenlong Dai and Paul R. Woodward. An approximate riemann solver for ideal magnetohydrodynamics. *Journal of Computational Physics*, 111(2):354 – 372, 1994.

[67] D. Ryu and T. W. Jones. Numerical magetohydrodynamics in astrophysics: Algorithm and tests for one-dimensional flow. *The Astrophysical Journal*, 442:228–258, March 1995.

[68] K. Waagan, C. Federrath, and C. Klingenberg. A robust numerical scheme for highly compressible magnetohydrodynamics: Nonlinear stability, implementation and tests. *Journal of Computational Physics*, 230(9):3331 – 3351, 2011.

[69] R. Samtaney, D. I. Pullin, and B. Kosovic. Direct numerical simulation of decaying compressible turbulence and shocklet statistics. *Physics of Fluids*, 13:1415–1430, 2001.

[70] C. Hirsch. *Numerical Computation of Internal and External Flows: The Fundamentals of Computational Fluid Dynamics*. Number v. 1. Elsevier Science, 2007.

[71] Lony L. Thompson and Peter M. Pinsky. Complex wavenumber fourier analysis of the p-version finite element method. *Computational Mechanics*, 13(4):255–275, 1994.

[72] S. B. Pope. *Turbulent Flows*. Cambridge University Press, 2000.

[73] P.A. Davidson. *An Introduction to Magnetohydrodynamics*. Cambridge Texts in Applied Mathematics. Cambridge University Press, 2001.

[74] P.A. Davidson. *Turbulence : An Introduction for Scientists and Engineers: An Introduction for Scientists and Engineers*. Oxford University Press, 2004.

[75] J. C. Richard, B. M. Riley, and S. S. Girimaji. Magnetohydrodynamic turbulence decay under the influence of uniform or random magnetic fields. *J. Fluids Eng.*, 133, 2011.

[76] T.J Poinsot and S.K Lelef. Boundary conditions for direct simulations of compressible viscous flows. *Journal of Computational Physics*, 101(1):104 – 129, 1992.